

Graphene-based materials with tailored nanostructures for energy conversion and storage



Yingkui Yang^{a,b,c,*}, Cuiping Han^a, Beibei Jiang^a, James Iocozzia^a, Chengen He^{b,c},
Dean Shi^{b,c}, Tao Jiang^{b,c}, Zhiqun Lin^{a,*}

^aSchool of Materials Science and Engineering, Georgia Institute of Technology, Atlanta, GA 30332, USA

^bMOE Key Laboratory for Green Preparation and Application of Functional Materials, and Hubei Collaborative Innovation Center for Advanced Organic Chemical Materials, Hubei University, Wuhan 430062, China

^cSchool of Materials Science and Engineering, Hubei University, Wuhan 430062, China

ARTICLE INFO

Article history:
Available online

Keywords:
Graphene
Nanostructures
Nanocomposites
Graphene-based materials
Energy storage
Energy conversion

ABSTRACT

Intensive interest in graphene has centered on its unique 2D crystal lattice and remarkable properties that offer unique opportunities to address ever-increasing global energy demands. The past years have witnessed considerable advances in the fabrication of graphene-based materials and significant breakthroughs in advanced energy applications. In this Review, two methodologies for graphene production, namely, the bottom-up growth from hydrocarbon precursors and the top-down exfoliation of graphite (to graphene) and graphite oxide (to graphene oxide followed by reduction) are first summarized. The advantages and disadvantages of these methods regarding their accessibility, scalability, graphene quality, and inherent properties are compared. Particular attention is concentrated on tailored nanostructures, electronic properties, and surface activities of these intriguing materials. The preparation of graphene-based composites containing a wide range of active constituents (e.g., transition metals, metal oxides, and conducting polymers) by *in-situ* hybridization and *ex-situ* recombination is also discussed with an emphasis on their microstructures and hybrid architectures. This Review is devoted largely to current developments of graphene and its derivatives and composites in energy conversion (i.e., polymer solar cells, dye-sensitized solar cells, perovskite solar cells, and fuel cells) and energy storage (i.e., lithium-ion batteries and supercapacitors) on the basis of their intrinsic attributes in improving photovoltaic and electrochemical performance. By critically evaluating the relationship between the nanostructures and the device performance, we intend to provide general guidelines for the design of advanced graphene-based materials with structure-to-property tailored toward specific requirements for targeted energy applications. Lastly, the potential issues and the perspective for future research in graphene-based materials for energy applications are also presented.

Abbreviations: AFC, alkaline fuel cell; AFM, atomic force microscopy; BET, Brunauer-Emmett-Teller; BHJ, bulk-heterojunction; CNT, carbon nanotube; CTAB, cetyltrimethyl ammonium bromide; CVD, chemical vapor deposition; CV, cyclic voltammetry; DMAC, *N,N'*-dimethylacetamide; DMF, *N,N'*-dimethylformamide; DMFC, direct-methanol fuel cells; DMSO, dimethyl sulfoxide; DSSC, dye-sensitized solar cell; ECSA, electrochemically-active surface area; EDLC, electric double-layer capacitors; EIS, electrochemical impedance spectroscopy; ETL, electron transport layer; FOM, figure of merit; FTO, fluorine doped tin oxide (FTO); GBM, graphene-based material; GIC, graphite intercalated compound; GO, graphene oxide; GQD, graphene quantum dot; HF, hydrofluoric acid; HOMO, highest occupied molecular orbital; HOPG, highly oriented pyrolytic graphite; HRTEM, high resolution transmission electron microscopy; HTL, hole transport layer; IPA, Isopropanol; IPCE, incident photon-to-current conversion efficiency; ITO, indium tin oxide; LBL, layer-by-layer; LED, light-emitting diode; LIB, lithium-ion battery; LUMO, lowest unoccupied molecular orbital; MCFC, molten-carbonate fuel cell; MOR, methanol oxidation reaction; MPECVD, microwave plasma-enhanced CVD; MPN, 3-methoxypropionitrile; NMP, *N*-methylpyrrolidone; ORR, oxygen reduction reaction; PAA, poly(acrylic acid); PAFC, phosphoric-acid fuel cell; PANI, polyaniline; PC, propylene carbonate; PCBM, [6,6]-phenyl C₆₁-butyric acid methyl ester; PC71BM, [6,6]-phenyl C₇₁-butyric acid methyl ester; PCE, power conversion efficiency; PDAA, poly(diallyldimethylammonium chloride); PEDOT, poly(3,4-ethylenedioxythiophene); PEG, poly(ethylene glycol); PEM, polymer electrolyte membrane; PEMFC, polymer-electrolyte membrane fuel cell; PEO, polyethylene oxide; PET, poly(ethylene terephthalate); P3HT, poly(3-hexylthiophene); PMIL, 1-propyl-3-methyl imidazolium iodide; P3OT, poly(3-octylthiophene); PPy, polypyrrole; PS-*b*-PMMA, poly(styrene-*b*-methyl methacrylate); PSC, polymer solar cell; PSS, polystyrene sulfonate; PVSC, perovskite solar cell; QD, quantum dot; QSSE, quasi-solid-state-electrolyte; RGO, reduced GO or reduced graphene oxide; RIE, reactive ion etching; SAED, selected-area electron diffraction pattern; SDBS, sodium dodecyl benzene sulfonate; SEI, solid electrolyte interphase; SEM, scanning electron micrograph; SOFC, solid-oxide fuel cells; SSA, specific surface area; STM, scanning tunneling microscopy; TCE, transparent conducting electrode; TEM, transmission electron microscopy; vdW, van der Waals; *R*_{CT}, charge-transfer resistance; *FF*, fill factor; δ_T , Hildebrand solubility parameter; *V*_{OC}, open-circuit voltage; γ , surface tension; *R*_s, sheet resistance; *J*_{SC}, short-circuit current density; *T*, transparency (optical).

* Corresponding authors. Tel.: +86 27 8866 1729; fax +86 27 8866 5610 (Y. Yang), Tel.: +1 404 385 4404; fax +1 404 385 3734 (Z. Lin).

E-mail addresses: ykyang@hubu.edu.cn (Y. Yang), zhiqun.lin@mse.gatech.edu (Z. Lin).

By summarizing the current state-of-the-art as well as the exciting achievements from laboratory research, this Review aims to demonstrate that real industrial applications of graphene-based materials are to be expected in the near future. (1346 references).

© 2016 Elsevier B.V. All rights reserved.

Contents

1.	Introduction	2
1.1.	Overview of graphene toward energy applications	3
1.2.	The scope of this review	3
2.	Structure, properties and synthesis of graphene	3
2.1.	Structure and properties	3
2.2.	General synthesis	5
2.2.1.	Exfoliation of graphite	5
2.2.2.	Reduction of graphene oxide	9
2.2.3.	CVD growth	12
2.2.4.	Epitaxial growth	13
3.	Graphene-based materials for lithium-ion batteries	13
3.1.	Graphene-based materials as anodes	13
3.1.1.	Graphene anode	13
3.1.2.	Carbonaceous hybrid anodes	14
3.1.3.	Alloying graphene hybrids	16
3.1.4.	Metal oxide/graphene composites	24
3.2.	Graphene-based materials as cathodes	29
4.	Graphene-based materials for supercapacitors	31
4.1.	Graphene-based materials for electric double-layer capacitors	31
4.1.1.	Graphene paper/film electrodes	31
4.1.2.	3D Graphene-based electrodes	32
4.1.3.	Carbonaceous hybrid electrodes	34
4.1.4.	Volumetric capacitive performance	36
4.2.	Graphene-based materials for pseudocapacitors	37
4.2.1.	Conducting polymer/graphene composites	37
4.2.2.	Metal oxide/graphene composites	38
5.	Graphene-based materials for fuel cells	39
5.1.	Hybrid electrocatalysts	39
5.2.	Electrolyte membranes	43
6.	Graphene-based materials for solar cells	44
6.1.	Graphene-based materials for polymer solar cells	45
6.1.1.	Electron-acceptor materials	45
6.1.2.	Charge transport layers	45
6.1.3.	Intermediate layers for tandem cells	46
6.1.4.	Transparent conducting electrodes	49
6.2.	Graphene-based materials for dye-sensitized solar cells	49
6.2.1.	Counter-electrodes	50
6.2.2.	Photoanodes	53
6.2.3.	Solid state electrolytes	53
6.3.	Graphene-based materials for perovskite solar cells	55
7.	Conclusions and perspectives	57
7.1.	General challenges in production of graphene	57
7.2.	Engineering graphene for future energy applications	58
7.2.1.	Toward electrochemical energy storage	58
7.2.2.	Toward electrochemical energy conversion	59
7.2.3.	Toward solar energy conversion	59
7.2.4.	Toward flexible energy devices	60
	Acknowledgements	60
	References	61

1. Introduction

In response to the limited fossil fuel resources, emerging ecological concerns and global warming, ever-increasing energy consumption and human reliance on energy-based appliances, the emerging development of clean, renewable, and sustainable energy techniques has become increasingly important than ever. In this context, current energy systems including solar cells, [1–3] fuel cells, [4–6] lithium batteries [7–9] and supercapacitors, [10–12] have

attracted much attention in academia and industry alike. It is well known that these energy devices in general possess an active or electrolyte layer sandwiched by two electrodes with their overall performance intrinsically and sensitively dependent on the materials used [13]. Over the past decade, an exciting set of emerging nanomaterials such as nanocarbons, metal-containing compounds and functional nanocomposites with unusual nanoscopic structure-dependent properties, have been largely developed. These materials are promising for fundamental research and

advances in energy conversion and storage applications [14–17]. However, such technologies must meet demanding performance characteristics including large conversion efficiency, high power delivery and energy storage, acceptable performance-to-cost ratio, long-term cyclability, and operational safety. Should these challenges be surmounted, such materials will have applications in consumer electronics, portable devices, electric vehicles, hybrid electric vehicles, and power grids as well as military and industrial technologies. Clearly, the exploration of innovative nanomaterials with tailored nanostructures and desired functionalities for advanced energy applications is a necessary and attractive area of research. To this end, graphene offers unique advantages over conventional nanomaterials, and has motivated tremendous efforts to capitalize on its advantageous attributes for high-performance energy devices.

1.1. Overview of graphene toward energy applications

Graphene is a one-atom-thick layer of sp^2 -hybridized carbons tightly arranged into a 2D honeycomb lattice. Initially labelled as an ‘academic material’, graphene has quickly become a real ‘miracle material’ since its first successful isolation in 2004 [18]. With superior optical transparency (T , 97.7%), high electrical conductivity ($\sim 10^6$ S/cm) and inherent flexibility, graphene is the most promising candidate for the replacement of expensive, brittle indium tin oxide (ITO) as transparent electrodes for next-generation optoelectronics and photovoltaics [19,20]. The high charge mobility ($\sim 2 \times 10^5$ cm²/Vs, 200 times higher than silicon) and electron transport capability of graphene render it a competitive alternative for charge transport and separation layers for solar cells [21–23]. The large specific surface area (SSA, 2630 m²/g), excellent chemical stability and electrochemical activity enable graphene to be either an efficient metal-free electrocatalyst or a catalyst-support for fuel cells [24,25]. The high theoretical specific capacity (744 mAh/g) and specific capacitance (550 F/g) and ultra-large surface-to-volume ratio, when combined with the appealing properties noted above, make graphene an ideal platform for enhanced energy storage and faster transportation of ionic species and electric charges in lithium batteries [26] and supercapacitors [27]. Monolayer graphene also possesses an ultrahigh Young’s modulus of ~ 1.1 TPa, an intrinsic fracture strength of ~ 125 GPa [28] and a high thermal conductivity (5×10^3 W/mK) [29]. Due to these unique multifunctional properties, graphene carries great potential to revolutionize energy conversion and storage [30–32].

In addition, graphene exhibits excellent compatibility with dissimilar active components (such as metal oxides, transition metals and conducting polymers), thereby enabling the fabrication of high-performance graphene-based composites via *in-situ* hybridization and *ex-situ* recombination [33]. In these composites, graphene and active components coexist in various forms of microstructures such as anchored, wrapped, encapsulated, layered, sandwich-like and mixed modes to form 1D, 2D or 3D macroscopic architectures [31,34]. Devices employing such hybrids have considerably improved performance because of their synergistic effects through suppressing the aggregation of graphene and inter-particles, facilitating the charge transfer, electron transport and ion diffusion, enabling the porosity and more exposure of active sites, enhancing the catalytic activity and electrochemical stability and/or buffering the volume variations during the redox reactions and charging/discharging processes. For simplification, graphene and its composites or hybrids are hereafter referred to graphene-based materials (GBMs). Such GBMs, with tailorable nanostructures, can open up new and exciting opportunities to tackle the challenges triggered by the ever-increasing global energy demands.

1.2. The scope of this review

As noted above, graphene carries many unique properties over conventional materials. Hence, research into GBMs has grown at an unprecedented rate. This has given rise to the so-called ‘graphene gold rush’ or ‘graphene fever’ [35]. Clearly, it is timely and necessary to systematically summarize recent progress in GBMs with tailored nanostructures and their impressive applications in energy conversion and storage. Herein, we first describe the state-of-the-art synthesis of graphene based on top-down (mostly derived from graphite) and bottom-up (from hydrocarbons) techniques. Special attention is given to chemical and electronic structures and energy-related properties. Moreover, the advantages and disadvantages of synthetic methods in terms of accessibility, scalability, crystal structures (i.e., crystal quality and intrinsic and extrinsic defects), and inherent properties are compared as well.

Significant advances of GBMs in energy conversion (i.e., fuel cells, polymer solar cells (PSCs), dye-sensitized solar cells (DSSCs), perovskite solar cells (PVSCs)) and energy storage (i.e., lithium-ion batteries (LIBs) and supercapacitors) are then systematically scrutinized. In this section, cell configuration, working principles and current issues for each energy device are first briefly introduced. Device performance is further detailed and critically evaluated by employing GBMs as electrodes, active layers, transport layers and/or electrolytes. We attempt to clarify the relevance of GBMs in the as-fabricated devices with particular emphasis on the relationships between the nanostructures and observed performance characteristics. Representative references are discussed by focusing on new breakthroughs, in which the reported laboratory performance competes with or outperforms commercially available state-of-the-art materials. The benefits of incorporating GBMs in these devices are highlighted by outlining the most significant results. Finally, current issues and an outlook for future research directions of GBMs in respective energy applications are provided.

This Review makes no attempt to be exhaustive although a large amount of work is included. Notably, regardless of what work has been done so far, to be commercially viable, a potential material is required to exhibit the properties surpassing those of existing ones at comparable costs. With the progress continuously being made and the knowledge and technology being gained from engineered GBMs and energy devices built upon them, a transition from the laboratory research to real commercial applications in the near future is likely.

2. Structure, properties and synthesis of graphene

2.1. Structure and properties

Graphene can be considered an isolated single layer (~ 0.34 nm in thickness) of graphite. The lateral size of graphene varies from several nanometers to centimeters depending on the synthetic methods [36–38]. Pristine graphene sheets serve as basic building blocks for all graphitic carbon allotropes. It can be wrapped up into 0D fullerene, rolled into 1D carbon nanotubes (CNTs) and stacked into 3D graphite [35]. Note that graphene is the name initially given to a single-layer (or monolayer) sheet of graphite [18]. The term ‘graphene’ now is frequently prefixed by bi-/double-layer [39–41] and few-layer [42–46] where ‘few’ usually indicates less than 10 layers including bilayers unless otherwise stated [35]. The term ‘multilayer’ [47–49] is also used to define graphene and includes bilayer and few-layer but is not rigorously limited to below 10 layers [50]. In addition, the terms ‘sheet’, [51–53] ‘flake’, [54–56] and ‘platelet’ [57–59] are commonly used as suffixes to describe graphene materials. Generally, the terms ‘sheet’ and

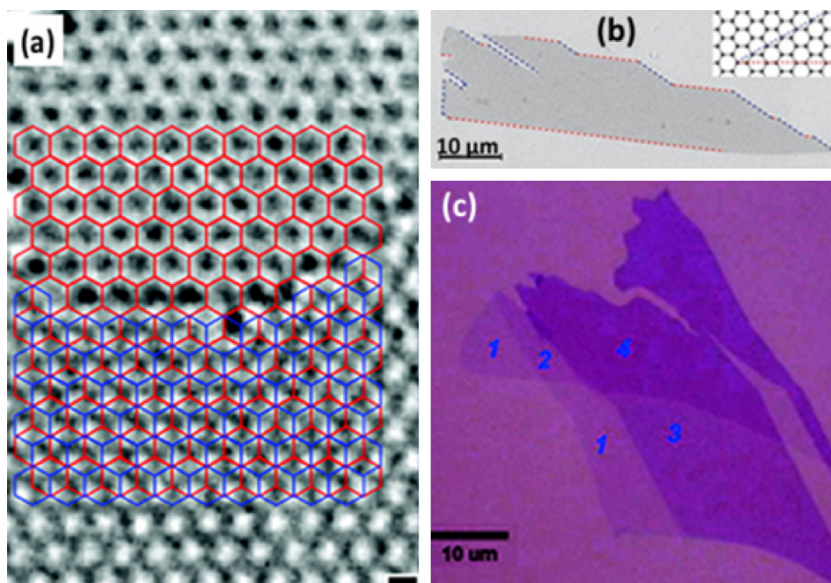


Fig. 1. (a) Graphene imaged by transmission electron aberration-corrected microscope showing a monolayer (upper part), and a bilayer (lower part) with an overlay of graphene lattice (red) and the second layer (blue), offset in the Bernal (AB) stacking of graphite [78]. Copyright 2008 American Chemical Society. (b) Scanning electron micrograph (SEM) of graphene which shows that most of crystal's edges are zigzag (blue lines) and armchair (red lines) configurations [35]. Copyright 2007 Nature Publishing Group. (c) Optical photograph of graphene with one, two, three, and four layers as marked by number [79]. Copyright 2007 American Chemical Society (For interpretation of the references to color in this figure legend, the reader is referred to the web version of this article.).

'flake' correspond to monolayer or few-layer graphene while the 'platelet' indicates thick multilayer (close to or more than 10 layers) graphene [60–62]. These prefixes and suffixes are independent of the synthetic methods. Thicker layered structures should be regarded as thin films of 3D graphite, not as 2D graphene crystals. It has been reported that the electronic structure is highly dependent on the number of graphene layers, approaching the 3D limit of graphite at 10 layers [63].

In graphene, each carbon atom covalently connects with each other by three σ bonds (in-plane) with the remaining π orbital (out-of-plane) contributing to a delocalized network of electrons (Fig. 1a) [18]. The edges of graphene exist in an armchair or zigzag configuration (Fig. 1b) with the zigzag type being more stable [64]. Two types of edges generally coexist for the majority of graphene synthesized, and they have different electronic structures and properties that can be potentially tuned for specific applications [65–68]. Monolayer graphene intrinsically exists in a rippled form like a corrugated sheet with no stacking due to thermal fluctuations [69,70]. Bilayer graphene retains the Bernal (AB) stacking (Fig. 1a) of bulk graphite in contrast to the AAA stacking [70]. However, both AB stacking and rhombohedral (ABC) stacking forms coexist in few-layer graphene, showing less commonly AAA stacking [71]. Both monolayer and multilayer graphene (Fig. 1c) have unique properties that are distinct from bulk graphite [72–77].

It is the electronic properties of graphene that have attracted the most attention. The electronic-band structure arises from its unique π electron system, where the empty conduction band (π^* band) touches the filled valence band (π band) at the K and K' points (Dirac points) in the reciprocal lattice space, accompanied by a small overlap between valence and conduction bands (Fig. 2a) [18]. Graphene can be considered a unique type of intrinsic semiconductor or semimetal with a linear Dirac-like spectrum around the Fermi energy (Fig. 2b) [20,80]. Bilayer graphene has a parabolic spectrum with an extremely small band overlap (1.6 meV), [63] and can be also referred to as a zero-gap semiconductor with one type of electron and one type of hole. For three and more graphene layers (Fig. 2c), their band structures become increasingly complicated along with the appearance of

several charge carriers and large overlaps of conduction and valence bands [63,71,81].

Near the Dirac points, electrons in graphene obey a linear dispersion relation on the wave vector and behave like massless relativistic particles, travelling at the Fermi velocity up to 10^6 m/s [82]. The charge mobility of graphene supported on an insulating substrate is $\sim 1.5 \times 10^4$ cm²/Vs at 300 K and $\sim 6 \times 10^4$ cm²/Vs at 4 K with electrons and holes in concentrations up to 10^{13} cm⁻² [18]. The low temperature mobility for suspended graphene can approach 2×10^5 cm²/Vs [83] and even exceed 2.5×10^5 cm²/Vs, [84] with 100 times higher mobility than that of silicon (1.5×10^3 cm²/Vs). The unusual quantum Hall effect and Berry's phase can be clearly observed for both electron and hole carriers in graphene [85]. Graphene has a sheet resistance (R_s) as low as 30 Ω /sq due to its exceptional conductivity [86].

Another important reason for the interest in graphene is its unique optical and optoelectronic properties [20]. In the visible region, monolayer graphene has negligible reflectance ($<0.1\%$) of incident light and an opacity of 2.3% (Fig. 2d), independent of wavelength [87]. Consequently, monolayer graphene is almost transparent (97.7%) and the transmittance linearly decreases with the number of layers. For few-layer graphene, each sheet can be considered as a 2D electron gas, with little interference from the adjacent layers, making it optically equivalent to a superposition of almost non-interacting monolayer graphene [88]. Graphene can be also made luminescent by cutting it into nanoribbons and quantum dots (QDs) or by doping to reduce the connectivity of the delocalized π -electron network [89].

Long-range π -conjugation in graphene also yields extraordinary thermal and mechanical properties. Graphene has been experimentally [92–94] and theoretically [54,95,96] shown to exhibit extremely high thermal conductivity of up to 5×10^3 W/mK. This value is comparable to that of CNTs but much higher than those of diamond and graphite [97]. It can be explained by the strong covalent sp^2 -bonding which result in highly efficient heat transfer by lattice vibrations via phonon-transport regimes. Due to strong in-plane σ bonds densely interconnected, pristine monolayer graphene has superior mechanical properties as well. Its

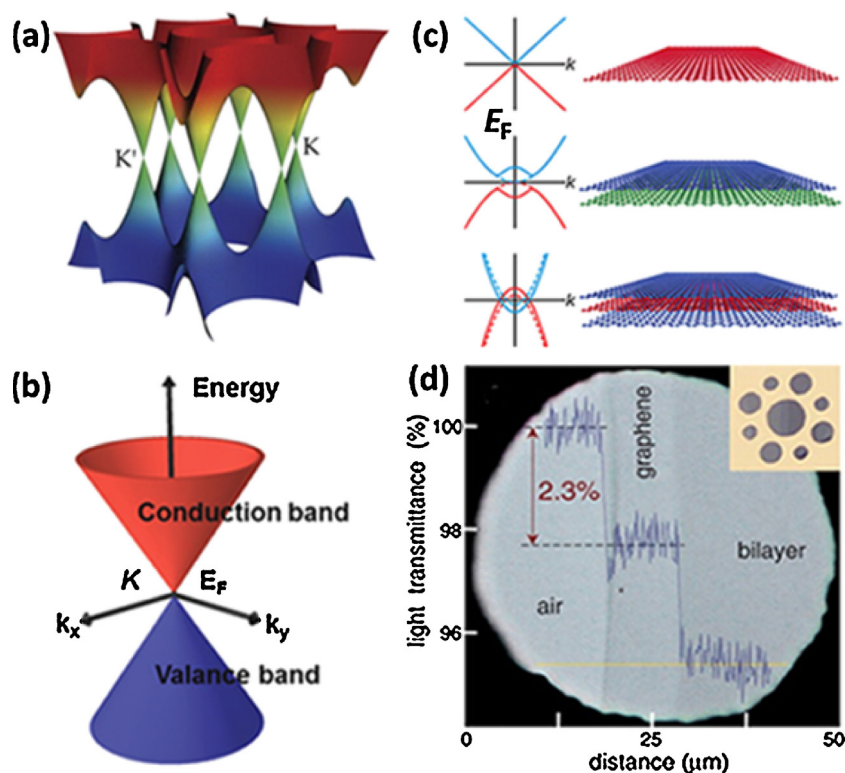


Fig. 2. Electronic band structure: (a) the conductance band of graphene touches its valence band at the K and K' points, and (b) linear band dispersion relation near the Dirac points having gapless features [90]. Copyright 2007 Elsevier Ltd. (c) Electronic and optical properties of graphene depend on the layer number. Schematic diagrams in the left of the panel show the graphene band structure with (solid curves) and without (dashed curves) an applied gate bias [91]. Copyright 2009 American Chemical Society. (d) Photograph of a 50-mm aperture partially covered by graphene and its bilayer with optical absorbance of 2.3% per layer. The line scan profile shows the intensity of transmitted white light along the yellow line [87]. Copyright 2008 American Association for the Advancement of Science (For interpretation of the references to color in this figure legend, the reader is referred to the web version of this article.).

Young's modulus and intrinsic strength can reach up to 1.0 TPa and 130 GPa, [28] respectively. Graphene also has an ultra-large specific surface area (SSA, 2630 m²/g) [98] due to its extremely high surface-to-thickness ratio. Moreover, defect-free or highly crystalline graphene is chemically stable and inert [99]. Its large conjugated surface can readily interact by physical adsorption and π - π stacking with other molecules, [100] and can be further activated by chemical functionalization [101]. Graphene also shows high flexibility, thermal stability and outstanding resistance to gas permeation. The combination of all these excellent properties suggests a wide range of advanced energy applications.

2.2. General synthesis

Graphene synthesis is the first step toward practical applications and can be categorized into two methodologies: *top-down* and *bottom-up*, as shown in Fig. 3. The top-down technique involves: (i) isolating graphene from the stacked parent-materials by solid-phase, liquid-phase or electrochemical exfoliation of pristine graphite and graphite intercalated compounds (GICs), and (ii) exfoliating graphite oxide into graphene oxide (GO) followed by chemical, thermal, and electrochemical reduction [102–104]. For clarity, we here define GO as graphene oxide and refer to it as such throughout this review. The bottom-up approach involves building up graphene from molecular precursors, typically including chemical vapor deposition (CVD), [105–107] and epitaxial growth [108]. The morphology, structure and properties of graphene, such as stacked-layer, lateral size, defect and impurity contents, surface chemistry, and solubility as well as electrical and thermal conductivities, depend strongly on the synthetic method used [109].

2.2.1. Exfoliation of graphite

The interlayer cohesive energy (61 meV/C) of bulk graphite originates from van der Waals (vdW) attractions between the π -stacked graphene layers in a spacing of 0.34 nm and is much weaker than the intra-layer covalent bonding [110]. The vdW binding energy amounts to ~ 2 eV/nm² within graphite, [111] and the equivalent force required is on the order of magnitude of ~ 300 nN/ μ m² [112]. Theoretical calculations have suggested that the vdW force can be reduced to zero for interlayer spacing greater than 0.5 nm [113,114]. Efficient exfoliation of graphite can be therefore achieved by introducing an external force beyond vdW interactions and/or increasing the interlayer spacing in the solid and liquid states.

2.2.1.1. Solid-phase exfoliation. Graphene was first experimentally produced by repeated peeling of highly oriented pyrolytic graphite (HOPG) using an everyday Scotch tape [18]. This process can isolate a monolayer graphene sheet with a thickness of ~ 0.4 nm and lateral size up to microns. This exfoliation method is quite simple yet highly reliable to achieve the best samples in terms of purity, defects, charge mobility, and optoelectronic properties. Such cleaved graphene has been widely employed in laboratories to study its intrinsic properties such as carrier mobility, [115,116] ballistic transport, [83] thermal conductivity, [29] Raman spectra, [117] and mechanical properties [28]. Despite its high structural and electronic quality, graphene derived from micromechanical cleavage is still low yield and low throughput [118].

Enlightened by the Scotch tape method, an industrial three-roll mill machine was employed for mechanically-cleaving graphite in the presence of a polymer adhesive [119]. This process can continuously produce graphene sheets of 2.7–5.0 μ m in size and

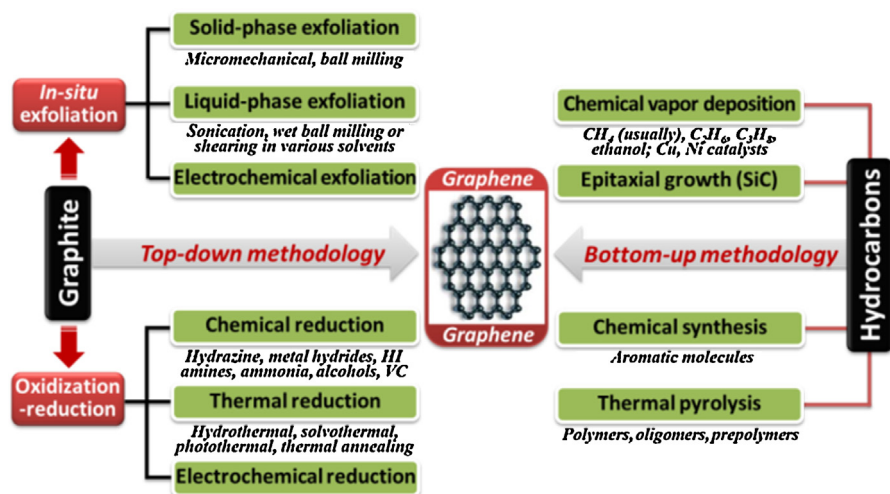


Fig. 3. Schematic for graphene synthesis through top-down and bottom-up methodologies.

1.13–1.41 nm in thickness. Dry ball-milling of graphite with aromatic triazines [120,121] or ammonia borane [122] was recently found to be efficient in exfoliating into few-layer graphene sheets due to extensive molecular adsorption and inter-adsorbate hydrogen bonding on the surface of graphene [123]. This milling process allows fast exfoliation of graphite into large quantities of few-layered graphene. Edge-functionalized graphene can be produced by adding dry ice, [124] KOH, [125], and oxide gases [126] during ball-milling of graphite. This technique also provides an alternative fabrication approach to graphene-based composites for versatile applications [127,128]. However, the obtained materials are a mixture of monolayer and few-layered graphene as well as un-exfoliated graphite flakes. Furthermore, such mechanically-split graphene sheets tend to re-aggregate in the solid state. Moreover, the presence of structural defects within graphene inevitably leads to low electrical quality.

2.2.1.2. Liquid-phase exfoliation. Solution processing of layered materials to 2D nanosheets has recently garnered much attention [129]. Generally, liquid-phase exfoliation of graphite involves wet chemical dispersion followed by sonication-induced exfoliation in suitable solvents in the absence/presence of surfactants [36,130,131]. Under sonication, shear forces and cavitation (the growth and collapse of bubbles and voids due to pressure

fluctuations) act on bulk graphite to overcome interlayer vdW forces and trigger exfoliation into smaller flakes gradually [102,103]. Note that solvent molecules by themselves cannot inherently dissolve graphene, and solvent-graphene interactions thus need to balance inter-sheet attractions of graphene after exfoliation so as to avoid their restacking. It has been suggested that an efficient solvent enables its Hildebrand solubility parameter (δ_T) of $\sim 23 \text{ MPa}^{1/2}$ and surface energy of $\sim 70 \text{ mJ/m}^2$ (equivalent to surface tension, γ , of $\sim 40 \text{ mJ/m}^2$) to be close to that of graphite (68 mJ/m^2) to minimize their entropy of mixing [36,132,133]. Based on the semi-empirical criterion proposed, many organic solvents have been explored to exfoliate graphite into graphene in the absence of surfactants (see Table 1).

N-methylpyrrolidone (NMP) was first used for the exfoliation of graphite into graphene [133]. The exfoliated graphene sheets consist of 28% monolayer and nearly 100% few-layer (≤ 5) pristine graphene with a few microns in lateral size. The yield of monolayer graphene (up to 12 wt% relative to graphite) and total concentration of graphene dispersions (up to 63 mg/mL) can be significantly improved by extension of sonication time [133,134] repeated exfoliation, [133,135] and subjecting to solvothermal [136], and supercritical treatments [137]. By controlling the centrifugation rate of graphene dispersions, sheets with different size can be further separated from each other [138]. Among organic solvents

Table 1
Solvents used for liquid-phase exfoliation of graphite to graphene.

Solvents	Boling point (°C)	δ_T [132] ($\text{MPa}^{1/2}$)	γ [133] (mJ/m^2)	C [132] ($\mu\text{g/mL}$)	N_1 [132] (%)	$N_{\leq 5}$ [132] (%)	Yield [133] (wt%)
NMP	203	23	40.1	4.7	29	97	7.6
DMEU	225	23	42.5	5.4	11	70	7.2
GBL	204.5	25.6	46.5	4.1	–	–	7.6
BBA	323.5	21.3	45.95	4.7	–	–	8.3
N12P	203.5	18.3	34.5	2.1	5	64	5.4
DMSO	189	26.7	42.98	3.7	–	–	4.1
DMA	165.1	22.4	36.7	3.9	–	–	7.2
DMF	154	24.9	37.1	4.1	–	–	4.5
CHO	155	20.3	–	7.3	–	–	–
CPO	130.5	22.1	–	8.5	5	69	–
NVP	92–95	19.8	42.7	5.5	–	–	6.6
IPA	82	23.6	21.66	3.1	–	–	3.4
Chloroform	61.2	18.9	27.5	3.4	–	–	–
Acetone	56	19.9	25.2	1.2	7	74	2.5
Water	100	47.8	72.8	1.1	–	–	–

N-methylpyrrolidone (NMP); N,N'-dimethylformamide (DMF); N,N'-dimethylacetamide (DMAC); dimethyl sulfoxide (DMSO); 1,3-dimethyl-2-imidazolidinone (DMEU); 1-vinyl-2-pyrrolidone (NVP); 1-dodecyl-2-pyrrolidinone (N12P); cyclohexanone (CHO); isopropanol (IPA). C: the concentration of graphene stabilized in solvents; yield: the weight fraction of the exfoliated graphene remaining after centrifugation relative to pristine graphite; N_1 : Number fraction of monolayer graphene; $N_{\leq 5}$: number fraction of 1–5 layer graphene.

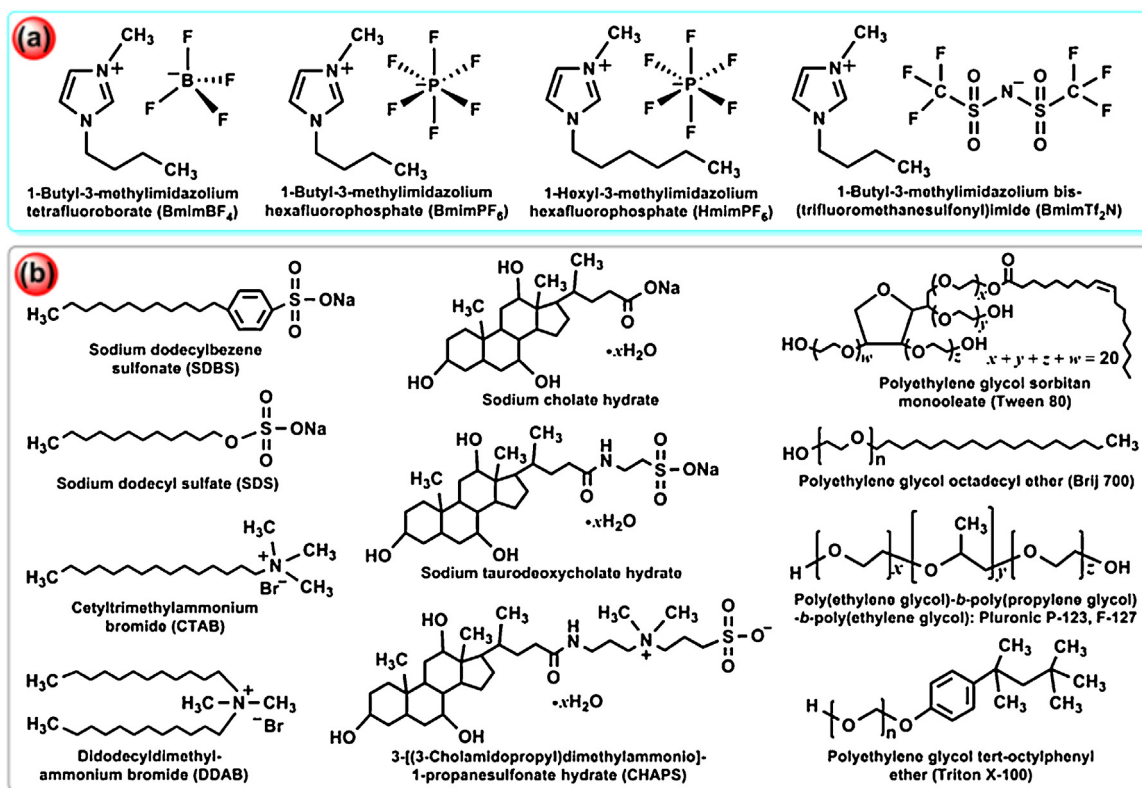


Fig. 4. Chemical structures, chemical names, and partial abbreviations of (a) ionic liquids, and (b) commercial surfactants used for liquid-phase exfoliation of graphite into graphene sheets.

used, NMP is the best solvent in terms of the fraction of monolayer and few-layer graphene due to its matchable δ_T and γ with graphene, while *N,N*-dimethylformamide (DMF) [137,139,140] dimethyl sulfoxide (DMSO), [132,133] and fluorinated aromatic solvents [141] exhibit an intermediate efficiency in exfoliating graphite. Ionic liquids (ILs) (Fig. 4a) also present surface tensions closely matching that of graphite, [142] and they have been adopted for exfoliating graphite to produce few-layer graphene with sheet sizes of several microns and dispersion concentrations of up to 5.33 mg/ml [143–146]. Due to a poor mismatch of δ_T and γ of water coupled with the hydrophobic nature of graphene, it is impractical for direct exfoliation of graphite in water [147].

Liquid-exfoliated graphene sheets are stabilized against re-aggregation by solvent-graphene interaction. This interaction alone is not strong enough to compensate for vdW attractions between graphene interlayers [147]. The addition of surfactants, [148] organic molecules [149,150] and polymers [151] to organic solvents was found to promote the exfoliation of graphite and long-term stabilization of graphene suspensions by virtue of molecular adsorption onto the basal planes and edges of exfoliated sheets. Furthermore, such additives can tune the surface tension of water to an appropriate level for aqueous exfoliation of graphite. Aqueous processing is ideal as it is a low cost and environmentally-friendly option. Commercial surfactants (see Fig. 4b) have been frequently used in recent years [152–156]. Generally, ionic surfactants adsorbed on the sides of graphene produce charged sheets. This arrangement provides a potential barrier by Coulomb repulsion to prevent aggregation (Fig. 5a). Non-ionic surfactants (usually amphiphilic block copolymers) are also attached to both sides of graphene via hydrophobic interaction, providing steric repulsion to separate graphene sheets (Fig. 5b). The presence of hydrophobic aromatic rings in surfactant molecules, such as Triton X-100 [153] and sodium dodecyl benzene sulfonate (SDBS) [157],

enables additional π - π interactions with graphene and more efficient exfoliation. It has been reported that surfactant-assisted aqueous processing of graphite produces suspensions of crystalline single-/few-layer graphene with yields up to $\sim 10\%$ and stable concentrations on the order of magnitude of 0.1–1.0 mg/mL.

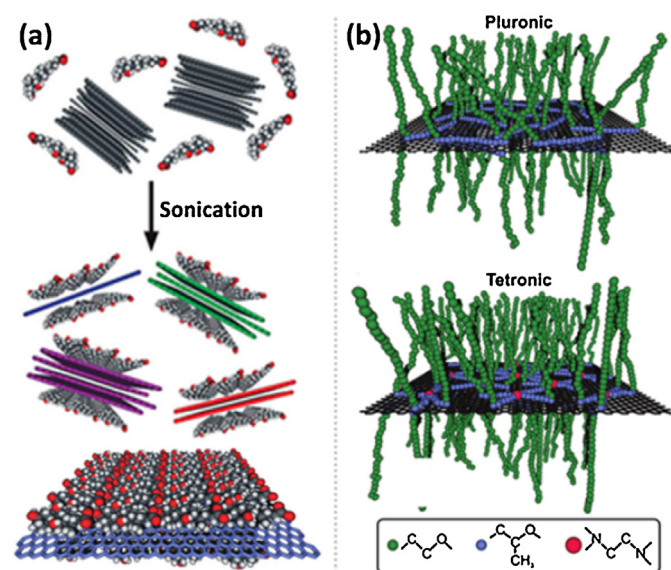


Fig. 5. (a) Schematic illustration of the graphene exfoliation process. Graphite flakes are combined with sodium cholate in aqueous solution. Sonication exfoliates few-layer graphene flakes that are encapsulated by sodium cholate micelles [155]. Copyright 2009 American Chemical Society. (b) Schematic illustrations of the interaction of Pluronic and Tetronic copolymers (consisting of hydrophobic polypropylene oxide and hydrophilic polyethylene oxide blocks) with graphene sheets [154]. Copyright 2011 American Chemical Society.

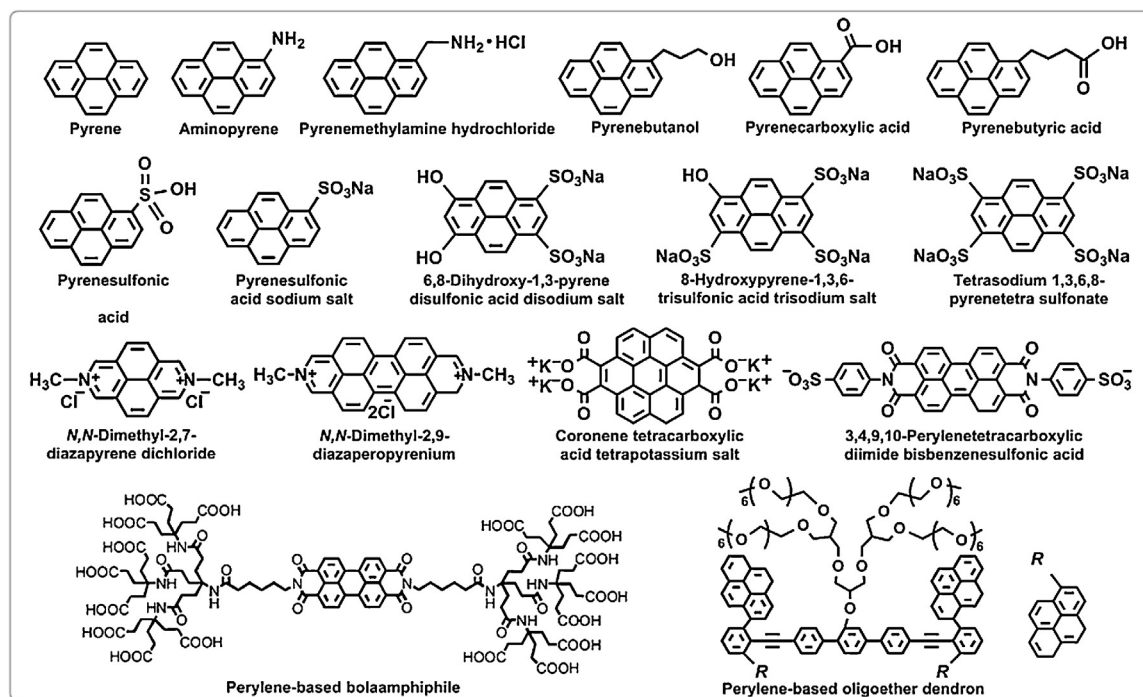


Fig. 6. Chemical structures, names, and abbreviations of pyrene- and perylene-containing organic molecules used for liquid-phase exfoliation of graphite into graphene sheets.

Additional incorporation of metallic salts such as FeCl_2 , [158] NaCl and CuCl_2 [159] into aqueous solutions of surfactants gives rise to the ion-intercalation induced expansion of graphite and hence fast exfoliation.

In addition to conventional surfactants, pyrene- and perylene-containing molecules (Fig. 6), with hydrophobic aromatic rings and hydrophilic functional groups, have been considered as surfactants to assist in the exfoliation of graphite in aqueous solutions [160–171]. While sonication serves to weaken vdW attractive forces between layers in graphite, these conjugated molecules can intercalate into interlayers and adsorb *in-situ* onto the graphene surface through hydrophobic and π - π interactions between them [172]. This process ensures efficient exfoliation of graphite and subsequent stabilization of graphene in water by reducing surface free energy and providing a repulsive potential barrier. By undergoing charge-transfer interactions with graphene, electron-rich groups of pyrene and perylene molecules can further enhance their exfoliation efficiency and stabilization ability. Moreover, conjugated molecules with higher aqueous solubility and stronger interactions with graphene are more effective in exfoliating graphite and stabilizing graphene. Among pyrene derivatives tested, pyrenesulfonic acid sodium salts were found to produce the highest yield of $\sim 70\%$ few-layer graphene with stable concentrations over 1.0 mg/mL [162]. Water-insoluble chemicals of pyrene, aminopyrene, and pyrenebutanol fail to induce the exfoliation of graphite, while partially-soluble pyrenesulfonic acid hydrate and pyrenemethylamine hydrochloride give rise to a limited number of graphene sheets in water. Aqueous processing of graphite assisted by perylene-containing molecules can also achieve stable dispersions of single- and few-layer graphene with concentrations up to 1.5 mg/mL [169]. These conjugated additives open up an alternative route to the liquid-phase exfoliation of graphite to graphene.

Liquid exfoliation of graphite has become an important technology to produce defect-free or defect-few graphene. In contrast to solid-phase exfoliation, this method is made even more

attractive due to the ease of scaling-up production and allowing solution processing [173]. Stable liquid-exfoliated graphene dispersions can function as conducting inks and hence enable top-down approaches to print electronics, [174–176] and they can also be processed into flexible, transparent, conducting, and free-standing films for cell electrodes [166,177]. However, good exfoliating-solvents are usually high boiling-point organics (see Table 1) and ionic liquids, which are difficult to be fully removed when processing graphene dispersions [133,141,178]. Alternatively, poor solvents with low boiling-points serve to exfoliate graphite into graphene with low yield and poor stability. Extended sonication of graphite in low boiling-point solvents like chloroform was found to achieve graphene concentrations up to 0.5 mg/mL [179]. Unfortunately, this leads to increased defects and decreased sheet sizes. Incorporation of organic molecules [180,181] and functional polymers [182–185] into these poor solvents can improve the efficiency by virtue of molecular intercalation/adsorption induced exfoliation of graphite and steric stabilization against restacking of graphene as detailed in aqueous solutions. However, it is impossible to fully separate graphene from these additives due to high affinity between the two. Moreover, liquid-phase processing scalability is limited to the use of sonication as a dominant source, and graphene yield rates are typically less than 0.04 g/h; far from being commercially viable. Therefore, new liquid exfoliation techniques such as high-shear mixing [186] still needs to be developed for achieving large-scale production of graphene particularly in low boiling-point solvents with volumes of hundreds or more.

2.2.1.3. Electrochemical exfoliation. Electrochemical exfoliation of graphite into graphene involves utilizing graphite/HOPG rods or foils as the sacrificial electrodes (mostly at the anode) in an electrolysis cell and then collecting the exfoliated graphene from the electrolyte solution. Various aqueous and non-aqueous electrolyte solutions have been developed. The aqueous electrolytes of surfactants [187,188] and polymers [189,190] are

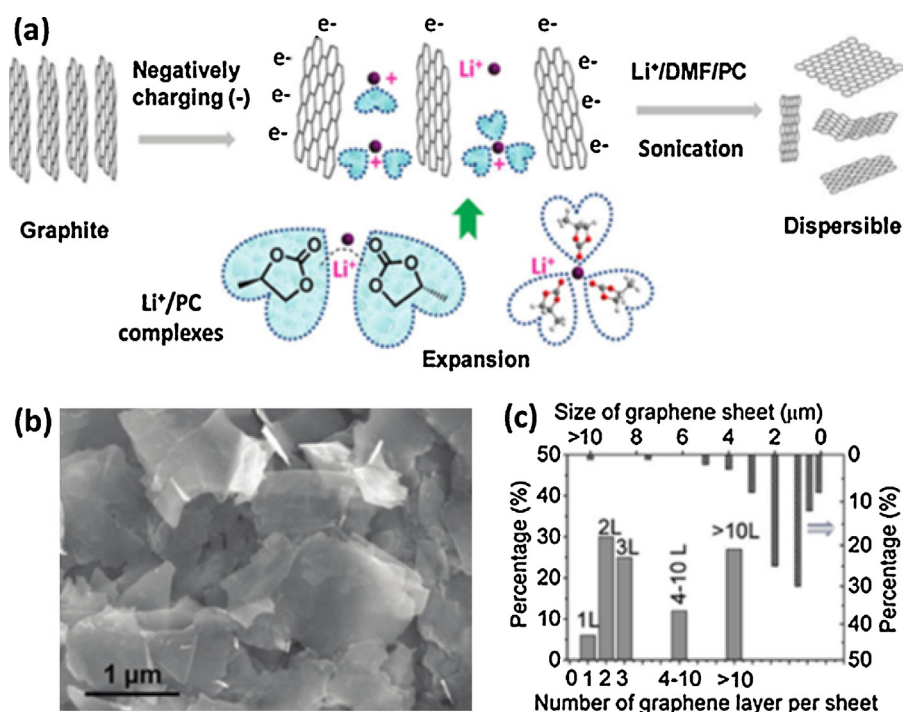


Fig. 7. (a) Schematic illustration for the exfoliation of graphite into few-layer graphene flakes via intercalation of Li^+ complexes, where graphite was electrochemically charged in Li^+/PC using a high voltage. (b) Low magnification SEM image of the exfoliated graphene sheets, and (c) their thickness and size distribution histograms [199]. Copyright 2011 American Chemical Society.

responsible for the electrolytic exfoliation of graphite into graphene due to their hydrophobic aromatic rings interacting with the π -orbitals of graphene. However, the adsorbed surfactants and polymers cannot be fully removed, resulting in interference with the electrical and electrochemical properties of graphene. Protonic acids, such as sulfuric acid (H_2SO_4) and phosphoric acid (H_3PO_4), are found to be good electrolytes for the exfoliation of graphite due to the intercalation of electrolyte anions, radicals and their solvated complexes between the layers [191–194]. The intercalation and hydrolysis of GICs can trigger the expansion and cleavage of graphene sheets. Therefore, electrochemical exfoliation of graphite or HOPG electrodes in H_2SO_4 solution can be finished in a few minutes. However, it produces thin sheets with high defect densities due to the strong oxidation of graphite caused by H_2SO_4 itself. The addition of KOH can lower the acidity of the electrolyte and reduce the degree of oxidation [191].

In addition, incorporating ILs into aqueous electrolytes can provide wide working potential windows with high electrochemical stability through a large temperature range. ILs have a strong tendency to intercalate graphitic electrodes and yield large quantities of graphene sheets [195,196]. Meanwhile, both oxygen and hydroxide radicals derived from the anodic oxidation of water serve as electrochemical “scissors” in the oxidative cleavage reaction. High-yield (86%) graphene has been recently reported by electrochemical exfoliation of graphite in organic electrolytes containing ILs [197]. Graphite was also electrochemically exfoliated in NaCl/DMSO complexes [198].

Of note, electrochemical exfoliation of graphite usually occurs at the anode where the oxidation reaction inevitably leads to the formation of structural defects in graphene. A nonoxidative electrochemical process was developed by using the electrochemical charging of a negative graphite electrode in a LiClO_4 /propylene carbonate (PC) electrolyte [199]. The exfoliation mechanism lies in the expansion of the graphite electrode during charging at high current density (-15 ± 5 V) due to the co-intercalation of PC with Li^+

to form ternary GICs, as shown in Fig. 7. Further sonication-assisted exfoliation of GICs in a mixture of DMF and PC was found to give >70% graphene sheets with layer number below 5. Besides a two-electrode system reported in most cases, a three-electrode system has been successfully performed for exfoliating graphite into graphene in pure ILs, [200] IL/water, [201], and organic electrolytes [202,203]. This process can be also promoted by adding lithium salts into the electrolytes [201].

2.2.2. Reduction of graphene oxide

2.2.2.1. An introduction to GO.

GO is an atomically thin sheet of graphite oxide, and its chemical structure intrinsically originates from graphite oxide. Several structures have been proposed including Hofmann, [204,205] Ruess, [206] Scholz-Boehm, [207] Nakajima-Matsuo, [208,209] Lerf-Klinowski, [210,211] and Dékány [212,213] models (Fig. 8). Among them, the Lerf-Klinowski model is currently the most widely accepted configuration [211]. This model consists of unoxidized aromatic regions and aliphatic six-membered rings containing OH, epoxide and isolated $\text{C}=\text{C}$ bonds whereas the edges are terminated with OH and COOH groups [214,215]. Recently, Ajayan et al. [216] have suggested the additional presence of five- and six-membered-ring lactols decorating along the peripheral edges of GO as well as esters of tertiary alcohols on the surface. The type of oxygen functionalities and their relative proportion and coverage density on GO vary drastically with the synthetic methods and graphite sources used [217].

GO samples obtained by exfoliating graphite oxide are naturally polydisperse in both their size and lateral dimensions with ranges from several tens of nanometers to hundreds of microns [218]. The apparent thickness of a monolayer GO sheet is theoretically predicted to be ~ 0.8 nm [219] with reported experimental values close to 1 nm [218]. The height is larger than that of a monolayer pristine graphene (~ 0.34 nm) due to the presence of protruded oxygen-containing groups and absorbed water molecules on both

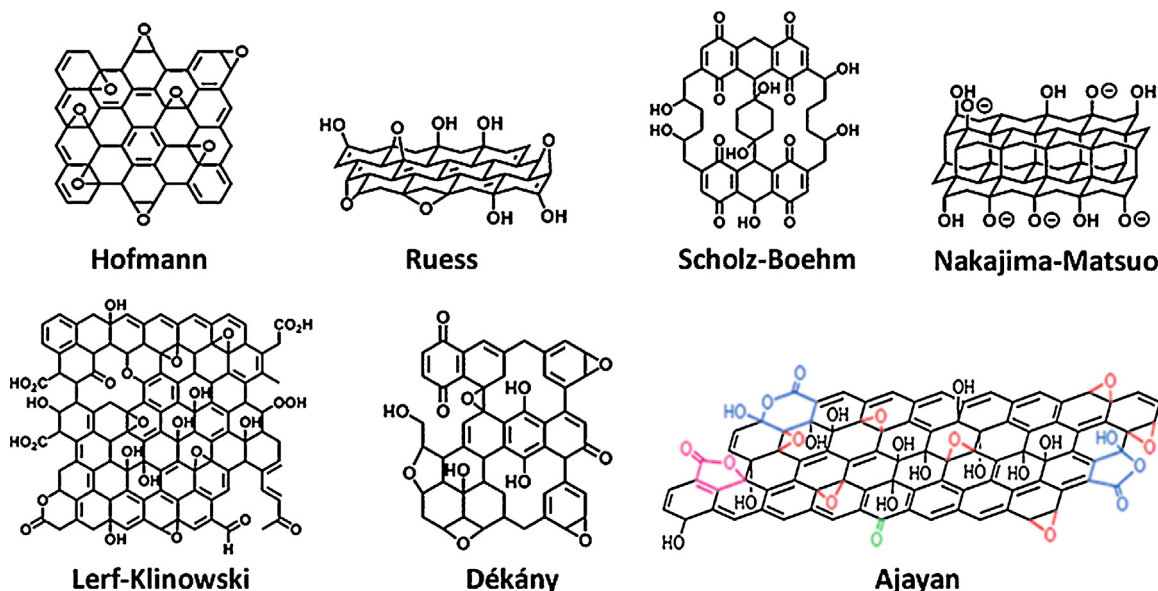


Fig. 8. Structural models of graphite oxide (and hence GO) proposed.

faces [220]. The mechanical strength of GO is reported to be lower than that of graphene, [28] but it still has a large Young's modulus (~ 207.6 GPa) [221]. GO is electrically insulating with a R_s of $\sim 10^{12} \Omega/\text{sq}$ or higher, [222] due to the disruption of the delocalized π -electron conjugation pathways by $\text{sp}^3\text{C-O}$ bonding and vacancy defects. The bandgap of GO can open and increases with increasing $\text{sp}^3\text{C-O}$ fractions [215,223]. Because of full removal of π -electrons, GO gives a direct electronic bandgap of up to 3.1 eV [224]. Consequently, GO can transform from an insulator to a semiconductor and to a graphene-like semi-metal by reduction or restoration of $\text{sp}^2\text{-C}$ fractions [215,223, 225,226]. Such tunable conductivity and bandgap are highly desirable to fabricate electronics and optoelectronics devices such as solar cells [23,227].

Direct reduction of GO has been the most commonly used method to produce large-quantities of graphene by removing oxygen functionalities while restoring sp^2 conjugated network [38,228,229]. The reduced GO is usually referred as reduced GO (RGO) and can be also considered as chemically derived, converted or modified graphene [230]. RGO shares close resemblance to pristine graphene in both structure and properties. In general, a color change from yellow (solution) or brown (solid) to black can be experimentally observed upon the transformation of GO to graphene. The C/O atomic ratio and conductivity generally increase after GO reduction. However, the reduction efficiency largely depends on the methods and processing parameters, resulting in graphene with various properties [229–231]. There are numerous routes for reducing GO, typically including thermal and chemical reduction strategies.

2.2.2.2. Thermal annealing. Thermal reduction *via* deoxygenation is typically carried out above 200°C by annealing GO under vacuum, inert or reducing atmosphere [222,232–235]. Chabal et al. [236] have suggested that thermal annealing can facilitate the formation of oxygen-containing free radicals in trapped water found in GO which further attack carboxyl, hydroxyl, and carbonyl groups to facilitate the restoration of π -conjugation networks in graphene. A recent study [237] has shown that GO reduction first occurs at 127°C and then continues smoothly above 600°C with oxygen and hydrogen loss and the conversion of sp^3 hybridized carbons into sp^2 ones. The critical temperature appears to be

1000°C for GO reduction, and the resultant graphene contains $<2\%$ oxygen and 81.5% sp^2 -carbon atoms. Further reduction above 2000°C results in almost oxygen-free graphene with a dramatic restoration of pristine graphite structure. Higher heating temperature usually leads to higher reduction degree and hence higher electrical conductivity [219,238–240]. For instance, the electrical conductivity of the thermally-annealed GO film (~ 10 nm in thickness) at 500°C is 5000 S/m , which increases to $10,000$ and $55,000\text{ S/m}$ at 700 and 1100°C , [232], respectively. The conductivity can drastically rise up to $200,000\text{ S/m}$ by hydrogen arc discharge treatment partially due to extremely high temperature ($>2000^\circ\text{C}$) in this process [241]. Further improvement in the electrical conductivity can be achieved by thermal annealing of GO in reducing gas [242]. Moreover, the direct thermal-decomposition reduction of GO in air at relatively low temperatures was also reported by Zangmeister [243] at 220°C and Zhang [244] at 300 – 350°C , respectively, due to the deoxygenation *via* evolution of O_2 , CO , CO_2 , and H_2O . The thermal annealing method is highly favorable for direct use of graphene in its film form made by vacuum filtration, spray coating, [245], or inkjet printing [246]. The technique is unsuitable for GO used in a matrix material or on substrates with low thermal tolerances [247,248]. Structural damage and lattice defects throughout graphene are inevitably caused by the release of gases during thermal annealing [236,249,250].

2.2.2.3. Hydrothermal reduction. GO can be well-dispersed in water and polar solvents to form stable suspensions due to the presence of abundant hydrophilic and polar groups [251]. This makes it very favorable for hydrothermal and solvothermal treatments in a sealed autoclave at temperatures exceeding the boiling-points of solvents, and hence provides alternative, facile routes to convert GO to graphene. Such closed systems can induce high temperatures and internal pressures for promoting the π -conjugation recovery of GO. In the case of hydrothermal processing, GO reduction is typically performed at 120 – 180°C for 1 – 18 h, [38] and the overheated supercritical water plays the role of reducing agent to remove oxygen-containing groups from GO while restoring aromatic structures in the carbon lattice [252,253]. It should be noteworthy that hydrothermal reduction of GO is highly sensitive to the pH of aqueous solution

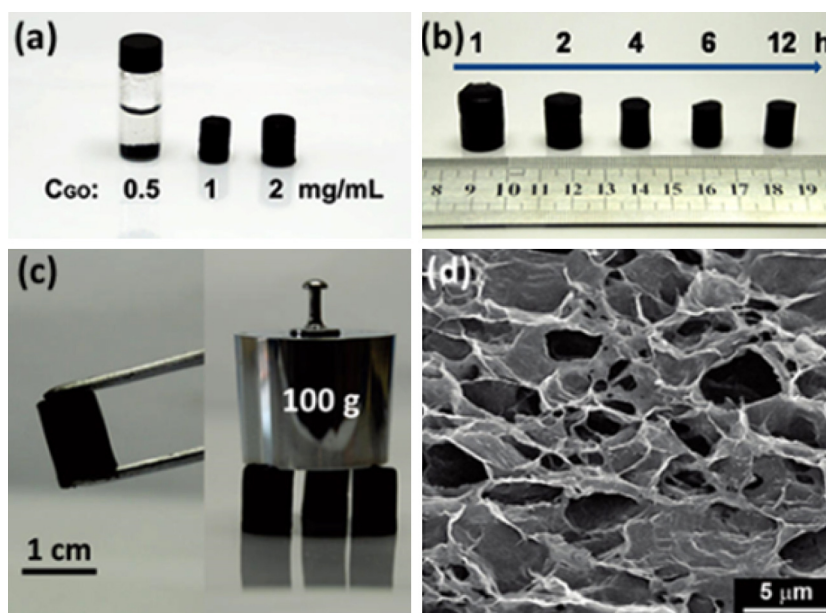


Fig. 9. Photographs of (a) graphene products obtained by hydrothermal reduction of GO dispersions with different concentration at 180 °C for 12 h, (b) graphene hydrogels obtained by hydrothermal reduction of 2 mg/mL of GO at 180 °C for different reaction times, and (c) strong hydrogels allowing easy handling and supporting weight, and (d) SEM image of hydrogels interior porous microstructures [255]. Copyright 2010 American Chemical Society.

[252,254]. Basic conditions (e.g., pH = 11) lead to stable suspensions of graphene, while retaining large graphitic domains with low defect concentration. In contrast, acidic solutions (e.g., pH = 3) often yield aggregates of graphene sheets and even other graphitic nanostructures. Acidic conditions also produce smaller lateral sizes and larger numbers of defects. The reduction process is likely analogous to the acid-catalyzed dehydration of alcohol where water acts as a source of H^+ for the protonation of OH [252]. Another reaction parameter to consider is the concentration of the GO suspension. Generally, hydrothermal reduction of GO suspensions produces black powder materials at low concentrations and forms mechanically stable graphene hydrogels at high concentrations (Fig. 9a–c) [255]. The apparent sizes of hydrogels tend to increase with GO concentration but gradually decrease with reaction time until steady state (Fig. 9b). The shape of graphene hydrogels is also dependent on the shape of containers used [256]. The resulting hydrogels have a well-defined and interconnected network consisting of graphene sheets (Fig. 9d) and can be directly frozen to produce porous graphene aerogels (also called sponges) at a low cost. Both graphene hydrogels and aerogels possess 3D nanostructures, large surface area, high conductivities, flexibility and elasticity, and excellent chemical/electrochemical properties [257–259]. Such properties make them potentially useful as electrode materials for electrochemical energy storage and conversion devices [260,261].

2.2.2.4. Solvothermal reduction. Hydrothermal reduction of GO in water offers a green chemistry alternative to organic solvents. However, such RGO materials appear in powdery or gel shapes, and they are difficult to reprocess into films, coatings, or composites by solution routes. The reason lies in the conversion of hydrophilic GO to hydrophobic graphene upon reduction. Alternatively, solvothermal reduction of GO in organic solvents can produce relatively stable graphene dispersions which are amenable to solution-processing applications. Typically, solvothermal reduction of GO has been carried out in polar organic solvents including NMP, [262,263] DMF, [264–266] PC, [267] DMSO, [268] *N,N'*-dimethylacetamide (DMAc), [269] tetraethylene glycol, [270] and acetonitrile [271]. These solvents have high boiling-points (>150 °C)

excepting acetonitrile and high stabilization potential of GO [251]. For instance, thermal treatment of GO in NMP at ~205 °C for 24 h produces a stable, black suspension which can be further filtered to remove NMP along with contaminants [262]. The resulting graphene materials are readily re-dispersed into a variety of polar organic solvents such as NMP, DMF, DMSO, and acetonitrile to form stable colloidal suspensions. Similarly, good redispersion is observed for RGO obtained in DMF with a stable concentration of up to 1.0 mg/mL [265]. Interestingly, the C/O ratio and electrical conductivity of RGO typically increase with increasing time and temperature [267,268,272]. The effectiveness of reduction can be further improved by adding reductants due to the combination of chemical and solvothermal effects [272,273].

2.2.2.5. Chemical reduction. Both sides of the GO basal-plane are decorated with hydroxyl and epoxy groups while its edge-plane mainly consists of carboxyl and carbonyl groups [274]. Reduction of GO by chemical reagents therefore aims at removing, transforming, or deoxidizing these functional groups through chemical reactions. Chemical reduction has been generally realized at ambient to modest temperatures (~100 °C). Early on, hydrazine (N_2H_4) was used for the reduction of graphite oxide, [275] and consequently it became the first reagent for chemical conversion of GO to graphene [276]. The resulting graphene has a SSA (466 m²/g), a high C/O atomic ratio (10.3), and comparable conductivity (2420 S/m) to graphite (2500 S/m). The reduction mechanism has been postulated to proceed by a nucleophilic attack of hydrazine on epoxide groups of GO to result in hydrazine alcohol moieties, which release water molecules to form aminoaziridines followed by thermal elimination of diimides to form double bonds on the basal plane [229,276]. Hydrazine treatment of GO also enables the formation of pyrazoline or pyrazole aromatic rings accompanied with an elimination of carbonyl groups at the edges [277]. The reduction effectiveness is dependent on the reaction temperature. For example, the reduction at 95 °C for 3 h can produce a much higher C/O ratio (15.1) relative to GO (3.1), but it is impossible to realize at low temperature (<80 °C) for even extended reducing times [278]. At present, hydrazine [279–282] and its derivatives such as hydrazine hydrate, [225,283–285] dimethylhydrazine,

[286,287], and phenylhydrazine [288], have been frequently used for the mass-production of RGO materials.

In addition to hydrazine, there are a wide range of reagents available for the reduction of GO including metal hydrides of NaBH_4 [216,289–291] and LiAlH_4 [292,293], hydrogen halides, [294–300] alcohols, [301] amines, [302–306] ammonia, [307–310] ammonia borane, [311,312] urea, [313–316] saccharides, [317,318] Vitamin C, [319–321] bacteria, [322–324] amino acids, [325–327] metal/acids [328–334], metal/alkaline hybrids, [335,336], and sulfur-containing organic [337–340] and inorganic [337,341] compounds. Reduction mechanisms for each of these reagents have been recently summarized [229]. The effectiveness of reduction, quality and properties of the as-prepared RGO depend on the methods used. For instance, N_2H_4 is highly active in reducing epoxy groups but has extremely low efficiency for hydroxyl reduction even at high temperatures [278]. NaBH_4 is very effective at reducing carbonyl species, but shows low to moderate efficiency in the reduction of epoxide and carboxylic acids while leaving most of hydroxyl groups unaltered after reduction. An additional dehydration process involving concentrated H_2SO_4 can remove the majority of hydroxyl groups from NaBH_4 -reduced GO, and further decarboxylation can be realized by thermal annealing to give an extremely high C/O ratio (>246) and conductivity ($2.02 \times 10^4 \text{ S/m}$) [216]. It has been reported that that R_s of NaBH_4 -reduced GO films is much lower than that of N_2H_4 -reduced films despite having similar C–O composition [289]. Other chemical reduction routes have been proposed such as electrochemical [342–345] and photocatalytic [346–349] reduction as well as a combination of several routes [216,350].

Note that it is very difficult to remove oxygen completely and thereby produce pure graphene from GO as described by experimental and theoretic studies [215,351,352]. In addition, direct treatment of aqueous GO with reductants usually results in the agglomerated graphene materials [276]. The incorporation of surfactants into aqueous GO before reduction can lead to stable graphene dispersions [353,354]. Chemical reduction of GO is favorable for scalable production and versatile functionalization for graphene. However, many of the reducing agents employed are not environment-friendly or are even highly toxic such as N_2H_4 . Of note, Vitamin C and N_2H_4 have been found to show comparable efficiency and capability in reducing GO [319,321]. Vitamin C-reduced GO can be also obtained in water or organic solvents such

as DMF and NMP to form stable suspensions without aggregation. In addition, Vitamin C is clearly non-toxic in contrast to N_2H_4 and is also more stable than NaBH_4 in water. It is for these reasons that reduction by Vitamin C would facilitate the use of graphene materials for large-scale applications in a safer, greener and more sustainable fashion.

2.2.3. CVD growth

CVD has emerged as an important method for scalable production of high quality and large-area graphene films [107]. This technique involves the pyrolysis of hydrocarbon compounds on the surface of transition metal catalysts. The quality of graphene is mainly determined by processing parameters such as catalysts, precursors, gas flow rate, temperature, pressure, and time. As a typical heterogeneous catalysis system, the CVD process generally includes four steps: [355] (i) adsorption and catalytic decomposition of gas-phase precursors, (ii) diffusion and dissolution of decomposed carbon species into bulk metals, (iii) segregation of dissolved carbon atoms onto the surface of metals, and (iv) surface nucleation and graphene growth. Transition metals with an incomplete d shell (e.g., Ni and Co) exhibit a certain degree of carbon solubility and thus produce large-area few-layer polycrystalline graphene in most recipes (see Fig. 10a–d) [356,357]. For metals with completely filled d shells (e.g., Cu and Zn) having poor affinity to carbon, both dissolution and subsequent segregation steps are prohibited in the CVD process [358]. In this case, carbon atoms derived from hydrocarbon precursors can directly diffuse on the metal surface and build up thermodynamically stable graphene. This process easily results in the formation of large-area monolayer graphene [359]. Over 95% monolayer graphene films were also achieved by combining Cu with Ni to form Ni–Cu binary alloys as a catalytic substrate [360].

Cu- and Ni-based CVD graphene has received the most attention so far, [37,361] and other transition metals, such as Fe, Ru, Co, Rh, Ir, Pd, Pt, Au and alloys such as Co–Ni, Au–Ni, Ni–Mo are able to support the growth of graphene [362]. By tuning CVD parameters, composition of catalysts and precursors, graphene with desired layer number, grain size, band gap and doping effect can be achieved [37,106]. However, CVD is usually limited to the use of gas precursors. In addition, the current methods for transferring graphene is to etch away the metal substrate with etchants which leads to higher cost, toxic wastes and structural

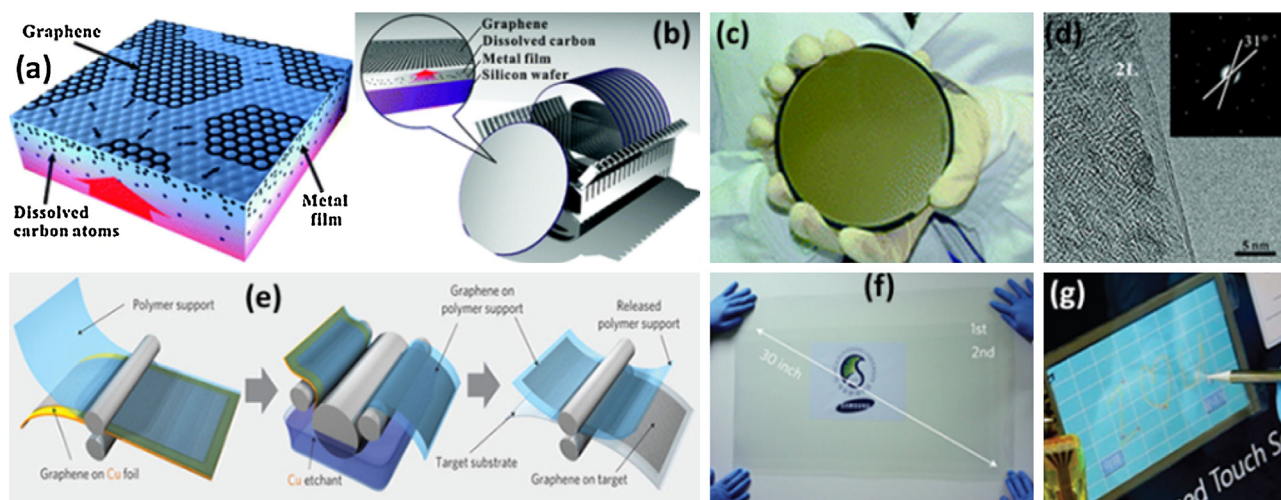


Fig. 10. CVD-grown graphene. (a and b) Segregation of graphene from bulk metal at high temperature, the inset in (b) illustrates the layered surface structure of growth substrate, (c) graphene wafer segregated on a Ni film, and (d) corresponding TEM image and selected-area electron diffraction pattern (SAED) revealing good crystallinity and disordered AB stacking structure of bilayer graphene [357]. Copyright 2011 American Chemical Society. (e) The process for the roll-based production of graphene films grown on a Cu foil and subsequent dry transfer-printing on a target substrate, (f) a transparent ultralarge-area graphene film transferred on a 35-inch PET sheet, and (g) a graphene-based touch-screen panel connected to a computer with control software [86]. Copyright 2010 Macmillan Publishers Limited.

damage to graphene. It should be highlighted that Ahn et al. [86] have developed a roll-to-roll CVD technique (Fig. 10e) for the mass production of monolayer 30-inch graphene films on flexible Cu substrates. The as-produced films exhibit a R_s as low as $\sim 125 \Omega/\text{sq}$ and 97.4% optical transmittance (Fig. 10f). Graphene film electrodes can be further incorporated into a fully functional touch-screen panel device capable of withstanding high strain (Fig. 10g). Further development along such lines would likely create novel pathways to electronic and optoelectronic applications.

2.2.4. Epitaxial growth

Thermal decomposition of SiC to produce monolayer graphene has been demonstrated through the graphitization of SiC by Si sublimation during high temperature vacuum annealing [363,364]. The advantage of this approach is that insulating SiC substrates are used so that transfer to another insulator is not required. Unfortunately, thermal annealing under vacuum often yields graphene layers with small graphene domains (30–200 nm) [365]. Thermal decomposition of SiC is also not a self-limiting process and hence graphene regions with different thicknesses often coexist [366]. The presence of disilane during SiC decomposition was found to reduce the Si sublimation rate, thus enabling the formation of high quality graphene [367]. Seyller et al. [368] reported on the *ex-situ* graphitization of Si-terminated SiC(0001) in Ar close to atmospheric pressure to produce homogeneous monolayer graphene films, which have high electronic mobility ($2000 \text{ cm}^2/\text{Vs}$ at 27 K) and much larger sizes ($\sim 3 \mu\text{m}$ in width and $> 50 \mu\text{m}$ in length) than previously attainable. Large-scale homogeneous films are particularly desirable for electronics production [369,370]. Epitaxial graphene seems to be suitable for wafer-based electronic and component applications; however, commercial SiC is still expensive, particularly for large area films. Moreover, for epitaxial graphene, high temperature ($> 1000^\circ\text{C}$) is usually required, and this is not compatible with current silicon electronics technology.

3. Graphene-based materials for lithium-ion batteries

Lithium-ion batteries (LIBs) were commercially introduced for the first time by Sony Corporation in 1991. They are electrochemical storage devices that are composed of negative (anode) and positive (cathode) electrodes, a porous separator (allowing Li ions to transport through), and an electrolyte (conducting Li ions during charging/discharging) [371]. LIBs work through a “rocking-chair” mechanism to interconvert chemical and electrical energy reversibly, in which Li ions continuously shuttle between the Li-accepting anode and Li-releasing cathode. Today LIBs are the most popular rechargeable battery type due to their high energy density (up to 400 Wh/kg theoretically and $120\text{--}170 \text{ Wh/kg}$ experimentally), relatively low self-discharge, low maintenance, and improved safety compared to conventional batteries. Over the past two decades, LIBs have revolutionized consumer electronics (e.g., cell phones, laptops and digital cameras) and are being intensively pursued for large-scale energy applications typically including electric vehicles and grid energy management. Currently commercialized LIBs still suffer from low power densities, long charging times, and poor cycle stability compared to supercapacitors [372,373]. However, in addition to high capacity and low cost, LIBs intended for use in the future electric vehicles must also possess high power capability and fast charging rate, whereas LIBs for stationary energy storage require longevity. To simultaneously achieve such goals, it is necessary to develop new electrode materials with high electrical conductivity for fast electron transport, well-designed nanostructures for shortening diffusion distance of Li ions, and large accessible SSA for lithium storage [374,375]. Owing to their unusual properties, GBMs have attracted much interest as electrode materials in LIBs [376–378].

3.1. Graphene-based materials as anodes

3.1.1. Graphene anode

Graphite is the most commonly used anode material in LIBs, and has a specific capacity of 372 mAh/g (340 mAh/g if including Li own weight) by forming LiC_6 upon Li-intercalation between the stacked layers [379]. It has been proposed that graphene can accommodate Li ions through an adsorption mechanism on both sides to form Li_2C_6 with a theoretical capacity of 744 mAh/g , [380], which is twice that of graphite and other carbonaceous materials such as CNTs [381,382]. Substituting graphene for graphite has been explored to increase the lithiation sites and storage capacity. In most studies previously reported, GO-derived graphene materials are the anode of choice for LIBs [383]. The pioneering work was reported by Honma et al. [384] who used hydrazine-reduced GO sheets (consisting of 6–15 stacked layers) as an anode material in LIBs. The resulting device gave a reversible capacity (usually referring to charge capacity) of 540 mAh/g at a current density of 50 mA/g . The crumpled flower-petal graphene sheets with 2–3 stacked layers were also obtained by chemical reduction of GO with hydrazine [381]. LIBs based on this anode architecture can deliver a specific capacity of 945 mAh/g in the initial discharge and a reversible capacity of 650 mAh/g in the first charge at 744 mAh/g (1 C rate) and still maintain a specific capacity of 460 mAh/g after 100 cycles with 70.8% retention of initial capacity. The thermally-reduced GO sheets, consisting of wrinkled fewer layers (~ 4 layers) and large SSA ($492.5 \text{ m}^2/\text{g}$), can provide more Li-insertion active sites such as edges and nanopores [385]. The first discharge capacity of such graphene anodes is as high as 2035 mAh/g at 100 mA/g and the first reversible specific capacities can reach up to 1264 and 718 mAh/g at 100 and 500 mA/g , respectively. After 40 cycles, the reversible capacity remains 848 mAh/g at 100 mA/g , corresponding to a capacity retention of 67.1%. However, similar thermally-reduced GO sheets with 20–30 layers show relatively lower reversible capacities of 672 and 554 mAh/g at 0.2 and 1.0 mA/cm^2 , [386] respectively, due to the strong stacking of graphene layers reducing the number of Li^+ intercalation sites.

It is clear that the Li-storage capability in graphene is strongly dependent on the production method. In a comparison study (Fig. 11), Pan et al. [387] reported that for the hydrazine-reduced GO, the first discharge and charge capacities at 50 mA/g are 708 and 330 mAh/g , respectively, which dramatically increase to 1544 and 1013 mAh/g for the thermally-reduced GO at 300°C . The discharge capacity remains high (1528 mAh/g) while the charge capacity decreases to 794 mAh/g for the 600°C -reduced GO. The electron-beam-reduced GO also shows initial discharge and charge capacities as high as 2042 and 1054 mAh/g , respectively. It has been shown that GO sheets reduced by low-temperature pyrolysis and electron-beam irradiation provide reversible capacities over 1000 mAh/g , which is much higher than values reported for the hydrazine-reduced GO (330 mAh/g), pure GO (335 mAh/g) and pristine graphite (350 mAh/g). With regards to the cycling performance, the 300°C -reduced GO exhibits high reversible capacities of $1013\text{--}834 \text{ mAh/g}$ with a capacity retention of 82% after 15 cycles and high Coulombic efficiencies over 90% except the first cycle ($\sim 65.6\%$). The electron-beam-reduced GO also shows reversible capacities in the range of $1054\text{--}784 \text{ mAh/g}$ with 74% retention of capacity after 15 cycles. The big difference in specific capacity of reduced GO materials originates intrinsically from their structural parameters.

Previous studies have suggested that a high specific capacity for LIBs can be achieved by using carbon anode materials with a large interlayer spacing due to the large accessible space [388]. According to the Li_2 covalent molecule model, the Li-storage capacity can reach 1116 mAh/g using the carbon materials

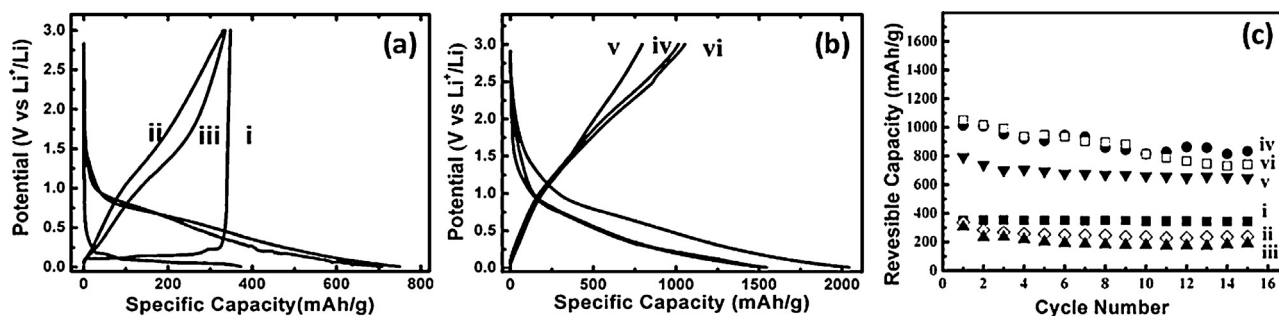


Fig. 11. (a) Charge-discharge profiles of natural graphite (i), pristine GO (ii), and hydrazine-reduced GO (iii); (b) charge-discharge profiles of 300 °C pyrolytic GO (iv), 600 °C pyrolytic GO (v), and electron-beam-reduced GO (vi); (c) reversible (charge) capacity vs cycle numbers at a current density of 0.05 A/g [387]. Copyright 2009 American Chemical Society.

with an interlayer spacing of ~ 0.4 nm. [389,390] Zhou et al. [391] experimentally reported that triple-coaxial electrospun amorphous carbon nanotubes decorated with hollow graphitic carbon nanospheres display an inter-planar distance of 0.34 nm, and obtained a high reversible capacity of ~ 969 mAh/g and a volumetric capacity of ~ 1.42 Ah/cm³. They further developed an *in-situ* CVD method to grow CNTs on the surface of N-doped carbon nanofibers (CNFs), and found that the *d*-spacing (d_{002}) of the (002) plane of graphene layer in CNTs and CNFs is in the range of 0.34–0.42 nm [392]. The anode with this hybrid material can deliver a reversible capacity up to 1150 mAh/g at a current density of 0.1 A/g even after 70 cycles. The same group recently used the Ni-diffusion-induced graphitization to fabricate the N-doped hollow-tunneled CNFs with a larger spacing of 0.36–0.45 nm [393]. This material exhibits a remarkably reversible capacity as high as 1560 mAh/g and an impressive volumetric capacity of ~ 1.8 Ah/cm³ at 0.1 A/g. LIBs using such materials also show outstanding rate capability and good cycling stability. However, in the work by Pan et al. [387] the electron-beam-irradiated GO and hydrazine-reduced GO have a comparable spacing (0.379 vs 0.381 nm), and the former exhibits a much higher capacity (1054 mAh/g) than the latter (330 mAh/g). Similarly, the GO reduced at 300 °C and hydrazine-reduced GO possess an identical interlayer spacing. However, the former has a capacity of 1.88 times that of the latter. This correlation of specific capacity with the interlayer spacing seems to be broken. There must be other parameters affecting the storage capability of graphene.

Furthermore, Pan et al. [387] found a large difference in the Raman intensity ratio of D to G band (I_D/I_G) for the abnormal samples. The I_D/I_G of the electron-beam-reduced GO (1.51) is two times that of the hydrazine-reduced GO (0.74) while the former has a specific capacity of 3.2 times that of the latter. Given that a higher I_D/I_G ratio usually indicates more disorder, more defects (edges, vacancies, dangling bonds, sp^3 -bonded carbon, and topological defects), and smaller sp^2 domains, [394] it is suggested that the highly-disordered graphene materials with enriched edges and defects may be responsible for enhanced Li-storage capacity and Li-ion diffusion [395,396]. However, Morales et al. [383] reported that the thermally-reduced GO at 500 °C has the highest I_D/I_G ratio and the smallest sp^2 domain, hence the greatest disorder and number of defects. Yet despite this, it still delivers a moderate capacity. There are some contradictory results, other factors should be further considered in evaluating the specific capacity of graphene anodes in the future.

Based on the above considerations, graphene sheets consisting of fewer layers (hence larger accessible surface area exposed), larger interlayer spacing, smaller sizes (hence more edges available), more defects, and more crumpled nanostructures (hence more nano-cavities and nano-voids between sheets) could be beneficial to improving the Li-storage, cyclic performance, and

rate capability (the ability to deliver capacity at high current rates), as evidenced by some theoretical [397] and experimental studies [264,398,399]. However, some points remain debatable. First, RGO-based anodes still suffer from high initial irreversible capacities (mostly > 500 mAh/g) and low first-cycle Coulombic efficiencies (usually $< 60\%$), which are mainly attributed to the formation of solid electrolyte interphase (so-called SEI, usually ~ 10 – 100 nm in thickness, arising from the irreversible decomposition of electrolyte to form a surface passivation layer around the electrode) [400,401] as well as chemical reactions of Li ions with the residual oxygen-containing functional groups in RGO [31,402]. The formed by-products adsorbed on the electrode surface can increase the energy barrier of the charge transfer reaction resulting in capacity fading upon cycling particularly at high rates [374]. During charging/discharging cycles, the residual oxygenated groups of RGO can also be progressively reduced. This leads to a re-stacking of graphene layers thus lowering Li-storage capacity [31,383]. All side reactions consume Li and/or active materials leading to a gradual decrease in storage capacity and thereby relatively low capacity retention. Second, large voltage hysteresis is often observed in RGO. This is possibly due to active defects which react with Li at low voltages upon discharging, while the breakage of strong Li-defect bonds requires higher voltages during charging [387]. Third, no obvious voltage plateaus occur from the discharge curve. This implies that such batteries may fail to provide stable potential outputs [386]. Finally, and more importantly, significant disordering and abundant defects inevitably compromise the electron transport and electrochemical stability of graphene sheets. This leads to low rate capability and low power density. This clearly contradicts the original purpose of using graphene-based anodes for LIBs. Therefore, it is highly advisable to tailor the structural parameters and active defects of graphene to an appropriate level to achieve consistent, high-performance LIBs.

3.1.2. Carbonaceous hybrid anodes

The integration of carbonaceous nanomaterials with graphene is highly conducive to enlarging the interlayer spacing and preventing the restacking of graphene sheets during the electrode fabrication and cycling operation and thereby making full use of the interior space for Li-ion diffusion and storage [403–405]. Carbon allotropes such as fullerenes, CNTs, CNFs, and porous carbon were found to combine well with graphene for fabricating carbonaceous hybrid electrodes, as summarized in Table 2.

Honma et al. [384] reported for the first time that incorporating CNTs and C₆₀ into graphene sheets can cause an expansion of the layer-to-layer distance (*d*-spacing) of graphene sheets from 0.365 nm to 0.4 nm, offering an enlarged interior space for accommodating lithium and a capacity over 730 mAh/g (540 mAh/g for graphene-only). Meanwhile, the presence of

Table 2

Electrochemical performance of carbonaceous hybrids with graphene for LIB anodes.

Carbonaceous hybrids			Voltage range V (vs Li/Li ⁺)	Specific capacity			Cycling performance (%) / cycles / current density (A/g)	Refs
Carbon materials	Graphene resource	Graphene loading (wt%)		ICE (%)	Current density (A/g)	Capacity (mAh/g)		
Porous carbon microrod	Carbonization of oriented polydopamine		0.01–3.0	34	0.1 0.5 1.0	1150 1089 841 (3rd)	100/50/0.1 101/150/0.5 99/700/1.0	[406]
S-doped porous carbon	Ionothermally reduced GO		0–3.0	55.6	0.05 20	1400 280	126.8/500/1 (2.7 C)	[407]
N-doped carbon	Thermally reduced GO	7.86 at% N in graphene	0.01–3.0	56.9	1.0	1203.4	100/100/1.0	[408]
C60	Hydrazine-reduced GO	~10	0.01–3.5		0.05	784	77/20/0.05	[384]
CNTs		~10				730	66/20/0.05	
CNFs	Thermally reduced GO		0.05–3.0	55	0.12 mAh/cm ²	667	91/30/0.12	[409]
Vertically aligned CNTs	Thermally reduced GO paper		0.001–3.0	95	0.1 C (1 C = 300 mA/g)	290	106.9/40/0.1 C	[410]
CNTs	Thermally reduced GO	50	1.5–4.5		155 (307 F/cm ³)	135		[411]
CNTs	Thermally reduced GO	33.3	0.005–3.0	35.4	0.1 C (1 C = 744 mA/g)	548	73.2/100/0.1 C	[404]
		66.7		39.9	0.1 C	618	78.5/100/0.1 C	
					0.5 C	439	97.7/100/0.5 C	
N-doped CNTs	Microwave-reduced GO	57.57	0.005–3.0	66	0.1	1620.3	82.8/142/0.1	[412]
CNTs	Microwave-reduced GO	20.67	0.005–3.0	48	0.25	1187	85.6/140/0.5	[413]
CNTs	Solar radiation reduced GO	50	0.05–3.0	66.5	0.09	1371	59/30/0.09	[414]
							56/100/0.09	
CNTs	Microwave-reduced GO	0	0–3.0	18.4	0.03	204	91.7/50/0.03	[415]
		30		22.3		219		
		70		30.8		293	103.4/50/0.03	

ICE: initial Coulombic efficiency.

highly-conductive CNTs can promote electron transport and ion diffusion and thereby reduce the charge-transfer resistance (R_{CT}) [414]. The reassembly of CNTs and graphene can also enable the formation of mechanically-robust, free-standing, and binder-free film electrodes for flexible LIBs [411,415,416]. Different from the mixing method usually reported, Wang et al. [417] developed 3D hierarchically-structured carbon hybrids by *in-situ* CVD growth of CNTs on graphene. In their work, Co(OH)₂ NPs were first deposited onto GO by single-mode microwave irradiation. GO and Co(OH)₂ were further reduced by C₂H₂ to graphene and Co at 500 °C, respectively. CNTs with tunable length were then grown from the surface of graphene by decomposition of C₂H₂ in the presence of Co NPs as the catalyst. For LIBs using such anodes, CNT/graphene hybrids decorated with short CNTs (200–500 nm) were found to exhibit higher reversible capacities (573 mAh/g at 74 mA/g) and better rate capabilities (520 mAh/g at 744 mA/g, 90.7% retention of initial capacity) than those of CNT/graphene anodes containing long CNTs (454 mAh/g and 73.1% for 400 nm–3 μm in length). It is believed that such hierarchical hybrids with short CNTs enable a good electrical contact, shortened diffusion distance for electrons and ions, and nanoporous spaces for the electrolyte immersion and diffusion, thus improving the electrochemical performance [410].

Based on a similar CVD method, Fan et al. [409] used the Co-deposited GO sheets as a catalyst support to grow CNFs with an outer diameter of ~20 nm and a length less than 1 μm. The effective intercalation of CNFs into graphene sheets produced CNF/graphene hybrids with a higher SSA (315 m²/g) relative to graphene (202 m²/g). Such hierarchical hybrid materials consist of many cavities, nanochannels, open tips, and exposed edges of graphene sheets, offering more extra spaces for Li storage. This leads to a higher reversible capacity (667 mAh/g) compared to graphene (453 mAh/g). In addition, 3D interconnected architectures are favorable for facilitating contact between the electrolyte and active materials to achieve fast Li-ion diffusion. These 3D architectures are also beneficial to the collection and transport of electrons while suppressing volume expansion/shrinkage during cycling. The synergistic effect between CNFs and graphene sheets therefore imparts CNF/graphene composites with high rate

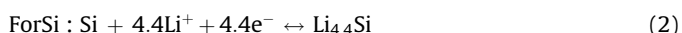
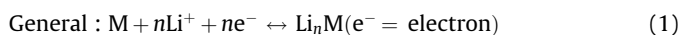
performance and cycling stability. The reversible capacity of CNF/graphene and pure graphene after 30 cycles decreases by 9% and 38%, respectively. This is an encouraging improvement that underscores how significant the architecture can be in performance characteristics. The above CVD techniques enable the large-scale production of hierarchical graphene hybrids with tunable microstructures. It offers an alternative pathway to design electrodes for electrochemical energy storage.

In addition, porous carbon materials can serve as physical spacers reducing the aggregation of graphene sheets [418]. Furthermore, such porous nanostructures also have the ability to shorten the Li-ion transport path, accommodate large volume changes, and enlarge the electrode–electrolyte interface. This can lead to large capacities, high lithiation capability, and good cycling stability [419]. The electrochemical performance can be further improved by using doped carbon materials as hybrid components [420]. As an example, S-doped porous carbon hybrid with graphene (SPC/G) was obtained by an ionothermal method using D-glucose and GO as the starting materials, and an IL of 1-butyl-3-methylimidazolium hydrosulfate as the stabilizer for graphene and sulfur source [407]. The SPC/G has micropores of ~0.5–1.7 nm and a larger SSA (928 m²/g) than that of graphene-free SPC (706 m²/g). When using this hybrid material as an anode, a high reversible capacity of ~1400 mAh/g at 50 mA/g and a Coulombic efficiency over 99% remains in the first three cycles. The first discharge capacity of SPC/G at 1 A/g is 615 mAh/g and increases gradually after 10 cycles until reaching 780 mAh/g in the 500th cycle. The capacity of 520 mAh/g can be recovered again at 1 A/g. Moreover, the SPC/G still delivers a high capacity of 280 mAh/g at 20 A/g, while SPC and graphene only deliver 82.5 and 66.1 mAh/g, respectively. Therefore the SPC/G electrode exhibits high capacity, good reversibility, high cycling stability, and excellent rate performance, which are attributed to the combined effect of two kinds of nanocarbons. Herein SPC serves as the main host for Li adsorption and reservoir while 2D graphene sheets can further impart SPC/G with more active sites for Li storage. S-doping further increases the electrochemical activity of porous carbon by increasing the number of nanopores and interlayer spacing.

Besides, graphene sheets can favor SPC/G with high electronic conductivity for fast Li diffusion and storage. Furthermore, the enhanced capacity upon cycling arises from the gradual electrochemical activation process of SPC/G partially due to S-doping and residual oxygenated groups in graphene [421].

3.1.3. Alloying graphene hybrids

Dey [422] found for the first time that Li can electrochemically alloy with other metals in many organic electrolytes containing Li-ions at ambient temperature. Electrochemical alloying reactions can also occur spontaneously for a wide range of metalloids and metallic compounds [423]. The Li alloying/dealloying mechanism of such metals (M) in LIBs can be given in Eqs. (1) and (2).



Over the past decades, such alloy-based anodes have been extensively explored for the development of high energy LIB applications due to their high theoretical capacities and low working potentials [424,425]. Typically, theoretical specific capacities of fully-lithiated Silicon ($\text{Li}_{4.4}\text{Si}$), Germanium ($\text{Li}_{4.4}\text{Ge}$), and Tin ($\text{Li}_{4.4}\text{Sn}$) are calculated to be as high as ~ 4200 , 1624, and 994 mAh/g, respectively, and their corresponding discharge voltages are ~ 0.4 , 0.5, and 0.6 V (vs Li) [426]. However, the commercial use of bulk alloy anodes in LIBs has been limited by their low capacity retention and low cycling stability. For instance, the irreversible capacity loss of the Si anode in the first cycle is as high as 2650 mAh/g and its reversible capacity drops by 70% after only five cycles [426,427]. Both high initial-irreversible capacity loss and rapid capacity fading during cycling for such anodes are due to their large volume changes upon alloying/dealloying (lithiation/delithiation). The volume expansion, originating from a 440% increase in the number of atoms present in each active material in the fully lithiated state, was reported to be near 434% for amorphous and 399% for crystalline Si, 382% for amorphous and 353% for crystalline Ge, and 305% for amorphous and 259% for crystalline Sn, respectively [428]. Such huge volume variation can produce ultrahigh internal stress that induces dramatic pulverization of electroactive materials, electrode cracking and fracture, and hence electrical disconnection from current collector [429]. The mechanical failure of active materials and anodes therefore brings about low capacity retention, poor cyclability, and reversibility. In this case, the SEI layer formed in alloy anodes is usually unstable and unavoidably becomes thick upon cycling due to a continuous reaction of active materials with the electrolyte. This results in a gradual increase in capacity fading and cell resistance and hence low power delivery [430]. To mitigate the above setbacks, the most common method is to hybridize metallic NPs with carbonaceous materials such as amorphous/mesoporous carbon, graphite, CNFs, and CNTs [424,425]. With great structure-property advantages over traditional carbon materials, graphene has been more extensively explored for fabricating hybrid anodes alloyed by metalloids and metals such as Si, Ge, and Sn over the past years.

3.1.3.1. Si/graphene hybrids. Si has the highest theoretical capacity among all active materials, and it is environmentally benign, abundant, inexpensive, and also safer than graphite [431,432]. Moreover, the burgeoning semiconductor industry enables a scalable infrastructure for processing Si-based materials. A commercially available Si/graphene hybrid was recently used in LIB anodes [433]. Considerable effort has been invested in Si/graphene anodes for high-performance LIBs over the past years. Recently, various Si nanostructures such as NPs, [434–437] nanowires, [438–440] mesoporous Si, [441], and porous Si

[442,443] have been combined with graphene via three synthetic routes.

The simplest methodology is to directly blend graphene with pre-synthesized Si in solid or in solution states. Direct solid-phase mixing cannot effectively induce uniform dispersion of graphene sheets and Si NPs, thus showing only moderate improvement in capacity fading [444]. Zhu et al. [445,446] demonstrated a discharge-plasma-assisted milling (P-milling) method that enables embedding Si NPs into graphene sheets (Fig. 12a). After 20 h, the solid-milled sample consists of ~ 20 -layered graphene sheets with thickness of 7–8 nm and Si NPs with diameter of 20–200 nm (Fig. 12b,c). LIBs with this anode (~ 30 wt% Si) can deliver the first discharge and charge capacity of 1184 and 847 mAh/g at 0.2 A/g, respectively. This corresponds to an initial Coulombic efficiency of 71.6% and an irreversible capacity loss of 337 mAh/g. The reversible capacity at 50 mA/g after 50 cycles remains 976 mAh/g, which drops to 853 and 723 mAh/g at 100 and 400 mA/g after 50 cycles (Fig. 12d), indicating capacity retentions of 87 and 74% of that at 50 mA/g, respectively. Very recently, Yuan et al. [447] reported on the solution mixing of bulk Si particles (~ 90 wt%) and hydrazine-reduced GO under ultrasonication. The resulting alloy anode exhibits a reversible capacity of 2787 mAh/g at 0.1 A/g, and retains 1000 mAh/g at 1 A/g after 50 cycles with a Coulombic efficiency of 99%. This stable charge/discharge performance at high rates is mainly attributed to the self-encapsulation of micro-sized porous Si particles with the electrically-conductive and mechanically-flexible graphene sheets by electrostatic interaction.

The second methodology is based on the in-situ formation of Si NPs on graphene, and can be conducted by magnesiothermic reduction of SiO_2 to Si, [448–451] direct deposition with Si target, [452] and in-situ CVD growth with Si-containing precursors [440,453–456]. For instance, Zhu et al. [457] reported a 3D porous Si/graphene composite prepared by combining an in-situ sol-gel reaction of tetraethylorthosilicate and magnesiothermic reduction in the presence of GO sheets (Fig. 13a and b). The reversible capacity for this hybrid anode maintains 900 mAh/g at charge rates of 0.1–1 A/g (Fig. 13c), and remains at 360 and 290 mAh/g at 5 and 10 A/g after 100 cycles, respectively. Ren et al. [458] fabricated graphene-supported Si thin films by microwave plasma-enhanced CVD (MPECVD) to yield 3D graphene on Ni foil followed by direct deposition of Si onto this scaffold by radio frequency sputtering using a Si target (Fig. 13d and e). The resulting anodes deliver a specific capacity of 1560 mAh/g at 0.797 A/g with a Coulombic efficiency of 99.4% and capacity retention of 84% after 500 cycles. Specific capacities of 1083 and 803 mAh/g can be maintained after 1200 cycles at 2.39 and 7.17 A/g (Fig. 13f), respectively. Such high capacity, excellent cyclability, and rate capability are attributed to the highly-porous, conductive 3D graphene scaffold which provides high-speed pathways for transporting ions and electrons between the electrode and current collector, high mechanical flexibility, and porosity for relieving internal force inside Si and accommodating large volume changes during charge/discharge processes, and large SSA enabling more active sites and electrolyte immersion for high capacity and fast electrochemical kinetics [440,451,456]. In addition, this thin-film technology adopted for direct deposition of 3D graphene and Si is additive-free. This opens up new opportunities for the fabrication of all-solid-state thin film LIBs.

Recently, Wang et al. [459] used SiH_4 as a precursor to grow Si NPs on the surface of MPECVD-grown graphene on Cu foil current collectors. The resulting hybrids can be directly used as binder-free anodes, showing a high reversible capacity (1528 mAh/g at 0.15 A/g), high Coulombic efficiency (97–100%) after the 1st cycle, good cyclability (88.6% after 50 cycles), and fast charge/discharge rate (412 mAh/g at 8 A/g). Cho et al. [460] performed thermal

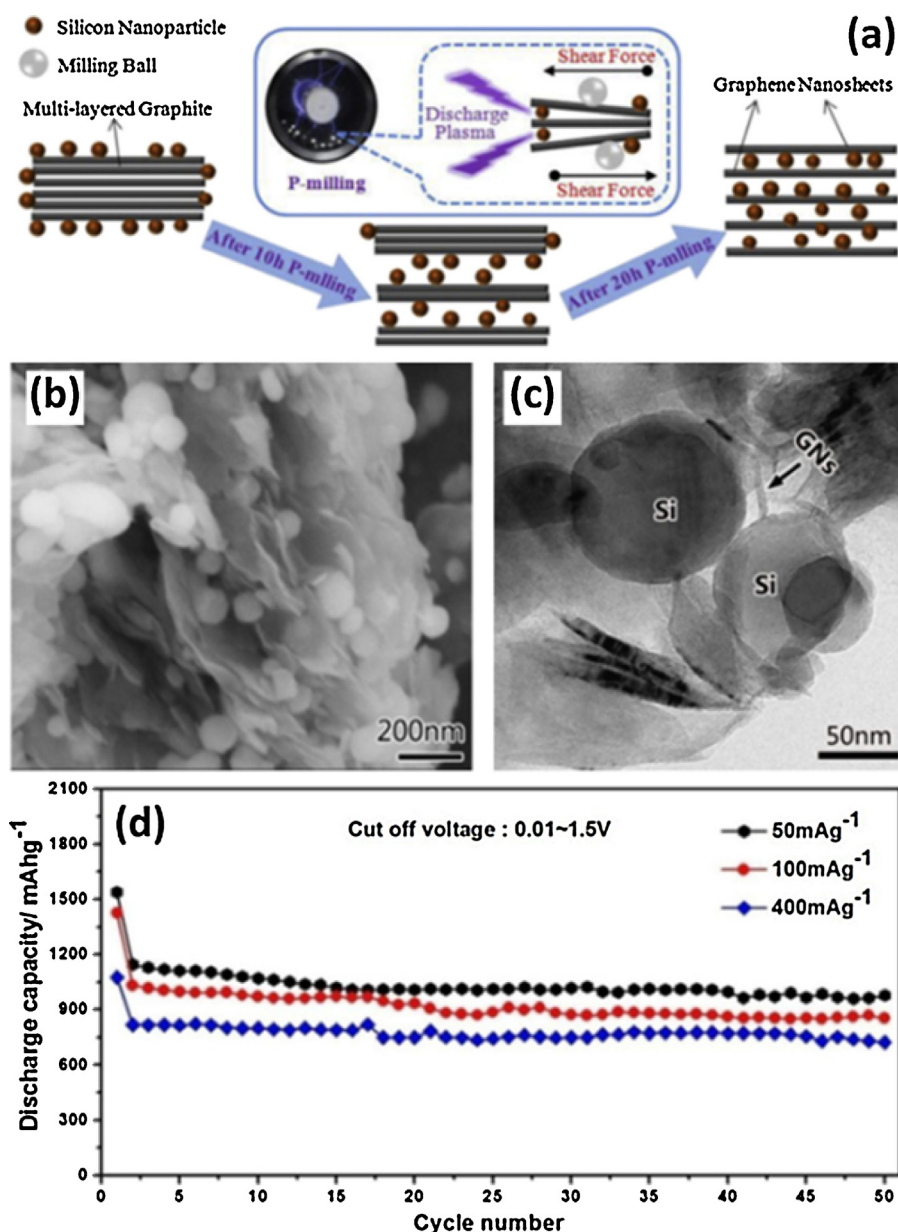


Fig. 12. (a) Schematic illustration of P-milling method to produce Si/graphene hybrids and their corresponding SEM (b) and TEM (c) images, and (d) cycle performance at different current rates between 0.01 and 1.5 V [445]. Copyright 2014 Elsevier B.V.

decomposition of SiH_4 to form the island structure of amorphous Si NPs (5–10 nm) that arranged homogeneously on both sides of thermally-reduced porous GO sheets (Fig. 14a). The as-fabricated Si NP (82 wt%) backbone-graphene (*a*-SiBG) electrode delivers charge capacities as high as 2699, 2450, 1622, and 1148 mAh/g at current densities of 0.56, 2.8, 14, and 28 A/g (Fig. 14d), respectively, with a high Coulombic efficiency ($\sim 92.5\%$) in the 1st cycle. The rate capability of *a*-SiBG is significantly higher than that of crystalline Si nanopowder (*c*-SiNP) (e.g., 1812 and 5 mAh/g at 0.56 and 28 A/g, respectively). Interestingly, *a*-SiBG exhibits almost no capacity fading while retaining average charge capacities of up to 1103 mAh/g over 1000 cycles and average Coulombic efficiencies close to 100% over all cycles (Fig. 14e). A coin-type full-cell consisting of an *a*-SiBG anode and LiCoO_2 cathode also exhibits a high specific energy of 468 and 288 Wh/kg under specific powers of 7 and 11 kW/kg, respectively. Such excellent electrochemical performance originates from the tailorable hybrid nanostructures which show an elastic behavior on volume variations during

lithium alloying/dealloying (Fig. 14a and b), a decreased electrode thickness upon cycling as a result of self-compacting (Fig. 14c) and fast electron transport/lithium diffusion.

The most widely used methodology is post-reduction of GO in the presence of Si NPs which are subsequently encapsulated in the graphene matrix [461–466]. Si/graphene hybrids can be made by chemically reducing the mixed suspension of Si/GO upon addition of reactants [467]. In most cases, Si/graphene alloys are produced by thermal annealing of the dried Si/GO hybrids from their suspensions which are subjected to either freeze-drying, [468,469] spray drying, [470] spin coating, [465] air drying, [471], or electrospinning [472,473]. The key advantage for these methods is that GO sheets can be individually dispersed into water to form stable suspensions and accordingly retard the aggregation of Si NPs by coating with graphene sheets after reduction. However, hydrophobic Si NPs still tend to self-aggregate in aqueous media, resulting in inhomogeneous mixing of Si NPs and GO sheets. A solvent exchange process was recently proposed in which Si NPs

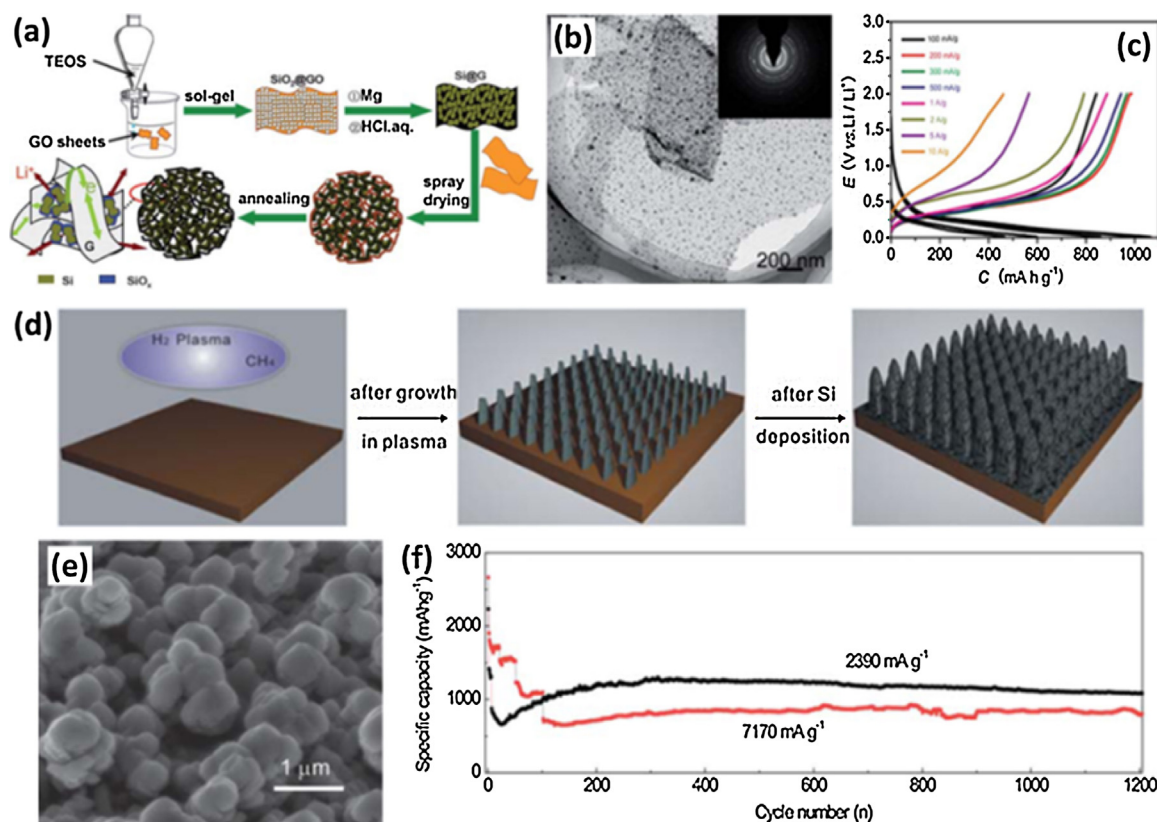


Fig. 13. Si/graphene composites fabricated by magnesiothermic reduction of SiO_2 to Si in the presence of GO sheets: (a) the preparation process and microstructure characteristics, (b) TEM image, and (c) galvanostatic charge/discharge (GCD) curves at different rates [457]. Copyright 2012 Royal Society of Chemistry. 3D Graphene-supported Si thin films by direct deposition of Si onto graphene: (d) the fabrication process, (e) typical SEM image, and (f) charge-discharge capacities at 2390 and 7170 mA/g [458]. Copyright 2013 Royal Society of Chemistry.

were ultrasonically dispersed in NMP, showing better dispersion and stability compared to in water [474,475]. After discarding the NMP supernatant by centrifugation, the residual NMP molecules adsorbed on the surface of Si NPs can improve the compatibility with aqueous suspensions of GO. The anode using this material (50 wt% Si) has a relatively low capacity loss (32%) compared to the untreated sample (46%) after 30 cycles [475]. This indistinctive improvement arises from some residual aggregates remaining after solvent exchange due to the weak interaction between NMP and Si NPs.

The exposure of Si NPs to air or O_2 is an alternative way to induce a very thin superficial layer of hydrophilic SiO_x that favors their dispersion in water [476]. This process effectively avoids the aggregation of Si and suppresses the re-stacking of graphene sheets, thus generating homogeneous Si/graphene composites. The alloy anode with ~31 wt% of Si NPs (~50 nm in diameter) was found to exhibit a stable reversible capacity on the order of 1000 mAh/g and a capacity retention of ~80% after 100 cycles at 0.5 A/g [477]. The presence of SiO_x around Si can be further modified by surface coupling of active molecules such as amino-silanes which can endow Si NPs with a positively-charged surface for dispersion in aqueous media [478]. On the other hand, GO sheets are known to be decorated with negatively-charged carboxyl and phenolic hydroxyl groups through ionization over a wide pH range [281]. These charged groups on Si and GO provide electrostatic repulsion to prevent their self-aggregation. More importantly, the oppositely-charged GO sheets and functionalized-Si enable the fabrication of homogeneous graphene-encapsulated Si hybrids (Si@G) by electrostatic-attraction co-assembly and subsequent reduction [479,480]. As an example using this method, aminopropyltriethoxysilane (APS)-modified Si NPs (72 wt%) were

uniformly encapsulated by graphene sheets [481]. The as-fabricated anode can contribute to exceptionally high capacity (2250 mAh/g at 0.1 A/g), good rate capability (1900 and 1000 mAh/g at 1 and 10 A/g respectively), and superior cycling stability (85% of initial capacity after 120 cycles). Si@G hybrids were also fabricated by electrostatic co-assembly between negatively-charged Si NPs and positively-charged graphene by poly(ionic liquid). The resulting anodes delivered a capacity of 803 mAh/g at 0.2 A/g at 100 cycles and <0.25% capacity fading per cycle before 150 cycles [482]. It should be highlighted here that this self-assembly strategy is highly effective in fabricating homogeneous GO-derived composites by electrostatic interactions between consecutively-adsorbed and oppositely-charged species [483–485].

The passivation layer of SiO_x can help to disperse Si into aqueous media, however, it also acts as an electronic insulator and a Li-ion diffusion barrier, leading to slow power delivery, incomplete lithiation and relatively low capacity and cycling performance of Si-based electrodes [486,487]. To overcome this issue, Guo et al. [488] extended an electrostatic self-assembly strategy to create homogeneous Si/graphene composites. As shown in Fig. 15a, a positively-charged polyelectrolyte of poly(diallyldimethylammonium chloride) (PDDA) is first adsorbed on Si NPs. The obtained positively-charged Si NPs then uniformly assemble with negatively-charged GO sheets through electrostatic interactions to produce well-mixed Si/GO composites. After freeze-drying, thermal reduction, and hydrofluoric acid (HF) treatment, PDDA decomposes almost completely and the SiO_x layer (Fig. 15b) is fully etched away from Si NPs. Then SiO_x -free Si NPs (80.1 wt%) are uniformly-encapsulated by wrinkled graphene sheets (Fig. 15c and d). The cyclic voltammetry (CV) curves of such Si@G exhibit

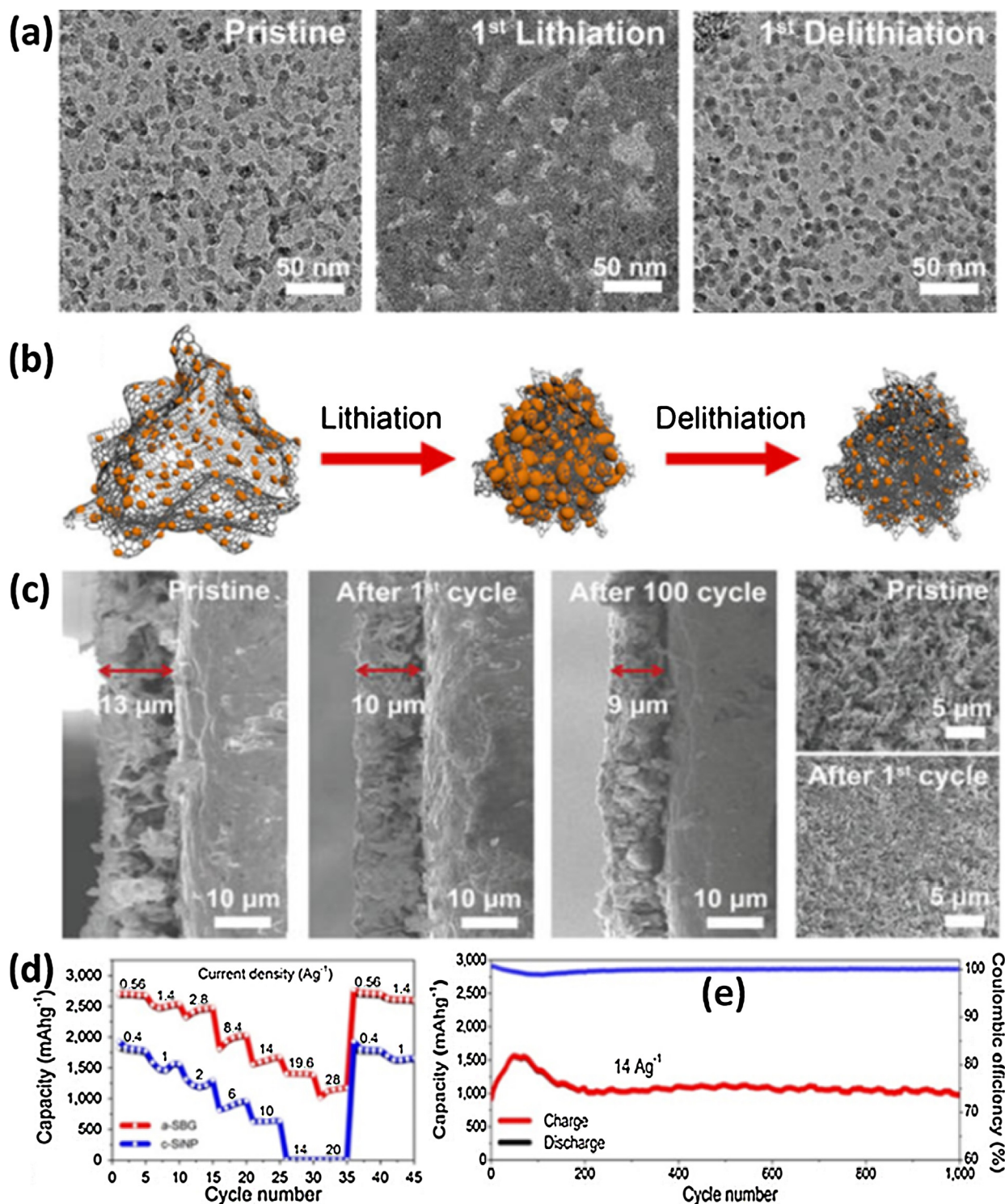


Fig. 14. (a) TEM images of α -SiBG in pristine state, after 1st lithiation, and after 1st delithiation, (b) Schematic view of α -SiBG before and after electrochemical cycling, and (c) cross-section and top-view SEM images of the α -SiBG electrode taken during electrochemical cycling. Electrochemical performance: (d) charge capacities of α -SiBG and c-SiNP at different current densities, and (e) cycling performance of α -SiBG at a charge current density of 14 A/g and a discharge density of 2.8 A/g over 1000 cycles [460]. Copyright 2014 American Chemical Society.

two cathodic peaks at 0.05 and 0.21 V due to the formation of Li–Si alloy phases, and two anodic peaks at 0.31 and 0.51 V correspond to the dealloying of Li–Si alloys (Fig. 15e). Si@G exhibits an initial discharge capacity of up to 2920 mAh/g at 0.1 A/g, and its reversible charge capacity reaches 1720 mAh/g and remains 1205 mAh/g after 150 cycles (Fig. 15f). Moreover, the reversible capacities are still as high as 1452, 1320, and 990 mAh/g with

increasing current densities from 400 to 800 to 1600 mA/g (Fig. 15g). Recently, Xie et al. [489] demonstrated the fabrication of oxide-free carbon-coated Si@G by co-assembly between polyaniline (PANI)-grafted Si NPs and GO through π – π and electrostatic interactions followed by thermal annealing. The Si@G (66 wt% Si) electrode exhibits a high initial Coulombic efficiency (73.2%) which increases rapidly and remains above 99% during the

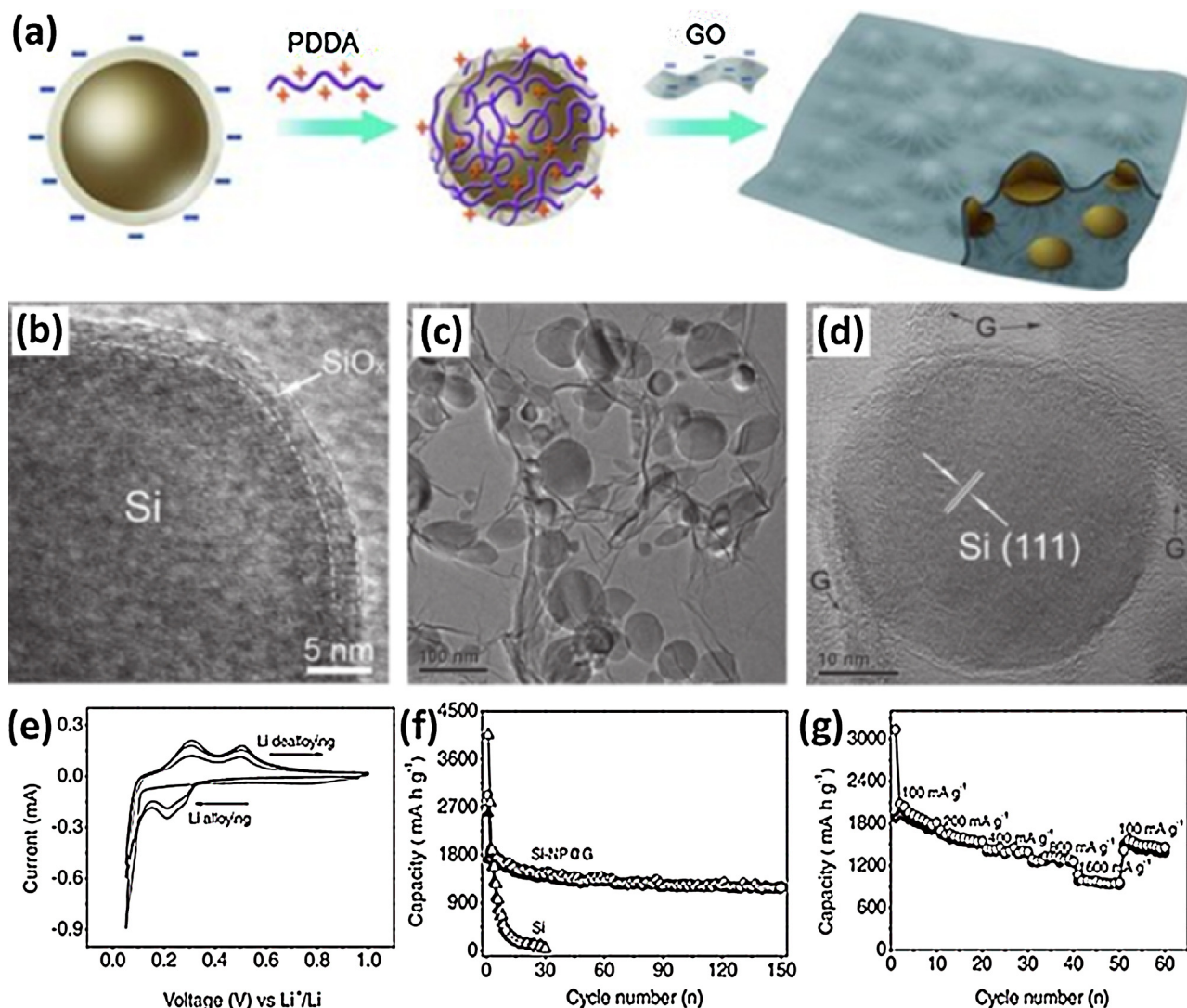


Fig. 15. (a) Fabrication process of self-assembled Si-NP@G composites: (i) Electrostatic adsorption of PDPA chains onto Si NPs to produce Si NPs charged positively and (ii) electrostatic assembly between positively-charged Si NPs and negatively-charged GO sheets followed by freeze-drying, thermal reduction of GO, and HF removal of SiO_x layer. The golden balls and grey coatings represent Si NPs and graphene sheets, respectively. TEM images of (b) a Si NP with a thin layer of SiO_x and (c and d) SiO_x-free Si NPs encapsulated by graphene. Electrochemical performance: (e) CV curves, (f) cycling performance and (g) rate capability of Si-NP@G electrodes [488]. Copyright 2012 Wiley-Vch.

following cycling tests. The reversible specific capacity is ~ 1500 mAh/g at 50 mA/g and retains above 900 mAh/g after 300 cycles at 2 A/g. Such high capacity, cycling performance and rate capability of Si@G hybrids are mainly attributed to the incorporation of graphene sheets which deliver sufficient electrons to Si NPs and buffer the mechanical deformation during Li–Si alloying/dealloying. Meanwhile, many nano-sized spaces between graphene sheets and Si NPs can promote Li diffusion and also accommodate the volume changes of Si NPs. In addition, carbon coating layers coated on Si NPs work together with graphene to suppress the re-aggregation of Si NPs and to avoid structural and interfacial destruction. This allows the overall electrode to be highly conductive and active during charging/discharging [478,490].

3.1.3.2. Sn/graphene hybrids. Sn has a lower gravimetric capacity but a comparable volumetric capacity (~ 2000 mAh/cm³) with respect to Li and Si and hence it is an attractive anode material [491]. Like other Li-alloying materials, however, the Sn anode has been limited by its large volume variation during cycling associated with the formation of a Li–Sn intermetallic phase

[423]. Based on the advantages of graphene, Sn/graphene alloy anodes have been proposed to minimize such volume changes and thereby lead to stable cycling profiles for LIBs [492]. Considerable efforts have been devoted to encapsulating Sn in graphene-based anodes by using various methods such as arc-discharge, [493] thermal-evaporation deposition, [494,495] electrophoretic deposition, [496] ball-milling, [497] solution mixing, [498], and melt mixing [499]. The most used method is based on the co-reduction of GO and Sn-containing precursors [500–509]. Zhi et al. [510] reported on the synthesis of graphene-confined Sn nanosheets by reduction of GO-supported SnO₂ NPs via hydrolysis, hydrothermal and annealing treatments. The as-fabricated 60.1 wt% Sn/graphene anode exhibits high reversible capacity (1380 mAh/g at 50 mA/g), an initial Coulombic efficiency of 66.5%, and excellent cycling performance (> 590 mAh/g after 60 cycles). It should be noted that metallic Sn usually melts at a low temperature (~ 232 °C) which is further reduced when particle sizes approach nanoscale levels. Sn NPs prefer to agglomerate during the high-temperature processing required in most cases. It therefore remains a challenge to effectively control Sn-based nanostructures when hybridized with graphene sheets.

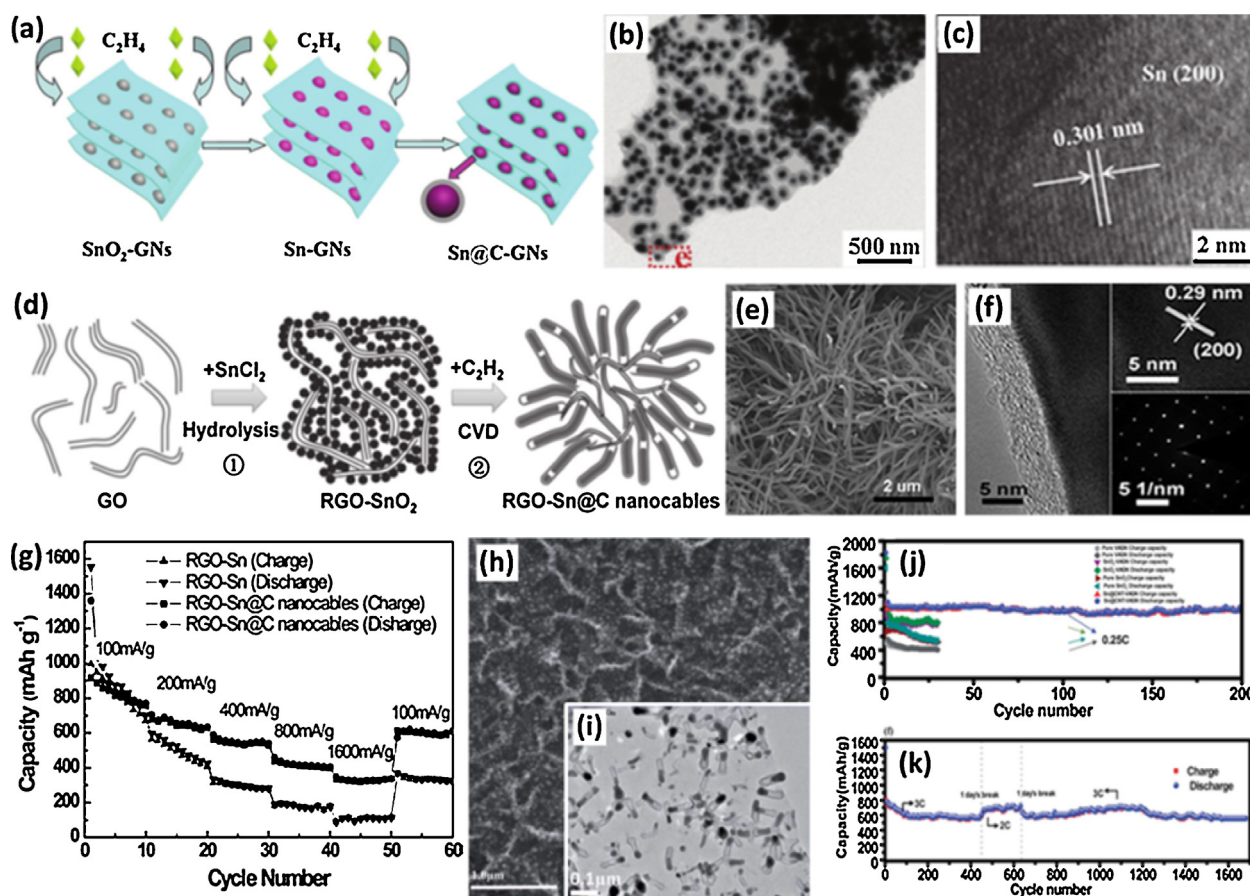


Fig. 16. Graphene-supported Sn@C NPs: (a) schematic sketch for growth procedure and (b) and (c) TEM images. The red rectangular region in (b) corresponds to the crystalline Sn core [513]. Copyright 2013 Royal Society of Chemistry. Graphene-supported Sn@C nanocables: (d) schematic of synthesis procedures, (e) SEM and (f) high resolution TEM (HRTEM) images, (g) Rate performances of graphene-Sn@C nanocables and graphene-Sn electrodes at different rates [515]. Copyright 2012 Wiley-Vch. VAGN-supported Sn@CNTs: (h) SEM and (i) TEM images, and (j) and (k) Cycling and rate performances [516]. Copyright 2014 Royal Society of Chemistry (For interpretation of the references to color in this figure legend, the reader is referred to the web version of this article.).

In order to avoid the coalescence between separated Sn NPs, Sn-carbon core-shell (Sn@C) nanostructures have been developed in which the carbon layer serves to stabilize the Sn NPs [511,512]. Hierarchical Sn@C NPs embedded graphene sheets were recently fabricated by a CVD procedure (Fig. 16a), in which SnO₂ NPs were reduced to crystalline Sn NPs followed by coating with a carbon layer via ethylene decomposition [513]. The Sn@C-graphene anode (Fig. 16b and c) exhibits an initial discharge capacity as high as 1069 mAh/g at 75 mA/g which remains as high as 566 mAh/g after 100 cycles. This is partially due to spatial confinement of individual Sn NPs by the outer shell [514]. Similarly, Zhi et al. [515] performed a hydrolysis process of SnCl₂ in the presence of GO to yield SnO₂ NP-decorated graphene sheets. When heated under a gas mixture of C₂H₂/Ar at 600 °C, the graphene-supported Sn@C nanocables could be obtained (Fig. 16d–f). As shown in Fig. 16g, the as-fabricated anode consistently exhibits much higher specific capacity at a series of current rates when compared to the graphene-Sn electrode (prepared by thermal reduction of graphene-SnO₂ at 700 °C in the absence of acetylene). Moreover, Sn NPs supported on graphene were found to catalyze the decomposition of ethylene for continuing CVD growth of CNTs [502]. The resulting Sn@CNT-graphene hybrid anode shows an initial charge capacity up to 1160 at 0.1 A/g and excellent rate capability (828 and 594 mAh/g at 1 and 5 A/g respectively), and retains 982 mAh/g after 100 cycles. Recently, Wang et al. [516] reported a new strategy to grow self-assembled Sn@CNTs on vertically-aligned graphene

nanosheets (VAGNs) (Fig. 16h and i) by microwave plasma irradiation reduction of SnO₂ and *in-situ* encapsulating Sn NPs in CNTs upon introducing CH₄/H₂. This hierarchical Sn@CNT-VAGN anode exhibits a high reversible capacity of 1026 mAh/g at 0.25C, excellent cycling performance and high-rate capability (Fig. 16j and k), high Coulombic efficiency of 92–100%, and a fast charge-discharge rate.

He et al. [517] used SnCl₂ as a catalyst and the 3D self-assembly of SnCl particles as a template to develop a one-step CVD method for 3D porous graphene networks anchored with graphene-encapsulated Sn NPs (Sn@G-PGNWs, see Fig. 17a and b). The high resolution TEM (HRTEM) image further shows that Sn NPs exist as a crystallized-amorphous core-shell nanostructure, and are encapsulated by a ~1 nm thick graphene shell (Fig. 17c). This 3D Sn@G-PGNW anode exhibits a large capacity (1022 mAh/g at 0.2 A/g), high Coulombic efficiency, long-term cycling stability (Fig. 17d) and superior rate capability (865, 652 and 270 mAh/g at 0.5, 2 and 10 A/g, respectively, see Fig. 17e). It's interesting to note that all of these properties are higher than values reported for LIB anodes based on commercial Sn NPs and Sn/C composites. Sn@G NPs tightly bound onto VAGNs (Sn@G-VAGNs, see Fig. 17f, g) was also realized by a combination of CVD and hydrothermal methods [518]. This Sn@G-VAGN anode exhibits a larger-than-theoretical reversible capacity of 1037 mAh/g, long-term cyclic stability at high rates (retaining 400 mAh/g at a 6C rate over 5000 cycles) and a power density of 1588.6 W/kg with an energy density of 117.67 Wh/kg.

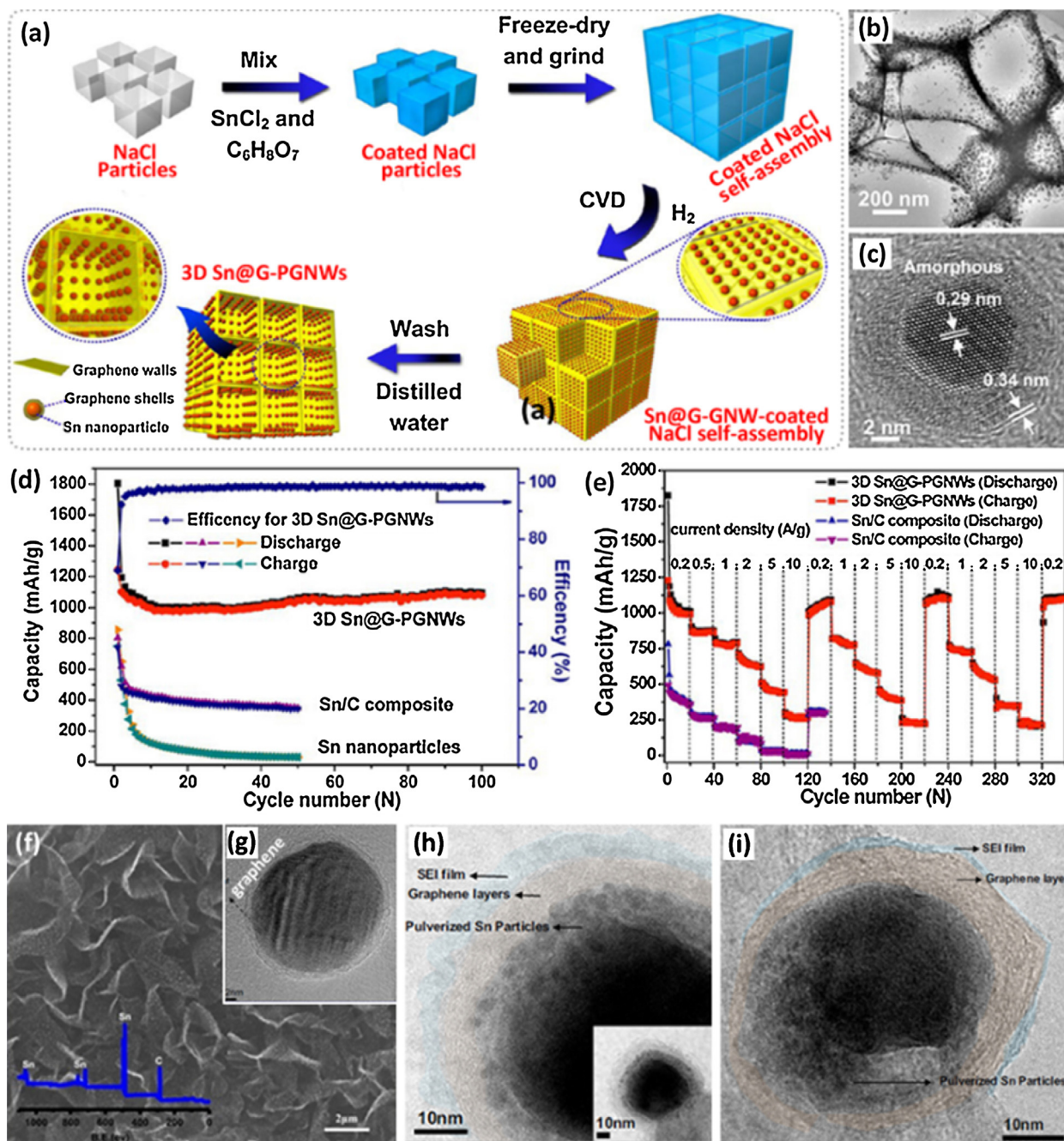


Fig. 17. Sn@G-PGNWs: (a) Schematic illustration for a one-step *in-situ* CVD process, (b) TEM and (c) HRTEM images, (d) Cycle performance of Sn@G-PGNWs, Sn/C composites and commercial Sn NPs at 0.2 A/g, and (e) Rate cycle performance of Sn@G-PGNWs and Sn/C composites at different rates for 340 cycles [517]. Copyright 2014 American Chemical Society. Sn@G-VAGNs: (f) SEM image (the inset XPS spectrum), and (g) HRTEM image (indicating a crystalline Sn core coated by graphene shells). Morphological and structural changes of the Sn@G-VAGN anode after 120 cycles: (h) TEM image of a typical Sn@G NP at the fully-discharged state. (i) TEM image of Sn@G NP at the fully-charged state. Sn NPs are pulverized into smaller ones which are still encapsulated in graphene shells [518]. Copyright 2014 Elsevier Ltd.

The outstanding electrochemical performances as demonstrated above are attributed to unique hierarchical nanostructures and synergetic effects of Sn/graphene hybrids. Taking Sn@G-VAGN as an example, the graphene sheath prevents Sn NPs from coalescing into bulk moieties. More importantly graphene acts as an effective physical barrier protecting the Sn core against direct contact with either each other or the electrolyte during battery cycling. Fig. 17h shows an expanded Sn core after 120 cycles upon lithiation due to the formation of a Sn–Li alloy. Fig. 17i displays a shrunken Sn core after delithiation. The initial Sn core was pulverized into smaller NPs which remained encapsulated in graphene with a well-preserved core-shell structure. The Li-ion conductive SEI film

remained unbroken and served as a protective layer to accommodate large volume changes during alloying/dealloying. This double-shielding effect is a key contributor to the excellent mechanical stability and cycle performance of this material. Moreover, the Sn core remained in intimate contact with the graphene shell during charging/discharging. The flexible graphene shell therefore can act as a conducting bridge between Sn NPs and the underlying matrix. This ensures permanent electrical interconnectivity and short transport pathways of Li-ions and electrons within the overall electrode. This promotes faster charging/discharging rates, higher energy delivery and improved rate capability. In addition, Sn@G NPs enable an efficient

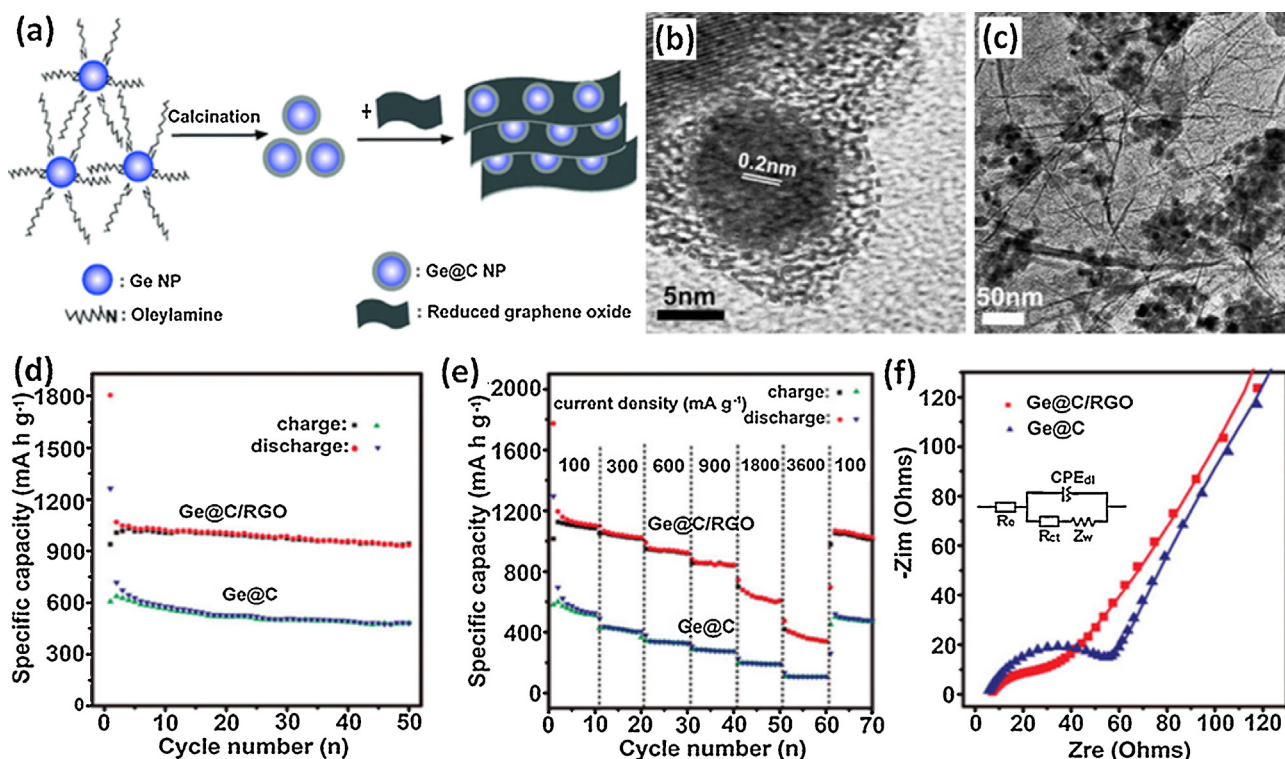


Fig. 18. (a) Synthesis route for Ge@C-graphene composites and TEM images of (b) Ge@C NPs, and (c) their distribution on graphene networks. Electrochemical performances of Ge@C-graphene and Ge@C anodes: (d) Cycling behaviors under a current density of 50 mA/g, (e) rate performance under different current densities, and (f) Nyquist plots [531]. Copyright 2012 American Chemical Society.

prevention of graphene agglomeration and 3D porosity retention in the electrode. This increases the accessible interface for the electrolyte and promotes fast charge transport. This results in an enhanced capacity and alleviates large volume changes. Therefore, graphene-alloy anodes containing Sn encapsulated in either carbon, CNTs or graphene shells show promise for high-performance LIBs.

3.1.3.3. Ge/graphene hybrids. Despite high theoretical capacity and low working potential, Ge has not been investigated as much as an anode material due to its higher cost compared to Si and Sn [425]. Ge typically exhibits a higher Coulombic efficiency than Si- and Sn-based anodes in the first cycle. Furthermore, the smaller bandgap (0.6 eV) of Ge allows for orders of magnitude higher electrical conductivity (~ 2.1 S/m) and Li-ion diffusivity (6.25×10^{-12} cm²/s) than Si (~ 1.6 mS/m, 1.9×10^{-14} cm²/s). This is promising for higher power capability [428,519,520]. It is therefore worth investigating the potential of Ge-based anodes toward high-rate LIBs for electric vehicles [521]. Similar to fabricating Si- and Sn-based anodes, the method of hybridizing/coating Ge with carbonaceous materials has been used to enhance the cycling stability and capacity retention of Ge-based anodes in LIBs [423,522].

At present, Ge/graphene hybrids have been fabricated by various methods such as solution mixing, [498] solvothermal reduction of GO and organic Ge precursor, [523] chemical reduction of GO and inorganic Ge precursors, [524,525] thermal annealing of GO and Ge precursors, [526] plasma-enhanced CVD growth of graphene and reduction of GeO₂, [527] and thermal evaporation deposition of Ge onto graphene [528,529]. Similar to fabricating Si- and Sn-based anodes, the co-reduction of GO and Ge-containing precursors has also appeared as a commonly-used method to produce Ge-based anodes. As an example, Tuan et al. [526] fabricated graphene composites with ~ 80 wt% single-crystal

Ge NPs (~ 4.9 nm) by thermal decomposition of GeI₂ in the presence of oleylamine-functionalized GO. The resulting Ge/graphene anode exhibits a superior capacity (1332 mAh/g at 0.2 C) and a high-rate capability over hundreds of cycles. Furthermore, pouch-type full cells assembled using this anode and LiCoO₂ cathode output a large current (20 mAh) capable of powering wide range of electronic devices such as a light-emitting diode (LED) arrays consisting of over 150 bulbs, blue LED arrays, a scrolling LED marquee, and an electric fan. This work clearly demonstrates a proof of concept of graphene-based anodes toward practical LIB applications.

As previously described, encapsulating Ge in an additional carbon shell ensures a double protection strategy for enhancing both cyclability and rate capability of Ge/graphene hybrid anodes [530]. For instance, Guo et al. [531] reported the fabrication of Ge@C-graphene composites by solution reaction between GeBr₂ and oleylamine and subsequent high-temperature carbonization followed by solution mixing with thermally-reduced GO sheets (Fig. 18a). Ge NPs were uniformly covered by a carbon layer (2–3 nm in thickness, see Fig. 18b), thus avoiding the self-aggregation and direct exposure to the electrolyte. Ge@C NPs (10–15 nm) were also dispersed in graphene networks (Fig. 18c) serving as an efficient mechanical support and electron-conducting pathway. This hierarchical composite shows higher initial discharge (1803 mAh/g) and charge (938 mAh/g) specific capacities and, better cycling performance (remaining ~ 940 mAh/g at 50 mA/g after 50 cycles, see Fig. 18d) and higher rate capability (Fig. 18e) compared to pristine Ge@C NPs. These improvements arise from the unique double protection of Ge NPs through Ge@C core-shell nanostructures and electronically-conductive, elastic graphene networks promoting low charge-transfer resistance (Fig. 18f).

Recently, direct growth of few-layer graphene from the surface Ge nanowires was successfully achieved using catalyst-free routes

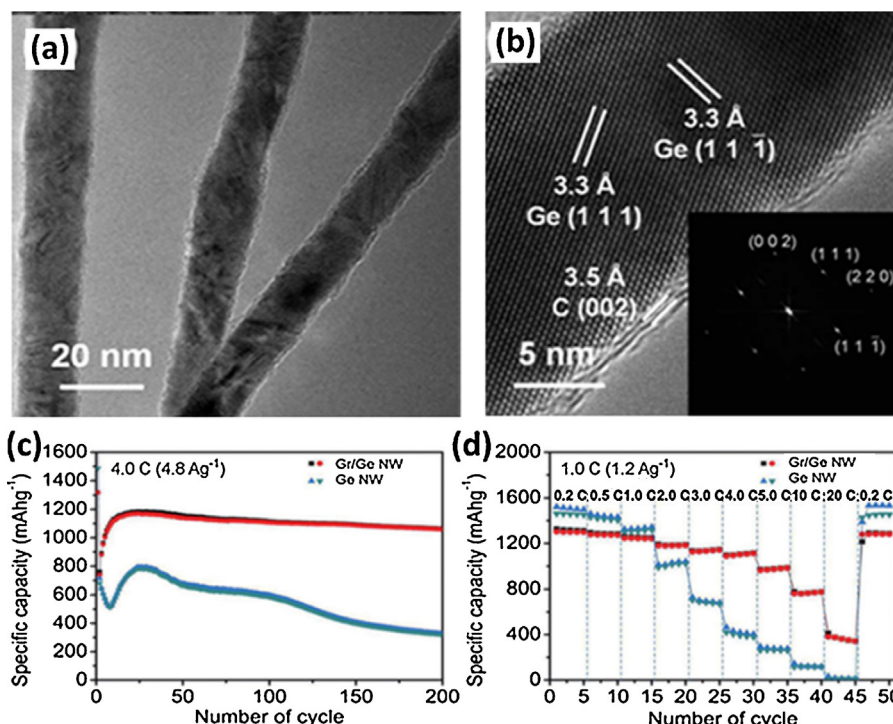


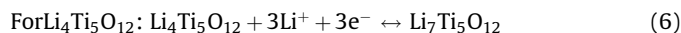
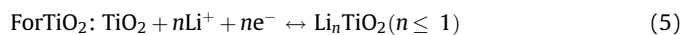
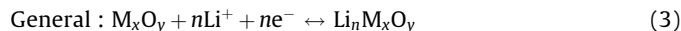
Fig. 19. (a and b) TEM images of Ge@G nanowires made by arc-discharge [532]. Copyright 2013 Royal Society of Chemistry. Electrochemical performances of Ge@G made by CVD (black ■ charging; red ● discharging) and bare Ge (blue ▲ charging; green ▼ discharging) nanowire anodes: (c) Cycle performance at a rate of 4.0 C, and (d) rate capability from 0.2 to 20 C [533]. Copyright 2013 Wiley-Vch (For interpretation of the references to color in this figure legend, the reader is referred to the web version of this article.).

via arc-discharge [532] and CVD [533] processes. The as-fabricated Ge@G composites are composed of a thin graphene sheath and a crystallized Ge nanowire core (Fig. 19a and b). Anodes based on such Ge@G core-shell nanowires exhibit specific capacities as high as 1059 mAh/g at a 4.0 C rate (1.0 C = 1.2 A/g) and capacity retention beyond 90% after 200 cycles (Fig. 19c). The Coulombic efficiencies range from 98.3% to 99.7% beyond the 2nd cycle up to the 200th cycle. In contrast, bare Ge nanowires provide much lower specific capacity (321 mAh/g) and poor capacity retention (41%) after 200 cycles. Ge@G nanowire anodes also show excellent rate capability even at a high C-rate (Fig. 19d). The specific capacity reaches ~363 mAh/g at 20 C, and can be recovered (98.6% retention) when the C-rate is returned to the initial 0.2 C after 45 cycles. For the graphene-free Ge nanowire anode, however, its specific capacity reduces rapidly with increasing the C-rate from 0.2 to 20 C, accompanied with a specific capacity as low as 20 mAh/g at 20 C. The improved performance of Ge@G nanowires can be attributed to mechanically robust Ge nanowire with high-quality graphene which promotes high electrical interconnectivity and conduction over the electrode. Meanwhile, a thin coating of few-layer graphene allows Li-ions to quickly diffuse into and out of the core Ge nanowire. Electrochemical performance can be further enhanced by using highly-conductive and electroactive N-doped graphene sheets as the matrix [534,535]. In addition, CNTs can be introduced to physically-disperse Ge NPs mechanically-stabilize and electrically-interconnect the Ge/graphene anode leading to better LIB cycling performance [536]. These strategies will contribute to future developments of graphene-protected alloy electrodes for electrochemical applications.

3.1.4. Metal oxide/graphene composites

LIB anodes based on metal oxides are generally classified into three main categories: insertion, conversion, and alloying types

in terms of reaction mechanisms with Li [424]. Insertion-type metal oxides typically include TiO_2 , vanadium oxides (e.g., V_2O_5 , V_6O_{13} , LiV_3O_8), lithium titanium oxides (e.g., $\text{Li}_4\text{Ti}_5\text{O}_{12}$, LiTi_2O_4 , LiCrTiO_4 , $\text{SrLi}_2\text{Ti}_6\text{O}_{14}$) and lithium phosphates (e.g., $\text{LiTi}_2(\text{PO}_4)_3$, $\text{Li}_3\text{V}_2(\text{PO}_4)_3$, LiVPO_4F) [425]. The fundamental electrochemical reactions for two typical insertion-type metal oxides are illustrated in Eqs. (3)–(6). Such Li-intercalating materials usually undergo a so-called “topotactic reaction” process which involves the insertion (intercalation) and extraction (deintercalation) of Li-ions into and from the host lattice with minor modification of the crystal structure. Insertion-type anodes thus exhibit long lifetimes, low irreversible capacity loss and small volume variation. They are currently limited to low inherent electrical conductivities, low specific capacities, high intercalation potentials (e.g., $<10^{-13}$ S/cm, ~175 mAh/g and ~1.55 V for commercial $\text{Li}_4\text{Ti}_5\text{O}_{12}$ in turn) and inter-particle aggregation [537].



Most metal oxides belong to conversion-type materials and include binary compounds (M_xO_y , M: Mn, Fe, Co, Ni, Cu, Mo, Ru, etc.), ternary (binary metal) oxides ($\text{A}_x\text{B}_y\text{O}_z$, A or B: Mn, Fe, Co, Ni or Cu, $A \neq B$), and complex oxides [538]. In principle, conversion-type anodes undergo a reversible “conversion (redox)/displacement” electrochemical reaction which involves the formation and decomposition of Li_2O along with the reduction to and oxidation of metallic NPs, as expressed in Eqs. (7)–(10). These reactions therefore involve the full reduction of transition metals to their

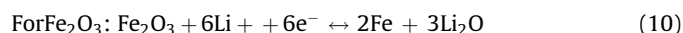
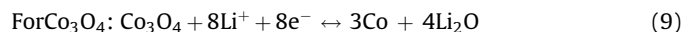
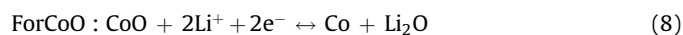
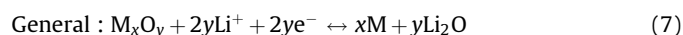
Table 3

Electrochemical performance of metal oxide/graphene composite anodes for LIBs.

Graphene composites			Voltage range V (vs Li/Li ⁺)	Specific capacity			Cycling performance	Refs
M _x O _y	M _x O _y nano-structures	M _x O _y loading (wt%)		ICE (%)	Current density (A/g)	Capacity (mAh/g)	Capacity retention (%) / cycles / current density (A/g)	
Insertion-type M _x O _y								
Li ₄ Ti ₅ O ₁₂	NPs	95	0.8–2.5	/	30 C (1C = 175mAh/g)	122	94.8/300/20 C	[571]
Li ₄ Ti ₅ O ₁₂	NPs	98.8	1.0–2.5	/		123.5	94.6/100/10 C	[572]
Li ₄ Ti ₅ O ₁₂	Nanosheets	84.5	1.0–2.5	/	60 C	82.5	96.9/100/1 C 97.5/100/10 C 97.1/100/60 C	[573]
TiO ₂	Nanotubes	84.5	1.0–3.0	/	10 C	118	79.5/150/5 C (1 C = 337 mAh/g)	[574]
TiO ₂	Nanosheets	77.8	1.0–3.0	/	40 C	200	80/1000/40 C (1 C = 335 mAh/g)	[575]
Conversion-type M _x O _y								
α-Fe ₂ O ₃	Nanorods	58.3	0.005–3.0	61.3	1	210.7	34.7/30/0.1	[576]
α-Fe ₂ O ₃	Nanodisks	75.6	0.005–3.0	/	10	337	85.6/50/0.2	[563]
α-Fe ₂ O ₃	Nanospindles	75.6	0.005–3.0	70.8	0.1	969 (100th)	62.3/100/0.1	[570]
					0.5	589 (100th)	65.6/100/0.5	
					1	368 (100th)	37.5/100/1	
					5	336 (100th)	48.1/100/5	
Fe ₃ O ₄	Hollow NPs	90.2	0.005–3.0	–	0.1	~900 (50th)	~100/50/0.1	[577]
Fe ₃ O ₄	Nanorods	75	0.01–3.0	60.2	4.864	569	95/100/1 C	[578]
Fe ₃ O ₄	NPs	50	0.01–3.0	61.6	5	300	58.7/50/0.1	[579]
Fe ₃ O ₄	NPs	80	0.01–3.0	66	60C	190	SI/500/1 C	[580]
Co ₃ O ₄	NPs	75.4	0.01–3.0	68.6	0.05	~935 (30th)	SI/30/0.05	[581]
Co ₃ O ₄	Hollow nanospheres	76.2	0.01–3.0	69.3	5	259	81.6/100/1	[582]
Co ₃ O ₄	Nanorods	80	0.01–3.0	70.4	1	1090	SI/40/0.1	[583]
Co ₃ O ₄	Nanosheets	/	0.05–3.0	76.6	5 C	130	63.9/50/0.2 C (1 C = 891 mAh/g)	[584]
MnO	Nanosheets	82.6	0.01–3.0	/	3	625.8	96/400/2	[545]
MnO	NPs	91.1	0.01–3.0	69.5	5	202	SI/90/0.1	[553]
Mn ₃ O ₄	Needles	65.7	0.01–3.0	/	0.075	720 (100th)	53.3/100/0.072	[585]
MnO ₂	Nanorods	/	0.2–3.0	/	0.4	698	51.7/15/0.050	[586]
MnO ₂	Nanotubes	~50	0.01–3.0	/	1.6	208	/	[587]
CuO	Nanorods	/	0.001–3.0	64.7	5 C	262	74/50/0.1 C (1 C = 674 mAh/g)	[588]
CuO	Nanosheets	50	0.01–3.0	91.6	0.067	736.8 (50th)	/	[589]
CuO/Cu ₂ O	Hollow nanospheres	/	0.005–3.0	65	5	183	45/60/0.2	[590]
NiO	NPs	68.5	0.01–3.0	65.1	4	152	76.6/100/0.1	[554]
Ni/NiO	Core-shell	<96	0.001–3.0	73	3	700	74.7/300/1.5	[591]
Al ₂ O ₃ /ZnO	Core-shell	53	0.01–3.0	53.1	1	415	60.8/2–100/0.1	[592]
Alloy-type M _x O _y								
SnO ₂	NPs	~80	0.01–2.5	74.3	2	580	~73/50/0.1	[593]
SnO ₂	NPs	90	0.01–2.0	61.6	4	212.8	60/120/0.08	[594]
SnO ₂	Mesoporous	78.8	0.01–3.0	69.4	0.782	621.5	53.1/50/0.0782	[560]
SnO ₂	Nanorods	69.5	0.01–3.0	/	2	583.3	96.2/100/0.2	[595]
SnO ₂	Nanorods	44	0.01–3.0	/	0.1	710 (50th)	61.9/50/0.1	[596]

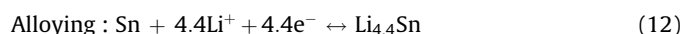
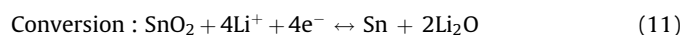
ICE: initial Coulombic efficiency; SI: slight increase.

metallic state. Due to the multiple-electron reactions, conversion-type anodes can deliver large capacities and high energy density. Unfortunately, they are limited by many drawbacks such as poor conductivity, high redox potential, large potential hysteresis between oxidation and reduction, large volume changes, severe inter-particle aggregation, unstable SEI, low cycling stability, and short lifetime [539].



Encouraged by high specific capacities, low potential (vs Li/Li⁺) and high cell operating voltage of metallic or semi-metallic elements like Sn, Ge, and Si, alloy-type metal oxides have been recently considered as prospective anodes for LIBs [538]. Meanwhile, metal oxides are easier to handle and process compared to metals. Such alloy anodes include binary tin oxides (SnO, SnO₂),

ternary tin oxides (M_xSnO_y, M: Mg, Mn, Fe, Co, Zn, Ca, Sr, Ba, Y, Nd, etc.) and mixed oxides ZnM₂O₄ (M: Fe, Co, and Mn) which involve the electrochemical reduction to the respective metals by Li-ions followed by the formation of Li alloys (usually intermetallic compounds). These oxides usually participate in the conversion and alloying reactions, as shown in Eqs. (11) and (12) using SnO₂ as a typical example. However, alloy anodes in LIBs have been limited by poor cyclic capability and high capacity fading due to the huge volume variation during alloying/de-alloying processes [371,425].



Due to the high intrinsic capacities of metal oxides coupled with their abundance, low cost, and easy preparation have stimulated a wide spectrum of materials engineering strategies to alleviate the associated problems mentioned above [540]. Over the past years, metal oxide/graphene composites have been developed in an intensive effort to improve the overall performance of metal oxide anodes in LIBs [26,34,541]. A wide variety of synthetic methods

have been investigated including: [33] (i) *ex-situ* hybridization of pre-synthesized metal oxides and graphene or GO followed by reduction, [542] (ii) co-reduction of metal-containing precursors and GO sheets by chemical, hydrothermal, solvothermal, microwave and/or thermal annealing ways, [543–547] (iii) *in-situ* growth of metal oxides onto graphene or GO followed by reduction [548–551], and (iv) post-deposition of nanostructured metal oxides onto graphene using electrochemical and thermal evaporation methods [552]. When making graphene-based composites, metal oxides occur in various nanostructured forms such as solid NPs, [553,554] hollow NPs, [555,556] core-shell NPs, [557] porous NPs, [558–560] quantum dots, [561,562] nanodisks, [563] nanotubes, [564] nanorods, [565,566] nanosheets, [567,568] nanoflowers, [569], and nanospindles [570]. Graphene hybrid anodes based on such nanostructured metal oxides have shown great improvements in LIB specific capacity, rate capability, and cycling performance (see Table 3).

As described above, the controllability of nanostructured metal oxides when meeting 2D graphene sheets allows us to tailor their spatial distribution and to build hierarchically-architected composites. Fig. 20 shows several structural models proposed for the formation of metal oxide/graphene composites [34]. Direct mechanical mixing of graphene sheets with pre-synthesized metal oxides is the simplest method for producing composite electrodes in which diverse nanostructures typically coexist [571,597]. In this system, graphene serves as an electrically-conductive additive that helps constructing an effective electron transfer network throughout the overall electrode [598]. However, nanostructured metal oxides and graphene sheets are prone to aggregate into large ones, thereby showing limited improvement in the electrochemical performance [599].

For a layered structure, metal oxides are alternated with graphene sheets to form a self-assembled layer-like composite [600–602] which can be further processed into a macroscopic paper or film by vacuum filtration or solution casting. [603,604] The most commonly used method is based on an electrostatic self-assembly between charged metal oxides or metal precursors and functionalized graphene/GO sheets [605,606]. For instance, Liu et al. [607] used anionic-surfactant functionalized graphene sheets as building blocks for chelating with oppositely charged metal cation species to construct ordered metal oxide/graphene composites in which alternating layers of graphene and metal oxide

nanocrystals are assembled into a layered nanostructure. Free-standing SnO_2 /graphene film anodes produced by vacuum filtration deliver steady specific capacities of 760 mAh/g (close to the theoretical 780 mAh/g) at 0.008 A/g, 625 mAh/g at 0.01 A/g after 10 cycles, and excellent rate performance (225 and 550 mAh/g at 0.08 and 0.02 A/g). Recently, Zhang et al. [608] fabricated binder-free, mechanically-robust layered CoO /graphene composites by an electrostatic spread growth of $\text{Co}(\text{OH})_2$ followed by drop casting and sintering. The as-fabricated anodes exhibit high rate capability over a wide temperature range (0–55 °C) and excellent cycle stability (retaining ~390 mAh/g at 0 °C and >800 mAh/g at 50 °C after 500 cycles at 1 A/g).

The structure of sandwich-like composites approximates that of layered composites. During fabrication of such materials, however, graphene usually serves as a template to generate metal oxides which are immobilized between graphene sheets [609,610]. Sandwich-like SnO_2 , [611] Co_3O_4 , [612] Fe_3O_4 , [613], and TiO_2 [614]/graphene composites have been reported with superior electrochemical performance. Unique textural features of layer- and sandwich-structured composite anodes allow them to be additive-free and even metal current-collector-free. This allows high storage capacities per mass and volume to be obtained [615,616]. Such hybrid anodes are mechanically-flexible and have promising applications in portable, wearable and implantable devices. The disadvantages stem from anisotropic Li-ion insertion and diffusion with kinetic barriers through graphene sheets [617]. Devices employing such anodes need to be rationally fabricated so as to achieve high performance [618]. At present, such layered and sandwich-like electrodes are also not suitable for industrial applications because of their limited processing techniques.

Graphene-wrapped metal oxides have been mainly fabricated by *in-situ* intercalation of metal-containing precursors into graphene or GO sheets followed by chemical and/or thermal treatment. Li et al. [619] reported on the synthesis of graphene nanosheet-wrapped Fe_3O_4 NPs ($\text{GNS}/\text{Fe}_3\text{O}_4$, see Fig. 21a–c) by hydrolysis of $\text{FeCl}_3 \cdot 6\text{H}_2\text{O}$ to obtain FeOOH particles embedded in few-layer graphene followed by annealing reduction of FeOOH to Fe_3O_4 NPs *in-situ*. The reversible capacity of $\text{GNS}/\text{Fe}_3\text{O}_4$ in the first cycle is 900 mAh/g, which gradually increases to 1026 mAh/g at 35 mA/g after 30 cycles with Coulombic efficiency close to 100% (Fig. 21e). The $\text{GNS}/\text{Fe}_3\text{O}_4$ anode retains a capacity of 520 mAh/g at

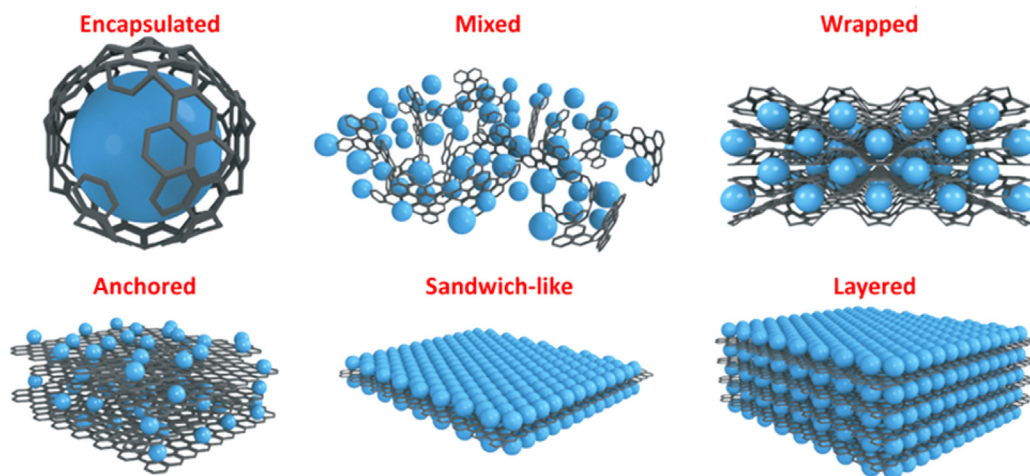


Fig. 20. Nanoarchitecture models of metal oxide/graphene hybrid electrode materials. Encapsulated: metal oxides are encapsulated by graphene shells. Mixed: graphene sheets and metal oxides are pre-synthesized separately and mechanically mixed during fabricating electrodes. Wrapped: metal oxides are usually surrounded by multiple graphene sheets in a more regular fashion. Anchored: metal oxides are *in-situ* anchored onto the surface of graphene sheets. Sandwich-like: graphene functions as a template to direct metal oxide/graphene sandwich-like structures. Layered: metal oxides are alternated with graphene sheets to build a layered composite [31]. Copyright 2014 Macmillan Publishers Limited.

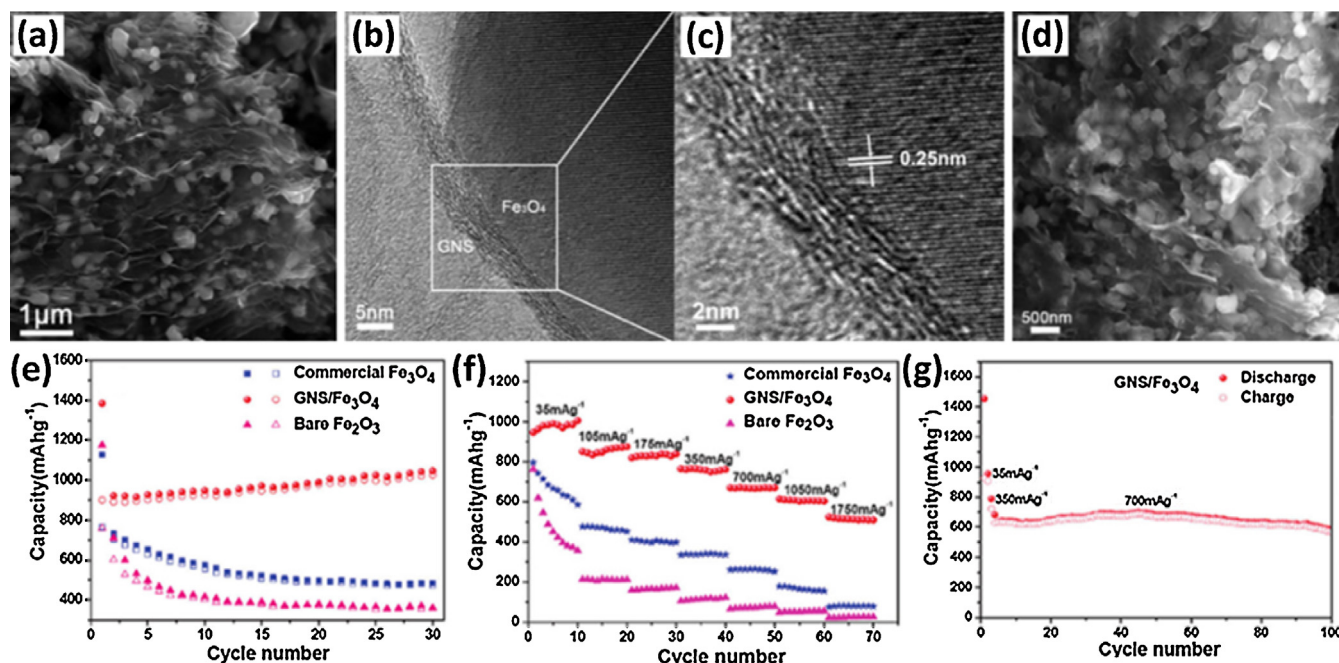


Fig. 21. (a) Cross-sectional SEM and (b and c) TEM images of graphene-wrapped Fe_3O_4 NPs (GNS/ Fe_3O_4), and (d) SEM image of GNS/ Fe_3O_4 anode after 30 discharge/charge cycles. Electrochemical performances of anodes based on commercial Fe_3O_4 particles, GNS/ Fe_3O_4 composite, and bare Fe_2O_3 particles: (e) at a current density of 35 mA/g and (f) at current densities of 35–1750 mA/g. (g) Cycling performance of GNS/ Fe_3O_4 at 700 mA/g over 100 cycles. Solid symbols: discharge; hollow symbols: charge [619]. Copyright 2010 American Chemical Society.

1.75 A/g (Fig. 21f). This corresponds to a 53% retention of initial capacity; much higher than the 10% and 3% of initial capacity retention for commercial Fe_3O_4 and bare Fe_2O_3 particles, respectively. This electrode retains 91% of its initial capacity at 700 mA/g after 100 cycles (Fig. 21g). Furthermore, after charging/discharging for 30 cycles, Fe_3O_4 NPs are still well-dispersed, and closely embedded in graphene sheets (Fig. 21d). The overall morphology and Fe_3O_4 particle size are nearly the same as in the initial state. Wrapping Fe_3O_4 NPs with flexible graphene sheets can effectively prevent the detachment and agglomeration of pulverized Fe_3O_4 NPs and accommodate the large stress and strain changes of the electrode during cycling. To date, a variety of metal oxides such as hollow Li_3VO_4 , [620] hollow Co_3O_4 spheres, [582] ZnMn_2O_4 nanorods, [621] hollow Zn_2SnO_4 boxes, [622,623] dandelion-like $\text{Li}_4\text{Ti}_5\text{O}_{12}$ microspheres, [624] $\text{Co}_2(\text{OH})_3\text{Cl}$ NPs, [625] CuO NPs, [626] rice-like FeCO_3 NPs, [627] SnO_2 nanotubes, [628], and MnO_2 nanorods [629] have been wrapped by graphene sheets to produce composite anodes which also provide superior electrochemical performance in terms of their specific capacity, rate capability and cycling performance.

For graphene-encapsulated metal oxides, Feng et al. [630] reported the encapsulation of Co_3O_4 (91.5 wt%) in ultrathin graphene shells by an electrostatic co-assembly between positively-charged Co_3O_4 NPs and negatively-charged GO sheets followed by chemical reduction. The Co_3O_4 @G anode exhibits a very high reversible capacity of 1100 mAh/g at 74 mA/g in the first 10 cycles and over 1000 mAh/g after 130 cycles. The 94% retention of initial capacity after 30 cycles is much higher than the 67% for the Co_3O_4 /graphene anode prepared by simple mechanical blending. Moreover, the film resistance (10.5Ω) and R_{CT} (27.9Ω) are significantly lower than those of bare Co_3O_4 NPs (27.8 and 97.9Ω) due to graphene shells that increase both the electrical conductivity of the overall electrode and electrochemical activity of Co_3O_4 NPs. Similar electrostatic self-assembly processes have been adopted for producing graphene-encapsulated mesoporous Co_3O_4 microspheres [631] and graphene-encapsulated hollow

Fe_3O_4 NPs, [577] all of which deliver a high and stable reversible capacity (>800 mAh/g) at 0.1 A/g over 35 cycles. Moreover, Fe_3O_4 @G NPs [632] and mesoporous TiO_2 @G microspheres [633] produced by hydrothermal method, $\text{Li}_2\text{MnTi}_3\text{O}_8$ @G NPs by sol-gel method, [634] graphene-encapsulated CoS_2 nanocages by solvothermal treatment of GO and the respective metal-containing precursors have all shown improved electrochemical performance. The key advantage of graphene encapsulation over other models arises from its double-shielding role that protects metal oxides against direct contact with the electrolyte and core pulverization. This ensures permanent electrical connectivity and short transport pathways of Li-ions and electrons within the overall electrodes [635].

Metal oxides anchored on graphene or graphene-supported metal oxides are mainly produced by wet-chemistry strategies such as hydro-/solvo-thermal synthesis, electrostatic assembly, chemical deposition, and sol-gel processes [550,568,636–640]. In these cases, graphene serves as an efficient support for immobilizing metal ions followed by hydrolysis or redox, nucleation and *in-situ* growth of nanostructures [543,547,641,642]. 2D Graphene sheets also enable a more uniform distribution of nanostructured metal oxides [643,644]. Of note, both GO and RGO sheets contain hydrophilic oxygen-containing functional groups, which enable them to be well dispersed in aqueous or polar organic solvents to form stable colloids through electrostatic stabilization [281,645,646]. Topology and structural defects (e.g., edges, vacancies, and holes) of GO and RGO also function as anchoring centers for directing the formation of various nanostructures [647–649]. Furthermore, the presence of oxygenated groups in GO or RGO has been found to promote the formation of ultrafine nanostructures. The amount of functional groups has a significant influence on the size, morphology, distribution, and crystallinity of metal oxides anchored on the surface [650,651]. Such functionality-rich GO or RGO suspensions are therefore an excellent template system for anchoring metal precursors and their oxide counterparts with tailored nanostructures [652–654].

Based on the advantages and underlying mechanism mentioned above, Dai et al. [655] demonstrated a two-step solution-phase method for anchoring Mn_3O_4 NPs on RGO by hydrolysis of $\text{Mn}(\text{Ac})_2$ on GO followed by hydrothermal treatment (see Fig. 22a). Well-crystallized Mn_3O_4 NPs (10–20 nm) were found to uniformly distribute on RGO sheets to form $\text{Mn}_3\text{O}_4/\text{RGO}$ composites (Fig. 22b and c) which exhibit large specific capacity (~ 900 mAh/g at 40 mA/g), high rate capability (~ 390 mAh/g at 1600 mA/g) and good cycling stability (retaining 730 mAh/g at 400 mA/g after 40 cycles) (Fig. 22d). Cheng et al. [581] reported the synthesis of Co_3O_4 NPs anchored on RGO by dispersing a Co^{2+} salt and RGO into basic aqueous solution and transforming $\text{Co}(\text{OH})_2/\text{RGO}$ into $\text{Co}_3\text{O}_4/\text{RGO}$ by calcination at 450°C (see Fig. 22e). Single crystalline Co_3O_4 NPs (10–30 nm) are homogeneously anchored on RGO (Fig. 22f and g)

and the resulting hybrid anode exhibits an initial reversible capacity of 753 mAh/g which increases to 935 mAh/g after 30 cycles with better cycling performance than pure graphene and Co_3O_4 anodes (Fig. 22h). They also used RGO and metal precursors as the starting materials to fabricate graphene composites containing mesoporous anatase TiO_2 nanospheres which show a specific capacity of 97 mAh/g at a 50 C rate. This is six times higher than that of the reference TiO_2 anode [559]. Of note, hydro-/solvo-thermal reduction of GO sheets can be used to easily form porous graphene hydrogels, aerogels or foams. Such 3D templates can be used to anchor metal oxides to produce 3D porous composites [656]. Such hybrid anodes consist of 3D graphene conductive networks which enable fast ion and electron transfer kinetics, easy access of the electrolyte, and a shortened ion

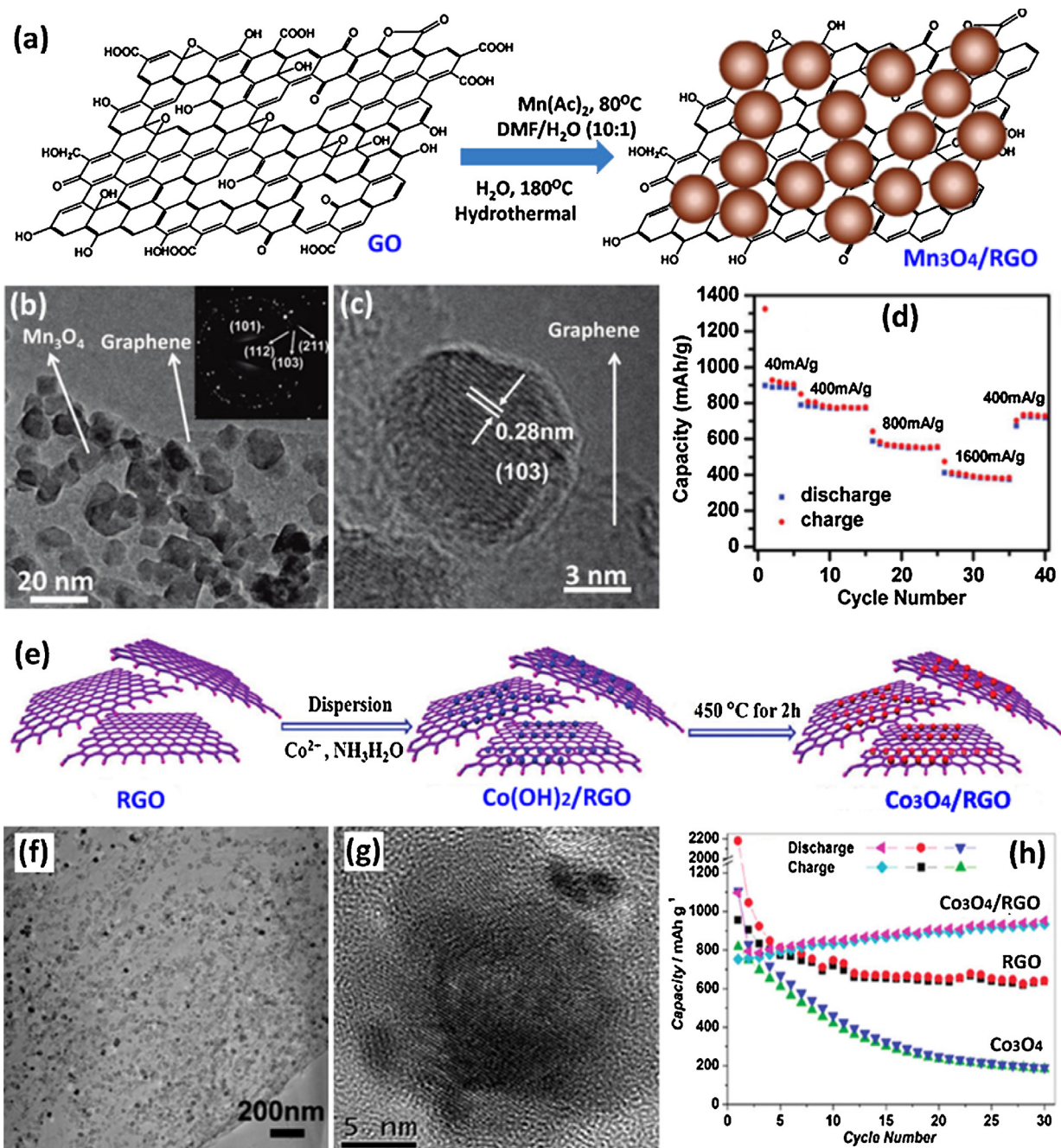


Fig. 22. Mn_3O_4 NPs anchored on RGO: (a) schematic representation of the fabrication process, (b) TEM (inset shows the electron diffraction pattern of Mn_3O_4 NPs on RGO) and (c) HRTEM images, and (d) capacity retention at various current densities [655]. Copyright 2010 American Chemical Society. Co_3O_4 NPs anchored on RGO: (e) the fabrication process, (f) TEM and (g) HRTEM images, and (h) cycling performance of graphene, Co_3O_4 , and $\text{Co}_3\text{O}_4/\text{RGO}$ composite anodes [581]. Copyright 2010 American Chemical Society.

diffusion length. This translates to large storage capability, high-rate performance, and cycling stability [657–659].

However, there are no available data and direct evidences to identify which structural model enables a larger capacity, higher rate capability or better cyclic performance than others. Irrespective of the structural models of metal oxide/graphene composites, these unique hierarchical hybrid architectures lead to overall improvements in their electrochemical performance. For nano-structured metal oxides, they can prevent graphene sheets from restacking during material preparation and electrode charging/discharging [543,651,660,661] and also provide high storage capacities for LIBs by reversible insertion/extraction, conversion (redox) or alloying/de-alloying reactions with Li [605,662,663]. Graphene plays a multifunctional role in synthesizing composites, fabricating electrodes, and improving performance. First, graphene functions as a large scaffold to support, separate, disperse and stabilize metal oxides thus alleviating the inter-particle aggregation during materials and electrode processing [664,665]. Second, graphene sheets serve as an elastic matrix buffering large volume changes during charging/discharging and suppressing the pulverization of metal oxides, the degradation of electrode, the electrical disconnection from current collectors and the disintegration of the battery [666–668]. Third, graphene networks act as an efficient electron-conducting pathway between metal oxides and current collectors. Each graphene sheet can be considered as a mini-current collector to bridge a 3D conductive network throughout the electrode [669–671]. Moreover, graphene improves the electrochemical activity and reaction kinetics in hybrid electrodes especially when it is properly doped with heteroatoms [611,672]. Graphene can also stabilize the SEI layer when metal oxides are tightly encapsulated, coated, and/or wrapped by graphene shells [629,630,673,674]. This enables metal oxide/graphene hybrid anodes to have large specific capacity, high energy/power density, long-term life, and excellent cyclic and rate performance. This makes commercial applications for such hybrid anodes are quite promising [26,34].

3.2. Graphene-based materials as cathodes

The cathode of LIBs is typically a transition metal compound that serves as the host for reversible Li-ion intercalation/deintercalation during charge/discharge processes [675]. The important characteristics for the cathode include: the voltage at which it exchanges lithium, the amount of reversible Li-ion intercalation, the stability of the intrinsic material, and the transportation of electron conduction and Li-ion diffusion [676]. The first two factors determine the energy density (usually high voltage leading to high energy density), and the latter factors limit the lifetime and rate performance of LIBs. LiCoO_2 is the first commercial material for LIBs introduced in 1990, and is still commonly used in LIBs manufactured today. Recently, a wide variety of nanostructured metal compounds have been explored as cathode materials with improved storage capacity, Faradaic reaction kinetics and cyclability [677–679]. However, practical applications of these cathode materials are limited by several issues such as low electrical conductivity, slow Li-ion diffusion, inter-particle aggregation, large volume expansion, and irreversible phase transitions [680,681].

Carbonaceous materials including graphene usually provide a low voltage window (below 1.5 V vs Li/Li^+), and therefore they have been widely used as anodes but rarely reported as a cathode material in LIBs [384,682–684]. A few recent studies found that oxygen functional groups on CNTs can interact with Li-ions in the voltage window above 1.5 V vs Li/Li^+ [411,685]. The reaction between Li-ions and carbonyl/carboxylic acid groups occurs at a higher voltage of ~ 3 V vs Li/Li^+ [686,687]. In this context, Lee et al.

[688] fabricated free-standing RGO films with controlled C/O ratios by thermal reduction of GO. When evaluating RGO films as cathodes, the presence of hydroxyl, carbonyl, and carboxylic groups on RGO were identified as lithiation-active species. The RGO film cathode (C/O: 15) can deliver an initial specific discharge capacity of 125 mAh/g at 0.137 A/g, which decreases with increasing the C/O ratio (e.g., 80 mAh/g for C/O: 25) due to lower amount of oxygen functional groups. This RGO cathode also shows excellent rate capability (~ 115 and 82 mAh/g at 1.37 and 5.48 A/g, respectively) due to fast Faradaic reactions of surface oxygen-containing groups. Recently, Liu et al. [689] fabricated a graphene-porous polyaryltriazine-derived framework material in which electroactive aromatic networks are immobilized on electrically-conductive RGO sheets through covalent bonding. This hybrid cathode exhibits high capacity and long cycle life (retaining capacity of ~ 395 mAh/g at 5 A/g over 5100 cycles) and excellent rate capability (135 mAh/g at a high rate of 15 A/g). Although few studies on graphene cathodes have been reported, these results suggest the possibility of oxygen-rich graphene materials as promising cathodes for high power application.

As mentioned previously, pristine graphene cannot be used directly to increase the storage capacity of Li-ions. However, it does provide a large surface to anchor and separate metal oxides, high electrical conductivity, and mechanical support to the cathode. Most studies have focused on utilizing graphene as a new promoter in the cathode [26,690]. Recently graphene-based composite cathode materials have been prepared by sol-gel, [691] hydrothermal, [692] solvothermal, [693,694] photothermal, [695] spray-drying, [696] electrophoresis, [697] co-precipitation, [698], and thermal annealing [699] methods. Similar to anodes of metal oxide/graphene composites, these cathode composites can also form wrapped, [700–702] anchored, [703–705] encapsulated, [706] layered, [707] mixed, [708,709], and sandwich-like architectures [710,711]. Various active materials have been used for fabricating graphene hybrid cathodes including vanadium oxides (e.g., VO_2 [692,712]) and lithium-containing compounds such as $\text{Li}_3\text{V}_2(\text{PO}_4)_3$, [713–716] LiMnPO_4 , [717] $\text{Li}_2\text{FeSiO}_4$, [718,719] $\text{LiCo}_{1/3}\text{Ni}_{1/3}\text{Mn}_{1/3}\text{O}_2$, [720–722] $\text{LiNi}_{0.5}\text{Mn}_{1.5}\text{O}_4$, [723], and LiMn_2O_4 [724–727]. Among them, V_2O_5 [728–730] and LiFePO_4 (LFP) [731–737] have been widely reported to exhibit improved performances when combined with graphene in the cathode.

Olivine-structured LFP is one of the most promising cathode materials due to its low cost, low toxicity, relatively large capacity (170 mAh/g), high electrochemical potential, intrinsic stability, and safety [679,738,739]. The key limitations associated with LFP are its low electrical conductivity (10^{-9} S/cm) and low Li-ion diffusivity (10^{-15} – 10^{-12} cm^2/s) resulting in poor rate capability for hampering high power applications of LIBs [740,741]. Recently, Tour et al. [706] reported the fabrication of graphene-encapsulated LFP NPs (LFP@G) by a solid state reaction between graphene-coated Fe NP and LiH_2PO_4 (see Fig. 23a–c). When used a cathode, LFP@G gives a small gap (~ 45 mV) between the charge and discharge plateaus (Fig. 23d). This corresponds to a low over-potential during the charge-discharge process due to the good ionic and electronic conductivity of LFP NPs capped by graphene shells. The first discharge and charge specific capacities of LFP@G are 145 mAh/g and 150 mAh/g, respectively, giving an initial Coulombic efficiency of 97% at 0.1 C (17 mA/g). The LFP@G cathode also exhibits excellent cycling stability (95.3% capacity retention after 1000 cycles at 1 C) and rate capability (128, 98, 84, and 54 mAh/g at rates of 1, 5, 10, and 20 C, respectively) (Fig. 23e) due to fast ionic diffusion in LFP NPs and efficient electron transport and transfer benefiting from graphene coatings. Direct solution mixing of electrochemically-exfoliated few-layer graphene with commercially-available LFP particles was also performed to produce graphene-coated LFP composites [742]. This hybrid

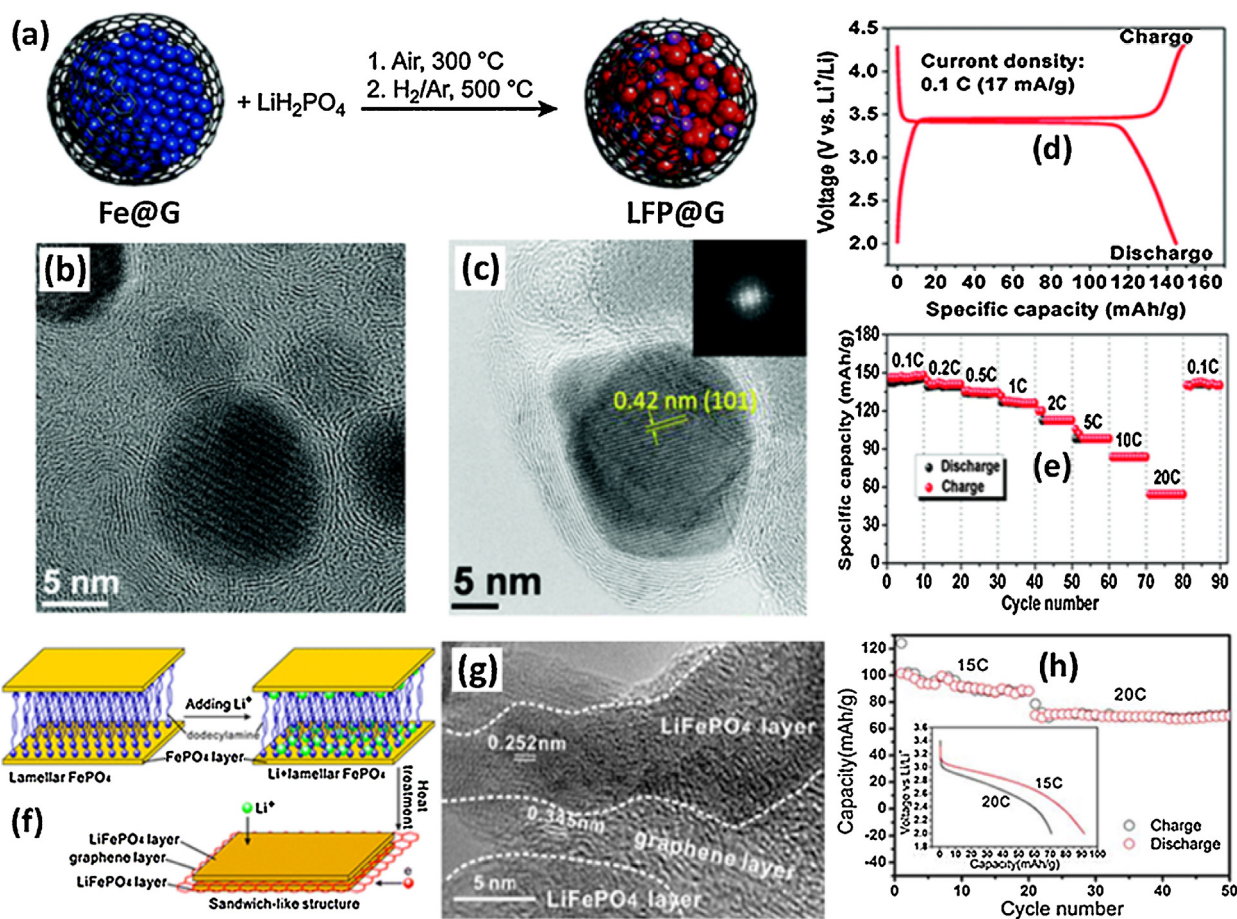


Fig. 23. Graphene-encapsulated LFP NPs: (a) the synthetic route to LFP@G starting from Fe@G, HRTEM images of (b) Fe@G and (c) LFP@G with core-shell structures, (d) charge-discharge profiles at 17 mA/g (0.1 C) in a potential range of 2.0–4.3 V (vs Li/Li⁺), and (e) specific capacity and rate performance at different current densities of the LFP@G cathode [706]. Copyright 2014 Royal Society of Chemistry. Sandwich-like LFP/graphene hybrids: (f) the proposed formation mechanism, (g) HRTEM image, and (h) rate performance at rates of 15 and 20 C. The inset corresponds to the discharge curves [711]. Copyright 2013 Royal Society of Chemistry.

cathode with 2 wt% graphene has an energy density as high as 686 Wh/kg and can deliver a capacity of 208 mAh/g (beyond the theoretical 170 mAh/g) due to the reversible redox reaction between Li-ions and graphene. Guo et al. [711] used an *in-situ* graphitizing interlayer of dodecylamine between two lamellar FePO₄ layers to achieve conductive (18.9 S/cm) sandwich-like LFP/graphene sheets (Fig. 23f and g). In this case, the thin LFP sheets provide short channels for Li-ion diffusion and the intercalated-graphene can facilitate electron transportation. This contributes to high-rate performance with high capacities of 90 mAh/g at 15 C and 70 mAh/g at 20 C, respectively (Fig. 23h). Coating LFP NPs with carbon produces a double protection layer which further contributes to performance improvements [743,744].

V₂O₅ is a very attractive candidate for the cathode materials in LIBs because of its abundance and much higher theoretical capacity (443 mAh/g) compared to other commonly used cathode materials such as LiCoO₂ (140 mAh/g), LiMn₂O₄ (148 mAh/g), and LFP (170 mAh/g) [675]. In addition to irreversible phase transition upon deep discharge, like most metal oxides, V₂O₅ has low electrical conductivity (10⁻²–10⁻³ S/cm) [745] and low Li-ion diffusivity (10⁻¹²–10⁻¹³ cm²/s) [746,747] and hence poor cyclability and rate capability. To address those problems, various nanostructured V₂O₅/graphene composites have been recently developed as cathode materials for LIBs. For example, single crystalline V₂O₅ nanowires supported on graphene ensure short diffusion pathways for Li-ions and excellent electrical conductivity [748]. The as-fabricated cathode delivers an initial discharge

capacity as high as 412 mAh/g at 50 mA/g and remains 316 mAh/g at 1600 mA/g showing high capacity and exceptional rate capability. Porous V₂O₅ spheres anchored on graphene sheets were realized by hydrothermal and annealing treatments of GO and vanadium isopropoxide [749]. The resulting composites display superior cathode performance with high reversible capacity and good cycling stability (remaining ~202 mAh/g at 90 mA/g in the 50th cycle) as well as excellent rate capability (102 mAh/g at 19 C) due to the formation of a highly-conductive and structurally-robust network and the inhibition of inter-particle agglomeration induced by graphene support. Recently, Kang et al. [712] fabricated ball-like V₂O₅/graphene hybrids by spray-pyrolysis of colloidal GO and ammonium vanadate assisted by thermal post-treatment in which V₂O₅ nanocrystals are uniformly decorated on the crumpled-graphene balls. This hierarchically-designed cathode delivers higher initial charge (280 mAh/g at 1 A/g) and discharge (282 mAh/g) capacities than macroporous V₂O₅ (221 and 205 mAh/g, respectively). This hybrid cathode also retains a discharge capacity up to 214 mAh/g at 1 A/g after 100 cycles with ~100% Columbic efficiency. More recently, Xie et al. [750] incorporated 2 wt% graphene into V₂O₅ nanoribbons via a sol-gel process. The V₂O₅/graphene hybrid cathode exhibits a specific capacity as high as 438 mAh/g (approaching the theoretical 443 mAh/g), long cyclability (80% retention of initial capacity at 1 C after 150 cycles) and high rate capability (419, 315, and 201 mAh/g at 0.1, 1, and 10 C, respectively) all of which are much higher than pure V₂O₅ nanoribbons. The introduction of a small

amount of graphene into V_2O_5 can effectively improve the hybrid nanostructure resulting in significant improvements in electronic conduction, vanadium redox reaction, Li-ion diffusion, and structural stability. Nanostructure-tailored V_2O_5 combined with 2D graphene provides a new avenue to create hierarchical-architecture materials by solution-phase processing. Such methods can be easily scaled-up, and the starting materials are abundant. These points motivate promising widespread industrial potential for new cathode materials.

4. Graphene-based materials for supercapacitors

Electrochemical capacitors have been frequently called supercapacitors and also ultracapacitors because of their extraordinarily high capacitance compared to conventional electrostatic and electrolytic capacitors [751]. Supercapacitors consist of two electrodes electrically connected with an electrolyte and mechanically separated by an ion-permeable but electron-insulating membrane (separator). Supercapacitors were first introduced in 1978 on the market to provide computer memory backup power [752]. A more recent example is the use of supercapacitors in emergency doors on the Airbus A380 [10]. Supercapacitors are very similar to lithium batteries in device configuration and manufacture. Unlike batteries, supercapacitors especially electric double-layer capacitors (EDLCs) can operate at high charge/discharge rates over a million cycles, and store and release energy in seconds. Consequently, supercapacitors enable large current density within a short time interval, high energy-delivery-capability with high power density (10 kW/kg), long cycle life (>100 times battery life) and low maintenance cost as well. However, the energy density (4–5 Wh/kg) in supercapacitors is much lower than that in batteries (120–170 Wh/kg for LIBs) [753,754]. In addition, the voltage delivered for supercapacitors varies with the state of discharge whereas batteries tend to have a fairly constant output voltage [754]. Supercapacitors are therefore considered as a complement for batteries especially in high-rate applications such as electric vehicles or hybrid electric vehicles.

Supercapacitors can be divided into EDLCs and pseudocapacitors based on their energy storage mechanisms [752,755]. For a supercapacitor, CV, galvanostatic charge/discharge (GCD), and electrochemical impedance spectroscopy (EIS) are the three common techniques used to evaluate the electrochemical performance parameters such as [663] specific capacitance, power density, energy density, operating voltage, equivalent series resistance (ESR), charge/discharge rate, and capacity retention. That increasing energy density while retaining high power density and long cycle life has remained central to supercapacitors. The intrinsic properties and microstructure of electrode materials are crucial for achieving such goals [10,754].

4.1. Graphene-based materials for electric double-layer capacitors

EDLCs store electrical energy through electrode polarization under an applied voltage followed by electrostatic adsorption of electrolyte ions to form electric double layers at the electrode-electrolyte interface. The electrostatic storage in EDLCs is a non-Faradic process without charge transfer across the interface. Currently, porous carbonaceous materials, including activated carbon, carbide derived carbon, templated carbon, carbon aerogels, xerogels, carbon fibers and CNTs, have been widely used as electrode materials in EDLCs [756,757]. However, these active materials are limited to one or several factors among intrinsic capacitance, SSA, production cost, and electrode processing. The intrinsic double-layer capacitance of monolayer graphene was measured to be $\sim 21 \mu\text{F}/\text{cm}^2$ with a theoretical capacitance as high

as 550 F/g for EDLCs if the entire SSA of pristine graphene is fully utilized [758].

Graphene EDLCs were first reported by Rao et al. [759] who used thermally annealed GO at 1050 °C as electrode materials with a SSA of 925 m^2/g . Specific capacitances were measured to be 117 and 75 F/g in 1 M H_2SO_4 and IL electrolytes at a scan rate of 100 mV/s, respectively, which are more than that of single-walled CNTs (64 F/g) and multi-walled CNTs (14 F/g). Subsequently, hydrazine-hydrate-reduced GO sheets with 15–25 μm in lateral dimension and a SSA of 705 m^2/g were used as electrodes to fabricate EDLCs [760]. Specific capacitances of 135 and 99 F/g at a current density of 10 mA/g, and 107 and 85 F/g at a scan rate of 40 mV/s were obtained in aqueous KOH and organic electrolytes, respectively. Using microwave-reduced GO as an electrode material in an EDLC, [761] a specific capacitance of 191 F/g was achieved at 150 mA/g with KOH electrolyte, and was retained to be 174 F/g at 600 mA/g. However, experimental results obtained from graphene EDLCs are usually less than 200 F/g in specific capacitance which is far below its theoretical value.

4.1.1. Graphene paper/film electrodes

Due to strong π – π interaction between graphene sheets, aggregation or restacking is one major problem that limits individual graphene sheets from realizing their full potential in electrodes. This compromises high SSA of graphene and accounts for low specific capacitances due to low accessible SSA for electrolyte ions. Meanwhile, high electrical conduction of graphene is also compromised by inter-sheet contact resistance. Many strategies have been developed to improve the capacitive performance over the past years. Reduction of GO with gaseous hydrazine was proposed, [762] resulting in an EDLC with high specific capacitance (205 F/g), power density (10 kW/kg), energy density (28.5 Wh/kg), and excellent cyclability with 90% retention of initial capacitance after 1200 cycles in a KOH electrolyte. A low-temperature method to highly reduce GO was recently proposed by Li et al. [763] using a sodium-ammonia (Na-NH_3) system (in a dry ice-acetone bath) as a reducing agent. The resulting graphene films have a SSA of 648 m^2/g , and can be directly used as electrodes for EDLCs showing a high specific capacitance (263 F/g). Recently, Kaner et al. [764] used a commercial CD/DVD optical drive to perform laser reduction of GO films to graphene (Fig. 24). The as-produced films have high electrical conductivity (1738 S/m), and SSA (1520 m^2/g) can be directly used as electrodes for EDLCs. The devices offer specific capacitances of 265 and 275 F/g in organic and IL electrolytes, respectively. They also exhibit ultrahigh energy density (1.36 mWh/ cm^3) while maintaining high power density ($\sim 20 \text{ W}/\text{cm}^3$) and excellent cycle stability. KOH activation of reduced GO paper was also reported to give highly conductive, free-standing, and flexible porous graphene films with a very high SSA (2400 m^2/g) and a high in-plane conductivity (5880 S/m) [765]. An EDLC using such electrodes gives an extremely low ESR on the order of 0.1 Ω , and high-power delivery of $\sim 500 \text{ kW}/\text{kg}$ while maintaining a high specific capacitance (120 F/g) and energy density (26 Wh/kg).

Moreover, intercalating foreign molecules between graphene sheets is a straightforward method to prevent them from aggregating. For instance, Li et al. [766] demonstrated that face-to-face-stacked multilayered graphene films remain largely separated in a solvated state. In this case, water molecules act as spacers existing between graphene sheets (Fig. 25a and b) thereby showing a highly open pore structure that allows electrolyte ions to easily gain access to the surface of individual sheets. Supercapacitors fabricated with such solvated graphene film electrodes give specific capacitances of up to 156.5 F/g in H_2SO_4 at an ultrahigh current of 1080 A/g. The devices also provide one to three orders of magnitude higher power density (414.0 kW/kg at 108 A/g) with respect to freeze-dried/thermally annealed

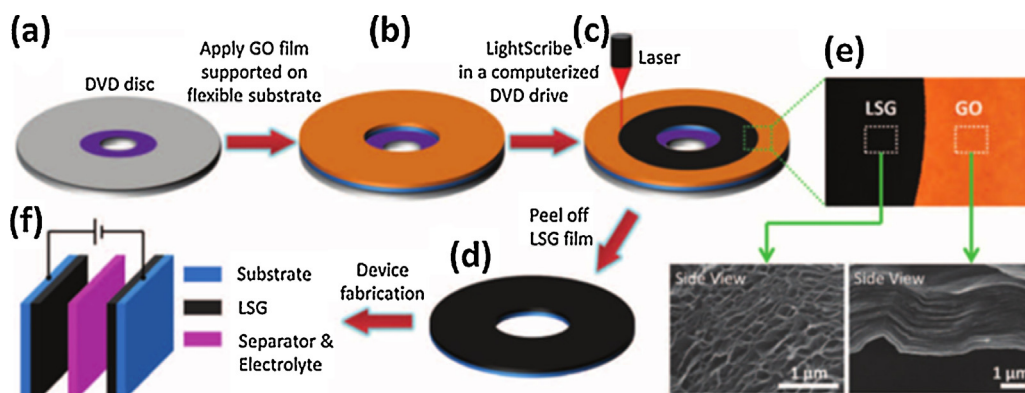


Fig. 24. (a–d) A GO film supported on a flexible substrate is placed on the top of a LightScribe-enabled DVD media disc. A computer image is then laser-irradiated on the GO film in a computerized LightScribe DVD drive. (e) The GO film changes from golden brown color to black after reduction to laser-scribed graphene (LSG). The cross-sectional SEM images show that the low-power infrared laser changes stacked-GO sheets immediately into well-exfoliated few-layered LSG film. (f) An illustration of a symmetric EC constructed by two identical LSG electrodes, an ion-porous separator, and an electrolyte. [764] Copyright 2012 American Association for the Advancement of Science.

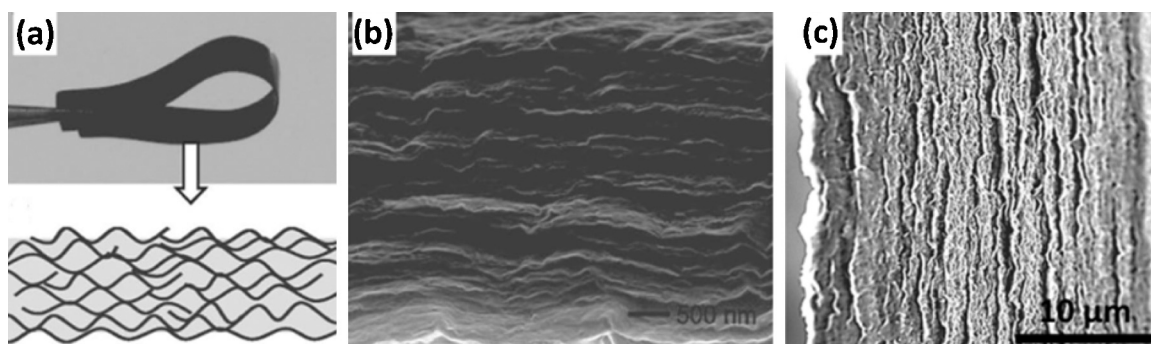


Fig. 25. (a) An optical photograph of water-solvated flexible graphene film and its cross-section cartoon. SEM images of cross-sections for (b) a freeze-dried film of water-solvated graphene [766] and (c) an electrolyte-mediated graphene film containing 78.9 vol% H₂SO₄ [767]. Copyright: 2011 Wiley-Vch and 2013 American Association for the Advancement of Science.

counterparts and other carbon materials and exhibit excellent cyclability with over 97% retention of initial capacitance over 10,000 cycles at 100 A/g. Furthermore, the water-solvated graphene films can be converted to IL-solvated graphene films by solvent-exchange with ILs. Supercapacitors using IL-solvated graphene films can offer higher values of specific capacitance (273.1 F/g), energy density (~ 150.9 Wh/kg) and power density (~ 776.8 kW/kg). Note that the highest energy density is even comparable to that of LIBs based on CNT electrodes [687]. By taking advantage of RGO's intrinsic micro-corrugated 2D configuration and self-assembly behavior, Li et al. [767] further demonstrated that liquid-solvated graphene materials can be formed by capillary compression of adaptive graphene gel films in the presence of liquid electrolytes (Fig. 25c). The electrolyte-mediated graphene films can create a continuous ion transport network resulting in exceptional volumetric energy densities (60 Wh/L).

4.1.2. 3D Graphene-based electrodes

3D GBMs with continuously interconnected porous architectures, such as hydrogels, aerogels, foams, and sponges can preserve the intrinsic properties of individual graphene sheets [768]. More importantly, such frameworks could provide electrodes with good mechanical stability, high SSA, highly conductive network, and fast carrier transport kinetics resulting in dramatic improvements in storage capacitance, cyclability, and rate capability [769,770]. Hydrothermal reduction of GO has been widely used to produce 3D porous materials [257,768,771]. This method can produce graphene materials with desired macroscopic shapes *via* molding in a one-pot, low-cost, time- and energy-saving, and low-temperature process

(see Fig. 26) [772]. Graphene hydrogels with 3D networks have been realized by one-step hydrothermal reduction of aqueous GO with concentrations above 0.5 mg/mL at 180 °C for 1–12 h [255]. The as-prepared graphene hydrogels with high SSA (964 m²/g) are electrically conductive, mechanically strong, and thermally stable. EDLCs based on such electrodes exhibit a specific capacitance of 152 F/g at 20 mV/s which is about 50% higher than that of EDLCs based on RGO agglomerated particles under the same testing conditions (100 F/g at 20 mV/s) [98]. Further reduction of graphene hydrogels with hydrazine or HI can improve their conductivity by one order of magnitude. EDLCs made from hydrazine-reduced hydrogels exhibit a large specific capacitance of 220 F/g at 1 A/g, moderate power density (30 kW/kg), and energy density (5.7 Wh/kg at 100 A/g) as well as long cycle life along with $\sim 92\%$ capacitance retention after 2000 cycles at 4 A/g [773]. Chemically modified graphene hydrogels with organic molecules can further improve the specific capacitances of devices [774,775]. Solvothermal reduction of GO has been reported to form 3D organogels [776,777]. Graphene organogels can also be used as the electrodes of supercapacitors which show specific capacitances of 140 F/g at 1 A/g, high energy density (15.4 Wh/kg), and power density (16.3 kW/kg) at 30 A/g [776].

Recently, Ruoff group developed an effective method to produce 3D porous (0.6–5 nm pores in width) graphene by microwave-induced exfoliation/reduction of GO followed by chemical activation with KOH [778]. The resulting graphene materials have an ultrahigh SSA of up to 3100 m²/g, high electrical conductivity (500 S/m), and low oxygen and hydrogen content. The constructed EDLCs give high specific capacitance (166 F/g), energy density (70 Wh/kg) and power

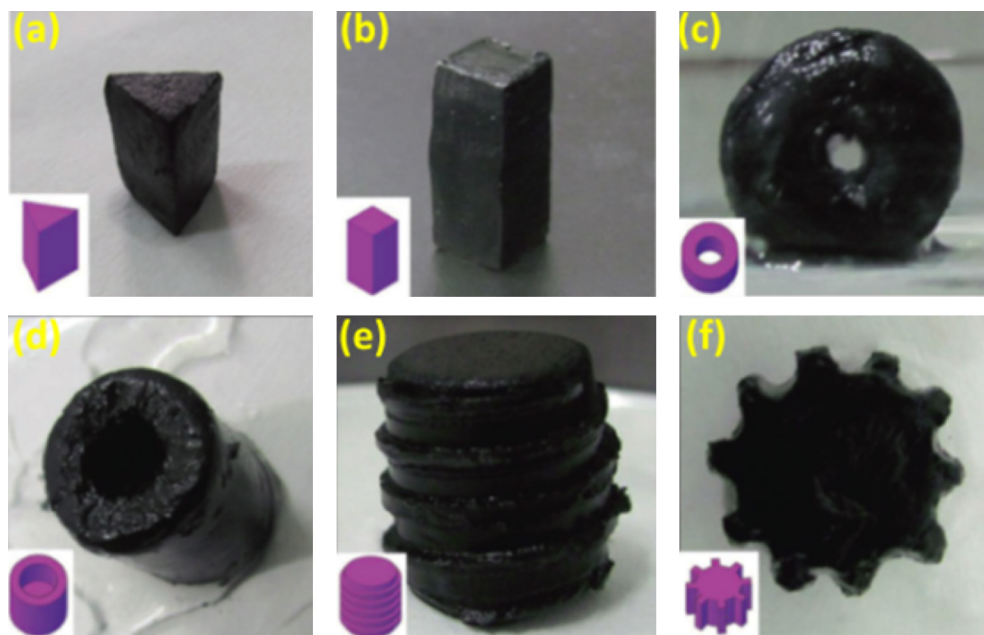


Fig. 26. Different macroscopic shapes of graphene hydrogels via low temperature casting; (a) triangular prism, (b) quadrangular prism, (c) joint ring, (d) crucible, (e) screw stem, and (f) gear. The insets at each bottom-left corner correspond to their three dimensional cartoons [772]. Copyright 2012 Wiley-Vch.

density (250 kW/kg) at 5.7 A/g with organic electrolytes. Moreover, 97% of initial capacitance can be retained after 10,000 charge/discharge cycles at 2.5 A/g in an IL electrolyte indicating excellent cycling stability. Zhang et al. [779] reported a facile, green, and scalable method to prepare porous 3D graphene-based bulk materials. The technique involves two standard industry steps (see Fig. 27a): (i) *in-situ* hydrothermal polymerization/carbonization of the mixture of GO with biomass or industrially-sourced carbon and (ii) chemical activation with KOH. These as-produced materials

mainly consist of defective/wrinkled monolayer graphene sheets with partial covalent-bonding between each other. They exhibit a sponge-like morphology and porous structure (Fig. 27b and c) with an ultrahigh SSA (3523 m²/g) and excellent bulk conductivity (303 S/m) when using phenol and formaldehyde as carbon sources. The outstanding properties are demonstrated by their supercapacitors which produce high values of specific gravimetric capacitance (231 F/g), volumetric capacitance (92 F/cm³), and energy density (98 Wh/kg) with over 90% capacitance retention

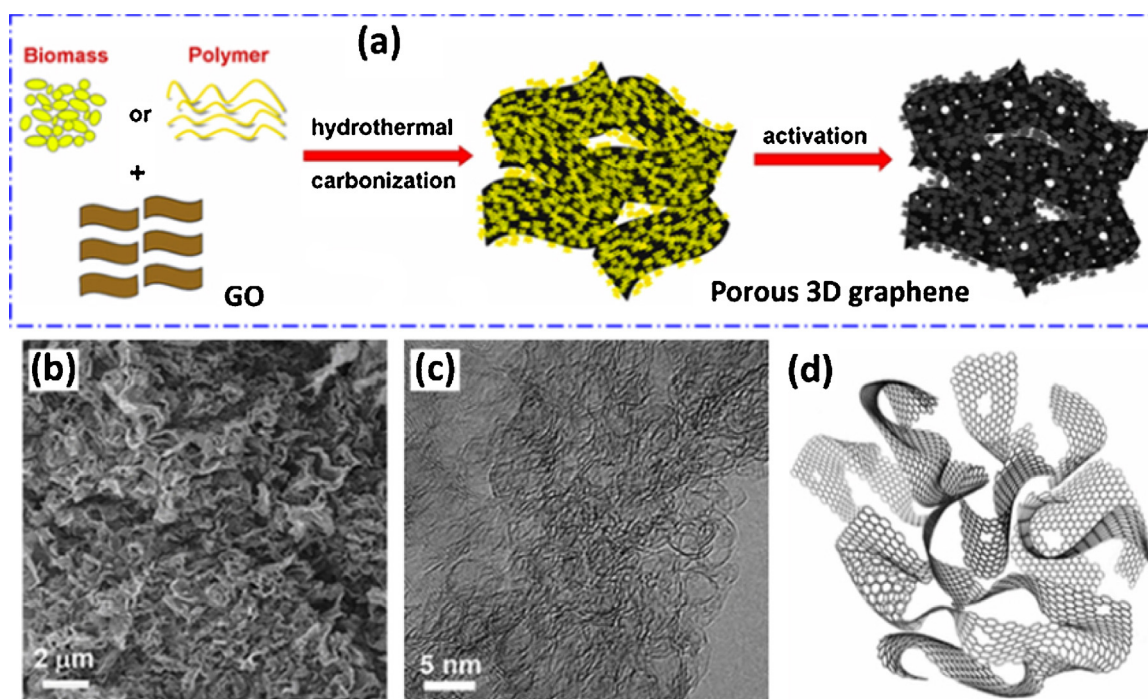


Fig. 27. (a) A schematic for synthesizing porous 3D GBMs, (b) SEM and (c) TEM images of graphene using phenol and formaldehyde as carbon sources, and (d) a 3D porous model [779]. Copyright 2013 Macmillan Publishers Limited.

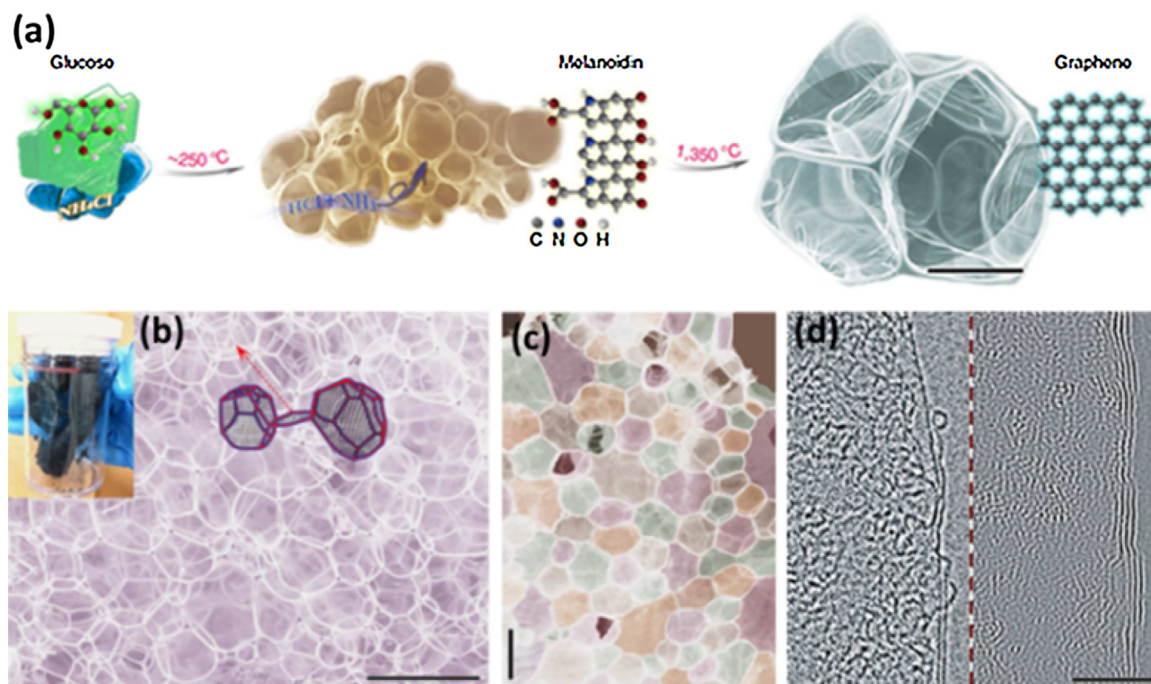


Fig. 28. (a) Schematic illustration for producing a 3D bubble-like graphene network by a sugar-blowing approach using glucose and NH_4Cl . (b) SEM image of 3D graphene. The insets correspond to a photograph of graphene film in a bottle and a topological configuration connected by two bubbles, respectively. (c) SEM image of the flat backside of 3D graphene with regular arrangement of connected cells identified by artificial quilt colors. (d) HRTEM images of a one- to two-layered graphene (left), and a three- to four-layered graphene (right). Scale bars: 50 μm (in a), 200 μm (in b and c) and 5 nm (in d) [792]. Copyright 2013 Macmillan Publishers Limited.

after 5000 cycles at 1 A/g in IL electrolytes. Moreover, deposition of GO sheets or graphene hydrogels into porous conductive substrates (e.g., nickel foam) [780] or matrices [781,782] also forms well-defined 3D hybrid materials which can be directly used as high-performance EDLC electrodes. In the case of flexible conductive supports, the resulting graphene hybrid materials are beneficial for the fabrication of flexible supercapacitors [782–785].

CVD techniques have been also used to produce 3D graphene materials [786,787]. 3D Graphene sheets have been grown on various inert substrates (Al_2O_3 , Si, GaN, or Quartz) from PVA/iron precursors [788] showing high conductivity (5200 S/m), SSA (1025 m^2/g), and great porosity ($\sim 3.4 \text{ cm}^3/\text{g}$). This provides easy contact and transportation of both charges and electrolyte through the 3D conducting pathways and enables EDLCs with high specific capacitance (245 F/g at 5 mV/s) and 96.5% retention after 6000 cycles in H_2SO_4 electrolyte. When using conductive substrates instead, the 3D topological configuration can provide intimate interfacial contact between the current collector and active materials. This is highly desirable to reduce the contact resistance and mitigate the constriction/spreading resistance [789]. When vertically oriented graphene sheets are grown directly on metal current collectors, and they can work as electrically conducting bridges to facilitate charge transport and minimize electronic and ionic resistances [790]. This allows for supercapacitors with high power and rate capabilities as well as ultrafast resistor-capacitor time constants ($< 200 \text{ ms}$, in contrast with $\sim 1 \text{ s}$ for conventional EDLCs) [791]. Recently, Bando et al. [792] developed a sugar-blowing approach to grow 3D self-supported graphene bubble networks through heating of glucose and NH_4Cl . As shown in Fig. 28, the bubble-like mesoporous material consists of continuous mono- or few-layered graphitic membranes that are firmly scaffolded by micrometre-scale graphitic struts. High SSA (1005 m^2/g), and ultralow density ($3.0 \text{ mg}/\text{cm}^3$) are achieved simultaneously. An EDLC using this material has specific capacitances as high as 250 F/g at 1 A/g and 130 F/g at 100 A/g.

4.1.3. Carbonaceous hybrid electrodes

Table 4 summarizes the electrochemical performance of graphene hybrid electrodes containing carbonaceous materials of fullerenes, CNTs, CNFs, porous carbon, and activated carbon. Of particular interest, the incorporation of 1D CNTs into 2D graphene can form 3D networks and prevent them from restacking by steric hindrance [793–795]. Reducing GO in the presence of CNTs is a direct method [796,797]. A hybrid electrode consisting of reduced GO and CNTs (9:1 in weight) exhibits much higher values of SSA (538.9 m^2/g) and specific capacitance (326.5 F/g at 20 mV/s) than pure graphene (138.2 m^2/g , 83 F/g at 20 mV/s) [796]. Both energy and power densities are as high as 21.74 Wh/kg and 78.29 kW/kg, respectively. Dai et al. [798] created a 3D pillared vertically aligned CNT-graphene architecture by intercalated growth of CNTs into thermally expanded HOPG (Fig. 29a–c). The resulting hybrid electrode exhibits a modest SSA of $\sim 213.7 \text{ m}^2/\text{g}$ and specific capacitance of $\sim 110 \text{ F/g}$ at 10 mV/s. Fan et al. [799] fabricated 3D CNT/graphene hybrids by CVD approach using Co particles deposited GO as catalytic substrates in the presence of CO or C_2H_4 as the carbon source. As shown in Fig. 29(d–f), CNTs pillars are grown in between graphene sheets and distributed uniformly but sparsely on the whole sheet surface. The resulting hybrid materials have a higher SSA (612 m^2/g) compared to pure graphene (202 m^2/g) due to the effective intercalation and distribution of CNTs between graphene sheets. Supercapacitors based on such hybrid electrodes have high specific capacitance (385 F/g at 10 mV/s) and excellent electrochemical stability. Recently, Ozkan et al. [800] used nickel foam as a catalytic substrate to grow CNTs and graphene simultaneously via a one-step ambient pressure CVD process. The resulting few-layer graphene/CNT foams possess a large SSA of 743 m^2/g and EDLCs based on such hybrid foams show large values of specific capacitance (286 F/g), energy density (39.72 Wh/kg), and power density (154.67 kW/kg) as well as high cyclability with 99.34% capacitance retention after 85,000 cycles. In addition, carbon spheres can also be intercalated between

Table 4
Supercapacitors based on carbonaceous hybrids with graphene and their super-capacitive performance.

Hybrid electrode			Electrolyte and voltage window	Super-capacitive performance							Ref
Carbon materials	Graphene resource	SSA (m ² /g)		E_{\max} (Wh/kg)	P (W/kg) at E_{\max}	Specific capacitance and rate capability				Cyclability	
						Initial rate (C_{SPI})	Final rate (C_{SPF})	Final rate/Initial rate	Retention of C_{SPI} (%)	Retention (%) after cycles	
CNTs ~25 wt%	KOH activated GO	652	EmimBF ₄ 0–4 V	110.6	400k	0.5 A/g 199 F/g	20 A/g 99 F/g	40	49.7	98.2_10 k@10 A/g	[810]
CNTs	Ascorbic acid reduced GO		1 M KOH –1.0~0 V			3.2 mA/cm ² 18 mF/cm ²	24 mA/cm ² 16.2 mF/cm ²	80	90	93.1_10 k@6.4 mA/cm ²	[811]
CNTs ~50 wt%	Hydrothermally/chemically reduced GO		TEABF ₄ /polycarbonate	34.3	400	0.5 A/g 109.7 F/g	5 A/g 78.3 F/g	10	71.4		[812]
CNTs	Hydrothermally reduced GO	396	PVA/H ₃ PO ₄ 0–1.0 V	6.3 mWh/cm ³		26.7 mA/cm ³ 300 F/cm ³				93_10 k@250 mA/cm ³	[813]
CNTs	N ₂ H ₄ -reduced GO	421.3	1 M EMI-TFSI 0–4.0 V	155.6		0.3 A/g 280 F/g	3.1 A/g 161.9 F/g	10.3	57.8	129_1 K@2 A/g	[814]
CNTs	HI-reduced GO		PVA/H ₃ PO ₄ 0–0.8 V	0.5 W/cm ³	1 mWh/cm ³	0.05 A/cm ³ 38.8 F/cm ³	1.6 A/cm ³ 19.9 F/cm ³	32	50	93_10 k@0.8 A/cm ³	[815]
CNTs	CVD graphene	807	6M KOH 0–1.0 V			10 mV/s 98.5 F/g	500 mV/s 77 F/g	50	78.2	100_5 k@450 mV/s	[816]
Activated carbon	Annealing GO	798	EMI-TFSI 0–4.0 V	99.2	1 k	0.5 A/g 179 F/g	4 A/g 80.5 F/g	8	45	89_3 k@1 A/g	[817]
Activated carbon	Hydrothermally reduced GO	2106	6 M KOH 0–1.0 V	22.3	33.2	1 mV/s 210 F/g	200 mV/s 100 F/g	200	47.6	94.7_5 k@100 mV/s	[818]
Activated carbon	Hydrothermally reduced GO	2806	1 M TEABF ₄ in AN 0–2.3 V	32.2	1.1 k	2 A/g 171 F/g	16 A/g 143 F/g	8	83.6	90_2.5 k@4 A/g	[819]
Carbon fibres	Electrochemically reduced GO		1 M Na ₂ SO ₄ 0–1.0 V	8.5 mW/cm ²	21.4 μWh/cm ²	10 mV/s 22.6 μF/cm ²				95_5 k@10 mV/s	[820]
Cellulose nanofiber	VC-Na reduced GO		PVA/H ₂ SO ₄ 0–1.0 V	20 μWh/cm ²	15.5 mW/cm ²	0.7 mA/cm ² 203 F/g	11.2 mA/cm ² 134 F/g	16	66	99.1_5 k@3.4 mA/cm ²	[821]
C ₆₀ ~10 wt%	Glucose-reduced GO		6 M KOH 0–1.0 V			1 A/g 135.4 F/g	10 A/g 104.4 F/g	10	77.1	92.4_1 k@1 A/g	[822]
Porous carbon	Pyrolysis GO with KOH	2927	6 M KOH –1 to 0 V	11.3 Wh/L	45 W/L	0.5 A/g 481 F/g	20 A/g 313 F/g	40	65.1	97.2_5 k@500 mV/s	[823]
Porous carbon 6 wt%	Hydrothermal/annealing GO	254	6 M KOH –1.0 to 0 V	6.2@5 mV/s	3545	0.5 A/g 197 F/g	10 A/g 141 F/g	20	71.6	92.6_1 k@300 mV/s	[809]
Porous carbon	Hydrothermally reduced GO	460	6 M KOH –1.0 to 0 V			0.1 A/g 324 F/g	10 A/g 190 F/g	100	58.6	>90_10 k@2 A/g	[824]
Porous carbon fabrics	Hydrothermally reduced GO (15 wt%)	322.6	6 M KOH 0–1.0 V			0.1 A/g 391 F/g	5 A/g 195 F/g	50	49.1	92_10 k@3 A/g	[825]
Carbon black 20 vol%)	N ₂ H ₄ -reduced GO		6 M KOH 0–1.0 V		5.1 k	10 mV/s 138 F/g	500 mV/s 81.6 F/g	50	60	96.15_2 k@10 A/g	[826]
			1 M LiPF ₆ 0–3.0 V	26		10 mV/s 83.2 F/g				95.65_2 k@10 A/g	

E_{\max} : Maximum energy density; P : power density; C_{SPI} : initial specific capacitance; C_{SPF} : final specific capacitance; TEABF₄: tetraethyl ammonium tetrafluoroborate; EMI-TFSI: 1-ethyl-3-methyl imidazolium bis(trifluoromethane sulfone) imide; EmimBF₄: 1-ethyl-3-methylimidazolium tetrafluoroborate; AN: acetonitrile.

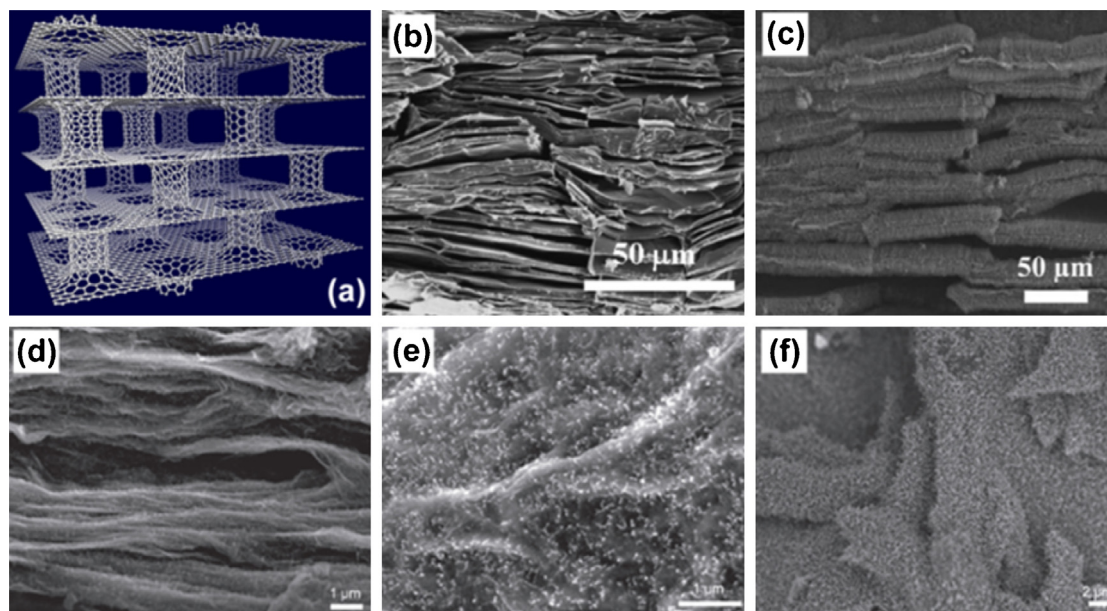


Fig. 29. (a) Schematic diagram for a 3D CNT-graphene hybrid nanostructure and SEM images of (b) thermally expanded HOPG, and (c) 3D pillared CNT-graphene architectures under different magnifications [798]. SEM images of graphene/CNT hybrids obtained by CVD using Co-anchored GO sheets as catalysts with CO (d and e), and C₂H₄ (f) as carbon sources, respectively [799]. Copyright: 2011 American Chemical Society and 2010 Wiley-Vch.

graphene sheets to form 3D architectures with improved capacitive performances [801,802]. These graphitic hybrid materials are promising electrodes for EDLCs due to large electrolyte-accessible SSA, highly conductive pathways, and rapid electron and electrolyte ions transport [803–808]. It should be noted that the specific capacitance decreases with an excess amount of carbon additives in such hybrids since graphene has the highest intrinsic capacitance among carbon nanomaterials [809].

4.1.4. Volumetric capacitive performance

Supercapacitors have been usually reported using gravimetric rather than volumetric capacitive performance [10,768,769]. However, volumetric capacitance, energy, and power density are crucial to assemble devices in realistic applications [827]. Especially for microdevices, gravimetric energy density is almost irrelevant compared to volumetric energy because the weight of active materials used in devices is negligible. Porous electrodes such as GBM aerogels, due to low packing density ($<0.5 \text{ g/cm}^3$), have large empty spaces flooded by the electrolyte. This increases the weight of devices without enhancing capacitance and energy

[827]. Moreover, there is often a very limited volume available for power sources when assembling the integrated devices and portable electronics [828]. It is significantly more important for an electrode material to possess a high volumetric capacitance.

Tao et al. [829] reported a highly compact but porous graphene material (abbreviated as HPGM) that was produced by room-temperature vacuum drying of the hydrothermally-reduced GO hydrogels. HPGM consists of densely interlinked few-layer sheets and have a low pore volume ($0.16 \text{ cm}^3/\text{g}$) and high apparent density (1.58 g/cm^3) which is much higher than that ($\sim 0.02 \text{ g/cm}^3$) of the freeze-dried porous graphene material (PGM) due to the presence of abundant macropores and mesopores. Different formation mechanisms are proposed as shown in Fig. 30. Although HPGM and PGM exhibit comparable SSA ($367 \text{ vs } 370 \text{ m}^2/\text{g}$) and similar gravimetric capacitances ($238 \text{ vs } 235 \text{ F/g}$ at 0.1 A/g), the volumetric capacitance of HPGM reaches up to 376 F/m^3 which is nearly 40 times higher than that of PGM (10 F/m^3). Meanwhile, HPGM shows an excellent cyclability with $\sim 96\%$ capacitance retention at 0.5 A/g after >4000 cycles, and also a good rate capability with $\sim 69\%$ retention at 15 A/g . The maximum energy density of such a supercapacitor is up to

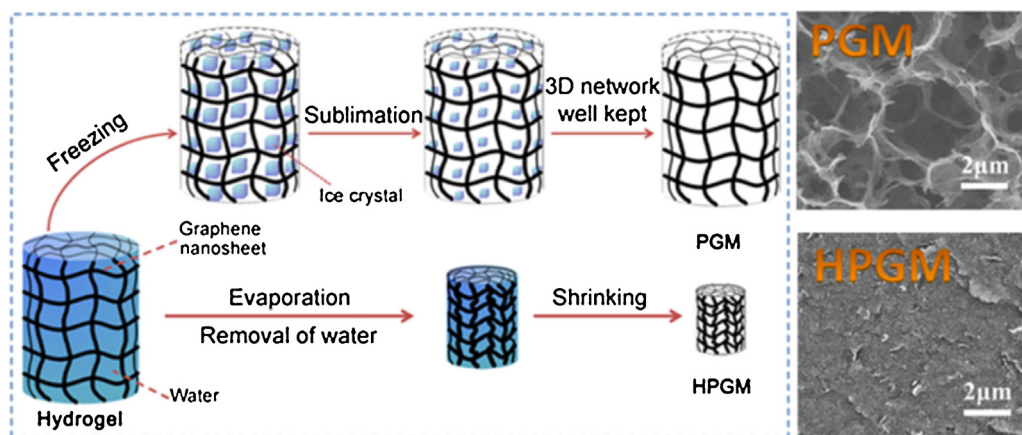


Fig. 30. Formation process of PGM and HPGM starting from graphene hydrogels, and corresponding SEM images (Upper: PGM through freeze drying, lower: HPGM through evaporation-induced drying at room temperature under vacuum) [829]. Copyright 2013 Macmillan Publishers Limited.

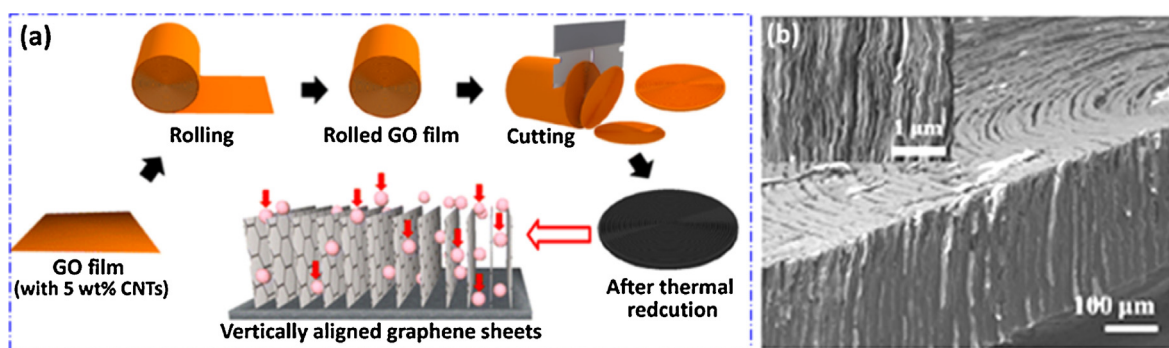


Fig. 31. (a) Schematic illustration for fabricating vertically-aligned graphene electrodes where electrolyte ions (pink dots) can be homogeneously and directly diffused into graphene sheets. (b) Cross-sectional SEM image of graphene electrodes [831]. Copyright 2014 American Chemical Society (For interpretation of the references to color in this figure legend, the reader is referred to the web version of this article.).

13.1 Wh/L at a power density of 39.5 W/L in aqueous electrolyte, and can be further increased to 37.1 Wh/L and 98.8 W/L in organic electrolyte, respectively. This implies low-temperature vacuum-drying of hydrogels is an alternative method to produce electrode materials with low pore volume and high packing density while retaining large SSA and hence, excellent volumetric capacitance.

Low-temperature treatment of GO using $\text{Mg}(\text{OH})_2$ nanosheet templates was found to produce graphene sheets with high SSA and low pore volume, and consequently ultrahigh specific gravimetric (456 F/g) and volumetric (470 F/cm³) capacitances which are over 3 times higher than hydrazine-reduced GO [830]. The assembled supercapacitor also exhibits an ultrahigh volumetric energy density (27.2 Wh/L) and excellent cycling stability with 134% capacitance retention after 10,000 cycles. Lee et al. [831] fabricated highly dense and vertically aligned graphene (VAG) electrodes by a combination of hand-rolling and cutting processes using GO/CNT hybrid films as the starting materials, as shown in Fig. 31. The opened-edge VAG electrode exhibits a high packing density (1.18 g/cm³). CNTs herein act as spacers for suitable pore sizes close to 0.9 nm and additives to improve conductivity. The as-prepared VAG electrode demonstrates high rate capability and much higher volumetric (171 F/cm³) and area (1.83 F/cm²) capacitances than reduced GO powder (62 F/cm³, 0.06 F/cm²). Chemically bonded graphene/CNT hybrids were achieved by amide bonding and used as flexible electrodes to show a large volumetric capacitance (165 F/cm³) [812].

4.2. Graphene-based materials for pseudocapacitors

Pseudocapacitors store energy through highly reversible Faradic redox reactions between the electrolyte and active electrodes in addition to electric double-layer storage [752]. Conducting polymers and metal oxides are the most attractive materials for pseudo-capacitive storage because of their electrochemical activity and their capability to carry out the Faradaic redox reaction [10]. In principle, compared to EDLCs, pseudocapacitors exhibit higher capacitance and energy density due to the coexistence of electrostatic and electrochemical storage occurring at the surface and also near-surface areas (several tens of nanometers from the surface) of the electrodes, [10] but relatively low power density due to low electrical conductivity of materials and slow electron transfer kinetics [756]. In addition, pseudocapacitive materials generally suffer from low stability and short lifetimes because of their degradation and aging by swelling and shrinking during redox reactions. In this regard, GBMs are exceptionally attractive due to their high electrical conductivity, large SSA, low cost, high mechanical strength and flexibility, and

tunable porous microstructures as well as easy fabrication of the electrodes [15,832].

4.2.1. Conducting polymer/graphene composites

Among conducting polymers, PANI is the most widely used for supercapacitors due to its large theoretical capacitance (2000 F/g), high electroactivity, low cost and facile synthesis [833,834]. Graphene/PANI composites have been successfully prepared by *in-situ* polymerization, [835–842] physical mixing, [843–845] layer-by-layer (LBL) assembly, [846] electrodeposition, [847,848] electrospinning, [849] and chemical grafting [850,851] methods. Among them, the *in-situ* polymerization technique is easy, widely accepted and capable of high volume production due to the good solubility of GO and aniline precursors [852–855]. Wei et al. [856] reported a hierarchical composite of PANI nanowire arrays grown vertically on GO sheets by *in-situ* chemical polymerization. In the case of dilute aniline (0.05 M), heterogeneous nucleation on GO sheets was observed, resulting in a high yield of uniform aligned PANI arrays (see Fig. 32). GO/PANI supercapacitors show a high specific capacitance of 555 F/g at 0.2 A/g while retaining 227 F/g at 2 A/g due to good rate capability. Meanwhile, 92% capacitance retention after 2000 cycles is reported for GO/PANI while pure PANI retains only 74% of its initial capacitance. GO/PANI composites thus possess a synergistic effect of PANI and GO with higher electrochemical capacitance and better stability than each individual component. Yu et al. [837] developed a method to fabricate free-standing graphene paper on which uniform PANI nanorod arrays can be then grown *in-situ* by electropolymerization to produce flexible graphene/PANI composite paper. The graphene/PANI electrode exhibit a higher capacitance (763 F/g@ 1 A/g) compared to that of graphene paper and PANI film (180 and 520 F/g, respectively) due to the contribution of both dual-layer capacitance and pseudocapacitance, and better cycling stability with 82% capacitance retention after 1000 cycles relative to the 51.9% of PANI film. Recently, chemically-grafted graphene with PANI nanowire arrays was performed by grafting aminophenyl groups as active sites for *in-situ* vertical growth of PANI arrays onto graphene sheets [857]. The resulting composites have a high capacitance of 590 F/g at 0.1 A/g and no loss of capacitance after 200 cycles at 2 A/g.

Graphene/polypyrrole (PPY) composites have been also prepared by electropolymerization, [858,859] chemical polymerization, [860–862] electrodeposition, [863,864], and physical mixing [865]. All show improved supercapacitive performance compared to their individual components. Other conducting polymers, such as poly(3,4-ethylenedioxythiophene) (PEDOT), [859] have been rarely reported due to their high cost. In a recent study, PANI, PPY, and PEDOT were coated on the surface of graphene by *in-situ*

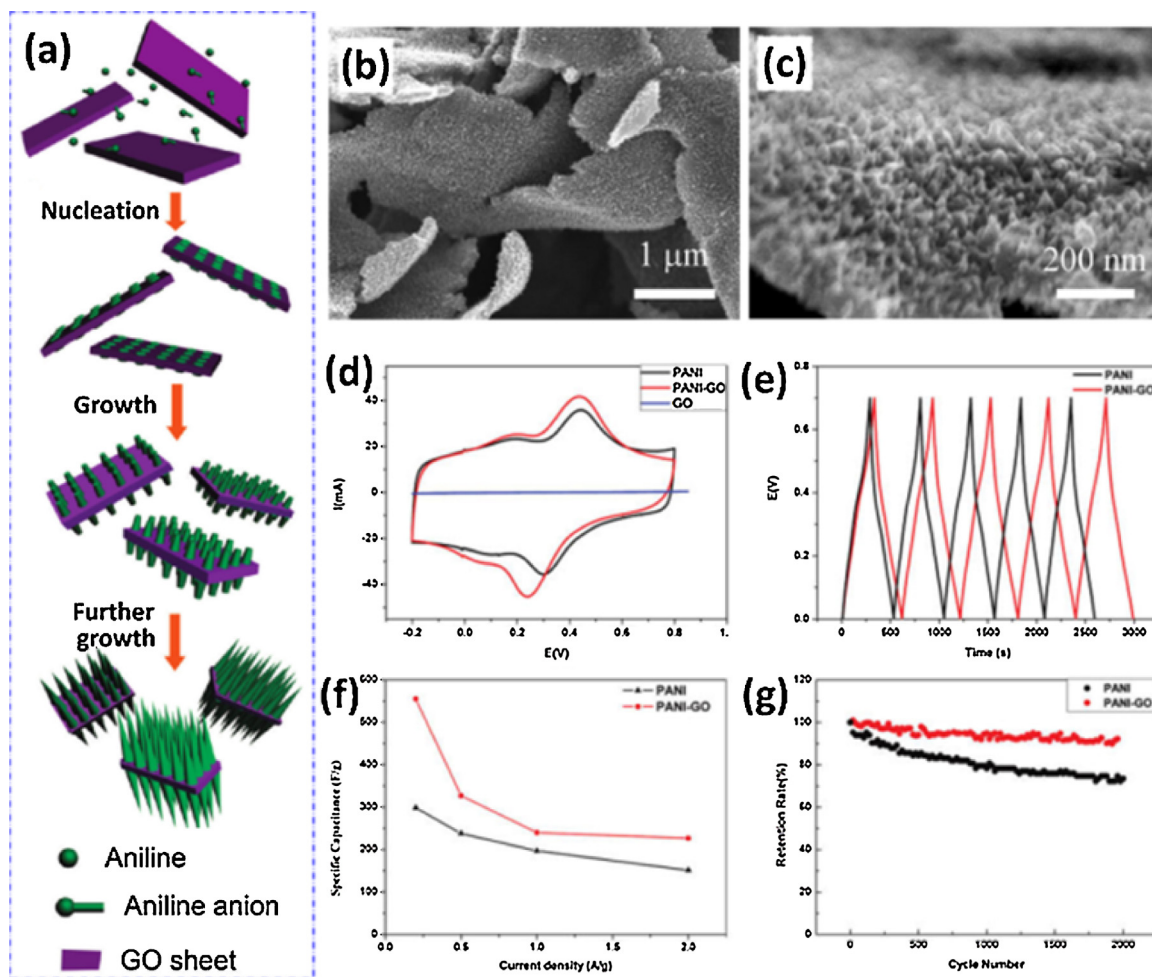


Fig. 32. (a) Schematic illustration of heterogeneous nucleation and growth mechanism of PANI nanowires on GO nanosheets, and (b and c) SEM images of GO/PANI composites. Electrochemical performance: (d) CV curves of GO, PANI, and GO/PANI composites at a scan rate of 20 mV/s; (e) charge-discharging curves, (f) specific capacitance of at different current densities, and (g) cycling stability of PANI and GO/PANI [856]. Copyright 2010 American Chemical Society.

polymerization to obtain conducting polymer composites (Fig. 33a–c) [866]. Graphene/PANI, graphene/PPY, and graphene/PEDOT electrodes have specific capacitances of 361, 249, and 108 F/g at 0.3 A/g, respectively, which correspondingly decrease to 305, 189, and 99 F/g at 2.0 A/g (see Fig. 33d–f). Graphene/PANI composites have a higher capacitance and better rate performance with a higher retention of initial capacitance compared to the other two composites. These composites show high cycling ability with comparable capacitive retentions (81–88%) after 1000 cycles with higher retentions than that of pure PANI (68% retention after 600 cycles). Graphene sheets are here believed to provide a robust support for conducting polymers; preventing them from swelling and shrinking during long-term cycling.

4.2.2. Metal oxide/graphene composites

Metal oxides have long been studied as potential electrode materials for pseudocapacitors due to the ease of mass production, and specific capacitance over twice that of conventional carbon-based electrode materials [867]. However, metal oxides are low conductive and relatively expensive. Pseudocapacitors based on these materials show low cyclability and rate performance which fail to meet practical requirements of commercial applications [15]. Graphene is a preferred candidate to couple with metal oxides in light of its high conductivity, large SSA, and excellent mechanical/electrochemical stability [34].

Among all pseudocapacitive materials, RuO_2 appears to be the most promising electrode material due to its high theoretical capacitance (1358 F/g) and metallic conductivity (300 S/cm) for efficient charge transport [868]. Its hydrous nature allows a high rate of proton exchange and hence, rapid charging-discharging [868]. RuO_2 -based supercapacitors can also exhibit a wide voltage window of ~ 1.2 V in acidic electrolytes and thus possess high energy density [869]. However, like all nanoparticles (NPs), RuO_2 NPs easily form large aggregates which often induce incomplete redox reactions and significant degradation in the electrochemical performance. Recently, a combination of sol-gel and low-temperature annealing processes was used to prepare graphene/ RuO_2 composites [651] in which RuO_2 nanoparticles (5–20 nm) were uniformly anchored on the graphene surface. Graphene/ RuO_2 -based supercapacitors exhibit high specific capacitance (570 F/g for 38.3 wt% Ru loading), enhanced rate capability, excellent cycling stability (97.9% retention after 1000 cycles), high energy density (20.1 Wh/kg at 0.1 A/g) and high power density (10 kW/kg). Ozkan et al. [870] fabricated a 3D graphene and CNT hybrid foam architecture for uniformly anchoring RuO_2 (sub-5 nm) NPs. Supercapacitors based on such 3D hybrids have high gravimetric (502.78 F/g) and area (1.11 F/cm^2) specific capacitances, and both energy and power densities are as high as 39.28 Wh/kg, and 128.01 kW/kg, respectively. These devices also give an excellent cyclability with 106% capacitance retention over

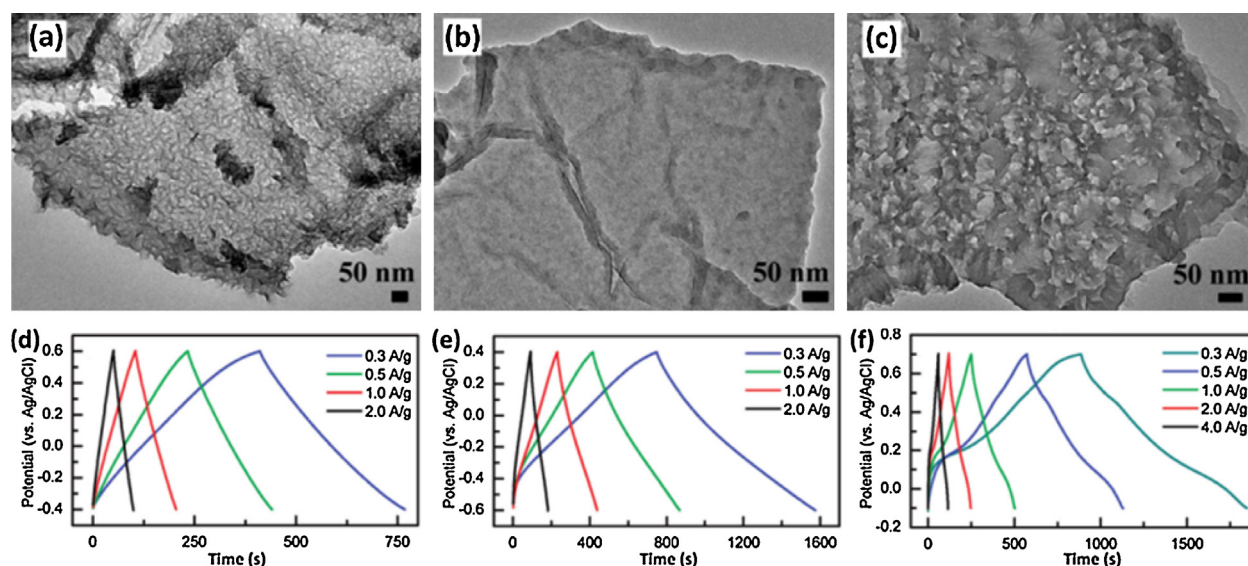


Fig. 33. TEM images (upper) and charge/discharge curves (lower) of (a, d) graphene/PEDOT, (b, e) graphene/PPY, and (c, f) graphene/PANI composites and corresponding electrodes [866]. Copyright 2012 American Chemical Society.

8100 cycles. However, RuO_2 is too expensive for widespread practical applications and it also exhibits high toxicity. Hence it has long been used as a model material for exploring fundamental mechanisms of super-capacitive performance [868].

Manganese oxide, typically MnO_2 , is frequently considered as a potential electrode material for supercapacitors because of its high theoretical capacitance (up to 1380 F/g), low cost due to abundant availability on earth, environmental benignity and ease of large-scale production [871,872]. Unfortunately, its poor conductivity (10^{-5} – 10^{-6} S/cm) limits the rate capability for high-power applications [12]. He et al. [873] used highly conductive (5500 S/m) graphene networks to support MnO_2 by electrodeposition. Supercapacitors based on such graphene/ MnO_2 show high area capacitance of 1.42 F/cm² (2 mV/s) and power density (62 W/kg). In addition to RuO_2 [651,874–877] and MnO_2 , [873,878–884] graphene has also been hybridized with other metallic compounds, such as ZnO, [885–887] NiO, [888–890] SnO_2 , [891–893] CeO_2 , [894] Mn_3O_4 , [895–901] Fe_3O_4 , [902–905] Co_3O_4 , [906–909] V_2O_5 [910–914] as well as $\text{Co}(\text{OH})_2$ [915–917] and $\text{Ni}(\text{OH})_2$, [918–921] to fabricate the electrode materials. Supercapacitors based on such hybrid electrodes have shown improved electrochemical performance (see Table 5). In these cases, metal oxides contribute to large pseudocapacitance by means of rich surface/near-surface redox reactions while graphene contributes an electric dual-layer capacitance via the adsorption/desorption of electrolyte ions. Meanwhile, graphene serves as a robust framework for supporting metal oxide particles and also forms a conductive network having a high transportation rate for electrolyte ions and electrons throughout the electrode.

5. Graphene-based materials for fuel cells

Fuel cells are electrochemical devices that directly convert chemical energy into electrical energy through chemical reactions at the electrode–electrolyte interface [751]. A primitive fuel cell was first reported over 175 years ago [936]. Fuel cells have drawn tremendous attention since then due to their high energy density, high efficiency, and low emission of pollutants. Fuel cells under active development typically include six types based on the electrolyte used in cells, [937] and they are alkaline fuel cells (AFCs), polymer-electrolyte membrane fuel cells (PEMFCs, also called proton-exchange membrane fuel cells, or solid polymer

electrolyte fuel cells), direct-methanol fuel cells (DMFCs), phosphoric-acid fuel cell (PAFCs), molten-carbonate fuel cell (MCFCs), and solid-oxide fuel cells (SOFCs) in an order of increasing operational temperature while decreasing overall efficiency (Fig. 34) [938]. DMFCs can be considered as a subcategory of PEMFCs in which methanol is electrochemically oxidized directly in cells [939,940]. Each fuel cell has its own advantages, limitations, and potential applications [751,937,938].

5.1. Hybrid electrocatalysts

Reactions in fuel cells usually involve the oxidation of fuels (such as hydrogen, methanol, and formic acid) on the anode and the oxygen reduction reaction (ORR) on the cathode where the oxygen source is from air in most cases. Platinum (Pt) has long been regarded as the best catalyst for anode and cathode reactions especially for low-temperature fuel cells. Other noble metals such as Au, Ru, Pd, Ni, and their alloys have also been reported to catalyze the electrode reactions in fuel cells [941–943]. Noble metal catalysts still suffer from sluggish reaction kinetics, high cost, crossover effects (caused by the diffusion of fuel molecules from the anode to the cathode), carbon monoxide (CO) deactivation, and susceptibility to time-dependent drift [944]. On the other hand, these catalyst NPs are usually required to be dispersed uniformly on a catalyst support so as to increase electroactive surface area and catalytic activities, improve cycling stability and lifetime and also lower the electrode cost. Carbon black has been the most widely used support for state-of-the-art commercial catalysts in fuel cells mainly due to its low cost [945]. Other carbon materials such as active porous carbon, [942,946] CNTs, [947] graphite, [948] carbon aerogels, [949], and non-carbon materials [950,951] have also been proposed as catalyst supports. An excellent catalyst-support material should exhibit low cost, large SSA for uniform dispersion of catalysts, high electrical conductivity, strong coupling with catalysts as well as high chemical and electrochemical stability in the electrolytes [951,952]. However, such hybrid catalysts are still hindered by self-aggregation of catalyst NPs, activity degradation, catalyst poisoning, or corrosion and oxidation of catalysts and supports under operating conditions [950,953,954]. The key breakthrough for fuel cells lies in developing cost-effective, highly-conductive electrocatalysts that can accelerate ORR and fuel oxidation while retaining high stability and durability.

Table 5
Pseudocapacitors based on metal oxide/graphene composites and their super-capacitive performance.

Composite electrode			Super-capacitive performance								Refs
Capacitive materials	Graphene resource	SSA (m ² /g)	Electrolyte & voltage window	E_{\max} (Wh/kg)	P (W/kg) at E_{\max}	Specific capacitance and rate capability				Cyclability	
						Initial rate (C_{SPI})	Final rate (C_{SPF})	Final rate/ Initial rate	Retention of C_{SPI} (%)	Retention (%) after cycles	
RuO ₂ (5–20 nm; 38.3 wt% Ru)	GO, annealing	281	1 M H ₂ SO ₄ –0.2 to 0.8 V	20.1@0.1 A/g	50@0.1 A/g	1 mV/s		50	36	~97.9_1 k@ 1 A/g	B [651]
	100 wt% graphene	108									
				570 F/g					42_1 k@ 1 A/g		
100 wt% RuO ₂		3.0		3.1@0.1 A/g		1 mV/s				90.9_1 k@1 A/g	
RuO ₂ (<2 nm)	CVD graphene		1 M H ₂ SO ₄ 0–0.9 V	57.5	23 k	148 F/g				70_4 k@0.5 V/s	B [877]
RuO ₂ (40 wt%)	N ₂ H ₄ -reduced GO		0.5 M H ₂ SO ₄ 1.2 V	20.28 (14.03)	600 (12k)	10 mV/s				94_1 k@5 A/g	A [874]
MnO ₂ (100–300 nm), 100 wt% 99 wt% 97 wt% 90 wt%	Thermally reduced GO		3 M KCl 0–1.0 V	50.2 42.9 36.6		5 A/g					
						100 F/g					
						5 mV/s	1 V/s	200	32	~80_1.5 k@50 mV/s	B [922]
						215 F/g	68 F/g			~100_1.5 k@50 mV/s	
MnO ₂ sheets (~66.9 wt%)	N-graphene (GO, urea)	158.74	1 M Na ₂ SO ₄ 0–1.0 V			365 F/g	167 F/g		46		
MnO ₂ needle (~90 wt%)	GO		1 M Na ₂ SO ₄ 0–1.0 V			310 F/g	183 F/g		49		
MnO ₂ (38.1 wt%)	Activated GO	1391	1 M H ₂ SO ₄ 0–1.0 V			265 F/g	227 F/g		86		
Hollow MnO ₂ (53.3 wt%)	GO, heating/150 °C			69.8@0.5 A/g		0.2 A/g	2 A/g	10	74.9	94.2_2 k@0.2 A/g	B [923]
						257 F/g	192.5 F/g				
						0.15 A/g	1 A/g		54	84.1_1 k@0.2 A/g	B [879]
MnO ₂ (300–400 nm, 90 wt%)	N ₂ H ₄ -reduced GO	152	1 M H ₂ SO ₄ –0.1 to 0.9 V			216 F/g	111.1 F/g				
Layered MnO ₂ (78 wt%)	N ₂ H ₄ -reduced GO		1 M Na ₂ SO ₄ 0–1.0 V			0.25 A/g	20 A/g	80		87.7_1 k@15 A/g	A [924]
MnO ₂	N ₂ H ₄ -H ₂ O-reduced GO		1 M Na ₂ SO ₄ 0–1.0 V	17.2@0.2 A/g	200@0.2 A/g	256 F/g	187 F/g				
Flower-like MnO ₂	Sponge-supported GO, HI reduction		1 M Na ₂ SO ₄ 0–1.0 V	8.34		0.5 A/g	1.5 A/g	3		83_1k@0.6 A/g	B [925]
MnO ₂ (61 wt%)	Graphene aerogel (GO, resorcinol- formaldehyde)	793	0.5 M Na ₂ SO ₄ 0–0.9 V			578 F/g	136 F/g	50			B [926]
MnO ₂	CVD 3D graphene foam		0.5 M Na ₂ SO ₄ 0–1.0 V	6.8	62	0.2 A/g	10 A/g				
Mn ₃ O ₄ (68.4 wt%)	N ₂ H ₄ -reduced GO		1 M Na ₂ SO ₄ –0.1 to 0.8 V			250 F/g	162 F/g	250	73.5	95.4_1.5k@0.5 V/s	B [927,928]
Mn ₃ O ₄ (~18.4 nm, 82.4 wt%)	GO, MSHR		0.5 M Na ₂ SO ₄ 0–1.0 V	3.7@1.2 A/g	508@1.2 A/g	310 F/g	228 F/g			78.7_1k@0.2 A/g	B [929]
Fe ₃ O ₄ (~90 wt%)	GO reduced in NaOH solution at 80 °C		0.5 M LiOH –1.15 to 0.1 V			124 F/g				~90_10 k@10 V/s	A [930]
Fe ₃ O ₄ (~73.5 wt%)	Hydrothermally-reduced GO	192	1 M KOH –0.2 to 0.8 V	124@1 A/g	332@1 A/g	~450 F/g	2 mV/s	500		95_50 k@1 V/s	B [931]
Fe ₃ O ₄ (20–40 m)	GO, urea, MSHR	72.3	1 M H ₂ SO ₄ 0–1 V	9@3.75 A/g	3000@3.75 A/g	410 F/g	1 V/s				
Co ₃ O ₄ (20 nm, 92.8 wt%)	Hydrothermally-reduced GO	112.9	2 M KOH 0–0.85 V	39	8.3 k	1.5 mA/cm ²	264 F/g			~82_5 k@1.5 mA/cm ²	A [873]
V ₂ O ₅ nanorods (~92 wt%)	Solvothermally reduced GO	49.16	8 M LiCl –0.3 to 0.7 V	29.33 74.58	10 k 500	29.8 F/g	50 mV/s	10		248_300@10 mV/s	B [895]
						5 mV/s	86 F/g				
						153 F/g		40	81		A [899]
						25 mV/s					
						193 F/g					
						0.5 A/g	10 A/g	20	90	95_1 k@2 A/g	B [902]
						326 F/g	304 F/g				
						1 A/g	5 A/g			~112_10 k@10 A/g	B [904]
						843 F/g	480 F/g				
						0.25 A/g	3.75 A/g			~97_12 k@0.25 mA/g	A [932]
						88 F/g	72 F/g				
						2 mV/s	50 mV/s	50	82.6	~95.6_1 k@2 A/g	A [908]
						472 F/g	86 F/g				
						1 A/g	20 A/g	20		~84_1 k@1 A/g	B [933]
						537 F/g	211.2 F/g				

CeO ₂ (~20 wt%)	GO, eating/150 °C	487	3 M KOH 0–0.6 V	18	1 A/g 208 F/g	~96_1 k@1 A/g	B [894]
NiO flakes (~96 wt%)	GO		1 M KOH 0–0.6 V	16.8@2 A/g	2 A/g	~94_2 k@2 A/g	B [888]
ZnO (5–10 nm)	Thermally reduced GO in scCO ₂		2 M KOH –0.5 to 0.5 V		400 F/g 5 mV/s	~98_1 k@10 A/g	B [887]
Ni(OH) ₂ (~65.6 wt%)	Hydrothermally reduced GO	81	1 M KOH 0–0.7 V		303 F/g 10 mV/s	~95_1 k@100 mV/s	B [934]
MnO ₂ (70 wt%), PANI	Graphene	91.37	1 M Na ₂ SO ₄ 0–1.0 V		1250.3 F/g 1 A/g	~97_5.1 k@4 A/g	B [935]

E_{\max} : Maximum energy density; P : power density; C_{SP} : initial specific capacitance; C_{SPF} : final specific capacitance; A: performance data measured by a symmetrical cell; B: performance data measured by a single electrode; SILAR: successive ionic layer adsorption and reaction method; MSHR: microwave-assisted hydrothermal reduction.

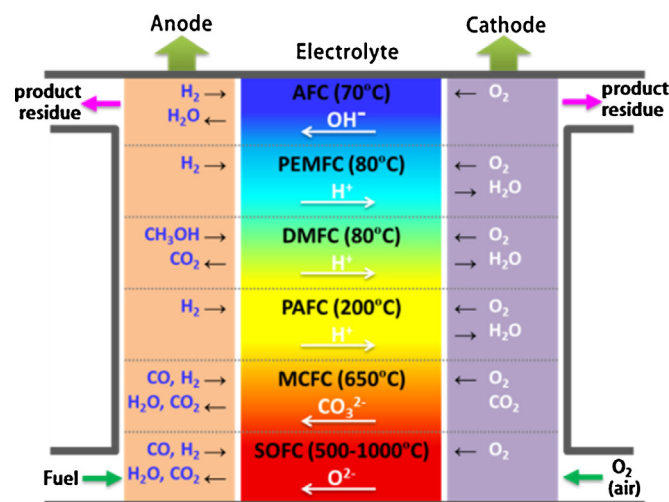


Fig. 34. Fuel-cell types, chemical reactions and processes that occur in various systems. The fuel oxidation reaction on the anode involves the liberation of electrons (e.g., $\text{O}^{2-} + \text{H}_2 = \text{H}_2\text{O} + 2\text{e}^-$ or $\text{H}_2 = 2\text{H}^+ + 2\text{e}^-$). These electrons travel round the external circuit producing electrical energy by means of the external load, and arrive at the cathode to participate in the reduction reaction (e.g., $1/2\text{O}_2 + 2\text{e}^- = \text{O}^{2-}$ or $1/2\text{O}_2 + 2\text{H}^+ + 2\text{e}^- = \text{H}_2\text{O}$). The reaction products such as H_2O are formed on the anode for SOFCs, MCFCs and AFCs, and on the cathode for PAFCs and PEMFCs.

As mentioned above, graphene can provide an ultra large SSA to support and disperse catalyst NPs uniformly thus suppressing inter-particle aggregation and enabling more exposure of available electroactive sites. Particularly for GO-derived graphene materials, they usually contains topographic defects (vacancies, holes, edges, and distortions) and residual functional groups (carbonyl, epoxide, hydroxyl, and carboxyl groups) which allow them to be active substrates for growing and immobilizing catalyst NPs with strong interactions and high structural stability [955]. The above features when combined with the high electrical conductivity and electrochemical stability of graphene can also facilitate the charge transfer from nanocatalysts to graphene and mass transport through the electrode surface thereby affording high conversion efficiency [956]. As reported extensively (see Table 6), [377,755,952,957] graphene hybrid catalysts for fuel cells have shown their advantages such as high electrocatalytic activity, long operation durability, great tolerance to crossover effect toward fuels, and low cost, all of which make graphene hybrid catalysts potential competitors to metal nanocatalysts [24,25,958].

Graphene-supported nanocatalysts have been mainly produced by reducing catalyst precursors and GO through *in-situ* or *ex-situ* methods [984–986]. For instance, Pt NPs (5.1 nm in diameter) were uniformly deposited onto graphene sheets by synchronous reduction of H_2PtCl_6 and GO using NaBH_4 [987]. The resulting Pt/graphene catalysts exhibit higher catalytic activity for both methanol oxidation reaction (MOR) and ORR, and also better stability compared to Pt (5.7 nm) supported on carbon black due to the uniform distribution of Pt NPs and enhanced interaction between Pt and graphene. Ravishanker et al. [988] reported an ultrafast microwave-assisted process to produce graphene-supported Pt catalysts by co-reduction of GO and H_2PtCl_6 in ethylene glycol. Ultrafine Pt NPs (2–3 nm) were uniformly distributed on graphene and showed excellent catalytic activity for MOR. Electrochemical reduction was demonstrated to produce Pt/graphene catalysts for fuel cells with high electrocatalytic activity and long-term stability [989]. In addition, Pt NPs can be directly deposited onto the surface of N_2H_4 -reduced GO [990] and show a larger electrochemically-active surface area (ECSA; $24.01 \text{ m}^2/\text{g}$) than carbon black-supported Pt catalysts ($20.61 \text{ m}^2/\text{g}$) and higher

Table 6
Graphene hybrid electrocatalysts and their applications in fuel cells.

Graphene-supported electrocatalysts			Catalytic performance			Applications	Refs
Graphene source	Catalysts	Graphene (wt%)	ECSA	Max. current/power density	Current or ECSA Retention (%)		
Graphene-supported metals							
GO, NaBH ₄	Pt (5–6 nm)	~40	44.6 m ² /g (30.1 m ² /g) ^a	199.6 mA/mg (101.2 mA/mg) ^a		MOR	[959]
PDDA-GO, NaBH ₄	Pt (~4.6 nm)		141.6 m ² /g	2.53 mA/cm ²		MOR	[960]
S-graphene (GO, phenyl disulfide)	Pt NPs (2.1 nm)		139 mA/mg (121 mA/mg) ^a	87%@500 cycles (48%) ^a	ORR	[961]	
Graphene (GO)	Pt NPs (2.25 nm)		101 mA/mg	54%@500 cycles			
CVD 3D graphene	Pt (~3 nm)		16.8 m ² /g (13.1) ^a	~2.5 mA/cm ²	~65%@2 k cycles (~45%) ^a	MOR	[962]
S-graphene (GO, (C ₆ H ₅ S) ₂ , 1000 °C)	Pt NWs (3–25 nm in diameter)		24.5 m ² /gm (53 m ² /gm) ^a	167 mA/mg (125 mA/mg) ^a	58%@3 k cycles (1%) ^a	ORR	[963]
GO, 1000 °C	Pt NWs		24.0 m ² /gm	132 mA/mg _{Pt} ⁻¹	28%		
DNA-graphene	Pd NPs (5 nm)	32	147.1 m ² /g	140.1 mA/mg (63.9 mA/mg) ^a		FAOR	[964]
Graphene	Pd NPs (12 nm)	30	73.2 m ² /g	93.8 mA/mg			
GO, N ₂ H ₄ H ₂ O, hydrothermal	Ni NPs			16.3 mA/cm ² (0.5 M EtOH)		EOR	[965]
GO, hydrothermal	Cu nanocubes (~50 nm)				95.3%@200 cycles	DHFC	[966]
GO	Au NPs (~29.2 nm)			2.70 mA/cm ² (2.96 mA/cm ²)	92.5%@5 k s (7.8%) ^a	ORR	[967]
GO, electrochemical reduction	Au NPs (~6.8 nm)		0.862 cm ²		133%@50 k s (55%) ^a	ORR	[968]
Graphene-supported alloys							
Graphene	PtRu		68 m ² /g	20.8 mA/cm ²		MOR	[969]
GO, heating	PtAu (~4.5 nm)	~60		185 mW/cm ²		FAOR	[970]
GO, melamine, annealing	Pt ₃ Au (4–5 nm)	72.7	60.9 m ² /g (45.7 m ² /g) ^a	0.417 A/g ² (0.064 A/g ²)	76.5%@2 k cycles (39.9%) ^a	MOR	[971]
GO, annealing	Pt ₃ Au (4–5 nm)	72.9	49.2 m ² /g	0.186 A/g ²			
GO, microwave	Pt ₃ Pd		49.8 m ² /g	394 mA/mg		MOR	[972]
GO, NaBH ₄	PtRu (~2.8 nm)	80	157.2 m ² /g (52 m ² /g) ^a	860 A/g (206 A/g)		MOR	[973]
CVD 3D graphene	PtRu (~4.24 nm)	80	186.2 m ² /g (54.2 m ² /g) ^a	109.3 mA/cm ² (MeOH)	99.3%@900 cycles (21.2%) ^a for MOR	MOR	[974]
				78.6 mA/cm ² (EtOH)	32.5%@900 cycles (0.9%) ^a for EOR	EOR	
GO, EG reduction	NiPd (2–6 nm)	81.8	108.3 m ² /g	4428 mA/mg _{Pd}		MOR	[975]
GO, EG reduction	Ir ₂ V NPs (2.02 nm)		15.331 cm ² (0.619 cm ²) ^a	231 μA/cm ²		ORR	[976]
GO, NH ₃	TiN (8.8 nm)	20.27			90%@25,000 s (27%) ^a		[977]
GO, heating	Pt ₃ Co (4–5 nm)	~60	57 m ² /g	875 mW/cm ²		ORR	[978]
GO, heating	Pt ₃ Cr (4–5 nm)	~60	55 m ² /g	985 mW/cm ²			
3D Graphene (GO, hydrothermal)	PtPdCu (30 nm)	75.32		183 mA/cm ² (55 mA/cm ²) ^a	~94%@1 k cycles		[979]
Graphene-supported metal oxides							
GO, NH ₃ H ₂ O	Mn ₃ O ₄ spheres	17		2.47 mA/cm ²		ORR	[980]
	Mn ₃ O ₄ cubes	20		3.41 mA/cm ² ^a			
	Mn ₃ O ₄ ellipsoids	16		3.70 mA/cm ²			
GO, NH ₃ H ₂ O	Co ₃ O ₄ NPs (4–8 nm)	30		52.6 mA/cm ² (68.0 mA/cm ²) ^a	~100%@10–25 k s (20–48%) ^a	ORR	[981]
						OER	
GO, hydrothermal reduction	Co ₃ O ₄ NPs (12–25 nm)			12.3 mA/cm ²			
3D graphene (GO, polypyrrole, 180 °C)	Fe ₃ O ₄ NPs (20–80 nm)	53.8		–2.56 mA/cm ²	79.3%@20 k s (61%) ^a	ORR	[982]
GO, NH ₃ H ₂ O	MnCo ₂ O ₄ (~10 nm)	~20		151 mA/cm ²	96.5%@20 k s (67%) ^a	ORR	[983]

J_k : Kinetic current density; n : electron transfer number; ECSA: electrochemically active surface area calculated by integrating the hydrogen adsorption–desorption region.

^a Data from the commercial Pt/C; FAOR: Formic acid oxidation reaction; EOR: ethanol oxidation reaction; DHFC: Direct hydrazine fuel cell; OER: Oxygen evolution reaction; EG: Ethylene glycol.

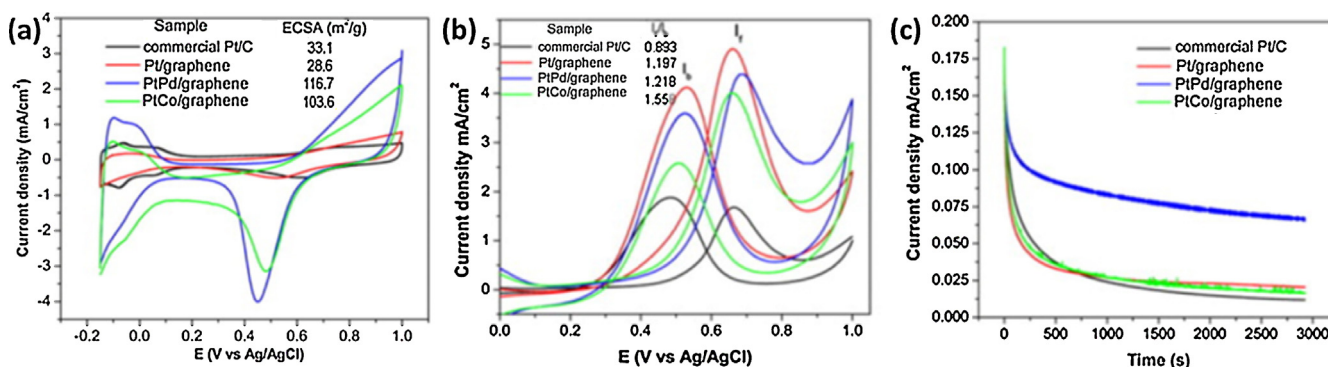


Fig. 35. CV cures of commercial Pt/C, Pt/graphene, PtPd/graphene and PtCo/graphene in (a) N_2 -saturated 0.5 M $HClO_4$ and (b) 0.5 M $CH_3OH/0.5$ M $HClO_4$ electrolytes at 50 mV/s, and (c) Chronoamperometric curves recorded at 0.65 V (vs Ag/AgCl) of electrocatalysts in 0.5 M $CH_3OH/0.5$ M $HClO_4$ electrolyte for 3000 s [994]. Copyright 2013 Elsevier Ltd.

tolerance to CO. ECSAs for Pt/chemically reduced GO hybrids can be significantly enhanced by thermal annealing as well [956].

Defect sites of reduced GO can serve as anchoring centers for the formation of catalyst NPs. However, these structural defects often weaken the intrinsic electronic transport of graphene and also cause graphene-supported catalysts to be unstable under harsh electrochemical conditions [991]. Chen et al. [992] used a 3D CVD-graphene as an electrode support for pulsed electrochemical deposition of Pt NPs. The electrochemically active area is 58% higher for Pt/3D-graphene than for Pt/CNF due to better dispersion of Pt on 3D-graphene. Pt/3D-graphene hybrids give a higher peak current density of the forward anodic peak (I_f , ~ 1.6 mA/cm²) than Pt/CNF (0.8 mA/cm²) and Pt/C catalysts (1.39 mA/cm²), suggesting that 3D-graphene can effectively promote electron transport and MOR. Meanwhile, the current density ratio (I_f/I_b) of I_f to the reverse anodic peak (I_b) was calculated to be 2.25 for Pt/3D-graphene. The value is much higher than those reported for Pt/CNF (0.8) and Pt/C catalysts (~ 1) reflecting a more complete oxidation of methanol to CO_2 during the reverse anodic scan and less accumulation of carbonaceous residues on the catalyst surface [993].

Recently, few-layer graphene sheets were produced by liquid-phase exfoliation of graphite in NMP, and monodisperse Pt and its alloy NPs (2–3 nm) were then deposited onto the surface by solvothermal reaction [994]. The resulting electrocatalysts in DMFCs show ECSAs varying as follows: PtPd/graphene (116.7 m²/g) > PtCo/graphene (103.6 m²/g) > Pt/C (33.9 m²/g) > Pt/graphene (28.6 m²/g) (Fig. 35a). The I_f values (Fig. 35b) of Pt/graphene, Pt–Pd/graphene and Pt–Co/graphene are 4.93, 4.39 and 4.01 mA/cm², respectively. These values are more than twice that of commercial Pt/C (1.68 mA/cm²). The calculated I_f/I_b values of Pt/graphene (1.197), Pt–Pd/graphene (1.128), and Pt–Co/graphene (1.558) are also higher than that of commercial Pt/C (0.893). By comparison, graphene-supported catalysts provide more effective electron transfer through the electrode surface and more active sites for electrochemical reaction. This leads to higher catalytic activity and higher efficiency oxidation of methanol to CO_2 . These results are attributed to the high conductivity of graphene, good dispersion of catalysts, strong graphene–catalyst interaction, easy accessibility of electrolyte ions, and excellent mass transport. Moreover, graphene-supported bimetallic catalysts exhibit larger values of ECSA, I_f/I_b , and I_f as well as excellent electrocatalytic durability (Fig. 35c). This also leads to better electrocatalytic performance compared to pure Pt catalysts [994]. One reason is that the electronic structure of Pt atoms is modified by Co or Pd resulting in a favorable Pt–Pt distance [995]. Another lies in the fact that Pd and Co are relatively oxophilic metals compared to individual Pt and therefore act as promoters for oxidative removal of CO on the Pt

shell by the available oxygen-containing species formed on the neighboring secondary metal particles [996–998]. This is beneficial for increasing the resistance to Pt catalyst poisoning by chemisorbed CO formed during MOR in DMFCs [951,999].

To date, a variety of non-Pt catalysts including Pd, [1000–1002] Fe, [1003–1005] Au, [967,968,1006] Ag, [1007–1010] Cu, [966] Co, [1011] Ni metals, [965] bimetallic catalysts such as Pt–Ru, [973,974,1012–1014] Pt–Au, [970,1015–1017] Pt–Sn, [1018] Pt–Fe, [1019] Pt–Ni, [1020–1024] Au–Pd, [1025,1026] Ag–Pd, [1027] Ni–Pd, [975] Ru–Co, [1028], and Ir–V [976] as well as ternary metal catalysts (e.g., Pt–Pd–Au [979,1029]) have been widely exploited in combination with graphene to improve their catalytic performance in fuel cells and reduce the use of Pt. Transition metal oxides are particularly attractive catalyst materials due to their abundance, low cost and low toxicity [1030]. Recently, graphene-supported oxides such as cobalt oxides, [981,1031–1034] manganese oxides [1035–1038], iron oxides, [982,1039] copper oxides, [1040], and multimetallic oxides, [983] have also proven to be efficient catalysts that exhibit comparable ORR activity, long catalytic stability, and better tolerance to methanol crossover and CO poisoning compared to commercial Pt/C catalysts [1041]. Moreover, the electrocatalytic performance of these metal or oxide catalysts can be further improved by using doped-graphene [961,981,1042–1046] or functionalized graphene [960,964,1047–1049] as catalyst supports due to the presence of abundant active sites for uniform dispersion of catalyst NPs and hence improved graphene–catalyst binding and ECSAs.

5.2. Electrolyte membranes

For fuel cells, proton and water transport take place in membranes (usually ~ 10 – 100 μm in thickness) during cell operation. It is essential to develop polymer electrolyte membranes (PEMs) with favorable properties including strong tolerance to catalyst and various intermediates as well as high chemical, thermal, and mechanical stability [1050,1051]. PEMs require low fuel permeability and high ionic/proton conductivity while preventing electron transport and fuel crossover between two electrodes. Current PEMs are mostly based on perfluorosulfonic polymers, the most prominent of which, Nafion, has a mechanically robust backbone of polytetrafluoroethylene, and sulfonic acid group charge sites for proton transport. However, Nafion-based PEMs are still limited due to high cost, low conductivity at low humidity and/or high temperature, methanol permeability, and mechanical instability at operating temperatures [939,1052]. Due to its high SSA, mechanical strength, chemical stability and barrier properties, electrically-insulating GO has attracted great interest in

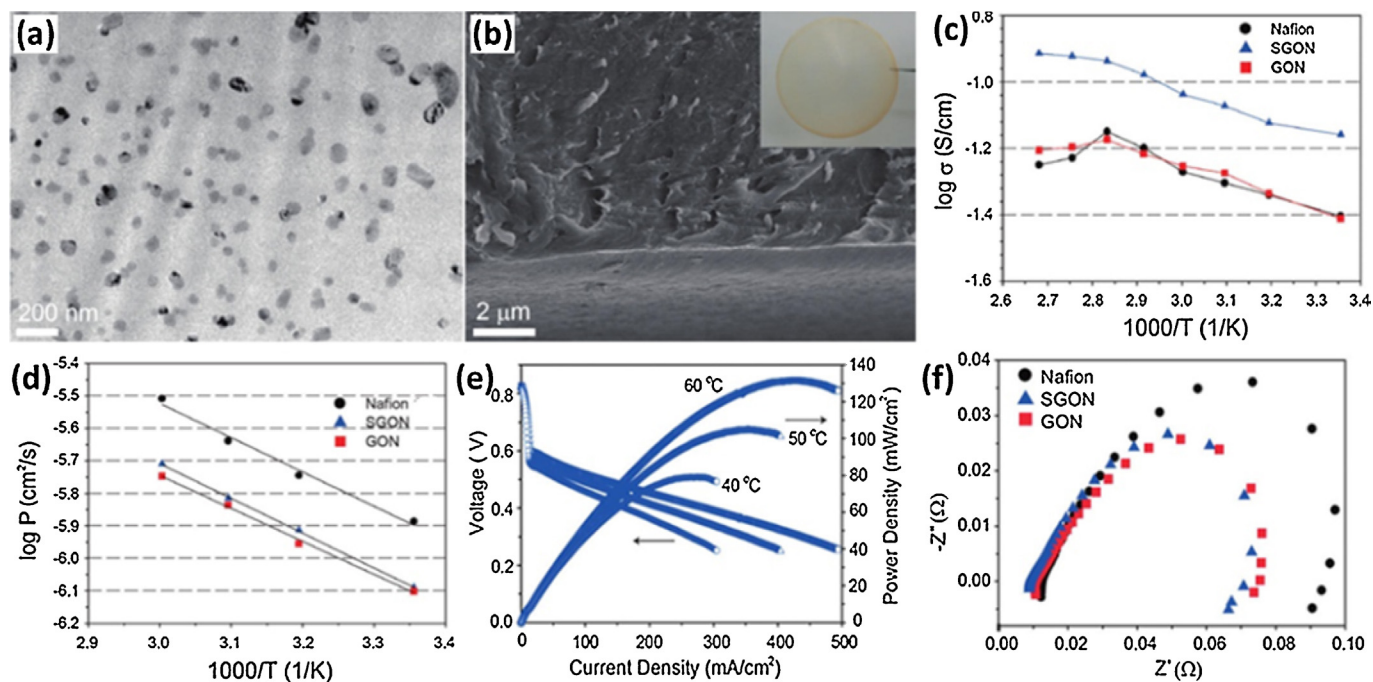


Fig. 36. Cross-sectional TEM (a), SEM (b) images and optical picture (inset) of SGON membrane. Proton conductivity (c) and methanol permeability (d) of Nafion, SGON, and GON membranes. (e) Polarization curves of DMFC single cells obtained from SGON membranes under operating temperatures of 40, 50, and 60 °C. (f) Nyquist impedance (Z) plots for Nafion, GO, and SGON membranes [1063]. Copyright 2011 American Chemical Society.

developing high-performance PEMs with improved mechanical and thermal stability, methanol crossover barrier, proton conductivity, and a wide temperature window [1053–1062].

In an early work reported by Hong et al. [1063] 0.5 wt% sulfonated GO (SGO) was mixed with Nafion in DMF followed by solution casting to obtain SGO/Nafion (SGON) composite membranes. The transport properties were then compared to those of pristine Nafion and 0.5 wt% GO/Nafion (GON) membranes. Due to good compatibility and strong interfacial interaction between SGO and Nafion, SGO sheets are well exfoliated, randomly dispersed, and also tightly held in the matrix (Fig. 36a and b). SGON membranes exhibit significantly enhanced proton conductivity over a wide temperature range (Fig. 36c), low activation energy for ionic conduction, high ion exchange capacity (0.97 eq/g) and reduced methanol permeability (Fig. 36d). This is predominantly due to the high water uptake (~95.4%) in nanochannels compared to Nafion (48.4%) and GON (71.1%) membranes. The excellent transport properties of SGON were further evaluated by a DMFC single cell under operating conditions of 1 M methanol at the anode side and for oxygen gas at the cathode side. For example at 60 °C operation temperature (Fig. 36e), the maximum power density of a SGON-based cell (132 mW/cm²) is higher than that of Nafion (101 mW/cm²) and GON-based cells (120 mW/cm²). Meanwhile, the cell resistance values are 13, 11, and 9 mΩ for Nafion, GON, and SGON membranes (Fig. 36f), respectively, indicating less electrolyte resistance in SGON as a consequence of chemical sulfonation improving proton transport.

A later study suggests that there exists an optimal ratio of SGO in SGON membranes [1064]. For a low SGO loading (0–1.0 wt%), the proton conductivity increases and methanol permeability decreases with increasing SGO content. Herein the uniformly-dispersed SGO sheets create more densely interconnected channels for proton transfer while blocking methanol from migrating through the membrane. With further loading (1.0–5.0 wt%), the aggregation of SGO sheets predominates throughout the matrix, thereby reducing the conductivity and barrier ability of SGON membranes. At the optimal loading of 0.05–0.5 wt%, SGON

membranes also show high methanol selectivity in conjunction with excellent transport properties and thus deserve to be implemented in DMFCs. The actual cells exhibit higher current and power densities, lower methanol crossover, and faster reaction kinetics compared to commercial Nafion membranes. Furthermore, the incorporation of SGO into PEMs leads to enhanced mechanical and thermal properties as well as improved tolerance to pressure during assembling the membrane electrode. It should be noted that during the fabrication of SGON membranes by a solution casting method, SGO sheets tended to preferentially form parallel to the film surface [1064,1065]. Nicotera et al. [1065] reported that these aligned SGON membranes show a significant blocking effect toward methanol crossover in the orthogonal direction due to an increase in the tortuosity of the pathway while maintaining high proton mobility even at high operating temperatures up to 130 °C. Electrochemical properties from a single DMFC also show a significant reduction in Ohmic loss and acceptable power density at high temperatures and therefore promise an extension of operating range of DMFCs toward high temperatures.

6. Graphene-based materials for solar cells

Solar cells or photovoltaic cells can convert solar energy directly into electrical energy by the photovoltaic effect. Such devices usually consist of active-layer materials sandwiched between an anode and a cathode one of which must be transparent to allow sunlight to pass through. Nowadays, the key to their commercial application lies in improving the power conversion efficiency (PCE) while lowering cost by developing high-performance active layer and electrode materials. With its unique structure and properties, graphene and its derivatives have been widely used as transparent electrodes, [1066–1071] and counter-electrodes, [1072] and also as active materials including light harvesting/acceptor layers, [1073–1075] charge transport layers, [21,23,1076–1080] Schottky junctions, [1081–1083] and intermediate layers for tandem SCs. Based on theoretical simulations, Tour and Yong [1084] claimed

that graphene-based organic photovoltaics have the potential for single-cell efficiencies exceeding 12% (and 24% in a stacked structure). This section will summarize recent advances of GBMs in PSCs, DSSCs, and PVSCs.

6.1. Graphene-based materials for polymer solar cells

Polymer solar cells (PSCs), also known as organic photovoltaic cells, have attracted great attention due to their light weight, relatively low cost, large-area manufacturing, and compatibility with flexible substrates [1085]. Currently, the most effective PSCs are fabricated by a bulk-heterojunction (BHJ) architecture using conjugated polymers as an electron donor and fullerene derivative [6,6]-phenyl C₆₁-butyric acid methyl ester (PCBM) as an electron acceptor [1086]. The state-of-the-art PSCs have achieved a PCE of 9.2% in a single BHJ device with an inverted structure, [1087] and are moving PCEs towards the goal threshold of 10% for commercial applications [1088]. The PCEs of PSCs are still lower than those of inorganic SCs [1089,1090]. In recent years, GBMs have demonstrated multiple improvements in the photovoltaic performance of PSCs [1066,1091–1095].

6.1.1. Electron-acceptor materials

Graphene's energy levels can be tuned by controlling its size and layers. It also exhibits improved electron transport properties and higher carrier mobility than fullerene derivatives [1096,1097]. Furthermore, high SSA and one-atom thickness 2D planar structure of graphene can provide a large donor-acceptor interface for fast charge separation and electron transfer. Graphene therefore is a competitive alternative to PCBM as an acceptor for PSCs. Cheng et al. [1073] presented the first fabrication of PSCs using phenyl-isocyanate functionalized graphene as the electron-acceptor and poly(3-octylthiophene) (P3OT) as the donor material, resulting in the best PCE (1.4%) for the devices with 5 wt% graphene. Similarly, the incorporation of graphene into poly(3-hexylthiophene) (P3HT) can induce a significant photoluminescence quenching for P3HT due to strong electron/energy transfer from P3HT to graphene [1098]. For devices with a configuration of ITO/PEDOT:PSS/P3HT:graphene/LiF/Al, the PCE increases first and then decreases with increasing graphene content. The device containing 10 wt% graphene shows the best performance with a PCE of 1.1%, an open-circuit voltage (V_{OC}) of 0.72 V, a short-circuit current density (J_{SC}) of 4.0 mA/cm², and a fill factor (FF) of 0.38 after thermal annealing at 160 °C for 10 min. The PCE is only 0.15% for the un-annealed device and only a moderate PCE (0.57%) for the device under annealing at 210 °C for 10 min. This indicates that in addition to graphene content, proper annealing conditions are also critical for the good device performance. Recently, 20 wt% functionalized-GO with phenyl-isothiocyanate (GO-PITC) was

used as the electron acceptor for an ITO/PEDOT:PSS/P3HT:GO-PITC/Al device to give a PCE of 1.02% [1099]. It seems that graphene exhibits inferior photovoltaic characteristics compared to fullerene derivatives when used as acceptor in the active layer [1100].

Gupta et al. [1101] used aniline-functionalized graphene quantum dots (ANI-GQDs) as the electron-acceptor to fabricate the device ITO/PEDOT:PSS/P3HT:ANI-GQDs/LiF/Al. The best performance is obtained from 1 wt% ANI-GQDs in the device with maximum values of PCE = 1.14%, V_{OC} = 0.61 V, J_{SC} = 3.51 mA/cm², and FF = 0.53 (Fig. 37a). PCE and FF values are much higher than 0.65% and 0.28 obtained from the optimized device with 10 wt% ANI-graphene sheets (ANI-GSs) in P3HT. For PSCs, photocurrent is mostly limited by photoinduced charge carrier generation and transport, thus the nanoscale morphology of active layer is an important factor for determining FF. Large domains (100–200 nm diameter) exist in the P3HT:ANI-GSs film (Fig. 37b) due to large-scale phase separation which are much larger than the diffusion length of excitons (10 nm). In comparison, uniform and fine features are seen in the AFM image of P3HT:ANI-GQDs film (Fig. 37c), suggesting nanoscale phase separation. This results in an enhancement of the exciton migration to the donor-acceptor interface and hence, a decrease in the resistance and a corresponding increase in FF. An electrochemical approach to green-luminescent GQDs (3–5 nm) was performed by Qu et al. using a filtration-formed graphene film as a working electrode [1102]. The as-prepared GQDs were then integrated into the ITO/PEDOT:PSS/P3HT:GQDs/Al device, giving a peak PCE of 1.28%. However, PCE values reported are still low, suggesting that graphene and its derivatives are still far from being used as an electron acceptor material in PSCs.

6.1.2. Charge transport layers

6.1.2.1. Hole transport layer (HTL). In PSCs, photon absorption by semiconducting polymers creates excitons (bound electron-hole pairs). Charge generation requires the dissociation of excitons at the donor-acceptor interface. However, in a pristine BHJ device, both donor and acceptor phases are in direct electrical contact with the anode and cathode, resulting in the recombination of carriers and current leakage. To minimize such detrimental effects and facilitate charge collection by the electrodes, PSCs often employ an electron blocking HTL between the transparent anode and active layer. The HTL should be a wide bandgap p-type material that has a proper work-function to ensure the Ohmic contact with the donor material without increasing the series resistance in devices [1103]. Semiconducting PEDOT:PSS is the most commonly used HTL in PSCs, but it has high acidity, hygroscopicity, and inhomogeneous electrical properties, resulting in the degradation of device performance and lifetime [1104]. Contrary to pristine

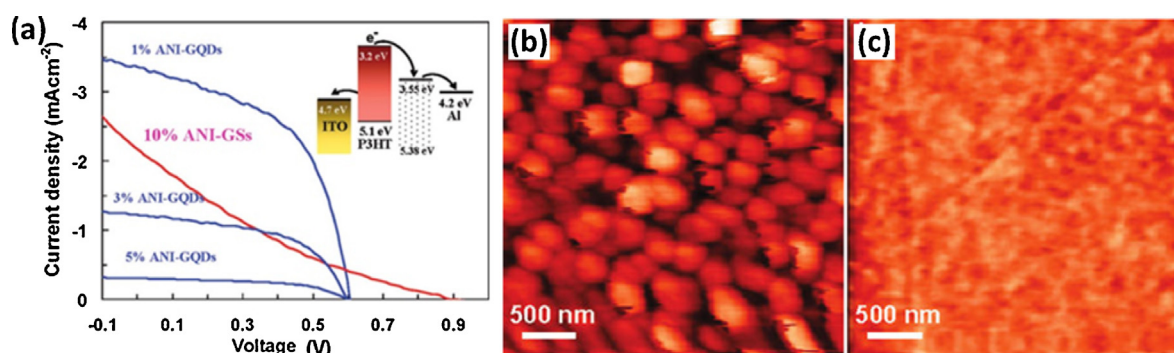


Fig. 37. (a) J - V characteristics of PSCs based on ANI-GQDs with different GQDs content and ANI-GSs annealed at 160 °C for 10 min. AFM images of (b) P3HT:ANI-GSs and (c) P3HT:ANI-GQDs films [1101]. Copyright 2011 American Chemical Society.

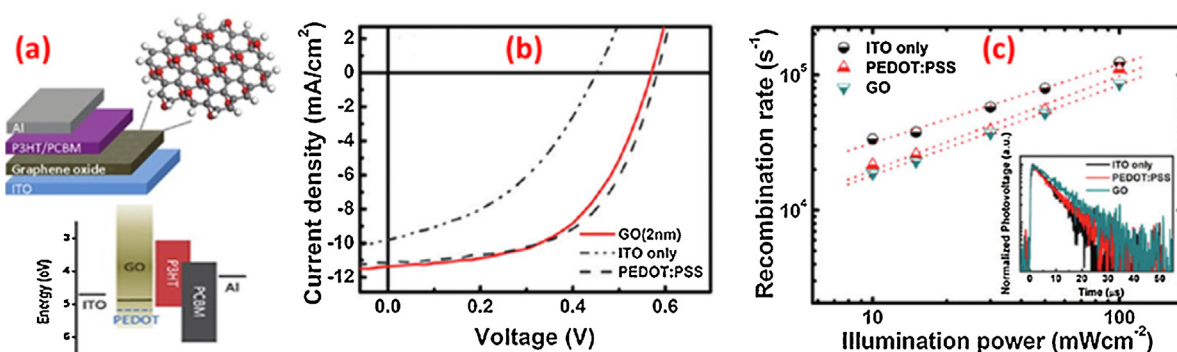


Fig. 38. (a) The device structure: ITO/GO/P3HT:PCBM/Al, and energy level diagrams, (b) Current-voltage characteristics of photovoltaic devices with no hole transport layer (curve labeled as ITO), with 30 nm PEDOT:PSS layer, and 2 nm thick GO film. (c) Charge recombination rate versus light intensities obtained using transient open-circuit voltage decay measurements for ITO-only, PEDOT:PSS, and 2 nm GO thin film devices. The inset shows the transient photovoltage decay curves of the corresponding devices [1107]. Copyright 2010 American Chemical Society.

graphene with highly efficient electron transport, GO and its derivatives showed high hole-transport capability in PSCs [21,1076,1105,1106]. Chen et al. [1107] demonstrated the use of GO thin films with large bandgap (~ 3.6 eV) and lateral resistivity in excess of $10^5 \Omega/\text{cm}$ as the HTL in the ITO/GO/P3HT:PCBM/Al device (see Fig. 38a). The ITO-only device exhibits a PCE of $1.8 \pm 0.2\%$ while the insertion of a 2 nm thick GO thin film between ITO and P3HT:PCBM shows substantial increases in V_{OC} , J_{SC} , and FF (Fig. 38b). This leads to an enhanced PCE ($3.5 \pm 0.3\%$) which is comparable to the PCE ($3.6 \pm 0.2\%$) of the device fabricated with PEDOT:PSS. Furthermore, the transient photovoltage decay lifetimes for ITO-only, PEDOT:PSS HTL, and GO HTL devices were found to be 8.1, 9.6, and 11.6 μs , respectively (Fig. 38c). The longer charge recombination lifetimes in GO indicate lower recombination rates. This suggests effective suppression of leakage current and separation of carriers via efficient transport of holes to ITO and blocking of electrons. A clear trend of decreasing PCE with increasing GO film thickness is observed. This is most likely due to the increase in serial resistance resulting in lower J_{SC} and FF and slightly lower film transmittance with thickness. Similar performance improvements and HTL thickness effects have been observed in the devices using *p*-toluenesulfonylhydrazide reduced GO [1108] and GQDs [1109] as the HTL materials.

6.1.2.2. Electron transport layer (ETL). The ETL between the cathode and active layer plays an important role in increasing the PCE with enhanced J_{SC} and FF due to improved charge transport and extraction [21,23]. ETL materials should have a proper work function to match the acceptor material to facilitate electron extraction and efficiently transport electrons to minimize series resistance in the device. Recently, Heeger et al. [1110] used a ~ 1 nm-thick GO film as the ETL. The active layer is composed of poly[*N*-9'-heptadecanyl-2,7-carbazole-alt-5,5-(4',7'-di-2-thienyl-2',1',3'-benzothiadiazole)] (PCDTBT) and [6,6]-phenyl C71-butyric acid methyl ester (PC71BM). The ITO/PEDOT:PSS/PCDTBT:PC71BM/GO/Al device shows values of PCE = 6.72% and $J_{SC} = 12.36 \text{ mA}/\text{cm}^2$ which are higher than the PCE = 5.35% and $J_{SC} = 10.36$ obtained for the same device without the GO layer. The improved J_{SC} and PCE are attributed to the efficient electron transport and extraction from the active layer to the Al cathode. Furthermore, the device with sequentially deposited GO and a TiO_x interlayer exhibits the highest PCE of 7.5% due to the synergistic effect of improved charge transport and enhanced optical field amplitude compared to devices with single coated TiO_x or GO. The GO ETL also improves device stability because it serves as an oxygen scavenger preventing degradation of the active layer in air. A RGO/fullerene composite was also used as the ETL for a PSC with

a PCE of 3.89%, which is higher than 3.39% of the control device without a ETL [1111].

6.1.2.3. Both HTL and ETL. Dai et al. [1112] reported that GO and Cesium-neutralized GO (GO-Cs, Fig. 39a) have bandgaps of 2.74 eV and 1.79 eV, respectively, and can be potentially used as hole- and electron-transport layers in the normal device ITO(anode)/GO/P3HT:PCBM/GO-Cs/Al (cathode) and the inverted device ITO(-cathode)/GO-Cs/P3HT:PCBM/GO/Al (anode) (Fig. 39b). As shown in Fig. 39c, the work function of GO (4.6–4.8 eV) matches both ITO and the HOMO level of P3HT to form an Ohmic contact with the active layer for efficient hole extraction. The work function of GO-Cs (3.9–4.1 eV) matches both the Al and the LUMO level of PCBM to form an Ohmic contact with the active layer for efficient electron extraction. Carboxyl groups on the periphery of GO can also dope P3HT at the interface to facilitate the Ohmic contact formation for effective hole extraction [1076,1113]. The normal device (Fig. 39d) shows better photovoltaic performance (PCE = 3.67%, $V_{OC} = 0.61$ V, $J_{SC} = 10.3 \text{ mA}/\text{cm}^2$, FF = 0.59) than that of the reference device (PCE = 3.15%, $V_{OC} = 0.61$ V, $J_{SC} = 9.67 \text{ mA}/\text{cm}^2$, FF = 0.52) with PEDOT:PSS and LiF as interlayers. Based on the *J*-*V* curve (Fig. 39e), the inverted device gives a PCE of 2.97% which is much higher than that of the control inverted device (1.2%) using Cs_2CO_3 and PEDOT:PSS as electron- and hole-extraction layers, respectively. The relatively weak light absorption characteristic of GO and GO-Cs, together with good solution-processability for forming ultrathin film (~ 2 nm), facilitates light transmission to the active layer. Furthermore, the high external quantum efficiency (68%) for the normal and inverted devices implies that the charge-extraction performance of GO and GO-Cs is independent of the electrode materials. These results clearly suggest that GO and GO-Cs can work very well in a single device and their charge-extraction performance is comparable to those of the state-of-art interface materials currently used in BHJ solar cells. Therefore, graphene derivatives seem to be versatile hole-/electron-transport materials for various BHJ SCs.

6.1.3. Intermediate layers for tandem cells

For PSCs, one of current limitations lies in the narrow absorption window compared to solar cells with inorganic semiconductors as photoactive materials. To utilize solar radiation effectively, an alternative approach is to stack high- and low-bandgap materials with complementary absorption spectra to fabricate tandem/multijunction cells [1114–1117]. By interconnecting a front subcell (using high-bandgap materials) with a rear subcell (using low-bandgap materials) by an intermediate layer either in series or in parallel fashion; V_{OC} or J_{SC} can be, in principle,

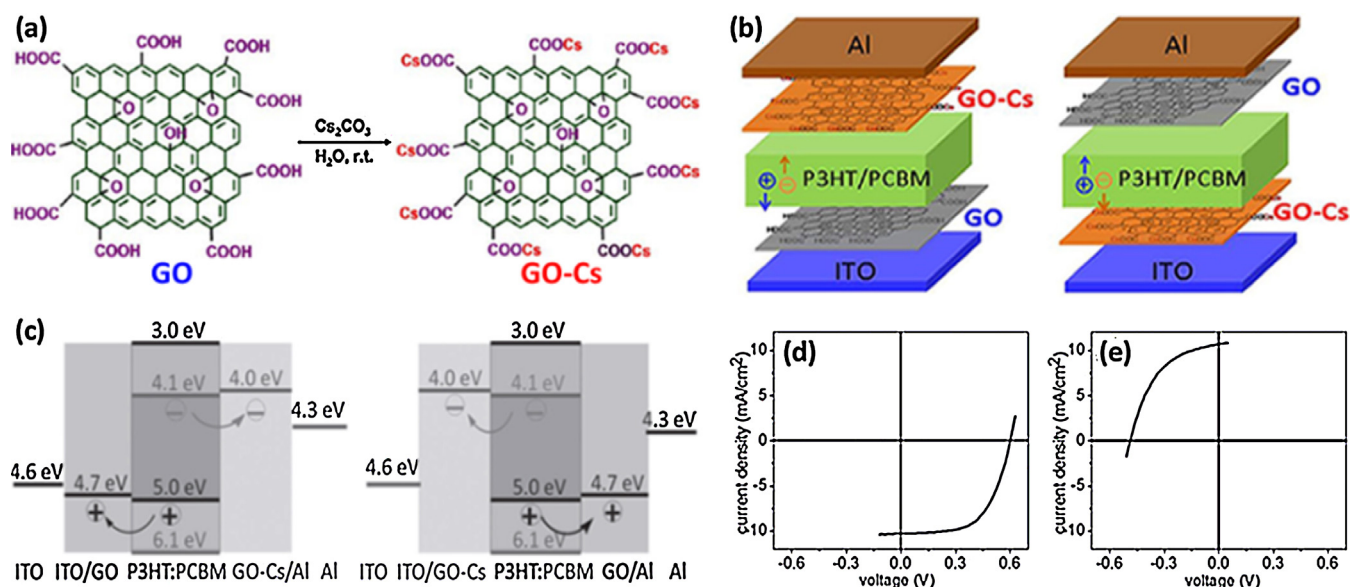


Fig. 39. (a) Schematic structure and synthetic route to GO-Cs, (b) device configurations and (c) energy level diagrams of the normal device (left) and inverted device (right) with GO as the hole-extraction layer and GO-Cs as the electron-extraction layer, and J - V curves of (d) the normal device and (e) the inverted device [1112]. Copyright 2012 Wiley-Vch.

doubled [1118]. High PCEs beyond 10% were recently achieved for tandem PSCs [1119]. In general, an efficient intermediate layer requires high conductivity, high transparency, low surface roughness, and high mechanical and chemical stability. The intermediate layer must serve as a strong physical boundary to prevent intermixing of the two subcells.

Graphene films meet most of the criteria needed in an intermediate layer and are also readily transferred to a wide range of substrates. As a proof of concept, Loh et al. [1120] used the CVD-grown graphene film as an intermediate layer to fabricate series and parallel connected tandem devices (Fig. 40a). Two BHJ layers include P3HT:PCBM as the active layer 1 (bottom cell) and zinc phthalocyanine:fullerene ($\text{ZnPc}:\text{C}_{60}$) as the active layer 2 (top cell). In the case of series connected cells, graphene serves as a recombination center for extracting both electrons and holes from bottom cell and top cell, respectively. Of note, low work function modification of graphene (4.2 eV) is only favorable for electron extraction. Graphene coated by MoO_3 with a high work function (6.76 eV) can increase the work function to 5.5 eV (Fig. 40b and c). As a consequence, using MoO_3 -modified graphene as the

intermediate layer, high V_{OC} (1 V) and J_{SC} ($11.6 \text{ mA}/\text{cm}^2$) values are achieved for series- and parallel-connected tandem devices, respectively. These are much higher than the V_{OC} (0.58 V) and J_{SC} ($7.6 \text{ mA}/\text{cm}^2$) of single cells. As expected, graphene can effectively join subcells to multiply V_{OC} and J_{SC} . The overall PCE of series-connected tandem cell is 2.3%, and the parallel-connected tandem cell gives a PCE of 2.9% which is close to the sum (3.3%) of the two subcells.

Huang et al. [1121] used a transparent GO/PEDOT composite gel as a sticky intermediate layer (Fig. 41a) to construct solution-processed tandem PSCs through direct adhesive lamination. As shown in Fig. 41b, the V_{OC} of the tandem cell is 0.94 V and reaches 84% of the V_{OC} sum of individual front and rear subcells (0.59 V and 0.53 V, respectively) due to good connection between the two subcells. The overall PCE of the tandem cell is 4.14%, which is higher than that of either individual subcell (2.92% and 3.75%, respectively). However, the reference device using PEDOT:PSS as an interconnect shows a lower V_{OC} and PCE than single-layer devices due to the inefficient separation between the two subcells. This essentially leads to convert the tandem device into a single

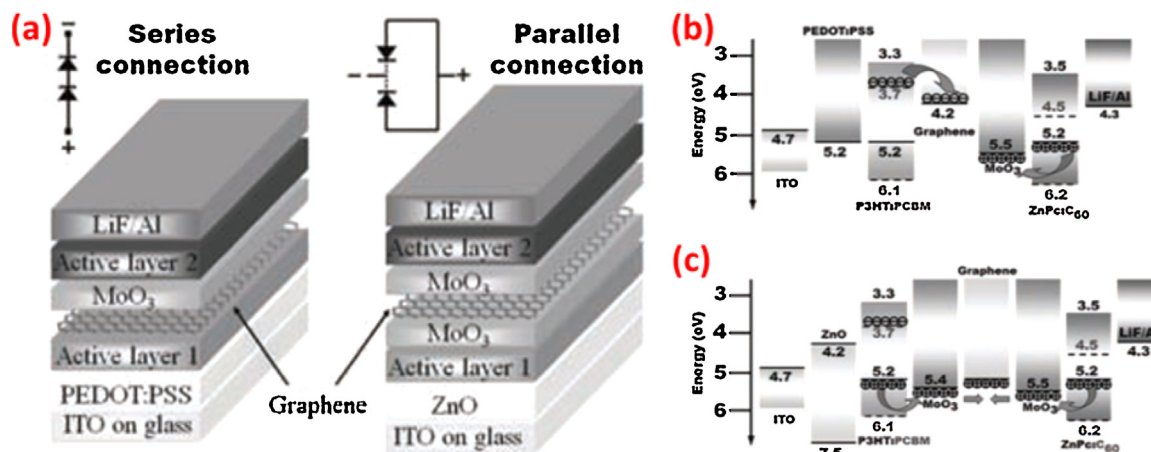


Fig. 40. Schematic diagram of device configurations (a), and energy level diagrams of tandem cells connected in series (b) and in parallel (c) fashions, respectively [1120]. Copyright 2011 Wiley-Vch.

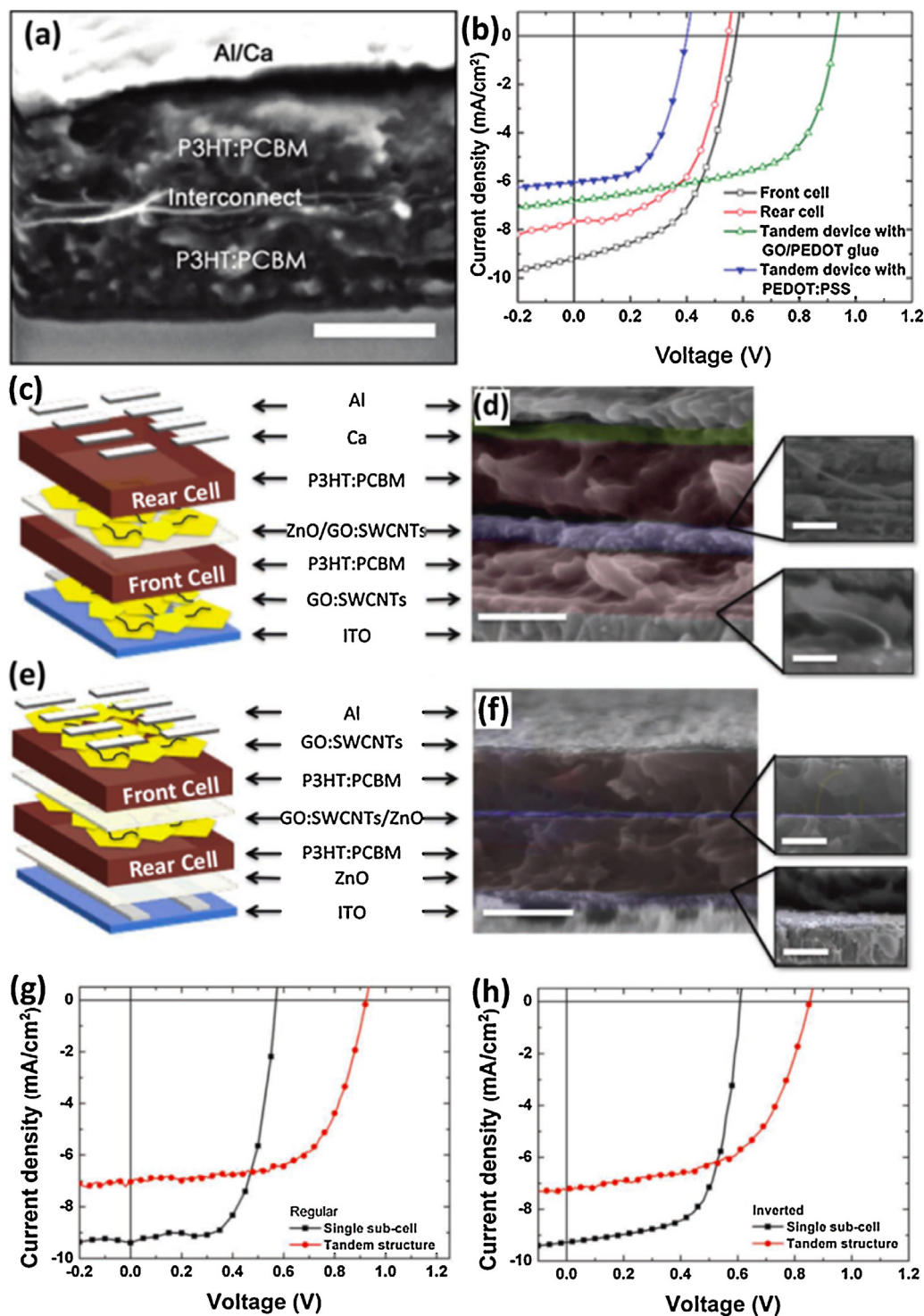


Fig. 41. (a) Cross-sectional SEM image of a tandem device using GO/PEDOT as the intermediate layer. Scale bar: 150 nm, and (b) J - V characteristics of separately-prepared front cells (black) and rear cells (red) along with tandem cells laminated with PEDOT:PSS only (blue) and GO/PEDOT gel (green), respectively [1121]. (c) A normal tandem cell configuration and (d) corresponding false-colored cross-sectional SEM image showing the layers in the tandem device using GO:SWCNTs as the intermediate layer. Scale bars are 200 nm (main) and 50 nm (insets). (e) An inverted tandem device configuration and (f) corresponding cross-sectional SEM images. Scale bars are 200 nm (main) and 50 nm (insets). (g) J - V characteristics of single subcell (black) and a normal tandem cell (red). (h) J - V characteristics of single subcell (black) and an inverted tandem cell (red) [1122]. Copyright: 2011 American Chemical Society and 2012 Wiley-Vch (For interpretation of the references to color in this figure legend, the reader is referred to the web version of this article.).

thickened device with much higher internal resistance. In contrast, GO's good barrier properties make it favorable for preventing intermixing in solution-processed tandem cells. Water-processable GO:SWCNT (1:0.2 in weight) thin films are also used as an effective intermediate layer to serially connect two BHJ SCs in both

normal (Fig. 41c and d) and inverted configurations (Fig. 41e and f) by all-solution processing routes [1122]. As shown in Fig. 41g, V_{OC} and PCE values for typical single-layer cells are calculated to be 0.56 V, and 3.41%, respectively. These are increased to 0.94 V and 4.10% for the normal tandem cell configuration. For the inverted

devices (Fig. 41h), V_{OC} and PCE values for subcells are calculated to be 0.83 V, and 2.90%, which are increased to 0.83 V, and 3.50% for their tandem cells, respectively. Both normal and inverted tandem cells produce significantly increased V_{OC} s, reaching 84% and 80% of the V_{OC} sum of subcells, respectively. These results clearly suggest that GO:SWCNTs thin films can serve as good mechanical separator and electrical interconnect between the two subcells.

6.1.4. Transparent conducting electrodes

Transparent conducting electrodes (TCEs) are an essential part of optoelectronic devices. Currently, TCEs based on n-type semiconductive ITO are used in PSCs and set the industrial standard with >80% transmittance (T) at 550 nm, R_S of 5–400 Ω/sq (Ohms per square), and a favorable work function (4.2–5.3 eV) [1123–1125]. However, ITO faces several serious issues including high production cost, limited reserves of indium, intrinsic brittleness and instability under acidic and basic environments [1093]. With high conductivity, transparency, excellent charge mobility, mechanical flexibility, and low cost, graphene transparent films can be considered as one of the most promising transparent electrode materials for replacing ITO [231,1093,1126–1128].

In general, T values of graphene films are inversely proportional to their thicknesses. For example, thermal polymerization of super phenylene derivatives can produce graphene films with thicknesses of 30, 22, 12, and 4 nm, which correspond to transmittances of 55, 66, 80, and 90%, respectively, at 500 nm [1129]. In the case of micromechanically-exfoliated [87] and CVD-grown graphene films, [356,1130] the T values linearly decrease with increasing layer number. For instance, CVD graphene films with 1, 2, 3, and 4 layers have transmittances of 97.4, 95.1, 92.9, and 90.1% at 550 nm, respectively [86]. However, compared to the exfoliated and CVD graphene films, graphene synthesized by aromatic molecules and GO-derived graphene films exhibit higher T values at the same layer of graphene and film thickness due to the presence of topological defects favorable for light transmission [1129,1131]. Moreover, thicker films of graphene have higher electron conductivities and lower R_S . In this scenario, Dai et al. [242] fabricated graphene films by assembly of liquid-exfoliated graphene sheets on quartz in a layer-by-layer manner, and found that the one-, two- and three-layer LB films afford R_S values of ~ 150 , 20 and 8 k Ω and transparencies of ~ 93 , 88, and 83% at 1000 nm, respectively. The enhancement of electron conductivity achieves low R_S at the cost of T for a TCE. An optimal balance between T and R_S is therefore required for graphene films.

The dependence of R_S on T for a given TCE can be expressed as $T = [1 + (Z_0/2R_S)(\sigma_{op}/\sigma_{dc})]^{-2}$, where Z_0 , σ_{op} and σ_{dc} are the free-space impedance (377 Ω), optical conductivity, and bidimensional d.c. conductivity of thin films [20,1132,1133]. R_S is linked to σ_{dc} by $R_S = (\sigma_{dc}N)^{-1}$ where N is the film thickness. The relationship between T and R_S seems to be controlled by the ratio of σ_{dc}/σ_{op} , which can be considered as a figure of merit (FOM) for TCEs since high values of σ_{dc}/σ_{op} endow them with desirable high T and low R_S [1134,1135]. Moreover the T and R_S of graphene films and consequently σ_{dc}/σ_{op} , are highly dependent on their crystal quality and film quality which are closely related to both the graphene source and fabrication methods. The fabrication of graphene films can be technically classified into dry (graphene grown on a substrate and subsequent transfer) [1136–1139] and wet/solution processing methods (spray depositing, [1140] dipping, [232] spin casting, [222] and vacuum filtration, [281,350], and LBL assembly [242]). In order to achieve the commercial target of $T \geq 90\%$ and $R_S \leq 100 \Omega/\text{sq}$, a FOM of $\sigma_{dc}/\sigma_{op} \geq 35$ is suggested for a TCE. From data published previously, graphene films made by CVD exhibit the best performance with σ_{dc}/σ_{op} of 4–11 while liquid-exfoliated graphene, chemically-synthesized graphene, and GO-derived graphene films show poorer quality and performance with much

lower σ_{dc}/σ_{op} ratios (usually <1) [1141] due to the presence of intrinsic defects, inter-sheet junctions and tunneling barriers in the solution-processed films. Currently, the σ_{dc}/σ_{op} of graphene TCEs appears to be much lower than the target FOM of 35. However, note that the above expression is appropriate for a bulk-like film (i.e., σ_{dc} is invariant with the film thickness). That is, this FOM is not always appropriate, particularly in the high T regime, due to the percolation behavior with characteristic of sparse networks with limited connectivity and few continuous conductive paths [1135,1142,1143].

In addition, the σ_{dc}/σ_{op} is suggested to be primarily controlled by σ_{dc} , where σ_{dc} can be rewritten as $\sigma_{dc} = n\mu e$, in which n , μ , and e are the carrier density, carrier mobility, and elementary charge, respectively [82]. A high σ_{dc} enables graphene films to have low R_S (high conductance) and high T simultaneously. There are two ways to enhance σ_{dc} by increasing either n or μ [1126]. Note that for multilayer graphene, n and μ are in the order of magnitude of $10^4 \text{ cm}^2/\text{V s}$ and $10^{12} \text{ cm}^2/\text{V s}$, respectively [18]. It is possible to achieve $\sigma_{dc}/\sigma_{op} \geq 35$ if graphene films have a level consistent with $n\mu > 1.3 \times 10^{16}/\text{V s}$ [1141]. As reported, both chemical doping [1144,1145] and substrate-induced doping [1146,1147] can effectively enhance the electrical properties of graphene films and give $n\mu$ values close to $10^{17}/\text{V s}$. This means that the σ_{dc}/σ_{op} of graphene films can be close to or even higher than the FOM of 35. Coleman et al. [1141] predicted that substrate-induced doping of graphene can result in a potential σ_{dc}/σ_{op} up to 330, i.e., $T \approx 91\%$ and $R_S = 11 \Omega/\text{sq}$, which is more than sufficient for industrial application of TCEs. Experimentally, Novoselov et al. [140] reported the use of a layer of PVA to induce n-type doping, resulting in the formation of micromechanically-exfoliated graphene films with $\mu \approx 3 \times 10^{12} \text{ cm}^2/\text{V s}$, $T \approx 98\%$ and $R_S = 400 \Omega/\text{sq}$. Using HNO_3 -treated CVD-graphene, Ahn et al. [86] achieved a p-doped film with R_S as low as $30 \Omega/\text{sq}$ at $T \approx 90\%$; comparable to commercial ITO. These results clearly show that TCEs derived from graphene, in combination with subsequent doping, could potentially outperform ITO in solar cell applications.

PSCs with graphene TCEs has been carried out in recent years as summarized in Table 7. It can be clearly seen that an optimal balance between R_S and T , i.e., σ_{dc}/σ_{op} , is crucial to achieve a high PCE for a PSC. The CVD-grown graphene thin films, with much better quality and higher electrical conductivity compared to both reduced GO and chemically-synthesized graphene films, usually allow their TCE-based PSCs to exhibit larger PCEs. However, CVD growth of other multicomponent layered materials is less matched to subsequent device application and often needs further transfer. TCEs derived from RGO films can be easily deposited on the desirable substrates by solution processing; which is inexpensive, reproducible high throughput manner and highly-compatible with existing roll-to-roll transfer processing [222,281,1148–1150]. The large-scale production of highly conducting films from RGO remains elusive. But current results can fulfill basic requirements for some optoelectronic devices such as touch screens, flat panel displays, and LEDs. It should be pointed out that a TCE is only one component in a PSC. The design, fabrication, and integration of practical devices also play crucial roles in realizing high-performance. Therefore, there is still potential for performance enhancements by perfecting the quality of graphene and its thin films [242,350,356,1130,1151,1152] and optimizing the choice of both active layer and transport layer materials and the fabrication process of devices [1153,1154].

6.2. Graphene-based materials for dye-sensitized solar cells

DSSCs pioneered by Grätzel, [1169,1170] have been considered as an attractive potential substitute for traditional silicon-based cells due to their respectable PCEs (over 10%), low production cost,

Table 7

Graphene-based TCEs used in PSCs and their photovoltaic performances.

Graphene-based TCEs			Cell configuration	Cell performance				Refs
Graphene source	R_s (Ω /sq)	T (%)		J_{sc} (mA/cm ²)	V_{oc} (V)	FF	PCE (%)	
CVD-grown graphene								
Ni catalyst;	210–1350	72–91	Graphene/PEDOT:PSS/	2.39	0.32	0.27	0.21	[1155]
PDMS-assisted transfer			P3HT:PCBM/LiF/Al					
Treated by UV				5.56	0.55	0.243	0.74	
Modified by PBASE				6.05	0.55	0.513	1.71 (3.10) ^a	
Cu catalyst PMMA-assisted transfer	250	92	Graphene/PEDOT:PSS/	4.43	0.53	0.36	0.85	[1156]
			CuPc/C ₆₀ /BCP/Ag					
	374	84.2	Graphene/PEDOT:PSS/	6.906	0.521	0.326	1.17 (3.43) ^a	[1157]
			P3HT:PCBM/Ca:Al					
	3.5 k	89	PET/Graphene/PEDOT/	4.73	0.48	0.52	1.18 (1.27) ^a	[1158]
			CuPc/C ₆₀ /BCP/Al					
	80	90	Graphene/MoO ₃ + PEDOT:	7–8	0.59	0.45–0.51	2.50 (3.0) ^a	[1154]
			PSS/P3HT:PCBM/LiF/Al					
	1.2 k	96	Au/Gra/Al-TiO ₂ /P3HT:	8.55	0.60	0.501	2.58 (3.45) ^a	[1159]
			PCBM/MoO ₃ /Ag (inverted)					
			Graphene/P3HT/Si nanowire	35.1	0.48	0.59	9.94	[1160]
Cu catalyst; thermal releasing			ITO/ZnO/P3HT:PCBM/	10.5	0.54	0.44	2.5	[1161]
tape-assisted transfer			GO/Graphene (inverted type)					
Cu catalyst; TCNQ-graphene	278	92.2	Graphene/PEDOT:	8.90	0.57	0.48	2.58 (4.1) ^a	[1153]
stacked films			PSS/P3HT:PCBM/Ca/Al					
Ni catalyst; etching followed	~606	~87	Graphene/PEDOT:	9.03	0.60	0.48	2.60 (3.80) ^a	[1162]
by scooping			PSS/P3HT:PCBM/TiO _x /Al					
Cu catalyst Roll-to-roll transfer	400		Graphene/PEDOT:	10.19	0.62	0.2525	3.98 (3.86) ^a	[1163]
			PSS/P3HT:PCBM/Al					
			Graphene/P3HT/Si nanohole	37.81	0.48	0.57	10.34	
Reduced GO								
Hydrazine vapor and	17.9 k	69	Graphene/PEDOT:	1.18	0.46	0.25	0.13 (3.59) ^a	[1164]
annealing/700 °C			PSS/P3HT:PCBM/LiF/Al					
Hydrazine vapor and	420	61.2	Graphene/ZnO/P3HT/			0.33	0.31	[1165]
annealing/1100 °C			PEDOT:PSS/Au					
Thermal annealing/1000 °C	16.0 k	88	PET/Graphene/PEDOT:	1.74	0.557	0.30	0.28	[1166]
			PSS/P3HT:PCBM/TiO ₂ /Al					
	6.6 k	78		3.31	0.560	0.31	0.61	
	3.2 k	65		4.39	0.561	0.32	0.78	
	1.6 k	55		4.24	0.557	0.32	0.77	
Thermal annealing/900 °C	401	21	Graphene/PEDOT:	2.97	0.50	0.57	0.86	[1167]
			PSS/P3HT:PCBM/LiF/Al					
	486	38		3.50	0.52	0.54	0.99	
	512	46		5.66	0.54	0.55	1.66	
	600	55		6.35	0.54	0.58	2.04 (3.00) ^a	
	750	65		2.39	0.52	0.34	0.41	
Hydrazine-reduced GO:SWCNTs	240	86	Graphene:CNTs/PEDOT:	3.47	0.583	0.421	0.85	[794]
			PSS/P3HT:PCBM/Ca:Al					
Chemically-synthesized graphene								
Superphenalene pyrolysis/1100 °C	18 k	85	Graphene/P3HT:PCBM/Ag	0.36	0.38	0.25	0.29 (1.17) ^a	[1129]
Camphor pyrolysis/900 °C	1.645 k	81	Graphene/PEDOT:	4.82	0.54	0.26	0.68 (1.21) ^a	[1168]
			PSS/P3HT:PCBM/Al					

^a The PCE of the control cell using TiO₂; TCNQ: tetracyanoquinodimethane; PBASE: pyrene buanoic acid succidymidyl ester.

and easy fabrication [1171]. A typical DSSC device (see Fig. 42a) consists of a dye-sensitized mesoporous semiconductor (usually TiO₂) scaffold on a transparent electrode (usually fluorine doped tin oxide, FTO) as the photoanode, a hole-conducting electrolyte containing the redox couple (usually iodide/triiodide, I^-/I_3^-), and a catalytic counter-electrode (or cathode, usually platinized FTO) [1172]. For DSSCs which use redox mediators for charge transport, the photon-induced oxidation of dye occurs at the photoanode, while the reduction of redox species used to regenerate the dye occurs at the counter-electrode [1173]. DSSCs therefore require relatively large over-potentials to drive electron injection to TiO₂ and regenerate the oxidized dye. With unique structure-dependent properties, GBMs have been incorporated into each component of DSSCs and have served as multifunctional roles (Fig. 42b) [1174].

6.2.1. Counter-electrodes

The counter-electrode (cathode) plays a key role in DSSCs and should be highly conductive and highly catalytic to ensure rapid

redox pair formation after electron injection. The most commonly used counter-electrode is based on a thin film (1–5 nm) of Pt deposited on an FTO or ITO substrate. However, Pt is expensive and also degrades over time while in contact with an iodide/triiodide liquid electrolyte. As an alternative, graphene-based counter-electrodes (GCEs) have been extensively investigated over the past years [1175].

6.2.1.1. RGO as GCEs. Shi et al. [160] reported for the first time FTO-supported N₂H₄·H₂O-reduced GO film (200 S/m in conductivity) as a GCE in DSSCs showing a much higher PCE of 2.2% compared to FTO-only DSSC (0.048%) but poorer than Pt-based DSSC (3.98%). Jeon et al. [1176] found that the PCE of DSSCs with GCEs based on electrophoretically-deposited GO thin films increases with reduction temperature (200–600 °C) while the R_{CT} between the electrolyte and electrode decreases due to the increased conductivity and charge transport ability [1177]. The highest PCE of 5.69% and the lowest R_{CT} of 38 Ω are achieved on a DSSC with GCE annealed at 600 °C. Huang et al. [1178] found that champion values

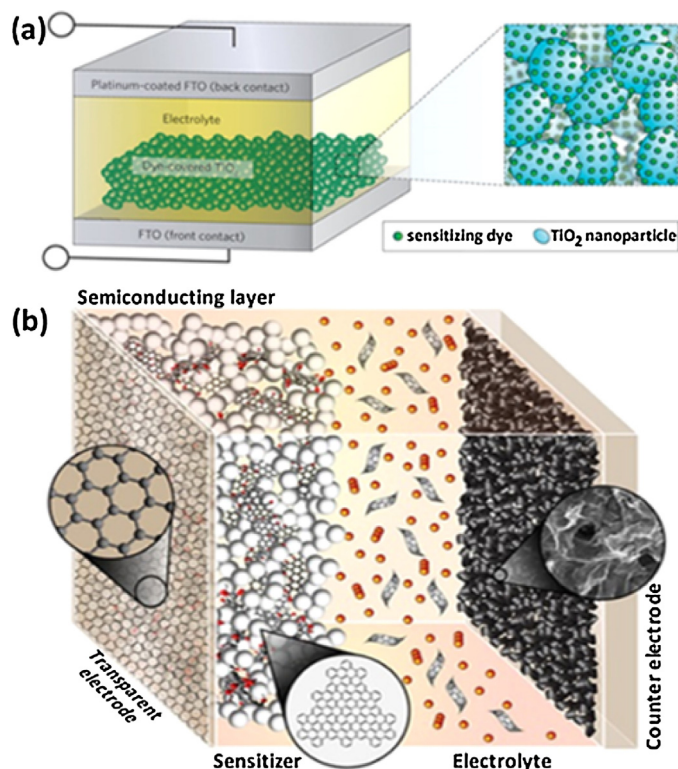


Fig. 42. (a) Schematic configuration of a typical DSSC device [1172]. Copyright 2012 Macmillan Publishers Limited. (b) Schematic of a DSSC incorporating graphene in each part [1174]. Copyright 2014 American Chemical Society.

of PCE (6.81%) and R_{CT} ($1.2 \Omega \text{ cm}^2$) for a DSSC are based on thermally-reduced GO films annealed at 400°C rather than at 450°C . Generally, thermal annealing of GO at high temperature can remove functional groups from GO to restore its π -conjugated structure. This leads to an increased conductivity which can facilitate charge transport [225]. The residual oxygen-containing functional groups and suitable defective structures can serve as active sites responsible for catalytic performance [1179]. Low R_{CT} values account for the enhanced reduction of triiodide ions at the interface between the electrode and electrolyte which increases the availability of I^- ions at the dye-electrolyte interface. This also enables the suppression of charge recombination in the photoanode leading to increases in both V_{OC} and PCE [1180]. However, reduced GO materials are usually limited by their low conductivity due to the presence of defects [1181,1182]. Pristine graphene is

also not an optimal candidate for GCEs due to the lack of active sites available for electrocatalysis [1183–1185].

6.2.1.2. 3D Graphene as GCEs. Performance improvements can be made on GCEs by tailoring their microstructures and architectures [1184,1186–1190]. Vertically oriented graphene (VOG) films (Fig. 43a) with graphene sheets perpendicular to the substrate were recently prepared by Zhu et al. using plasma-enhanced CVD with methane and nitrogen as source gases [1191]. As modelled in Fig. 43b, VOG electrodes provide rapid electron-transfer kinetics and high electrocatalytic activity toward the I^-/I_3^- redox couple due to the fully exposed active edges. Using VOG as a GCE, the corresponding DSSC gives a PCE of 7.63%; slightly lower than the PCE of 8.48% for the Pt-based cell. Hu et al. [1192] used a bottom-up method to produce 3D honeycomb-structured graphene through thermal reaction between Li_2O and CO at 550°C for different reaction times. The longer reaction time, the higher the R_{CT} and hence, the PCEs for graphene-based DSSCs are lower. The best materials made at 550°C for 12 h exhibit low resistance ($R_S = 24 \Omega$), low R_{CT} (20Ω) and excellent catalytic performance for their counter-electrodes. The highest PCE is 7.8% which is comparable to 8.0% for the Pt-based DSSC. The observed performance is attributed to the formation of a 3D conductive network that provides large SSA and porosity for improved electrolyte-electrode interaction and electrolyte/reactant diffusion. 3D porous GCEs have thus been proposed to have better performance in DSSCs compared to common bulk and film materials [1193,1194].

6.2.1.3. Graphene hybrids as GCEs. Impressive performance improvements have also been made in GCEs by combining them with metals (Pt [1195–1201] and Au [1202]), metal compounds (NiO, [1203,1204] ZnO, [1205] CoS, [1206,1207] CoS₂, [1208] MoS₂, [1209] NiS, [1210] Bi₂S₃, [1211,1212] Ni₁₂P₅, [1213] and Mn₃O₄ [1214]), carbonaceous materials (CNTs, [1215–1219] carbon black, [1220] mesoporous carbon, [1221] and activated carbon [1222]) conducting polymers (PPY, [1223,1224] PANI, [1225–1231] PEDOT, [1232,1233], and Nafion [1234]), and multiple components [1235–1237]. The above work aims at developing GCEs with high catalytic activity, low R_{CT} , large accessible SSA, and low cost in order to compete with Pt electrode. For instance, Choi et al. [1196] presented a dry-plasma reduction process to uniformly hybridize Pt NPs (0.5–4 nm) onto graphene (Fig. 44a) through co-reduction of Pt precursors and GO. The DSSC-based on Pt/graphene has a higher PCE of 8.56% and a lower R_{CT} of $0.61 \Omega \text{ cm}^2$ compared to DSSCs with GO-only (4.48%, $12.19 \Omega \text{ cm}^2$) and Pt-sputtered electrode (8.18%, $1.22 \Omega \text{ cm}^2$). Xu et al. [1238] reported on a thin

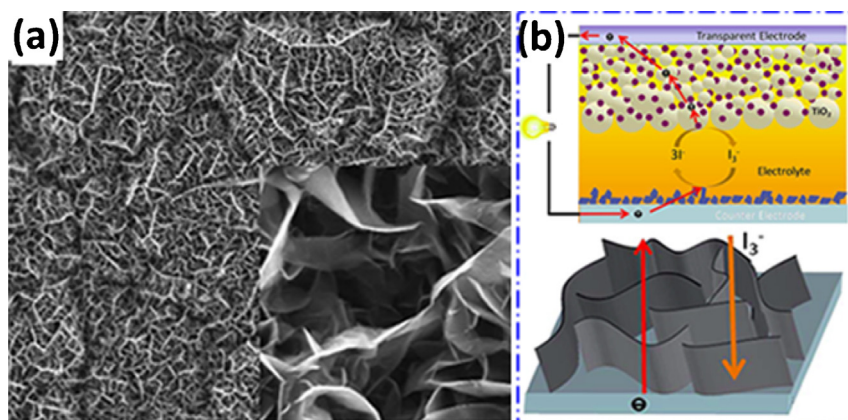


Fig. 43. SEM image of (a) vertically oriented graphene (VOG) and (b) a schematic showing VOG-based counter-electrodes with fast charge transfer [1191]. Copyright 2014 Royal Society of Chemistry.

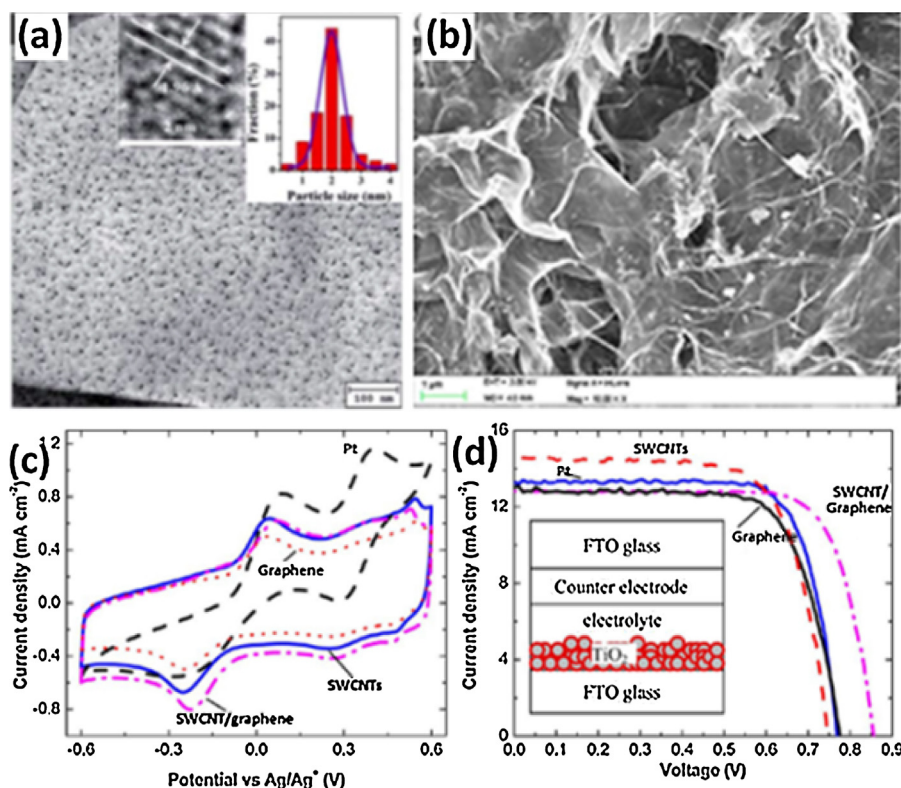


Fig. 44. TEM images of (a) Pt/graphene [1196]. Copyright 2013 Royal Society of Chemistry. (b) SEM image of SWCNT/graphene composites, (c) CV curves of I^-/I_3^- with different working electrodes, and (d) J - V characteristics of DSSCs with different materials as counter-electrodes [1241]. The inset in (d) shows the device structure. Copyright 2013 American Chemical Society.

film GCE using LBL assembly of GO and PDDA followed by electrochemical reduction. The device achieves a high PCE of 9.5%, which is slightly higher than 9.14% for the Pt-based cells. Yin et al. [1239] reported an electrochemical process to fabricate PPY/graphene porous composites as a GCE with excellent activity toward triiodide reduction. The PPY/graphene-based cell gives a comparable PCE (6.45%), but higher R_{CT} (80.07 Ω) compared to the thermally deposited Pt-based device (7.14%, 46.68 Ω). GQD-doped PPY films were also explored as GCEs [1240]. The performance in DSSCs achieves the highest PCE (5.27%) which is $\sim 20\%$ higher than that of the PPY-based cell (4.46%) and comparable to that of Pt-based devices (6.02%). The performance improvements mainly originate from large interfacial active sites and hybrid effects.

Recently, Ouyang et al. [1241] found that the incorporation of 20 wt% SWCNTs into graphene produces composite electrodes (Fig. 44b) that outperform individual Pt, graphene and SWCNTs in catalyzing I_3^- reduction (Fig. 44c). The as-fabricated DSSC achieves a V_{OC} of 0.86 V and PCE of 8.37% which are superior to all the control DSSCs with Pt (0.77 V, 7.79%), SWCNTs (0.75 V, 7.75%) and graphene-only (0.78 V, 7.19%) as counter-electrodes (Fig. 44d). By hybridizing N-doped graphene and SWCNTs to form a 3D aerogel, Ma et al. [1242] found that the resulting DSSC achieved a PCE of 8.31%. In these cases, graphene enables high electrocatalytic activity, while SWCNTs give rise to high conductivity for the composites and also facilitate the penetration of redox species into the graphene matrix. GCEs with a 3D porous structure provide a large SSA and good surface hydrophilicity to facilitate the electrolyte-electrode interaction, electrolyte-reactant diffusion, and charge transfer. Moreover, the composite electrodes have better stability than Pt in catalyzing the redox of I^-/I_3^- due to the degradation of Pt in the electrolyte whereas SWCNTs and graphene are quite stable [1190].

6.2.1.4. Transparent GCEs. Unlike the photoanode, optical transparency is not a prerequisite for the catalytic counter-electrode. In most cases, GCEs are nontransparent to visible light. Some additional benefits, nevertheless, from optically transparent counter-electrodes involve the fabrication of plastic DSSCs and integrated photovoltaic systems like tandem DSSCs as well as certain practical applications in windows, roof panels, and decorative installations [1183,1243,1244]. Transparent counter-electrodes based on GBMs have recently been reported for constructing DSSCs [1245–1248]. Kavan et al. [1249] reported transparent ($T > 85\%$ at 400–1100 nm) GCEs fabricated by drop-casting on FTO from commercial graphene nanoplatelets. Transparent GCEs in DSSCs exhibit low R_{CT} and high catalytic activity toward the I^-/I_3^- redox couple due to the presence of edge defects and oxide groups, resulting in PCEs of 5.16% and 5.73% in IL and traditional electrolytes, respectively. Recently, Choi et al. [1250] used graphene-supported Pt NPs as a transparent GCE achieving a PCE of 6.55% for front-side and 5.17% for back-side illumination, respectively. Ramaprabhu and Kaniyoor [1251] employed a cationic PDDA to functionalize graphene and to assist in uniform tethering of Pt NPs. The as-fabricated Pt-PDDA/graphene counter-electrode is highly transparent ($\sim 88\%$ at 550 nm) and highly catalytic ($R_{CT} < 1 \Omega \text{ cm}^2$) in DSSCs and results in an enhanced PCE of $\sim 5.7\%$ as compared to $\sim 4.5\%$ for the Pt-based reference cell. DSSCs based on transparent MoS_2 /graphene hybrid films ($>70\%$ at 400–800 nm) were also reported showing a lower R_{CT} (2.34 $\Omega \text{ cm}^2$) and a higher PCE (5.81%) compared to the devices with individual graphene (6.24 $\Omega \text{ cm}^2$, 2.68%) and MoS_2 (3.65 $\Omega \text{ cm}^2$, 4.15%) electrodes [1252].

Transparent GCEs have also demonstrated high electrocatalytic activity toward the $\text{Co}^{3+/2+}$ redox couples and hence potential applications in iodine-free DSSCs [1253]. Grätzel et al. [1254]

reported that commercial graphene nanoplatelets in the form of a thin semitransparent film on FTO exhibit high catalytic activity for $\text{Co}(\text{L})_2^{3+/2+}$ ($\text{L} = 6\text{-(1H-pyrazol-1-yl)-2,2'-bipyridine}$). The same GCE exhibits much better electrocatalytic activity for the $\text{Co}(\text{bpy})_3^{3+/2+}$ redox couple, [1255] even outperforming the Pt electrode under comparable conditions. GCEs also show better electrochemical stability under cycling potential when compared to the Pt electrode. All DSSCs, regardless of Co-based redox couples used, employing GCEs with 66% transparency under sun illumination by various light intensities (0.1–1.0) achieved PCEs over 9.0% (up to 9.7%), which is comparable to the device used the Pt electrode. These findings have promised a straight forward application in the development of DSSCs with PCEs exceeding 10%.

6.2.2. Photoanodes

Müllen et al. [232] used a thermally-reduced GO film as the FTO-free window electrode to fabricate the first solid-state DSSC which, however, gives an extremely low PCE (0.26%) due to the high series resistance, relatively low transmittance and electronic interfacial change. Although this seems to provide an alternative to the ubiquitously employed metal oxide window electrodes, the use of only graphene as a TCE has been rarely reported so far. A more frequent use of GBMs has been their incorporation into the blocking, scaffold and/or scattering layer of the photoanode. In these instances, graphene serves to accelerate photogenerated electron transport, [1256–1260] retard charge recombination, [1261–1265] inhibit back-transport reaction, [1266,1267] increase dye absorption, [1268–1270] and/or enhance light scattering and light harvesting [1256,1261,1271]. These lead to a large photocurrent density, high charge-carrier collection efficiency, and hence high-performance DSSCs.

6.2.2.1. GBMs in TiO_2 . Zhai et al. [1261] incorporated graphene into nanostructured TiO_2 to form the composite photoanode for DSSCs. Graphene can serve as a 2D bridge to enable fast electron transport, low charge recombination and high light scattering [1272]. As a consequence, J_{SC} is increased by 45% without sacrificing V_{OC} and the best PCE reaches 6.97% with a 39% increment relative to the TiO_2 -only photoanode (5.01%) and a significant improvement compared to CNT/ TiO_2 composite electrodes (0.58%). Graphene/ TiO_2 composite photoanodes were fabricated by a heterogeneous coagulation between Nafion-coated graphene and commercial TiO_2 NPs to ensure strong interfacial binding [1273]. Incorporation of graphene into TiO_2 results in both increased dye adsorption and longer electron lifetimes. The DSSC device with 0.5 wt% graphene yields a PCE of 4.28% which is 59% higher than that without graphene. The graphene/ TiO_2 film photoanode made by a hydrothermal reaction shows high porosity and large SSA which favor full adsorption of the sensitized dye [1274]. Compared to pure TiO_2 electrodes, the graphene/ TiO_2 electrode exhibits lower charge transfer resistance and thus suppresses charge recombination. The device based on graphene/ TiO_2 reaches a PCE of 7.52%, which is 17.7% higher than the TiO_2 -based cell. A 3D-hybridized graphene/CNT/ TiO_2 composite was also used as the photoanode to fabricate DSSCs showing a PCE of 6.11% with a 31% improvement compared to the TiO_2 -based device [1275]. Hu and Tang [1256] simultaneously incorporated graphene into the transport, scaffold, and scattering layers of the photoanode resulting in a DSSC with a much higher PCE (9.24%) compared to 6.25% for the TiO_2 -only device.

6.2.2.2. Dependence of GBM loading. The fraction of graphene in TiO_2 has a strong influence on the performance of DSSCs. PCEs of DSSCs usually increase and then decrease with increasing graphene content in the TiO_2 composites [1256]. Yu et al. [1271] reported an optimal amount of 0.75 wt% graphene in

TiO_2 composites in the range of 0.1–1.2 wt% and achieved a champion PCE of 5.77%, which is higher than that of pure TiO_2 cells (4.61%). Zhou et al. [1276] incorporated 2 wt% graphene into graphene/ TiO_2 photoanodes to obtain the highest PCE of 7.1% which is superior to 5.3% and 4.6% for DSSCs based on TiO_2 and 5.0 wt% graphene/ TiO_2 photoanodes, respectively. Stadler et al. [1262] found that the 1.6 wt% graphene/ TiO_2 hybrid has the highest SSA (229.13 m^2/g) compared to TiO_2 hybrids containing 0.8 wt% (203.07 m^2/g), 4 wt% (215.8 m^2/g), and 16 wt% (205.2 m^2/g) graphene and no graphene (193 m^2/g). Accordingly, DSSCs based on these photoanodes show PCEs of 7.68, 5.34, 4.24, 3.54, and 4.78% in turn. Recently, Chen et al. [1277] synthesized graphene/ TiO_2 composites (Fig. 45a and b) by *in-situ* thermolysis of 10,10'-dibromo-9,9'-bianthryl monomers ($\text{C}_{28}\text{H}_{16}\text{Br}_2$) in the presence of varied TiO_2 nanocrystals, and used these materials as photoanodes. They found that the incident photon-to-current conversion efficiency (IPCE) gradually increases with graphene content from 0.0 to 0.75 wt% and then decreases at graphene over 0.75 wt% loading in their TiO_2 composites (Fig. 45c). Also, the photoanode with the 0.75 wt% graphene/ TiO_2 composite has the smallest charge recombination resistance (18.0 Ω) at the dye-sensitized TiO_2 /electrolyte interface (Fig. 45d) and the longest electron lifetime (53.1 ms) (Fig. 45e). Therefore, DSSCs based on the 0.75 wt% graphene/ TiO_2 composite possess the highest PCE of 8.25% (Fig. 45f), which is increased by 65% compared to that of pure TiO_2 photoanode (5.01%).

The strong dependence of the device performance on the loading fraction of graphene in its TiO_2 composites can be explained as follows. A certain amount of graphene can effectively reduce R_{CT} at the anode–electrolyte interface. In this respect, graphene can facilitate interfacial transfer of photoinduced electrons from TiO_2 to graphene and then rapid transport to current collectors, thereby lowering backward reactions and charge recombination. Meanwhile, 2D graphene contributes to a large conjugated SSA for increased dye absorption which enables more light harvesting and more photogenerated electrons being injected into the conduction band of TiO_2 from the excited state of dye [1262,1277]. Moreover, the presence of graphene in the composite photoanode results in a large pore volume which can promote the efficient diffusion of I^-/I_3^- redox shuttle to regenerate dye [1271]. However, excessive graphene loading leads to reduced crystallinity of TiO_2 and poor electron diffusion and transport, and accordingly high interfacial resistance and high charge recombination [1262,1271]. In addition, high graphene loading causes self-agglomeration and severely shields light harvesting of dye and decreases the number of photogenerated electrons under illumination [1276]. Therefore, an optimal amount of graphene in the photoanode is vitally important to reach a high PCE for DSSCs.

6.2.3. Solid state electrolytes

The electrolyte plays an important role in charge carrier transport and dye regeneration, and therefore has great influence on the photovoltaic performance and long-term stability of DSSCs. In order to work efficiently, an electrolyte must fulfill certain characteristics including minimal potential losses, fast charge transport (arising from small redox species, high diffusion coefficient and good interfacial contact with two electrodes), weak absorption of visible light as well as high electrochemical, thermal and interfacial stability [1278]. Organic solvents like acetonitrile and valeronitrile are commonly employed as the solvents for DSSC electrolytes due to low viscosity, high dielectric constant, and rapid ionic transfer kinetics. DSSCs with high reported PCEs are almost based on such liquid electrolytes containing redox couples [1279,1280]. However, liquid redox electrolyte-based DSSCs face two significant problems including leakage of electrolytes and evaporation of organic solvents. These

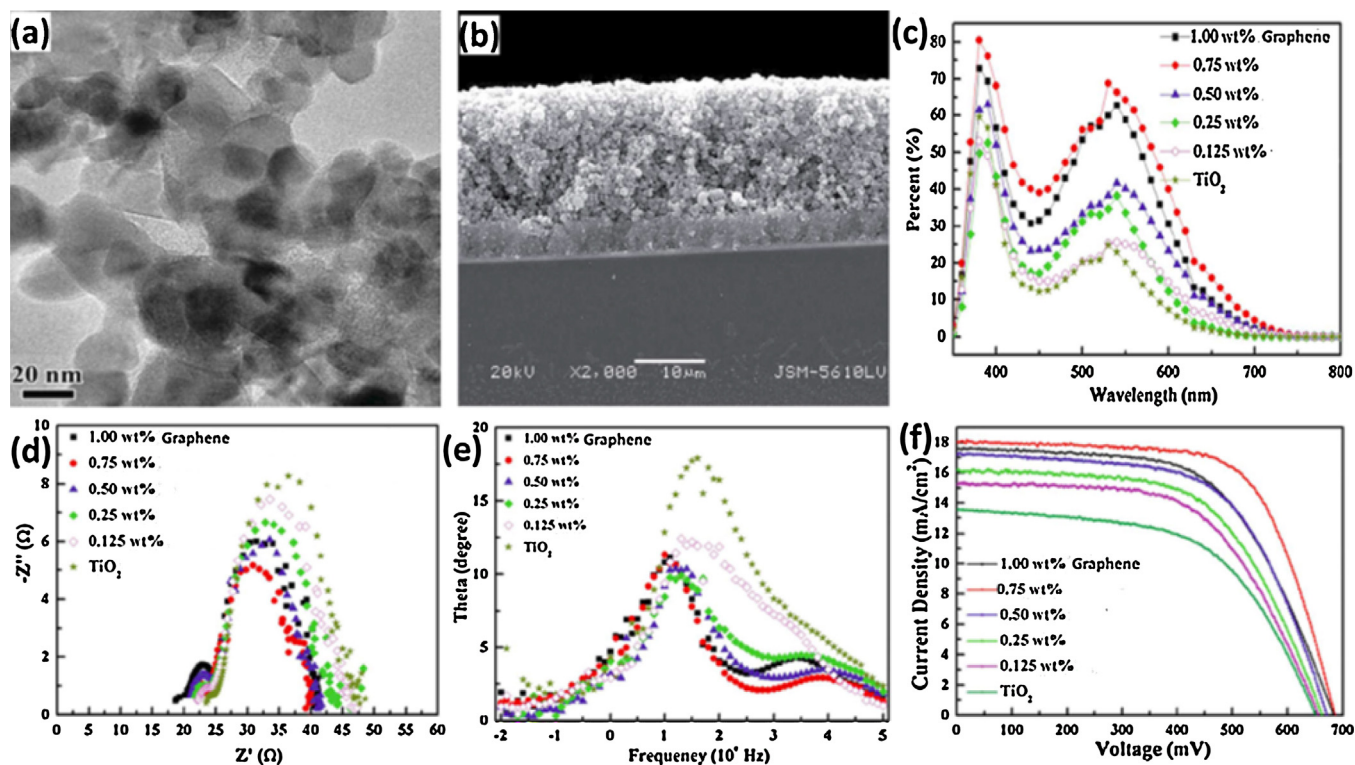


Fig. 45. (a) TEM image of 0.75 wt% graphene/TiO₂ composites and (b) cross-sectional SEM image of its film. (c) IPCE curves, (d) Nyquist curves, (e) Bode phase plots, and (f) *J*-*V* curves of DSSCs with graphene/TiO₂ composite films. [1277] Copyright 2014 Royal Society of Chemistry.

drawbacks induce higher overall internal resistance due to a lower concentration of charge carriers and significantly decrease the recovery of excited dye molecules due to the loss of medium for redox couple transport. Additional problems involve the corrosion of cells over time, high temperature instability (when using outdoors), and manufacturing complexity during sealing and integration into flexible devices. Alternative strategies have recently been made by developing quasi-solid-state-electrolytes (QSSEs) based on ILs, organic-inorganic hybrids and polymer electrolytes [1278]. Unfortunately, the PCEs of such DSSCs remain much lower than those of liquid electrolyte-based DSSCs due to the relatively low charge mobility of the redox couple in QSSEs, high recombination rate at the electrode-QSSE interface and incomplete penetration of QSSEs into the mesoporous photoanode. To address the above issues, some researchers have succeeded in incorporating graphene materials into DSSC electrolytes to serve as QSSEs with greatly improved cell performances [1281–1285].

6.2.3.1. Electrolytes based on ILs and hybrid gels. Gun'ko et al. [1286] incorporated small amounts (0.125–3 wt %) of graphene into an IL of 1-propyl-3-methyl imidazolium iodide (PMII) containing I^-/I_3^- to form a new hybrid electrolytes. DSSCs based on this electrolyte show a champion PCE of 2.6% at 1.0 wt% graphene, which is 25 times greater than the PMII-based DSSC (0.1%). This originates from the fact that graphene functions as an efficient transporter which lowers R_{CT} at the electrolyte-electrode interface and allows fast charge transfer throughout the electrolyte. Graphene also serves as an active electrocatalyst for the reduction of I_3^- in the electrolyte [1287,1288]. Ouyang et al. reported [1289] the formation of composite gel electrolytes by mixing GO with 3-methoxypropionitrile (MPN) solvent followed by addition of an iodide mediator. Dynamic rheological measurements suggest that GO sheets form 3D solid networks in the gels which hold MPN molecules due to both hydrogen bonding and polar-polar interactions between GO and MPN. The ionic conductivity of

2.5 wt% GO-MPN electrolyte is 7.24 mS/cm which decreases to 3.14 and 2.08 mS/cm with GO loadings at 4.0 and 6.0 wt%, respectively, due to the blocking of ionic transport by non-ionically conductive GO. Meanwhile, the prolonged ultrasonication allows GO sheets to be fragmented into smaller pieces which lead to higher ionic conductivity, larger diffusion constant of triiodide and higher PCEs for DSSCs with GO-MPN electrolytes. DSSCs with 2.5 wt% GO-MPN electrolyte with 10-min-sonicated-GO exhibit a champion PCE of 6.70% which is close to that (7.18%) of the control liquid DSSCs without GO. Additional incorporation of 0.25 wt% MWCNTs into the GO-MPN electrolyte can further reinforce GO networks and reduce the ionic diffusion length of redox species in the electrolyte [1290]. DSSCs based on GO-MWCNT-MPN electrolytes exhibit increased V_{OC} and J_{SC} and therefore the PCE increases to 7.12%. In addition to MPN, a wide range of solvents such as ethanol, 1-pentanol, 1-butanol, diethylene glycol, THF, acetonitrile, water, DMF, and DMSO, can form gels by incorporating small amounts (0.25–1.6 wt%) of GO [1282]. The use of 1.0 wt% GO-acetonitrile gel containing I^-/I_3^- as a QSSE achieves an improved PCE of 7.5% compared to the corresponding liquid electrolyte analogues (6.9%). These studies suggest that GO gel electrolytes can be used as potential candidates for quasi-solid state DSSCs.

6.2.3.2. Polymer composite electrolytes. Yang et al. [1291] suggested that graphene sheets could be uniformly coated by polyethylene oxide (PEO) to form graphene/PEO composite gels (Fig. 46a). Compared to bare PEO (1.21 mS/cm), the optimized 0.5% graphene/PEO composite electrolyte containing LiI, I_2 , and *tert*-butyl pyridine gives a higher ionic conductivity of 3.22 mS/cm due to the improved generation of the iodide redox couple and enhanced ionic interactions. A DSSC based on this QSSE exhibits a higher PCE (5.2%) than that of bare PEO-based DSSCs (1.9%). Recently, Tang et al. reported the use of freeze-dried microporous poly(acrylic acid)-poly(ethylene glycol) (PAA-PEG) (Fig. 46b) [1292] and PAA-CTAB (Fig. 46c) [1293] as scaffolds for the uptake

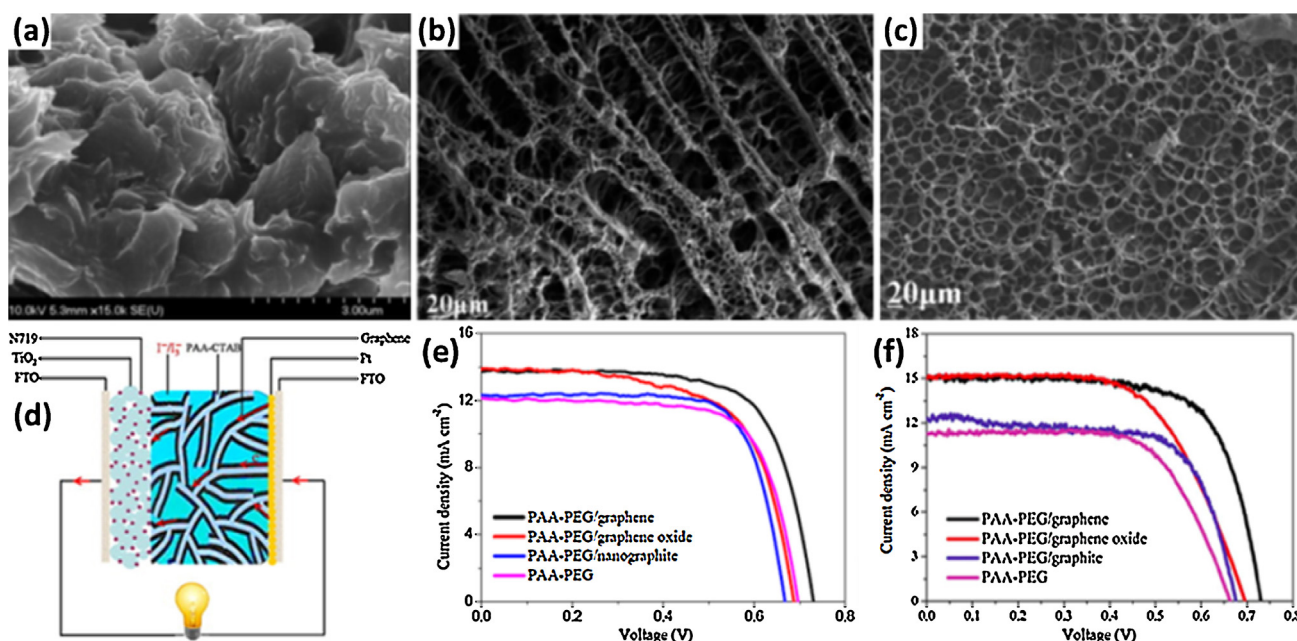


Fig. 46. (a) SEM image of 0.5 wt% graphene/PEO composites [1291]. Copyright 2013 Royal Society of Chemistry. SEM images of freeze-dried microporous samples of (b) PAA-PEG, [1292] Copyright 2014 Royal Society of Chemistry, and (c) PAA-CTAB, [1293] Copyright 2014 Elsevier Ltd. (d) Schematic diagram for a DSSC using a PAA-CTAB/graphene gel electrolyte. The transportation of reflux electrons along conducting channels within the PAA-CTAB/graphene gel electrolyte is marked. *J*–*V* characteristics of DSSCs from (e) PAA-CTAB and (f) PAA-PEG gel electrolytes.

of graphene, GO, graphite, and liquid electrolytes. PAA-CTAB/graphene was found to have a liquid electrolyte loading of 14.1 g/g (polymer gel electrolyte), which is higher than 13.1, 11.4, and 6.73 g/g for PAA-CTAB/GO, PAA-CTAB/graphite, and PAA-CTAB, respectively. PAA-CTAB/graphene thus shows a higher room-temperature ionic conductivity (10.56 mS/cm) compared to PAA-CTAB/GO (9.91 mS/cm), PAA-CTAB/graphite (7.33 mS/cm), and PAA-CTAB (6.78 mS/cm) due to its higher liquid electrolyte content in per unit volume. Similarly, the highest values of liquid electrolyte loading (21.1 g/g) and room-temperature ionic conductivity (11.60 mS/cm) were also observed in the PAA-PEG/graphene gel electrolyte. It is noteworthy to mention that the interconnected channels from graphene, GO, or graphite in QSSEs can conduct electrons from the Pt counter-electrode into the 3D framework and participate in the electrocatalytic reaction of I^-/I_3^- redox species (Fig. 46d). This leads to fast charge transport, lower R_{CT} , high electrocatalytic activity, and long-term electrochemical stability. DSSCs made from PAA-CTAB/graphene, PAA-CTAB/GO, and PAA-CTAB/graphite exhibit PCEs of 7.06, 6.35, and 6.17% (Fig. 46e), respectively. These are higher than PCEs reported for DSSCs based on PAA-PEG electrolytes (6.07%) [1293]. Also, the PAA-PEG/graphene based DSSC exhibits the highest PCE of 7.74% compared to DSSCs based on gel electrolytes of PAA-PEG/GO (6.49%), PAA-PEG/graphite (5.63%), and PAA-PEG (5.02%) (Fig. 46f). It should be noted that conductive graphene networks in contact with both electrodes can create a short circuit in DSSCs thus diminishing performance. In contrast, insulating GO is catalytic towards the redox couple and also highly compatible with many polar solvents and redox mediators making it easy to form gel electrolytes with good ionic conductivity. In this regard, GO is preferable in fabricating QSSEs for DSSCs.

6.3. Graphene-based materials for perovskite solar cells

Organic-inorganic hybrid solar cells based on organometal halide perovskites have triggered great attention in photovoltaic devices [1294] with reported PCEs skyrocketing from 3.8% [1295]

to 10.9% [1296] to 16.2% [1297] and finally to 19.3% [1089] in only five years. Both meso-superstructured [1296,1298–1300] and planar heterojunction [1301–1303] PVSCs have been developed with excellent cell performances. Organometal halide perovskites (typically taking the form of $CH_3NH_3MX_3$, $M = Pb$ or Sn , $X = Cl$, Br and/or I) play the key role serving as light-harvesting materials, which have advantages including large absorption coefficients, high carrier mobility, direct bandgap, low-temperature solution-processability, low cost, and high stability [1304–1307]. One prominent feature of halide perovskites is to have long electron and hole diffusion lengths (e.g., ~ 100 nm for $CH_3NH_3PbI_3$, [1308] and >1 μm for $CH_3NH_3PbI_{3-x}Cl_x$ [1309]) compared to solution-processed organic photovoltaic materials (~ 10 nm), [1310] and colloidal QD films (80 ± 10 nm) [1311]. The larger diffusion length is a result of longer recombination lifetime and hence is consistent with a high carrier-collection efficiency and superior performance [1309,1312,1313]. However, electron and hole extraction times in PVSCs are measured to be 0.4 and 0.66 ns, respectively, which are much longer than the hot carrier cooling (or thermalization) time (~ 0.4 ps) [1308]. Therefore some of photon energy is lost due to the thermalization and carrier trapping. Therefore, ultrafast electron injection is required in order to compete with carrier trapping and thermalization/cooling and achieve high PCEs in PVSCs [1314].

In this regard, Fan et al. [1315] fabricated PVSCs by inserting an ultrathin layer of electrochemically-produced QGDs between perovskite ($CH_3NH_3PbI_3$) and TiO_2 (Fig. 47a–d). As shown in Fig. 47e, QGDs-loaded devices give higher values of J_{SC} and V_{OC} and similar FF values compared to devices without QGDs. Therefore, the cells with the QGD layer achieve PCEs of 10.15% and those without QGDs achieve PCEs of 8.81%. The higher V_{OC} suggests that the ultrathin QGD layer can serve as a superfast bridge to facilitate electron injection from $CH_3NH_3PbI_3$ into TiO_2 leading to significant enhancement in the photocurrent and PCE. Further evidence from transient absorption measurements shows that IPCE and absorbed-photon-to-current conversion efficiencies are significantly enhanced upon the insertion of QGDs. Thus a faster electron extraction time is observed in the presence of QGDs (90–106 ps)

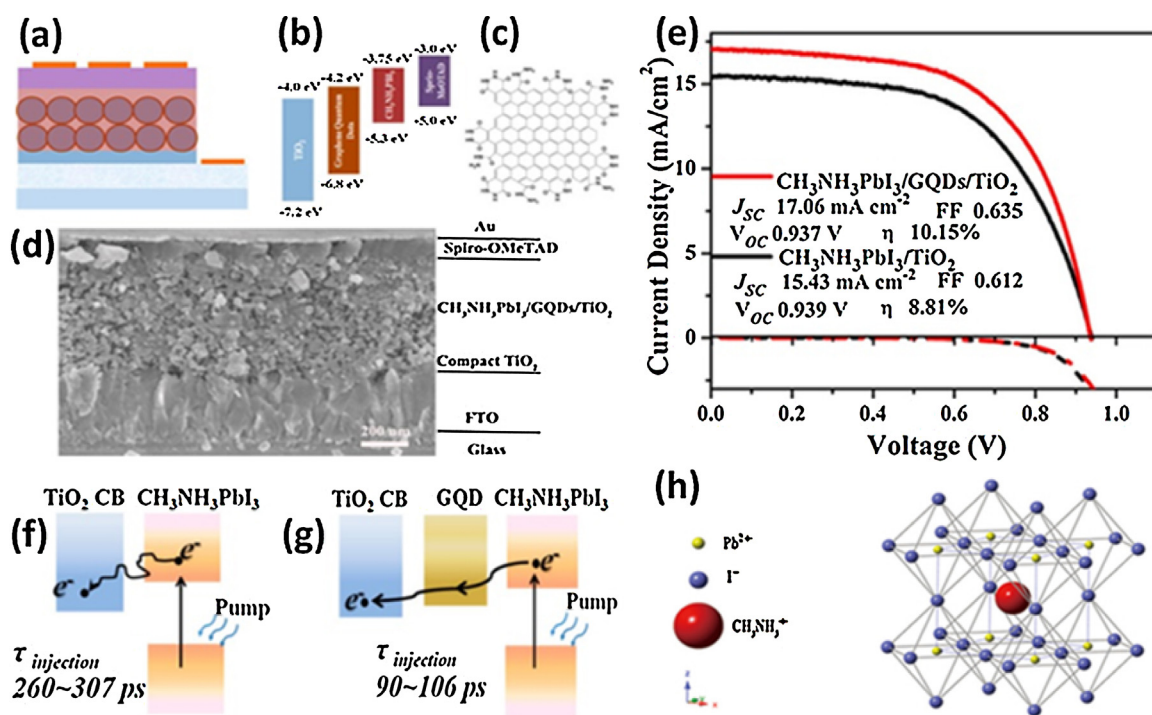


Fig. 47. Schematic representation of (a) cell configuration where mesoporous TiO₂ is either loaded with GQDs or not, (b) energy band alignment relative to vacuum, (c) edge-modified GQD structure, and (d) cross-sectional SEM image of a complete device. Schematic illustration for electron generation and extraction at (f) CH₃NH₃PbI₃/TiO₂ and (g) CH₃NH₃PbI₃/GQDs/TiO₂ interfaces, and (h) crystal structure of CH₃NH₃PbI₃. Spiro-MeOTAD corresponds to (2, 2', 7, 7'-tetrakis-(N, N-di-p-methoxyphenyl-amine)-9, 9'-spirobifluorene as a well-known HTL material [1315]. Copyright 2014 American Chemical Society.

than in their absence (260–307 ps). This allows for competition with carrier trapping (Fig. 47f and g) and results in greater performance enhancements. This work shows that GQDs can serve as a superfast electron tunnel for PVSCs. Further work on GQD-induced ultra-rapid electron injection may allow hot carrier extraction before cooling down to the band edges and trigger new pathways for future development of optoelectronic devices.

As mentioned above, GO can be used as an efficient HTL material in PSCs due to its appropriate work function, acceptable resistivity and surface doping effect [1076,1107,1316]. Recently, Sun et al. [1317] attempted to employ GO as a hole conductor in the inverted planar heterojunction PVSCs (see Fig. 48a and b). The CH₃NH₃PbI_{3-x}Cl_x perovskite on the spin-coated GO films exhibits homogeneous surface coverage (Fig. 48c), enhanced crystalliza-

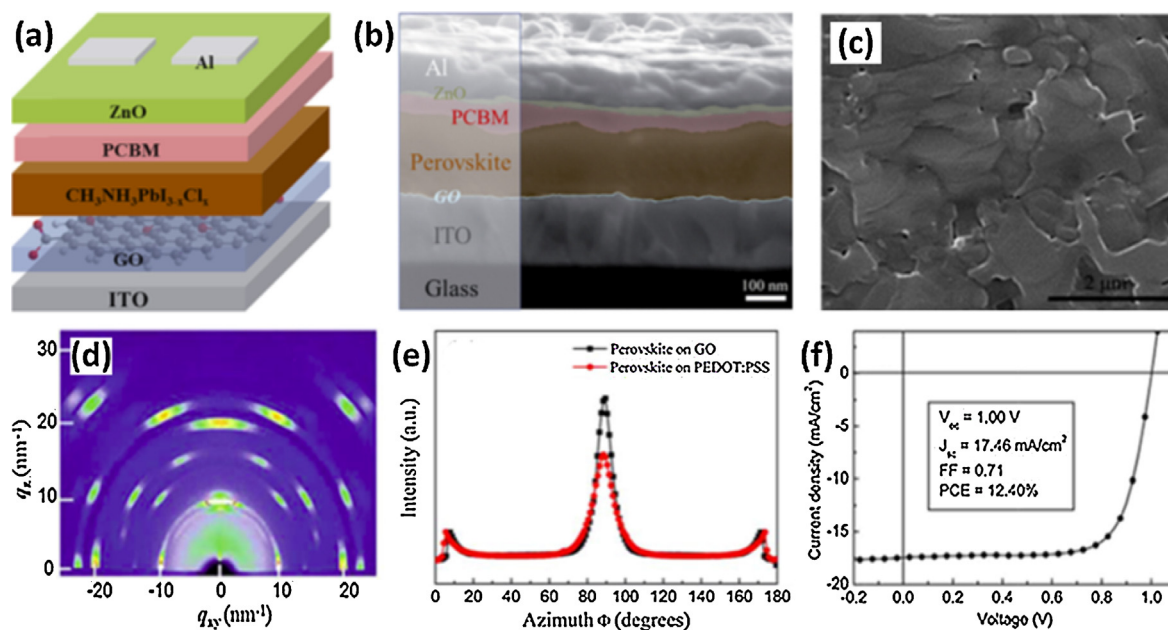


Fig. 48. (a) The inverted device configuration consisting of ITO/GO/CH₃NH₃PbI_{3-x}Cl_x/PCBM/ZnO/Al and (b) its corresponding cross-sectional SEM image in false color. SEM image (c) and 2D grazing incidence X-ray diffraction (GIXRD) profile (d) of CH₃NH₃PbI_{3-x}Cl_x film on the ITO/GO substrate and (e) radially integrated intensity plots along the ring at $q = 10 \text{ nm}^{-1}$ assigned to the (110) plane of CH₃NH₃PbI_{3-x}Cl_x perovskite structure. (f) J-V curve of the champion device employing ~2 nm-GO film as the hole conductor [1317]. Copyright 2014 Royal Society of Chemistry.

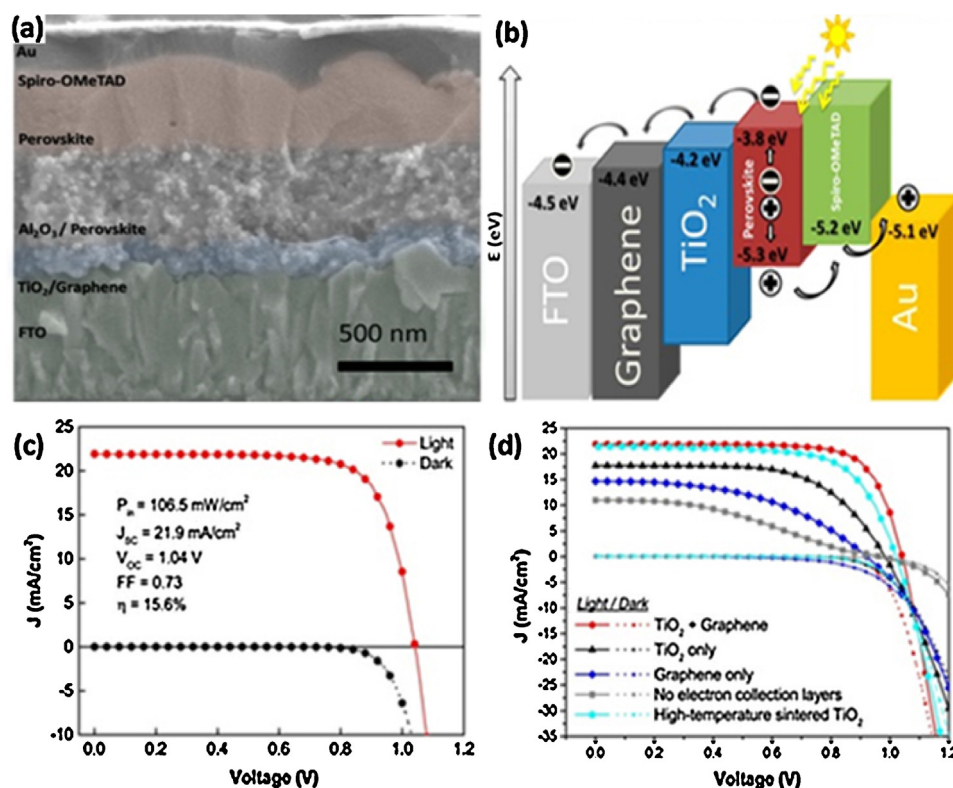


Fig. 49. (a) Cross-sectional SEM image with color-enhanced and annotated cross-section showing a general schematic of cell architecture, and (b) energy levels of the materials used. CV characteristics of (c) the best performing cell based on a graphene- TiO_2 composite and (d) cells from different electron collection layers under solar irradiation (solid line) and in the dark (dotted line) [1324]. Copyright 2014 American Chemical Society.

tion, and preferred in-plane orientation of the (110) plane (Fig. 48d and e). Photoluminescence quenching occurs upon coupling $\text{CH}_3\text{NH}_3\text{PbI}_{3-x}\text{Cl}_x$ with GO and gives a quenching efficiency of 52.8% for a 2 nm thick GO film. This is comparable to TiO_2 (47%) [1318] which indicates efficient charge transfer. A champion PCE of 12.4% has been reported for a device with a 2 nm thick GO film as the hole conductor (Fig. 48f). This value is much higher than 2.64% for the device without a hole conductor, and also larger than 9.26% for the PEDOT:PSS-based device. These findings demonstrate the efficient hole extraction from perovskite to GO. Recently, Wang et al. reported [1319] that GO can act as dual-function interface modifier for improving wettability and retarding recombination in PVSCs. Specifically, GO can form a buffer layer between $\text{CH}_3\text{NH}_3\text{PbI}_3$ and Spiro-MeOTAD. GO interacts with perovskite by forming Pb–O bonds and with HTL via π – π stacking. This leads to an improved interface contact between perovskite and HTL, enhanced charge-collection efficiency and an enhanced J_{sc} . Moreover, using GO as an insulating buffer layer can retard charge recombination in devices leading to increases in V_{oc} and FF. As a result, the average efficiency increased from 10.0% for cells without GO to 14.5% for GO-loaded devices (15.1% for a champion cell). GO may hold promise to replace the currently mostly used, expensive Spiro-OMeTAD, offering an alternative to develop high-performance PVSCs [1320].

High PCEs in solution-processed PVSCs have been frequently achieved using electron-collection layers (usually TiO_2) that often require sintering at over 400 °C to increase their crystallinity and achieve high charge carrier mobility [1307,1314,1321–1323]. High-temperature processing, however, is unfavorable for low-cost production, applications on plastic substrates, and multijunction devices. Recently, Snaith et al. [1324] developed a low-temperature-processed (≤ 150 °C) composite of pristine graphene (~ 5 layers) and anatase- TiO_2 NPs (~ 25 nm in diameter) and

used it as an electron-collection layer in mesostructured PVSCs (Fig. 49a and b) by a low-cost, solution-based deposition procedure. They observed a reduced series resistance and an unexpected reduction in recombination losses by incorporating graphene. The optimal concentration of graphene in graphene/ TiO_2 composites is 0.6 wt%. As shown in Fig. 49c, the best sub-150 °C-processed device exhibits high values of J_{sc} (21.9 mA/cm^2), V_{oc} (1.05 V), and FF (0.73) to give a champion PCE of up to 15.6%. This is higher than that of devices containing graphene-only (5.9%), TiO_2 -only (10.0%), and sintered TiO_2 -only (14.1%) layers (Fig. 49d). This work opens up an alternative pathway for fabricating high-efficiency solar cells by a low-temperature processing technique. By combining with fast printing deposition methods, graphene/ TiO_2 composites are potentially compatible with the reel-to-reel process for future industrial manufacture.

7. Conclusions and perspectives

7.1. General challenges in production of graphene

The past 10 years have witnessed substantial progress in the synthesis of GBMs by either top-down (mostly derived from graphite) or bottom-up (from hydrocarbons) techniques. There are many advantages and some disadvantages for each method in terms of crystal quality, accessibility and scalability (purity, cost, yield, quantity, etc.). For instance, solid-phase micromechanical exfoliation can yield high-quality graphene at the laboratory level, but suffers from extremely low throughput. Liquid-phase exfoliation of graphite produces graphene that is relatively scalable and highly crystalline; however, specific surfactants are usually required to improve the exfoliation efficiency and to stabilize graphene suspensions. These exfoliated materials are also a mixture of small amounts of monolayer, a majority of few-layered

graphene, and un-exfoliated graphite flakes. This requires subsequent separation and purification. Epitaxial growth on SiC and chemical synthesis from structurally-defined precursors are alternative methods to graphene and are often limited by their low yield, expensive cost, and high reaction temperature. CVD produces large-area graphene films with high structural and electronic quality. Nevertheless, CVD-grown graphene materials are usually polycrystalline with many rotational grain boundaries, and they are often required to transfer from the catalytic support to the substrate of interest. Both chemical and thermal reduction of GO to graphene allows for the production of bulk quantities with high yield and low cost. However, reduced GO usually exists in the low-to-medium quality due to the presence of intrinsic defects (edges, vacancies, distortions, etc.) and extrinsic defects (heteroatom-containing groups).

In spite of great advancements achieved in graphene production, there are still technical issues toward energy conversion and storage applications. “Mass-produced graphene has the same outstanding performance as the best samples obtained in research laboratories” [30] is the most critical challenge to address. The promising methods should be accessible, controllable, and scalable. In this regard, the reduction of GO, CVD, and liquid-phase exfoliation are three methods to be given serious consideration. In particular, CVD produces graphene with precise control of layer thickness, lateral size, stacking order, and crystallinity. Apart from its high production cost it is the most promising method. Future research toward CVD growth of graphene should focus on the following: (i) optimize the transfer process with the aim of minimizing the damage to graphene and of recovering the sacrificial metals; (ii) grow graphene directly on the targeted substrate to overcome the degraded properties caused by the transfer process; (iii) perform low-temperature growth of graphene on the insulating substrates for flexible devices; (iv) produce single-crystalline graphene of centimeter to wafer-scale size to minimize device-to-device variations in practical electronics and optics; [107], and (v) deeply understand growth mechanisms and dynamics to make graphene grains with precisely controlled layers and spatial structures.

Liquid-phase exfoliation of graphite to graphene has tended to exhibit either high production rates through long-time sonication or low yields with low defect concentrations, but usually not both. Future research is directed at optimizing the process to produce large-area single-/few-layer graphene with few defect, high purity, high yield, and productivity. This requires: (i) tailoring solvent systems to match surface energy of graphene; (ii) pretreating graphite by intercalation and/or thermal expansion in conjunction with surfactant assistance prior to exfoliation; and (iii) removing/recycling solvents and additives from the final product. It is also important to understand the mechanisms of exfoliation, dispersion, and subsequent stabilization of graphene in solutions. Reduction of GO has ensured mass production of graphene, but more attention should be paid to: (i) synthesizing graphite oxide with highly-effective oxidants by green processing; (ii) optimizing the exfoliation of graphite oxide into large-area, monolayer GO sheets; (iii) developing new reductants and/or reduction routes to high-quality graphene, in particular, to dope and functionalize graphene simultaneously; and (iv) identifying the reduction mechanisms so as to tailor the electronic and chemical structures of graphene for specific requirements.

Last but not least, a judicious selection of methods to produce graphene is required for targeted applications because each graphene has different properties integrally tied to its synthesis. Micromechanically-exfoliated graphene with a perfect 2D structure is suitable for fundamental research of intrinsic properties. Large-area films of CVD-grown graphene with high conductivity are preferably used as TCEs for flexible photovoltaics. GO-derived

graphene materials with abundant active sites are more effective in anode applications for LIBs and catalytic counter-electrodes for DSSCs. Furthermore, GO and RGO have high compatibility with metals, metallic compounds and conducting polymers. This enables the efficient fabrication of graphene-based composites which further serve as graphene-supported catalysts for fuel cells and hybrid electrodes for DSSCs, LIBs, and supercapacitors. Liquid processing of graphite can produce high-quality graphene and also allows for wet-chemical functionalization and further hybridization with other active components. This method can thus provide samples for fundamental characterization and has a potential to produce TCEs for solar cells and composite electrodes for fuel cells, LIBs, and supercapacitors if high yields can be obtained. In addition, solution-processed graphene from liquid-exfoliated graphene and RGO colloids enables the production of conducting inks and top-down approaches to print electronics. Therefore, liquid-phase exfoliation, in particular GO reduction, is an essential method for producing GBMs for energy conversion and storage applications. Other techniques such as epitaxial growth, chemical synthesis, and thermal pyrolysis remain relatively marginal and unsuitable for bulk production and electrode fabrication. Irrespective of the method used, to be commercially viable in the near future, GBMs must exhibit their properties which substantially surpass those of existing materials used at comparable costs. The device performance through synthesis-tailored structure-to-properties of GBMs is pivotal to achieve practical applications.

7.2. Engineering graphene for future energy applications

The integration of GBMs into LIBs, supercapacitors, fuel cells, and solar cells has achieved significant breakthroughs in recent years. An enormous amount of performance data reported for such devices using GBMs throughout research laboratories can compete with the existing commercial materials. The future commercial success of GBMs in practical applications depends on the development of low-cost production methods and more intrinsically, their nanostructures with on-demand properties for targeted applications. The looming issue, therefore, is how to tailor the nanostructure-to-properties of GBMs to fulfill specific requirements for particular devices since energy conversion and storage mechanisms are quite different for each one.

7.2.1. Toward electrochemical energy storage

GBMs have extensively demonstrated their feasibility and superiority in electrochemical energy storage. It has been well documented that lithium batteries and supercapacitors based on GBMs electrodes have achieved significant performance improvements in energy and power density, specific capacity/capacitance, charge/discharge rates, cycling life, capacity/capacitance retention, and rate capability. Early and sustained breakthroughs warrant the continued exploration of graphene-based electrochemical devices. In addition to developing cost-effective, green, and bulk-production methods, future research efforts on GBMs should be conducted to engineer their nanostructures, architectures and property parameters such as SSA, porosity, conductivity, surface activity, and chemical functionality.

7.2.1.1. Enlarging SSA accessible to charge storage. The amount of charge stored per unit mass, volume or area of an active material positively correlates with (but not in linearly) its SSA, and determines the specific capacity/capacitance and therefore energy density of LIBs and supercapacitors. Although monolayer graphene has high SSA and theoretical specific capacity/capacitance for boosting energy density, this does not seem to be the case in practical devices. Aggregation and restacking of graphene sheets can occur during material preparation, electrode manufacturing,

device fabrication, and cycling operation. Each of these cases can potentially reduce the effective surface available for charge storage. Therefore, future research efforts should concentrate on minimizing the graphene re-stacking and aggregation, i.e., maximizing SSA accessible to the electrolyte, by: (i) creating 3D porous nanostructures (such as hydrogels, aerogels, foams, or sponges) of GBMs prepared by hydrothermal/solvothermal treatment, chemical etching and activation, and hydrothermal carbonization; (ii) intercalating with spacer materials such as CNTs, carbon NPs, fullerenes, and ions in order to prevent the restacking of graphene sheets; and (iii) optimizing the electrode manufacturing process by direct growth or alignment of GBMs on the current collector, or by *in-situ* formation of free-standing, binder-free, and current-collector-free electrodes.

7.2.1.2. Enhancing packing density while retaining high SSA. Although GBMs have been reported with promising performance, most of them cannot yet compete with existing materials partially due to their low packing density and accordingly low volumetric energy and power density. Such GBMs exist with an excessively large pore volume, and thus some void spaces (especially macropores) in the electrodes are flooded by the electrolyte, increasing the weight and volume of the resulting devices without adding capacity/capacitance. This property is detrimental to the assembly of such power sources into integrated and portable electronics. Therefore, more attention should be paid to enhance the packing density (or decrease the pore volume) of GBM-based electrodes without sacrificing their high SSA. One can expect to achieve a high packing density by developing new methods such as template-directed synthesis, LBL assembly, and chemical activation of GBMs. Large densities can be also achieved by post-treatment of as-synthesized GBMs, such as evaporation drying of hydrogels, and capillary compression of aerogels. It should be emphasized that in addition to SSA and pore volume, pore sizes, and their distribution in GBM-based electrodes have significant influence on the electrochemical performance. The relationship between porosity and performance should be thoroughly explored both theoretically and experimentally in the future.

7.2.1.3. Hybridizing with electroactive components to improve performance. By utilizing *in-situ* or *ex-situ* methods, graphene has combined with various electroactive materials (usually metal oxides or conducting polymers) to produce hybrid electrodes in which graphene functions as an electrically-conductive scaffold, substrate, separator, or wrapper. The electrochemical performance of such electrodes has been considerably improved by suppressing the aggregation of graphene and particles, enhancing porosity, exposing more electroactive sites, facilitating electron transport and ion diffusion, extending the potential window and accommodating volume expansion/contraction during redox reactions, and charging/discharging. Graphene-based hybrid electrodes are commercially viable for supercapacitor and battery applications. However, several issues remain to be further addressed in the near future including: (i) functionalizing graphene to improve the interface with active materials and compatibility with the electrolyte for fast charge transport and diffusion; (ii) tailoring the phase composition and microscopic/macroscale morphology to ensure uniform dispersion, conductive interconnection, optimal porosity, good mechanical stability, high SSA and packing density, and finally high charge/discharge capacities without sacrificing cyclability and rate capability; (iii) clarifying the relationship between the composition, nanostructure (layer number, defect, size, doping, etc.), morphology (e.g., crumpled, porous, film, or 3D), electrode properties and device performance; and (iv) understanding the energy storage mechanism. Future generations of supercapacitors (LIBs) should be

expected to come close to existing LIBs in energy (power) density while retaining their high power (energy) density at reasonable cost.

7.2.2. Toward electrochemical energy conversion

GBM-based electrocatalysts on the anode and cathode of fuel cells have been widely reported and demonstrated their ability to enhance ORR and fuel oxidation. Meanwhile, long-term stability and lifetime and high resistance to corrosion have also been achieved while retaining good tolerance to methanol crossover and CO poisoning. Due to potentially low cost and high electrocatalytic activity, GBMs are potential replacements for conventional nanocatalysts. The catalytic performance is dependent on three factors, including: (i) nanostructures (size, shape, and composition) and surface distribution (uniformity, and density) of metallic NPs, (ii) quality of graphene, and (iii) interactions between them. Accordingly, future research should mainly follow the below directions. First, nanostructure-controlled synthesis methods which facilitate the homogeneous immobilization of well-defined catalyst NPs onto graphene are essential. This is because the catalyst NPs' activity is highly dependent on their nanostructures (especially the exposed crystal facet) and dispersion states. *In-situ* growth and *ex-situ* deposition of metallic NPs on the surface of graphene are two primary methods. The second requires uniform surface properties throughout graphene sheets for uniform deposition of catalyst NPs. Of note, more structural defects in graphene enable higher catalytic activity at the expense of electrochemical durability in fuel cells because of corrosion and degradation starting from the defects. However, the presence of defective sites can induce the growth and accumulation of metallic NPs. This enables strong coupling between graphene and catalyst NPs and hence imparts stable electrochemical performance to fuel cells. An optimal balance between catalytic activity and structural integrity of graphene should be considered to ensure electrochemical stability of hybrid catalysts. Lastly, greater efforts should be devoted to understanding the synergistic catalytic effects in fuel cells.

7.2.3. Toward solar energy conversion

GBMs can be incorporated into each part of solar cells and can serve a variety of roles which improve their performance and/or reduce the cost of such devices. For example, the use of GBMs for catalytic counter-electrodes to replace Pt in DSSCs and TCEs to replace ITO in PSCs has improved the performance-to-cost ratio of these devices. GBMs have also demonstrated their ability to function as charge transport materials in solar cells. The activity in these fields is currently growing rapidly; however, many significant issues remain to be addressed in order to develop high-performance solar cells based on GBMs.

7.2.3.1. GBMs toward TCEs. Despite substantial progress in both quality and scalability of graphene thin films, the combined T and R_s targets have not yet been achieved. Almost all PSCs based on graphene TCEs have exhibited lower PCEs compared to ITO-based cells. To compete with ITO for future applications in PSCs, there are four major routes for the fabrication of graphene TCEs: (i) synthesizing defect-free, large-area graphene with few layers and boundaries to lower R_s while retaining high carrier mobility (μ) and σ_{dc}/σ_{op} ; (ii) doping graphene thin films to increase the carrier density (n) and hence σ_{dc}/σ_{op} ; (iii) hybridizing with other materials such as metals to improve T , R_s , and σ_{dc}/σ_{op} simultaneously; and (iv) tuning the work function of GBMs by chemical functionalization to minimize the energy barriers for charge injection. In the case of DSSCs, the use of graphene-only photoanodes has given extremely low PCEs. Many reports have demonstrated that graphene can be well-integrated with the TiO_2 photoanode layer, imparting higher PCEs to DSSCs compared to

TiO₂-only counterparts. Note that TiO₂ NPs need to be homogeneously deposited onto the surface of graphene, and each TiO₂ NP has to be in close contact with graphene. An optimal fraction (usually <2.0 wt%) of graphene is also important for forming a percolated, conducting network through the TiO₂ matrix. Furthermore, thermal annealing is usually required to sinter TiO₂. Therefore, starting with GO followed by thermal reduction should be a primary option to produce graphene/TiO₂ composite photoanodes. In addition, there have been few reports on the use of GBMs as TCEs in PVSCs. New explorations and insights into graphene-based TCEs for PVSCs are highly encouraged since PVSCs can achieve higher PCEs with respect to PSCs and DSSCs, and especially many similarities with DSSCs in their photovoltaic mechanisms.

7.2.3.2. GBMs toward counter-electrodes. One of the widest and most successful uses of GBMs has been as counter-electrodes in DSSCs. The ability to facilitate electron transfer (high exchange current density) and lower R_{CT} between electrolyte and electrode has allowed GBMs to efficiently catalyze the reduction of redox species to regenerate the sensitizer after electron injection. Future research toward counter-electrodes is conceivable by: (i) developing new methods to produce graphene with controllable nanostructures; (ii) integrating graphene with highly-active components such as metals and metal compounds, and (iii) creating 3D porous architectures composed of graphene networks (or interconnected with other components). Each of these points aims at the production of GBMs with high electric conductivity, abundant active sites, and a large accessible SSA to achieve an optimal balance between electric conductivity and catalytic activity for high-performance DSSCs. Moreover, transparent counter-electrodes based on GBMs are important to the fabrication of tandem DSSCs and need to be further explored. GBMs may also open up new horizons in DSSCs when used with new redox mediators. As an emerging example, GBMs have been used as the best performing counter-electrodes in Co(bpy)₃^{3+/2+}-mediated DSSCs with the highest efficiency record to date (13%) [1280].

7.2.3.3. GBMs toward charge transport. GBMs with high work-functions as the HTL, low work-function as the ETL and both functions in tandem cells have shown the ability to enhance the charge transport rate and collection efficiency by minimizing energy barriers and suppressing carrier recombination to enhance PCEs and lifetime. Charge-collection and transport are important issues in photovoltaic devices. Future work should focus on tuning the work function and bandgap of GBMs to energetically match the electrode and active layer by: (i) controlling the reduction or oxidation degree of GO; (ii) adjusting the doping type or level of graphene; (iii) site-selective functionalization of graphene basal planes or its edges; (iv) tailoring the lateral size, layer and dimensionality of graphene; and (v) hybridizing with other wide-/narrow-bandgap p-/n-type materials. For instance, p-type GO with a high work-function is usually used as a HTL material in PSCs while zero or low bandgap graphene can enhance the electron transfer capability of the TiO₂ photoanode in DSSCs. Furthermore, to be a good interface the surface wettability of GBMs with their contact layers should be considered in terms of device processing. Solution-processable GBMs are probably advantageous. In this regard, graphene prepared via solution processing and incorporated in TiO₂ NPs was used as an ETL in PVSCs to achieve a PCE of 15.6% [1324]. This is the highest PCE among graphene-based solar cells reported to date. Continued research efforts in this field will likely yield promising developments in photovoltaic technologies.

7.2.4. Toward flexible energy devices

Flexible energy devices have promising applications in portable, wearable, and implantable devices such as roll-up displays, touch screens, electronic papers, wearable electronics, smart gloves, and implantable sensors [1325–1328]. With variable solution-processability (for graphene derived from liquid-phase exfoliation and soluble GO), transferability between substrates (for CVD and solution-processed graphene), and compatibility with roll-to-roll processing and printing, graphene has been demonstrated in the manufacturing feasibility of flexible fibers, thin films, papers, and 3D porous architectures. More importantly is that graphene intrinsically possesses high mechanical flexibility and elasticity, good compatibility with plastic/flexible substrates and nonplanar surfaces, and excellent tolerance to mechanical strain/stress. All of these enable it to maintain stable performance parameters under mechanical deformation. Representative examples based on GBMs include flexible supercapacitors, [764,785,1329–1331] LIBs, [1332–1335] LSBs, [1336–1338] fuel cells, [1339] organic photovoltaics, [1340–1343] DSSCs, [1237,1344,1345] and LEDs [19]. Such flexible devices are anticipated to convert and store energy upon repeated bending, folding, stretching, rolling or twisting without unduly sacrificing their performance. Rapid development and considerable achievements have been made in graphene-based flexible devices in recent years [1346].

Note that flexible devices and their conventional counterparts are identical in their working mechanisms and general issues and thereby a full summary for graphene-based flexible devices is not included here. The key challenge lies in maintaining stable performance for such devices under continuous mechanical deformation. The optimal fabrication of GBM-based flexible electrodes is the first step. For example, as for flexible TCEs of photovoltaics, high-quality graphene thin films are difficult to grow directly on plastic substrates because they cannot resist the high-temperatures required for annealing RGO or GO films. Graphene transferring processes and GO reduction methods still need to be carefully optimized to achieve satisfactory electrical conductivity and transparency. In the case of supercapacitors and LIBs, insulating-polymer binders are typically used in traditional electrodes resulting in an increased electrical resistivity and the addition of dead weight. Hybridization with electroactive materials (usually metal compounds) to produce composite electrodes is highly desirable in order to obtain larger capacities, higher energy densities and improved porosity. It is a challenge to maintain constant performance of graphene-based flexible electrodes containing relatively rigid, brittle inorganic components under mechanical deformation. In this regard, integrating nanosheet-/nanowire-like active materials with graphene or intercalating ultrasmall NPs into graphene sheets may produce structurally-stable flexible electrodes. An ideal flexible electrode should be binder-free, 3D, porous possess high conductivity, large electrochemically-accessible surfaces, short charge transfer/diffusion path, and high packing density.

As summarized in this review, because of extraordinary advantages over conventional materials, graphene has demonstrated its potential to tackle the challenges triggered by ever-growing global energy concerns. Graphene is not a panacea for all problems in this exciting field. However, it is reasonably believed that graphene could function as a promoter to revolutionize state-of-the-art energy techniques if GBMs are engineered by cost-effective, scalable methods adaptable to specific requirements for targeted applications.

Acknowledgments

We thank the financial support from the National Natural Science Foundation of China (51073050, 51273057), the Program

for New Century Excellent Talents in University (China) (NCET-12-0709), the Funds for Distinguished Young Scientists of Hubei Province (China) (2015CFA048), China Scholarship Council (no. 201308420033), and the Chutian Scholar Program of Hubei Province (China).

References

- [1] J.J. van Franeker, M. Turbiez, W. Li, M.M. Wienk, R.A. Janssen, *Nat. Commun.* 6 (2015) 6229.
- [2] Y.M. Yang, W. Chen, L. Dou, W.-H. Chang, H.-S. Duan, B. Bob, G. Li, Y. Yang, *Nat. Photonics* 9 (2015) 190.
- [3] W. Nie, H. Tsai, R. Asadpour, J.-C. Blancon, A.J. Neukirch, G. Gupta, J.J. Crochet, M. Chhowalla, S. Tretiak, M.A. Alam, *Science* 347 (2015) 522.
- [4] M.K. Debe, *Nature* 486 (2012) 43.
- [5] J. Suntivich, H.A. Gasteiger, N. Yabuuchi, H. Nakanishi, J.B. Goodenough, Y. Shao-Horn, *Nat. Chem.* 3 (2011) 546.
- [6] S. Sengodan, S. Choi, A. Jun, T.H. Shin, Y.-W. Ju, H.Y. Jeong, J. Shin, J.T. Irvine, G. Kim, *Nat. Mater.* 14 (2015) 205.
- [7] X. Liang, C. Hart, Q. Pang, A. Garsuch, T. Weiss, L.F. Nazar, *Nat. Commun.* 6 (2015) 5682.
- [8] M.-Q. Zhao, Q. Zhang, J.-Q. Huang, G.-L. Tian, J.-Q. Nie, H.-J. Peng, F. Wei, *Nat. Commun.* 5 (2014) 3410.
- [9] P.G. Bruce, S.A. Freunberger, L.J. Hardwick, J.-M. Tarascon, *Nat. Mater.* 11 (2012) 19.
- [10] P. Simon, Y. Gogotsi, *Nat. Mater.* 7 (2008) 845.
- [11] L. Kou, T. Huang, B. Zheng, Y. Han, X. Zhao, K. Gopalsamy, H. Sun, C. Gao, *Nat. Commun.* 5 (2014) 3754.
- [12] X. Lang, A. Hirata, T. Fujita, M. Chen, *Nat. Nanotechnol.* 6 (2011) 232.
- [13] G. Wang, L. Zhang, J. Zhang, *Chem. Soc. Rev.* 41 (2012) 797.
- [14] A.S. Arico, P. Bruce, B. Scrosati, J.-M. Tarascon, W. Van Schalkwijk, *Nat. Mater.* 4 (2005) 366.
- [15] G. Yu, X. Xie, L. Pan, Z. Bao, Y. Cui, *Nano Energy* 2 (2013) 213.
- [16] Y.-K. Sun, Z. Chen, H.-J. Noh, D.-J. Lee, H.-G. Jung, Y. Ren, S. Wang, C.S. Yoon, S.-T. Myung, K. Amine, *Nat. Mater.* 11 (2012) 942.
- [17] Y.G. Guo, J.S. Hu, L.J. Wan, *Adv. Mater.* 20 (2008) 2878.
- [18] K.S. Novoselov, A.K. Geim, S. Morozov, D. Jiang, Y. Zhang, S. Dubonos, I. Grigorieva, A. Firsov, *Science* 306 (2004) 666.
- [19] T.-H. Han, Y. Lee, M.-R. Choi, S.-H. Woo, S.-H. Bae, B.H. Hong, J.-H. Ahn, T.-W. Lee, *Nat. Photonics* 6 (2012) 105.
- [20] F. Bonaccorso, Z. Sun, T. Hasan, A.C. Ferrari, *Nat. Photonics* 4 (2010) 611.
- [21] L. Dai, *Acc. Chem. Res.* 46 (2013) 31.
- [22] Z. Yin, J. Zhu, Q. He, X. Cao, C. Tan, H. Chen, Q. Yan, H. Zhang, *Adv. Energy Mater.* 4 (2014) 1300574.
- [23] J. Liu, M. Durstock, L. Dai, *Energy Environ. Sci.* 7 (2014) 1297.
- [24] M. Liu, R. Zhang, W. Chen, *Chem. Rev.* 114 (2014) 5117.
- [25] X.-K. Kong, C.-L. Chen, Q.-W. Chen, *Chem. Soc. Rev.* 43 (2014) 2841.
- [26] M. Srivastava, J. Singh, T. Kuila, R.K. Layek, N.H. Kim, J.H. Lee, *Nanoscale* 7 (2015) 4820.
- [27] J. Zhu, D. Yang, Z. Yin, Q. Yan, H. Zhang, *Small* 10 (2014) 3480.
- [28] C. Lee, X. Wei, J.W. Kysar, J. Hone, *Science* 321 (2008) 385.
- [29] A.A. Balandin, S. Ghosh, W.Z. Bao, I. Calizo, D. Teweldebrhan, F. Miao, C.N. Lau, *Nano Lett.* 8 (2008) 902.
- [30] K.S. Novoselov, V.I. Fal'ko, L. Colombo, P.R. Gellert, M.G. Schwab, K. Kim, *Nature* 490 (2012) 192.
- [31] R. Raccichini, A. Varzi, S. Passerini, B. Scrosati, *Nat. Mater.* 14 (2015) 271.
- [32] F. Bonaccorso, L. Colombo, G. Yu, M. Stoller, V. Tozzini, A.C. Ferrari, R.S. Ruoff, V. Pellegrini, *Science* 347 (2015) 1246501.
- [33] X. Huang, X. Qi, F. Boey, H. Zhang, *Chem. Soc. Rev.* 41 (2012) 666.
- [34] Z.-S. Wu, G. Zhou, L.-C. Yin, W. Ren, F. Li, H.-M. Cheng, *Nano Energy* 1 (2012) 107.
- [35] A.K. Geim, K.S. Novoselov, *Nat. Mater.* 6 (2007) 183.
- [36] J.N. Coleman, *Acc. Chem. Res.* 46 (2013) 14.
- [37] Y. Zhang, L. Zhang, C. Zhou, *Acc. Chem. Res.* 46 (2013) 2329.
- [38] S. Park, R.S. Ruoff, *Nat. Nanotechnol.* 4 (2009) 217.
- [39] K. Lee, B. Fallahzad, J. Xue, D.C. Dillen, K. Kim, T. Taniguchi, K. Watanabe, E. Tutuc, *Science* 345 (2014) 58.
- [40] T. Ohta, A. Bostwick, T. Seyller, K. Horn, E. Rotenberg, *Science* 313 (2006) 951.
- [41] R.T. Weitz, M. Allen, B. Feldman, J. Martin, A. Yacoby, *Science* 330 (2010) 812.
- [42] M.-E. Ragoussi, G. Katsukis, A. Roth, J. Malig, G. de la Torre, D.M. Guldi, T. Torres, *J. Am. Chem. Soc.* 136 (2014) 4593.
- [43] J. Chen, J.H. Walther, P. Koumoutsakos, *Nano Lett.* 14 (2014) 819.
- [44] G. Melinte, I. Florea, S. Moldovan, I. Janowska, W. Baaziz, R. Arenal, A. Wisnet, C. Scheu, S. Begin-Colin, D. Begin, *Nat. Commun.* 5 (2014) 4109.
- [45] S. Ghosh, W. Bao, D.L. Nika, S. Subrina, E.P. Pokatilov, C.N. Lau, A.A. Balandin, *Nat. Mater.* 9 (2010) 555.
- [46] K.R. Paton, E. Varri, C. Backes, R.J. Smith, U. Khan, A. O'Neill, C. Boland, M. Lotya, O.M. Istrate, P. King, *Nat. Mater.* 13 (2014) 624.
- [47] A.G. Güell, N. Ebejer, M.E. Snowden, J.V. Macpherson, P.R. Unwin, *J. Am. Chem. Soc.* 134 (2012) 7258.
- [48] S.C. Bodepudi, A.P. Singh, S. Pramanik, *Nano Lett.* 14 (2014) 2233.
- [49] J.-B. Wu, X. Zhang, M. Ijäs, W.-P. Han, X.-F. Qiao, X.-L. Li, D.-S. Jiang, A.C. Ferrari, P.-H. Tan, *Nat. Commun.* 5 (2014) 5309.
- [50] J.-H. Lee, P.E. Loya, J. Lou, E.L. Thomas, *Science* 346 (2014) 1092.
- [51] H. Xia, C. Hong, B. Li, B. Zhao, Z. Lin, M. Zheng, S.V. Savilov, S.M. Aldoshin, *Adv. Funct. Mater.* 25 (2015) 627.
- [52] B. Rasche, A. Isaeva, M. Ruck, S. Borisenko, V. Zabolotnyy, B. Büchner, K. Koepfernik, C. Ortix, M. Richter, J. van den Brink, *Nat. Mater.* 12 (2013) 422.
- [53] W. Yuan, Y. Zhou, Y. Li, C. Li, H. Peng, J. Zhang, Z. Liu, L. Dai, G. Shi, *Sci. Rep.* 3 (2013) 2248.
- [54] D. Nika, S. Ghosh, E. Pokatilov, A. Balandin, *Appl. Phys. Lett.* 94 (2009) 203103.
- [55] L. Huang, L. Massa, C.F. Matta, *Carbon* 76 (2014) 310.
- [56] J. Xue, J. Sanchez-Yamagishi, D. Bulmash, P. Jacquod, A. Deshpande, K. Watanabe, T. Taniguchi, P. Jarillo-Herrero, B.J. LeRoy, *Nat. Mater.* 10 (2011) 282.
- [57] J. Liu, Z. Li, H. Yan, K. Jiang, *Adv. Eng. Mater.* 16 (2014) 1111.
- [58] R. Bajpai, S. Roy, N. Koratkar, D. Misra, *Carbon* 56 (2013) 56.
- [59] J. Ma, Q. Meng, I. Zaman, S. Zhu, A. Micheldore, N. Kawashima, C.H. Wang, H.-C. Kuan, *Compos. Sci. Technol.* 91 (2014) 82.
- [60] G. Ede, M. Chhowalla, *Adv. Mater.* 22 (2010) 2392.
- [61] S. Stankovich, R.D. Piner, S.T. Nguyen, S. Ruoff, *Carbon* 44 (2006) 3342.
- [62] K.S. Subrahmanyam, L.S. Panchakarla, A. Govindaraj, C.N.R. Rao, *J. Phys. Chem. C* 113 (2009) 4257.
- [63] B. Partoens, F. Peeters, *Phys. Rev. B* 74 (2006) 075404.
- [64] Ç.Ö. Girit, J.C. Meyer, R. Erni, M.D. Rossell, C. Kisielowski, L. Yang, C.-H. Park, M.F. Crommie, M.L. Cohen, S.G. Louie, A. Zettl, *Science* 323 (2009) 1705.
- [65] X. Jia, M. Hofmann, V. Meunier, B.G. Sumpter, J. Campos-Delgado, J.M. Romo-Herrera, H. Son, Y.-P. Hsieh, A. Reina, J. Kong, M. Terrones, M.S. Dresselhaus, *Science* 323 (2009) 1701.
- [66] H. Zhang, T. Zhou, G. Xie, J. Cao, Z. Yang, *Appl. Phys. Lett.* 104 (2014) 241908.
- [67] J.H. Warner, Y.-C. Lin, K. He, M. Koshino, K. Suenaga, *Nano Lett.* 14 (2014) 6155.
- [68] Y. Liu, A. Dobrinsky, B.I. Yakobson, *Phys. Rev. Lett.* 105 (2010) 235502.
- [69] A. Fasolino, J.H. Los, M.I. Katsnelson, *Nat. Mater.* 6 (2007) 858.
- [70] J.C. Meyer, A.K. Geim, M. Katsnelson, K. Novoselov, T. Booth, S. Roth, *Nature* 446 (2007) 60.
- [71] K.F. Mak, J. Shan, T.F. Heinz, *Phys. Rev. Lett.* 104 (2010) 176404.
- [72] Q. Liang, X. Yao, W. Wang, Y. Liu, C.P. Wong, *ACS Nano* 5 (2011) 2392.
- [73] G. Wang, Y. Kim, M. Choe, T.W. Kim, T. Lee, *Adv. Mater.* 23 (2011) 755.
- [74] A. Reina, J. Jia, J. Ho, D. Nezich, H. Son, V. Bulovic, M.S. Dresselhaus, J. Kong, *Nano Lett.* 9 (2008) 30.
- [75] P. San-Jose, R.V. Gorbachev, A.K. Geim, K. Novoselov, F. Guinea, *Nano Lett.* 14 (2014) 2052.
- [76] B.E. Feldman, J. Martin, A. Yacoby, *Nat. Phys.* 5 (2009) 889.
- [77] T. Low, F. Guinea, H. Yan, F. Xia, P. Avouris, *Phys. Rev. Lett.* 112 (2014) 116801.
- [78] J.C. Meyer, C. Kisielowski, R. Erni, M.D. Rossell, M.F. Crommie, A. Zettl, *Nano Lett.* 8 (2008) 3582.
- [79] Z.H. Ni, H.M. Wang, J. Kasim, H.M. Fan, T. Yu, Y.H. Wu, Y.P. Feng, Z.X. Shen, *Nano Lett.* 7 (2007) 2758.
- [80] D.L. Miller, K.D. Kubista, G.M. Rutter, M. Ruan, W.A. de Heer, P.N. First, J.A. Stroscio, *Science* 324 (2009) 924.
- [81] M. Terrones, A.R. Botello-Mendez, J. Campos-Delgado, F. Lopez-Urias, Y.I. Vega-Cantu, F.J. Rodriguez-Macias, A.L. Elias, E. Munoz-Sandoval, A.G. Cano-Marquez, J.-C. Charlier, H. Terrones, *Nano Today* 5 (2010) 350.
- [82] K.S. Novoselov, A.K. Geim, S.V. Morozov, D. Jiang, M.I. Katsnelson, I.V. Grigorieva, S.V. Dubonos, A.A. Firsov, *Nature* 438 (2005) 197.
- [83] X. Du, I. Skachko, A. Barker, E.Y. Andrei, *Nat. Nanotechnol.* 3 (2008) 491.
- [84] M. Orlita, C. Faugeras, P. Plochocka, P. Neugebauer, G. Martinez, D.K. Maude, A.-L. Barra, M. Sprinkle, C. Berger, W.A. De Heer, *Phys. Rev. Lett.* 101 (2008) 267601.
- [85] Y. Zhang, Y.-W. Tan, H.L. Stormer, P. Kim, *Nature* 438 (2005) 201.
- [86] S. Bae, H. Kim, Y. Lee, X. Xu, J.-S. Park, Y. Zheng, J. Balakrishnan, T. Lei, H. Ri Kim, Y.I. Song, Y.-J. Kim, K.S. Kim, B. Ozyilmaz, J.-H. Ahn, B.H. Hong, S. Iijima, *Nat. Nanotechnol.* 5 (2010) 574.
- [87] R.R. Nair, P. Blake, A.N. Grigorenko, K.S. Novoselov, T.J. Booth, T. Stauber, N.M.R. Peres, A.K. Geim, *Science* 320 (2008) 1308.
- [88] C. Casiraghi, A. Hartschuh, E. Lidorikis, H. Qian, H. Harutyunyan, T. Gokus, K.S. Novoselov, A.C. Ferrari, *Nano Lett.* 7 (2007) 2711.
- [89] Q. Tang, Z. Zhou, Z. Chen, *Nanoscale* 5 (2013) 4541.
- [90] M.I. Katsnelson, *Mater. Today* 10 (2007) 20.
- [91] A.A. Green, M.C. Hersam, *J. Phys. Chem. Lett.* 1 (2009) 544.
- [92] S. Ghosh, I. Calizo, D. Teweldebrhan, E. Pokatilov, D. Nika, A. Balandin, W. Bao, F. Miao, C.N. Lau, *Appl. Phys. Lett.* 92 (2008) 151911.
- [93] A.A. Balandin, S. Ghosh, W. Bao, I. Calizo, D. Teweldebrhan, F. Miao, C.N. Lau, *Nano Lett.* 8 (2008) 902.
- [94] I. Calizo, A. Balandin, W. Bao, F. Miao, C. Lau, *Nano Lett.* 7 (2007) 2645.
- [95] D. Nika, E. Pokatilov, A. Askerov, A. Balandin, *Phys. Rev. B* 79 (2009) 155413.
- [96] W.J. Evans, L. Hu, P. Keblinski, *Appl. Phys. Lett.* 96 (2010) 203112.
- [97] A.A. Balandin, *Nat. Mater.* 10 (2011) 569.
- [98] M.D. Stoller, S. Park, Y. Zhu, J. An, R.S. Ruoff, *Nano Lett.* 8 (2008) 3498.
- [99] C.N.R. Rao, A.K. Sood, K.S. Subrahmanyam, A. Govindaraj, *Angew. Chem. Int. Ed.* 48 (2009) 7752.
- [100] M.J. Allen, V.C. Tung, R.B. Kaner, *Chem. Rev.* 110 (2010) 132.
- [101] V. Georgakilas, M. Otyepka, A.B. Bourlino, V. Chandra, N. Kim, K.C. Kemp, P. Hobza, R. Zboril, K.S. Kim, *Chem. Rev.* 112 (2012) 6156.
- [102] M. Cai, D. Thorpe, D.H. Adamson, H.C. Schniepp, *J. Mater. Chem.* 22 (2012) 24992.
- [103] A. Ciesielski, P. Samori, *Chem. Soc. Rev.* 43 (2014) 381.
- [104] M. Inagaki, Y.A. Kim, M. Endo, *J. Mater. Chem.* 21 (2011) 3280.
- [105] A.W. Tsen, L. Brown, R.W. Havener, J. Park, *Acc. Chem. Res.* 46 (2013) 2286.
- [106] D. Wei, B. Wu, Y. Guo, G. Yu, Y. Liu, *Acc. Chem. Res.* 46 (2013) 106.
- [107] Z. Yan, Z. Peng, J.M. Tour, *Acc. Chem. Res.* 47 (2014) 1327.

- [108] L. Chen, Y. Hernandez, X. Feng, K. Mullen, *Angew. Chem. Int. Ed.* 51 (2012) 7640.
- [109] R.S. Edwards, K.S. Coleman, *Nanoscale* 5 (2013) 38.
- [110] K.F. Kelly, W.E. Billups, *Acc. Chem. Res.* 46 (2013) 4.
- [111] L.A. Girifalco, R.A. Lad, *J. Chem. Phys.* 25 (1956) 693.
- [112] Y. Zhang, J.P. Small, W.V. Pontius, P. Kim, *Appl. Phys. Lett.* 86 (2005) 073104.
- [113] S.D. Chakarova-Käck, E. Schröder, B.I. Lundqvist, D.C. Langreth, *Phys. Rev. Lett.* 96 (2006) 146107.
- [114] L. Spanu, S. Sorella, G. Galli, *Phys. Rev. Lett.* 103 (2009) 196401.
- [115] S. Morozov, K. Novoselov, M. Katsnelson, F. Schedin, D. Elias, J. Jaszczak, A. Geim, *Phys. Rev. Lett.* 100 (2008) 016602.
- [116] E.V. Castro, H. Ochoa, M. Katsnelson, R. Gorbachev, D. Elias, K. Novoselov, A. Geim, *F. Guinea, Phys. Rev. Lett.* 105 (2010) 266601.
- [117] S. Berciaud, S. Ryu, L.E. Brus, T.F. Heinz, *Nano Lett.* 9 (2009) 346.
- [118] R. Van Noorden, *Nature* 483 (2012) S32.
- [119] J. Chen, M. Duan, G. Chen, *J. Mater. Chem.* 22 (2012) 19625.
- [120] V. Leon, A.M. Rodriguez, P. Prieto, M. Prato, E. Vazquez, *ACS Nano* 8 (2014) 563.
- [121] V. Leon, M. Quintana, M.A. Herrero, J.L.G. Fierro, A.d.I. Hoz, M. Prato, E. Vazquez, *Chem. Commun.* 47 (2011) 10936.
- [122] L. Liu, Z. Xiong, D. Hu, G. Wu, P. Chen, *Chem. Commun.* 49 (2013) 7890.
- [123] J.D. Wuest, A. Rochefort, *Chem. Commun.* 46 (2010) 2923.
- [124] I.-Y. Jeon, Y.-R. Shin, G.-J. Sohn, H.-J. Choi, S.-Y. Bae, J. Mahmood, S.-M. Jung, J.-M. Seo, M.-J. Kim, D. Wook Chang, L. Dai, J.-B. Baek, *Proc. Natl. Acad. Sci. USA* 109 (2012) 5588.
- [125] L. Yan, M. Lin, C. Zeng, Z. Chen, S. Zhang, X. Zhao, A. Wu, Y. Wang, L. Dai, J. Qu, M. Guo, Y. Liu, *J. Mater. Chem.* 22 (2012) 8367.
- [126] I.-Y. Jeon, H.-J. Choi, S.-M. Jung, J.-M. Seo, M.-J. Kim, L. Dai, J.-B. Baek, *J. Am. Chem. Soc.* 135 (2013) 1386.
- [127] H. Wu, W. Zhao, H. Hu, G. Chen, *J. Mater. Chem.* 21 (2011) 8626.
- [128] S. Yang, P. Gao, D. Bao, Y. Chen, L. Wang, P. Yang, G. Li, Y. Sun, *J. Mater. Chem. A* 1 (2013) 6731.
- [129] V. Nicolosi, M. Chhowalla, M.G. Kanatzidis, M.S. Strano, J.N. Coleman, *Science* 340 (2013) 1226419.
- [130] X. Cui, C. Zhang, R. Hao, Y. Hou, *Nanoscale* 3 (2011) 2118.
- [131] J.N. Coleman, *Adv. Funct. Mater.* 19 (2009) 3680.
- [132] Y. Hernandez, M. Lotya, D. Rickard, S.D. Bergin, J.N. Coleman, *Langmuir* 26 (2009) 3208.
- [133] Y. Hernandez, V. Nicolosi, M. Lotya, F.M. Blighe, Z. Sun, S. De, I.T. McGovern, B. Holland, M. Byrne, Y.K. Gun'ko, J.J. Boland, P. Niraj, G. Duesberg, S. Krishnamurthy, R. Goodhue, J. Hutchison, A.C. Ferrari, J.N. Coleman, *Nat. Nanotechnol.* 3 (2008) 563.
- [134] U. Khan, A. O'Neill, M. Lotya, S. De, J.N. Coleman, *Small* 6 (2010) 864.
- [135] U. Khan, H. Porwal, A. O'Neill, K. Nawaz, P. May, J.N. Coleman, *Langmuir* 27 (2011) 9077.
- [136] Z. Tang, J. Zhuang, X. Wang, *Langmuir* 26 (2010) 9045.
- [137] D. Rangappa, K. Sone, M. Wang, U.K. Gautam, D. Golberg, H. Itoh, M. Ichihara, I. Honma, *Chem. – A Eur. J.* 16 (2010) 6488.
- [138] U. Khan, A. O'Neill, H. Porwal, P. May, K. Nawaz, J.N. Coleman, *Carbon* 50 (2012) 470.
- [139] A.V. Alafierdov, A. Gholamipour-Shirazi, M.A. Canesqui, Y.A. Danilov, S.A. Moshkalev, *Carbon* 69 (2014) 525.
- [140] P. Blake, P.D. Brimicombe, R.R. Nair, T.J. Booth, D. Jiang, F. Schedin, L.A. Ponomarenko, S.V. Morozov, H.F. Gleeson, E.W. Hill, A.K. Geim, K.S. Novoselov, *Nano Lett.* 8 (2008) 1704.
- [141] A.B. Bourlino, V. Georgakilas, R. Zboril, T.A. Steriotis, A.K. Stubos, *Small* 5 (2009) 1841.
- [142] M. Tariq, M.G. Freire, B. Saramago, J.A.P. Coutinho, J.N.C. Lopes, L.P.N. Rebelo, *Chem. Soc. Rev.* 41 (2012) 829.
- [143] X.Q. Wang, P.F. Fulvio, G.A. Baker, G.M. Veith, R.R. Unocic, S.M. Mahurin, M.F. Chi, S. Dai, *Chem. Commun.* 46 (2010) 4487.
- [144] D. Nuvoli, L. Valentini, V. Alzari, S. Scognamiglio, S.B. Bon, M. Piccinini, J. Illescas, A. Mariani, *J. Mater. Chem.* 21 (2011) 3428.
- [145] A. Safavi, M. Tohidi, F.A. Mahyari, H. Shahbaazi, *J. Mater. Chem.* 22 (2012).
- [146] N.G. Shang, P. Papakonstantinou, S. Sharma, G. Lubarsky, M. Li, D.W. McNeill, A.J. Quinn, W. Zhou, R. Blackley, *Chem. Commun.* 48 (2012) 1877.
- [147] C.-J. Shih, S. Lin, M.S. Strano, D. Blankschtein, *J. Am. Chem. Soc.* 132 (2010) 14638.
- [148] S. Vadukumpully, J. Paul, S. Valiyaveetil, *Carbon* 47 (2009) 3288.
- [149] J. Geng, B.-S. Kong, S.B. Yang, H.-T. Jung, *Chem. Commun.* 46 (2010) 5091.
- [150] J.S. Park, L. Yu, C.S. Lee, K. Shin, J.H. Han, *J. Colloid Interface Sci.* 417 (2014) 379.
- [151] T. Skaltsas, N. Karousis, H.-J. Yan, C.-R. Wang, S. Pispas, N. Tagmatarchis, *J. Mater. Chem.* 22 (2012) 21507.
- [152] L. Guardia, M.J. Fernández-Merino, J.I. Paredes, P. Solís-Fernández, S. Villar-Rodil, A. Martínez-Alonso, J.M.D. Tascón, *Carbon* 49 (2011) 1653.
- [153] M. Buzaglo, M. Shtein, S. Kober, R. Lovrincic, A. Vilan, O. Regev, *Phys. Chem. Chem. Phys.* 15 (2013) 4428.
- [154] J.-W.T. Seo, A.A. Green, A.L. Antaris, M.C. Hersam, *J. Phys. Chem. Lett.* 2 (2011) 1004.
- [155] A.A. Green, M.C. Hersam, *Nano Lett.* 9 (2009) 4031.
- [156] M. Lotya, P.J. King, U. Khan, S. De, J.N. Coleman, *ACS Nano* 4 (2010) 3155.
- [157] M. Lotya, Y. Hernandez, P.J. King, R.J. Smith, V. Nicolosi, L.S. Karlsson, F.M. Blighe, S. De, Z. Wang, I.T. McGovern, G.S. Duesberg, J.N. Coleman, *J. Am. Chem. Soc.* 131 (2009) 3611.
- [158] X. Liu, M. Zheng, K. Xiao, Y. Xiao, C. He, H. Dong, B. Lei, Y. Liu, *Nanoscale* 6 (2014) 4598.
- [159] L. Niu, M. Li, X. Tao, Z. Xie, X. Zhou, A.P.A. Raju, R.J. Young, Z. Zheng, *Nanoscale* 5 (2013) 7202.
- [160] Y. Xu, H. Bai, G. Lu, C. Li, G. Shi, *J. Am. Chem. Soc.* 130 (2008) 5856.
- [161] D. Parviz, S. Das, H.S.T. Ahmed, F. Irin, S. Bhattacharia, M.J. Green, *ACS Nano* 6 (2012) 8857.
- [162] H. Yang, Y. Hernandez, A. Schlierf, A. Felten, A. Eckmann, S. Johal, P. Louette, J.J. Pireaux, X. Feng, K. Mullen, V. Palermo, C. Casiraghi, *Carbon* 53 (2013) 357.
- [163] J.-H. Jang, D. Rangappa, Y.-U. Kwon, I. Honma, *J. Mater. Chem.* 21 (2011) 3462.
- [164] A. Schlierf, H. Yang, E. Gebremedhn, E. Treossi, L. Ortolani, L. Chen, A. Minoia, V. Morandi, P. Samori, C. Casiraghi, D. Beljonne, V. Palermo, *Nanoscale* 5 (2013) 4205.
- [165] M. Zhang, R.R. Parajuli, D. Mastrogianni, B. Dai, P. Lo, W. Cheung, R. Brukh, P.L. Chiu, T. Zhou, Z. Liu, E. Garfunkel, H. He, *Small* 6 (2010) 1100.
- [166] Q. Su, S. Pang, V. Alijani, C. Li, X. Feng, K. Mullen, *Adv. Mater.* 21 (2009) 3191.
- [167] S. Sampath, A.N. Basuray, K.J. Hartlieb, T. Aytun, S.I. Stupp, J.F. Stoddart, *Adv. Mater.* 25 (2013) 2740.
- [168] J.M. Englert, J. Röhr, C.D. Schmidt, R. Graupner, M. Hundhausen, F. Hauke, A. Hirsch, *Adv. Mater.* 21 (2009) 4265.
- [169] D.-W. Lee, T. Kim, M. Lee, *Chem. Commun.* 47 (2011) 8259.
- [170] F. Liu, J.Y. Choi, T.S. Seo, *Chem. Commun.* 46 (2010) 2844.
- [171] A. Ghosh, K.V. Rao, S.J. George, C.N.R. Rao, *Chem. Eur. J.* 16 (2010) 2700.
- [172] J. Björk, F. Hanke, C.-A. Palma, P. Samori, M. Cecchini, M. Persson, *J. Phys. Chem. Lett.* 1 (2010) 3407.
- [173] A. Hirsch, J.M. Englert, F. Hauke, *Acc. Chem. Res.* 46 (2013) 87.
- [174] F. Torrisi, T. Hasan, W. Wu, Z. Sun, A. Lombardo, T.S. Kulmala, G.-W. Hsieh, S. Jung, F. Bonaccorso, P.J. Paul, D. Chu, A.C. Ferrari, *ACS Nano* 6 (2012) 2992.
- [175] K.-Y. Shin, J.-Y. Hong, J. Jang, *Adv. Mater.* 23 (2011) 2113.
- [176] L. Huang, Y. Huang, J. Liang, X. Wan, Y. Chen, *Nano Res.* 4 (2011) 675.
- [177] S. De, P.J. King, M. Lotya, A. O'Neill, E.M. Doherty, Y. Hernandez, G.S. Duesberg, J.N. Coleman, *Small* 6 (2010) 458.
- [178] U. Khan, P. May, A. O'Neill, J.N. Coleman, *Carbon* 48 (2010) 4035.
- [179] A. O'Neill, U. Khan, P.N. Nirmalraj, J. Boland, J.N. Coleman, *J. Phys. Chem. C* 115 (2011) 5422.
- [180] J. Malig, A.W.I. Stephenson, P. Wagner, G.G. Wallace, D.L. Officer, D.M. Guldi, *Chem. Commun.* 48 (2012) 8745.
- [181] L. Brinkhaus, G. Katsukis, J. Malig, R.D. Costa, M. Garcia-Iglesias, P. Vázquez, T. Torres, D.M. Guldi, *Small* 9 (2013) 2348.
- [182] L. Xu, J.-W. McGraw, F. Gao, M. Grundy, Z. Ye, Z. Gu, J.L. Shepherd, *J. Phys. Chem. C* 117 (2013) 10730.
- [183] E.B. Secor, P.L. Prabhuramirasi, K. Puntambekar, M.L. Geier, M.C. Hersam, *J. Phys. Chem. Lett.* 4 (2013) 1347.
- [184] Y.T. Liang, M.C. Hersam, *J. Am. Chem. Soc.* 132 (2010) 17661.
- [185] M.S. Kang, K.T. Kim, J.U. Lee, W.H. Jo, *J. Mater. Chem. C* 1 (2013) 1870.
- [186] K.R. Paton, E. Varrla, C. Backes, R.J. Smith, U. Khan, A. O'Neill, C. Boland, M. Lotya, O.M. Istrate, P. King, T. Higgins, S. Barwich, P. May, P. Puczkarski, I. Ahmed, M. Moebius, H. Pettersson, E. Long, J. Coelho, S.E. O'Brien, E.K. McGuire, B.M. Sanchez, G.S. Duesberg, N. McEvoy, T.J. Pannycok, C. Downing, A. Crossley, V. Nicolosi, J.N. Coleman, *Nat. Mater.* 13 (2014) 624.
- [187] K. Kakaei, *Carbon* 51 (2013) 195.
- [188] D.A.C. Brownson, J.P. Metters, D.K. Kampouris, C.E. Banks, *Electroanalysis* 23 (2011) 894.
- [189] G. Wang, B. Wang, J. Park, Y. Wang, B. Sun, J. Yao, *Carbon* 47 (2009) 3242.
- [190] S.-H. Lee, S.-D. Seo, Y.-H. Jin, H.-W. Shim, D.-W. Kim, *Electrochem. Commun.* 12 (2010) 1419.
- [191] C.-Y. Su, A.-Y. Lu, Y. Xu, F.-R. Chen, A.N. Khlobystov, L.-J. Li, *ACS Nano* 5 (2011) 2332.
- [192] Z.Y. Xia, S. Pezzini, E. Treossi, G. Giambastiani, F. Corticelli, V. Morandi, A. Zanelli, V. Bellani, V. Palermo, *Adv. Funct. Mater.* 23 (2013) 4684.
- [193] J. Liu, C.K. Poh, D. Zhan, L. Lai, S.H. Lim, L. Wang, X. Liu, N.G. Sahoo, C. Li, Z. Shen, *J. Lin, Nano Energy* 2 (2013) 377.
- [194] L. Wu, W. Li, P. Li, S. Liao, S. Qiu, M. Chen, Y. Guo, Q. Li, C. Zhu, L. Liu, *Small* 10 (2014) 1421.
- [195] J. Lu, J.-x. Yang, J. Wang, A. Lim, S. Wang, K.P. Loh, *ACS Nano* 3 (2009) 2367.
- [196] N. Liu, F. Luo, H. Wu, Y. Liu, C. Zhang, J. Chen, *Adv. Funct. Mater.* 18 (2008) 1518.
- [197] A.T. Najafabadi, E. Gyenge, *Carbon* 71 (2014) 58.
- [198] M. Zhou, J. Tang, Q. Cheng, G. Xu, P. Cui, L.-C. Qin, *Chem. Phys. Lett.* 572 (2013) 61.
- [199] J. Wang, K.K. Manga, Q. Bao, K.P. Loh, *J. Am. Chem. Soc.* 133 (2011) 8888.
- [200] V.V. Singh, G. Gupta, A. Batra, A.K. Nigam, M. Boopathi, P.K. Gutch, B.K. Tripathi, A. Srivastava, M. Samuel, G.S. Agarwal, B. Singh, R. Vijayaraghavan, *Adv. Funct. Mater.* 22 (2012) 2352.
- [201] D. Wei, L. Grande, V. Chundi, R. White, C. Bower, P. Andrew, T. Ryhaenen, *Chem. Commun.* 48 (2012) 1239.
- [202] A.M. Abdelkader, I.A. Kinloch, R.A.W. Dryfe, *ACS Appl. Mater. Interfaces* 6 (2014) 1632.
- [203] A.J. Cooper, N.R. Wilson, I.A. Kinloch, R.A.W. Dryfe, *Carbon* 66 (2014) 340.
- [204] U. Hofmann, R. Holst, *Ber. Dtsch. Chem. Ges.* 72 (1939) 754.
- [205] A. Clause, R. Plass, H.P. Boehm, U. Hofmann, *Z. Anorg. Allg. Chem.* 291 (1957) 205.
- [206] G. Ruess, *Monatsh Chem.* 76 (1947) 381.
- [207] W. Scholz, H.P. Boehm, Z. Anorg. Allg. Chem. 369 (1969) 327.
- [208] T. Nakajima, A. Mabuchi, R. Hagiwara, *Carbon* 26 (1988) 357.
- [209] T. Nakajima, Y. Matsuo, *Carbon* 32 (1994) 469.
- [210] H. He, J. Klinowski, M. Forster, A. Lerf, *Chem. Phys. Lett.* 287 (1998) 53.
- [211] A. Lerf, H. He, M. Forster, J. Klinowski, *J. Phys. Chem. B* 102 (1998) 4477.

- [212] T. Szabó, O. Berkesi, P. Forgó, K. Josepovits, Y. Sanakis, D. Petridis, I. Dékány, *Chem. Mater.* 18 (2006) 2740.
- [213] T. Szabó, O. Berkesi, I. Dékány, *Carbon* 43 (2005) 3186.
- [214] L.B. Casabianca, M.A. Shaibat, W.W. Cai, S. Park, R. Piner, R.S. Ruoff, Y. Ishii, *J. Am. Chem. Soc.* 132 (2010) 5672.
- [215] D.W. Boukhvalov, M.I. Katsnelson, *J. Am. Chem. Soc.* 130 (2008) 10697.
- [216] W. Gao, L.B. Alemany, L.J. Ci, P.M. Ajayan, *Nat. Chem.* 1 (2009) 403.
- [217] D.R. Dreyer, S. Park, C.W. Bielawski, R.S. Ruoff, *Chem. Soc. Rev.* 39 (2010) 228.
- [218] L.J. Cote, F. Kim, J. Huang, *J. Am. Chem. Soc.* 131 (2008) 1043.
- [219] H.C. Schniepp, J.-L. Li, M.J. McAllister, H. Sai, M. Herrera-Alonso, D.H. Adamson, R.K. Prud'homme, R. Car, D.A. Saville, I.A. Aksay, *J. Phys. Chem. B* 110 (2006) 8535.
- [220] A. Buchsteiner, A. Lerf, J. Pieper, *J. Phys. Chem. B* 110 (2006) 22328.
- [221] J.W. Suk, R.D. Piner, J. An, R.S. Ruoff, *ACS Nano* 4 (2010) 6557.
- [222] H.A. Becerril, J. Mao, Z. Liu, R.M. Stoltenberg, Z. Bao, Y. Chen, *ACS Nano* 2 (2008) 463.
- [223] H. Chang, Z. Sun, Q. Yuan, F. Ding, X. Tao, F. Yan, Z. Zheng, *Adv. Mater.* 22 (2010) 4872.
- [224] Z. Luo, P.M. Vora, E.J. Mele, A.T.C. Johnson, J.M. Kikkawa, *Appl. Phys. Lett.* 94 (2009) 111909.
- [225] C. Mattevi, G. Eda, S. Agnoli, S. Miller, K.A. Mkhoyan, O. Celik, D. Mastrogiovanni, G. Granozzi, E. Garfunkel, M. Chhowalla, *Adv. Funct. Mater.* 19 (2009) 2577.
- [226] J.-A. Yan, L. Xian, M. Chou, *Phys. Rev. Lett.* 103 (2009) 086802.
- [227] Q. Zheng, Z. Li, J. Yang, J.-K. Kim, *Prog. Mater. Sci.* 64 (2014) 200.
- [228] S. Pei, H.-M. Cheng, *Carbon* 50 (2012) 3210.
- [229] C.K. Chua, M. Pumera, *Chem. Soc. Rev.* 43 (2014) 291.
- [230] G. Eda, M. Chhowalla, *Adv. Mater.* 22 (2010) 2392.
- [231] X. Wan, Y. Huang, Y. Chen, *Acc. Chem. Res.* 45 (2012) 598.
- [232] X. Wang, L. Zhi, K. Müllen, *Nano Lett.* 8 (2008) 323.
- [233] M. Acik, G. Lee, C. Mattevi, M. Chhowalla, K. Cho, Y.J. Chabal, *Nat. Mater.* 9 (2010) 840.
- [234] Y. Qiu, F. Guo, R. Hurt, I. Kueloats, *Carbon* 72 (2014) 215.
- [235] H.-B. Zhang, J.-W. Wang, Q. Yan, W.-G. Zheng, C. Chen, Z.-Z. Yu, *J. Mater. Chem.* 21 (2011) 5392.
- [236] M. Acik, G. Lee, C. Mattevi, A. Pirkle, R.M. Wallace, M. Chhowalla, K. Cho, Y. Chabal, *J. Phys. Chem. C* 115 (2011) 19761.
- [237] C. Botas, P. Alvarez, C. Blanco, R. Santamaria, M. Granda, M. Dolores Gutierrez, F. Rodriguez-Reinoso, R. Menendez, *Carbon* 52 (2013) 476.
- [238] X. Li, H. Wang, J.T. Robinson, H. Sanchez, G. Diankov, H. Dai, *J. Am. Chem. Soc.* 131 (2009) 15939.
- [239] H. Chen, M.B. Müller, K.J. Gilmore, G.G. Wallace, D. Li, *Adv. Mater.* 20 (2008) 3557.
- [240] C.H. Chuang, Y.F. Wang, Y.C. Shao, Y.C. Yeh, D.Y. Wang, C.W. Chen, J.W. Chiou, S.C. Ray, W.F. Pong, L. Zhang, J.F. Zhu, J.H. Guo, *Sci. Rep.* 4 (2014) 4525.
- [241] Z.-S. Wu, W. Ren, L. Gao, J. Zhao, Z. Chen, B. Liu, D. Tang, B. Yu, C. Jiang, H.-M. Cheng, *ACS Nano* 3 (2009) 411.
- [242] X. Li, G. Zhang, X. Bai, X. Sun, X. Wang, E. Wang, H. Dai, *Nat. Nanotechnol.* 3 (2008) 538.
- [243] C.D. Zangmeister, *Chem. Mater.* 22 (2010) 5625.
- [244] Z.-I. Wang, D. Xu, Y. Huang, Z. Wu, L.-M. Wang, X.-B. Zhang, *Chem. Commun.* 48 (2012) 976.
- [245] E.C. Mattson, H. Pu, S. Cui, M.A. Schofield, S. Rhim, G. Lu, M.J. Nasse, R.S. Ruoff, M. Weinert, M. Gajdardziska-Josifovska, J. Chen, C.J. Hirschmugl, *ACS Nano* 5 (2011) 9710.
- [246] L.T. Le, M.H. Ervin, H. Qiu, B.E. Fuchs, W.Y. Lee, *Electrochem. Commun.* 13 (2011) 355.
- [247] S. Ye, D. Hu, Q. Zhang, J. Fan, B. Chen, J. Feng, *J. Phys. Chem. C* 118 (2014) 25718.
- [248] S. Ye, J. Feng, *Polym. Chem.* 4 (2013) 1765.
- [249] R. Larciprete, S. Fabris, T. Sun, P. Lacovic, A. Baraldi, S. Lizzit, *J. Am. Chem. Soc.* 133 (2011) 17315.
- [250] C. Gong, M. Acik, R.M. Abolfath, Y. Chabal, K. Cho, *J. Phys. Chem. C* 116 (2012) 9969.
- [251] J.I. Paredes, S. Villar-Rodil, A. Martínez-Alonso, J.M.D. Tascón, *Langmuir* 24 (2008) 10560.
- [252] Y. Zhou, Q. Bao, L.A.L. Tang, Y. Zhong, K.P. Loh, *Chem. Mater.* 21 (2009) 2950.
- [253] S. Choudhary, H.P. Mungse, O.P. Khatri, *Chem. Asian J.* 8 (2013) 2070.
- [254] C. Bosch-Navarro, E. Coronado, C. Martí-Gastaldo, J.F. Sanchez-Royo, M. Gomez Gomez, *Nanoscale* 4 (2012) 3977.
- [255] Y. Xu, K. Sheng, C. Li, G. Shi, *ACS Nano* 4 (2010) 4324.
- [256] W. Chen, L. Yan, *Nanoscale* 3 (2011) 3132.
- [257] H. Hu, Z. Zhao, W. Wan, Y. Gogotsi, J. Qiu, *Adv. Mater.* 25 (2013) 2219.
- [258] Y. Li, J. Chen, L. Huang, C. Li, J.-D. Hong, G. Shi, *Adv. Mater.* 26 (2014) 4789.
- [259] H. Sun, Z. Xu, C. Gao, *Adv. Mater.* 25 (2013) 2554.
- [260] V. Chabot, D. Higgins, A. Yu, X. Xiao, Z. Chen, J. Zhang, *Energy Environ. Sci.* 7 (2014) 1564.
- [261] J.-L. Shi, W.-C. Du, Y.-X. Yin, Y.-G. Guo, L.-J. Wan, *J. Mater. Chem. A* 2 (2014) 10830.
- [262] S. Dubin, S. Gilje, K. Wang, V.C. Tung, K. Cha, A.S. Hall, J. Farrar, R. Varshneya, Y. Yang, R.B. Kaner, *ACS Nano* 4 (2010) 3845.
- [263] P. Viet Hung, C. Tran Viet, S.H. Hur, E. Oh, E.J. Kim, E.W. Shin, J.S. Chung, *J. Mater. Chem.* 21 (2011) 3371.
- [264] Y. Shen, H.-B. Zhang, H. Zhang, W. Ren, A. Dasari, G.-S. Tang, Z.-Z. Yu, *Carbon* 56 (2013) 132.
- [265] D. Zhou, Q.-Y. Cheng, B.-H. Han, *Carbon* 49 (2011) 3920.
- [266] K.L. Ai, Y.L. Liu, L.H. Lu, X.L. Cheng, L.H. Huo, *J. Mater. Chem.* 21 (2011) 3365.
- [267] Y. Zhu, M.D. Stoller, W. Cai, A. Velamakanni, R.D. Piner, D. Chen, R.S. Ruoff, *ACS Nano* 4 (2010) 1227.
- [268] O.C. Compton, B. Jain, D.A. Dikin, A. Abouimrane, K. Amine, S.T. Nguyen, *ACS Nano* 5 (2011) 4380.
- [269] W. Chen, L. Yan, P.R. Bangal, *Carbon* 48 (2010) 1146.
- [270] A.V. Murugan, T. Muraliganth, A. Manthiram, *Chem. Mater.* 21 (2009) 5004.
- [271] W. Qian, R. Hao, Y. Hou, Y. Tian, C. Shen, H. Gao, X. Liang, *Nano Res.* 2 (2009) 706.
- [272] H. Wang, J.T. Robinson, X. Li, H. Dai, *J. Am. Chem. Soc.* 131 (2009) 9910.
- [273] R. Wang, Y. Wang, C. Xu, J. Sun, L. Gao, *RSC Adv.* 3 (2013) 1194.
- [274] D. Chen, H. Feng, J. Li, *Chem. Rev.* 112 (2012) 6027.
- [275] N.A. Kotov, I. Dékány, J.H. Fendler, *Adv. Mater.* 8 (1996) 637.
- [276] S. Stankovich, D. Dikin, R. Piner, K. Kohlhaas, A. Kleinhammes, Y. Jia, Y. Wu, S. Nguyen, R. Ruoff, *Carbon* 45 (2007) 1558.
- [277] S. Park, Y. Hu, J.O. Hwang, E.-S. Lee, L.B. Casabianca, W. Cai, J.R. Potts, H.-W. Ha, S. Chen, J. Oh, S.O. Kim, Y.-H. Kim, Y. Ishii, R.S. Ruoff, *Nat. Commun.* 3 (2012) 638.
- [278] P.-G. Ren, et al. *Nanotechnology* 22 (2011) 055705.
- [279] Q. He, H.G. Sudibya, Z. Yin, S. Wu, H. Li, F. Boey, W. Huang, P. Chen, H. Zhang, *ACS Nano* 4 (2010) 3201.
- [280] Q. He, S. Wu, S. Gao, X. Cao, Z. Yin, H. Li, P. Chen, H. Zhang, *ACS Nano* 5 (2011) 5038.
- [281] D. Li, M.B. Muller, S. Gilje, R.B. Kaner, G.G. Wallace, *Nat. Nanotechnol.* 3 (2008) 101.
- [282] S. Park, J. An, I. Jung, R.D. Piner, S.J. An, X. Li, A. Velamakanni, R.S. Ruoff, *Nano Lett.* 9 (2009) 1593.
- [283] J.R. Lomeda, C.D. Doyle, D.V. Kosynkin, W.-F. Hwang, J.M. Tour, *J. Am. Chem. Soc.* 130 (2008) 16201.
- [284] Z. Wei, D.E. Barlow, P.E. Sheehan, *Nano Lett.* 8 (2008) 3141.
- [285] S. Park, J. An, J.R. Potts, A. Velamakanni, S. Murali, R.S. Ruoff, *Carbon* 49 (2011) 3019.
- [286] S. Villar-Rodil, J.I. Paredes, A. Martínez-Alonso, J.M.D. Tascón, *J. Mater. Chem.* 19 (2009) 3591.
- [287] S. Stankovich, D.A. Dikin, G.H.B. Dommett, K.M. Kohlhaas, E.J. Zimney, E.A. Stach, R.D. Piner, S.T. Nguyen, R.S. Ruoff, *Nature* 442 (2006) 282.
- [288] V.H. Pham, T.V. Cuong, T.-D. Nguyen-Phan, H.D. Pham, E.J. Kim, S.H. Hur, E.W. Shin, S. Kim, J.S. Chung, *Chem. Commun.* 46 (2010) 4375.
- [289] H.-J. Shin, K.K. Kim, A. Benayad, S.-M. Yoon, H.K. Park, I.-S. Jung, M.H. Jin, H.-K. Jeong, J.M. Kim, J.-Y. Choi, Y.H. Lee, *Adv. Funct. Mater.* 19 (2009) 1987.
- [290] Y. Si, E.T. Samulski, *Nano Lett.* 8 (2008) 1679.
- [291] C.K. Chua, M. Pumera, *J. Mater. Chem. A* 1 (2013) 1892.
- [292] J. Ji, G. Zhang, H. Chen, Y. Li, G. Zhang, F. Zhang, X. Fan, J. Mater. Chem. 21 (2011) 14498.
- [293] A. Ambrosi, C.K. Chua, A. Bonanni, M. Pumera, *Chem. Mater.* 24 (2012) 2292.
- [294] Y. Chen, X. Zhang, D. Zhang, P. Yu, Y. Ma, *Carbon* 49 (2011) 573.
- [295] P. Cui, J. Lee, E. Hwang, H. Lee, *Chem. Commun.* 47 (2011) 12370.
- [296] J. Zhao, S. Pei, W. Ren, L. Gao, H.-M. Cheng, *ACS Nano* 4 (2010) 5245.
- [297] S. Pei, J. Zhao, J. Du, W. Ren, H.-M. Cheng, *Carbon* 48 (2010) 4466.
- [298] I.K. Moon, J. Lee, R.S. Ruoff, H. Lee, *Nat. Commun.* 1 (2010) 73.
- [299] H.-P. Cong, X.-C. Ren, P. Wang, S.-H. Yu, *Energy Environ. Sci.* 6 (2013) 1185.
- [300] Y. Xu, K. Sheng, C. Li, G. Shi, *J. Mater. Chem.* 21 (2011) 7376.
- [301] D.R. Dreyer, S. Murali, Y. Zhu, R.S. Ruoff, C.W. Bielawski, *J. Mater. Chem.* 21 (2011) 3443.
- [302] J. Che, L. Shen, Y. Xiao, *J. Mater. Chem.* 20 (2010) 1722.
- [303] Y. Chen, X. Zhang, P. Yu, Y. Ma, *Chem. Commun.* (2009) 4527.
- [304] S. Liu, J. Tian, L. Wang, X. Sun, *Carbon* 49 (2011) 3158.
- [305] C.A. Amarnath, C.E. Hong, N.H. Kim, B.-C. Ku, T. Kuila, J.H. Lee, *Carbon* 49 (2011) 3497.
- [306] S. Mao, K. Yu, S. Cui, Z. Bo, G. Lu, J. Chen, *Nanoscale* 3 (2011) 2849.
- [307] R. Zhou, Y. Zheng, D. Hulicova-Jurcakova, S.Z. Qiao, *J. Mater. Chem. A* 1 (2013) 13179.
- [308] Z.-L. Wang, J.-M. Yan, H.-L. Wang, Y. Ping, Q. Jiang, *J. Mater. Chem. A* 1 (2013) 12721.
- [309] C. Zhang, R. Hao, H. Yin, F. Liu, Y. Hou, *Nanoscale* 4 (2012) 7326.
- [310] S. Zhao, H. Yin, L. Du, G. Yin, Z. Tang, S. Liu, *J. Mater. Chem. A* 2 (2014) 3719.
- [311] Z. Tang, H. Chen, X. Chen, L. Wu, X. Yu, *J. Am. Chem. Soc.* 134 (2012) 5464.
- [312] V.H. Pham, S.H. Hur, E.J. Kim, B.S. Kim, J.S. Chung, *Chem. Commun.* 49 (2013) 6665.
- [313] B. Zheng, J. Wang, F.-B. Wang, X.-H. Xia, *J. Mater. Chem. A* 2 (2014) 9079.
- [314] Z. Juanjuan, L. Ruiyi, L. Zaijun, L. Junkang, G. Zhiguo, W. Guangli, *Nanoscale* 6 (2014) 5458.
- [315] Y. Liu, K. Huang, H. Luo, H. Li, X. Qi, J. Zhong, *RSC Adv.* 4 (2014) 17653.
- [316] P. Kannan, T. Maiyalagan, N.G. Sahoo, M. Opallo, *J. Mater. Chem. B* 1 (2013) 4655.
- [317] Y.-K. Kim, M.-H. Kim, D.-H. Min, *Chem. Commun.* 47 (2011) 3195.
- [318] C. Zhu, S. Guo, Y. Fang, S. Dong, *ACS Nano* 4 (2010) 2429.
- [319] M. Fernandez-Merino, L. Guardia, J. Paredes, S. Villar-Rodil, P. Solis-Fernandez, A. Martínez-Alonso, J. Tascón, *J. Phys. Chem. C* 114 (2010) 6426.
- [320] J. Zhang, H. Yang, G. Shen, P. Cheng, J. Zhang, S. Guo, *Chem. Commun.* 46 (2010) 1112.
- [321] J. Gao, F. Liu, Y. Liu, N. Ma, Z. Wang, X. Zhang, *Chem. Mater.* 22 (2010) 2213.
- [322] G. Wang, F. Qian, C.W. Saltikov, Y. Jiao, Y. Li, *Nano Res.* 4 (2011) 563.
- [323] O. Akhavan, E. Ghaderi, *Carbon* 50 (2012) 1853.
- [324] E.C. Salas, Z. Sun, A. Luttge, J.M. Tour, *ACS Nano* 4 (2010) 4852.
- [325] J. Ma, X. Wang, Y. Liu, T. Wu, Y. Liu, Y. Guo, R. Li, X. Sun, F. Wu, C. Li, *J. Mater. Chem. A* 1 (2013) 2192.
- [326] S. Bose, T. Kuila, A.K. Mishra, N.H. Kim, J.H. Lee, *J. Mater. Chem.* 22 (2012) 9696.
- [327] D. Chen, L. Li, L. Guo, *Nanotechnology* 22 (2011) 325601.

- [328] B.K. Barman, P. Mahanandia, K.K. Nanda, *RSC Adv.* 3 (2013) 12621.
- [329] V.H. Pham, H.D. Pham, T.T. Dang, S.H. Hur, E.J. Kim, B.S. Kong, S. Kim, J.S. Chung, *J. Mater. Chem.* 22 (2012) 10530.
- [330] N.A. Kumar, S. Gambarelli, F. Duclairoir, G. Bidan, L. Dubois, *J. Mater. Chem. A* 1 (2013) 2789.
- [331] R. SundarāDey, C. RetnaāRaj, *Chem. Commun.* 48 (2012) 1787.
- [332] X. Mei, J. Ouyang, *Carbon* 49 (2011) 5389.
- [333] Z.-J. Fan, W. Kai, J. Yan, T. Wei, L.-J. Zhi, J. Feng, Y.-M. Ren, L.-P. Song, F. Wei, *ACS Nano* 5 (2010) 191.
- [334] Z. Fan, K. Wang, T. Wei, J. Yan, L. Song, B. Shao, *Carbon* 48 (2010) 1686.
- [335] S. Yang, W. Yue, D. Huang, C. Chen, H. Lin, X. Yang, *RSC Adv.* 2 (2012) 8827.
- [336] Y. Liu, Y. Li, M. Zhong, Y. Yang, Y. Wen, M. Wang, *J. Mater. Chem.* 21 (2011) 15449.
- [337] W. Chen, L. Yan, P. Bangal, *J. Phys. Chem. C* 114 (2010) 19885.
- [338] Q. Ma, J. Song, C. Jin, Z. Li, J. Liu, S. Meng, J. Zhao, Y. Guo, *Carbon* 54 (2013) 36.
- [339] C.K. Chua, A. Ambrosi, M. Pumera, *J. Mater. Chem.* 22 (2012) 11054.
- [340] S. Some, Y. Kim, Y. Yoon, H. Yoo, S. Lee, Y. Park, H. Lee, *Sci. Rep.* 3 (2013) 1929.
- [341] T. Zhou, F. Chen, K. Liu, H. Deng, Q. Zhang, J. Feng, Q. Fu, *Nanotechnology* 22 (2011) 045704.
- [342] Y. Shao, J. Wang, M. Engelhard, C. Wang, Y. Lin, *J. Mater. Chem.* 20 (2010) 743.
- [343] G.K. Ramesha, S. Sampath, *J. Phys. Chem. C* 113 (2009) 7985.
- [344] Z. Wang, X. Zhou, J. Zhang, F. Boey, H. Zhang, *J. Phys. Chem. C* 113 (2009) 14071.
- [345] A. Viinikanoja, Z. Wang, J. Kauppi, C. Kvarnstrom, *Phys. Chem. Chem. Phys.* 14 (2012) 14003.
- [346] G. Williams, B. Seger, P.V. Kamat, *ACS Nano* 2 (2008) 1487.
- [347] O. Akhavan, *Carbon* 49 (2011) 11.
- [348] T. Wu, S. Liu, Y. Luo, W. Lu, L. Wang, X. Sun, *Nanoscale* 3 (2011) 2142.
- [349] Y. Sang, Z. Zhao, J. Tian, P. Hao, H. Jiang, H. Liu, J.P. Claverie, *Small* 10 (2014) 3775.
- [350] G. Eda, G. Fanchini, M. Chhowalla, *Nat. Nanotechnol.* 3 (2008) 270.
- [351] X. Diez-Betruji, F.J. Mompean, C. Munuera, J. Rubio-Zuazo, R. Menendez, G.R. Castro, A. de Andres, *Carbon* 80 (2014) 40.
- [352] A. Bagri, C. Mattevi, M. Acik, Y.J. Chabal, M. Chhowalla, V.B. Shenoy, *Nat. Chem.* 2 (2010) 581.
- [353] X. Qi, K.Y. Pu, H. Li, X. Zhou, S. Wu, Q.L. Fan, B. Liu, F. Boey, W. Huang, H. Zhang, *Angew. Chem. Int. Ed.* 49 (2010) 9426.
- [354] X. Qi, K.Y. Pu, X. Zhou, H. Li, B. Liu, F. Boey, W. Huang, H. Zhang, *Small* 6 (2010) 663.
- [355] K. Yan, L. Fu, H. Peng, Z. Liu, *Acc. Chem. Res.* 46 (2013) 2263.
- [356] K.S. Kim, Y. Zhao, H. Jang, S.Y. Lee, J.M. Kim, K.S. Kim, J.-H. Ahn, P. Kim, J.-Y. Choi, B.H. Hong, *Nature* 457 (2009) 706.
- [357] N. Liu, L. Fu, B. Dai, K. Yan, X. Liu, R. Zhao, Y. Zhang, Z. Liu, *Nano Lett.* 11 (2010) 297.
- [358] X. Li, W. Cai, L. Colombo, R.S. Ruoff, *Nano Lett.* 9 (2009) 4268.
- [359] X. Li, W. Cai, J. An, S. Kim, J. Nah, D. Yang, R. Piner, A. Velamakanni, I. Jung, E. Tutuc, *Science* 324 (2009) 1312.
- [360] X. Liu, L. Fu, N. Liu, T. Gao, Y. Zhang, L. Liao, Z. Liu, *J. Phys. Chem. C* 115 (2011) 11976.
- [361] C. Mattevi, H. Kim, M. Chhowalla, *J. Mater. Chem.* 21 (2011) 3324.
- [362] R. Muñoz, C. Gómez-Aleixandre, *Chem. Vap. Depos.* 19 (2013) 297.
- [363] P. Sutter, *Nat. Mater.* 8 (2009) 171.
- [364] C. Berger, Z. Song, X. Li, X. Wu, N. Brown, C. Naud, D. Mayou, T. Li, J. Hass, A.N. Marchenkov, *Science* 312 (2006) 1191.
- [365] J. Hass, R. Feng, T. Li, X. Li, Z. Zong, W. De Heer, P. First, E. Conrad, C. Jeffrey, C. Berger, *Appl. Phys. Lett.* 89 (2006) 143106.
- [366] H. Hibino, H. Kageshima, F. Maeda, M. Nagase, Y. Kobayashi, H. Yamaguchi, *Phys. Rev. B* 77 (2008) 075413.
- [367] R. Tromp, J. Hannon, *Phys. Rev. Lett.* 102 (2009) 106104.
- [368] K.V. Emtsev, A. Bostwick, K. Horn, J. Jobst, G.L. Kellogg, L. Ley, J.L. McChesney, T. Ohta, S.A. Reshanov, J. Rohrl, E. Rotenberg, A.K. Schmid, D. Waldmann, H.B. Weber, T. Seyller, *Nat. Mater.* 8 (2009) 203.
- [369] J. Kunc, Y. Hu, J. Palmer, Z. Guo, J. Hankinson, S.H. Gamal, C. Berger, W.A. de Heer, *Nano Lett.* 14 (2014) 5170.
- [370] J. Kim, C. Bayram, H. Park, C.-W. Cheng, C. Dimitrakopoulos, J.A. Ott, K.B. Reuter, S.W. Bedell, D.K. Sadana, *Nat. Commun.* 5 (2014).
- [371] L. Croguennec, M.R. Palacin, *J. Am. Chem. Soc.* 137 (2015) 3140.
- [372] M. Obrovac, V. Chevrier, *Chem. Rev.* 114 (2014) 11444.
- [373] A. Manthiram, *J. Phys. Chem. Lett.* 2 (2011) 176.
- [374] N.S. Choi, Z. Chen, S.A. Freunberger, X. Ji, Y.K. Sun, K. Amine, G. Yushin, L.F. Nazar, J. Cho, P.G. Bruce, *Angew. Chem. Int. Ed.* 51 (2012) 9994.
- [375] Y. Tang, Y. Zhang, W. Li, B. Ma, X. Chen, *Chem. Soc. Rev.* (2015). <http://dx.doi.org/10.1039/C4CS00442F>.
- [376] S. Han, D. Wu, S. Li, F. Zhang, X. Feng, *Small* 9 (2013) 1173.
- [377] J. Hou, Y. Shao, M.W. Ellis, R.B. Moore, B. Yi, *Phys. Chem. Chem. Phys.* 13 (2011) 15384.
- [378] M. Pumera, *Chem. Soc. Rev.* 39 (2010) 4146.
- [379] M. Winter, J.O. Besenhard, M.E. Spahr, P. Novák, *Adv. Mater.* 10 (1998) 725.
- [380] N.A. Kaskhedikar, J. Maier, *Adv. Mater.* 21 (2009) 2664.
- [381] G.X. Wang, X.P. Shen, J. Yao, J. Park, *Carbon* 47 (2009) 2049.
- [382] J. Dahn, T. Zheng, Y. Liu, J. Xue, *Science* 270 (1995) 590.
- [383] O.A.C. Vargas, A. Caballero, J. Morales, *Nanoscale* 4 (2012) 2083.
- [384] E. Yoo, J. Kim, E. Hosono, H.-s. Zhou, T. Kudo, I. Honma, *Nano Lett.* 8 (2008) 2277.
- [385] P. Lian, X. Zhu, S. Liang, Z. Li, W. Yang, H. Wang, *Electrochim. Acta* 55 (2010) 3909.
- [386] P. Guo, H.H. Song, X.H. Chen, *Electrochim. Commun.* 11 (2009) 1320.
- [387] D. Pan, S. Wang, B. Zhao, M. Wu, H. Zhang, Y. Wang, Z. Jiao, *Chem. Mater.* 21 (2009) 3136.
- [388] Y. Chen, Z. Lu, L. Zhou, Y.-W. Mai, H. Huang, *Nanoscale* 4 (2012) 6800.
- [389] K. Sato, M. Noguchi, A. Demachi, N. Oki, M. Endo, *Science* 264 (1994) 556.
- [390] S. Yata, H. Kinoshita, M. Komori, N. Ando, T. Kashiwamura, T. Harada, K. Tanaka, T. Yamabe, *Synth. Met.* 62 (1994) 153.
- [391] Y. Chen, Z. Lu, L. Zhou, Y.-W. Mai, H. Huang, *Energy Environ. Sci.* 5 (2012) 7898.
- [392] Y. Chen, X. Li, K. Park, J. Song, J. Hong, L. Zhou, Y.-W. Mai, H. Huang, J.B. Goodenough, *J. Am. Chem. Soc.* 135 (2013) 16280.
- [393] Y. Chen, X. Li, X. Zhou, H. Yao, H. Huang, Y.-W. Mai, L. Zhou, *Energy Environ. Sci.* 7 (2014) 2689.
- [394] A.C. Ferrari, D.M. Basko, *Nat. Nanotechnol.* 8 (2013) 235.
- [395] F. Yao, F. Guenes, T. Huy Quang, S.M. Lee, S.J. Chae, K.Y. Sheem, C.S. Cojocaru, S.S. Xie, Y.H. Lee, *J. Am. Chem. Soc.* 134 (2012) 8646.
- [396] S. Yin, Y. Zhang, J. Kong, C. Zou, C.M. Li, X. Lu, J. Ma, F.Y.C. Boey, X. Chen, *ACS Nano* 5 (2011) 3831.
- [397] C. Uthaisar, V. Barone, *Nano Lett.* 10 (2010) 2838.
- [398] H. Kim, Z. Wen, K. Yu, O. Mao, J. Chen, *J. Mater. Chem.* 22 (2012) 15514.
- [399] X. Li, Y. Hu, J. Liu, A. Lushington, R. Li, X. Sun, *Nanoscale* 5 (2013) 12607.
- [400] P. Verma, P. Maire, P. Novak, *Electrochim. Acta* 55 (2010) 6332.
- [401] S. Shi, P. Lu, Z. Liu, Y. Qi, L.G. Hector Jr., H. Li, S.J. Harris, *J. Am. Chem. Soc.* 134 (2012) 15476.
- [402] L. Wan, Z. Ren, H. Wang, G. Wang, X. Tong, S. Gao, J. Bai, *Diam. Relat. Mater.* 20 (2011) 756.
- [403] T. Chen, L. Pan, K. Yu, Z. Sun, *Solid State Ion.* 229 (2012) 9.
- [404] S. Chen, W. Yeoh, Q. Liu, G. Wang, *Carbon* 50 (2012) 4557.
- [405] Y. Hu, X. Li, J. Wang, R. Li, X. Sun, *J. Power Sources* 237 (2013) 41.
- [406] Z. Zheng, X. Zhang, F. Pei, Y. Dai, X. Fang, T. Wang, N. Zhang, *J. Mater. Chem. A* 3 (2015) 19800.
- [407] Y. Yan, Y.-X. Yin, S. Xin, Y.-G. Guo, L.-J. Wan, *Chem. Commun.* 48 (2012) 10663.
- [408] H. Wang, H. Peng, G. Li, K. Chen, *Chem. Eng. J.* 275 (2015) 160.
- [409] Z.-J. Fan, J. Yan, T. Wei, G.-Q. Ning, L.-J. Zhi, J.-C. Liu, D.-X. Cao, G.-L. Wang, F. Wei, *ACS Nano* 5 (2011) 2787.
- [410] S. Li, Y. Luo, W. Lv, W. Yu, S. Wu, P. Hou, Q. Yang, Q. Meng, C. Liu, H.M. Cheng, *Adv. Energy Mater.* 1 (2011) 486.
- [411] H.R. Byon, B.M. Gallant, S.W. Lee, Y. Shao-Horn, *Adv. Funct. Mater.* 23 (2013) 1037.
- [412] V. Sridhar, I. Lee, H.-H. Chun, H. Park, *Carbon* 87 (2015) 186.
- [413] V. Sridhar, I. Lee, H.H. Chun, H. Park, *RSC Adv.* 5 (2015) 68270.
- [414] B.P. Vinayan, R. Nagar, V. Raman, N. Rajalakshmi, K.S. Dhathathreyan, S. Ramaprabhu, *J. Mater. Chem.* 22 (2012) 9949.
- [415] C. Zhong, J.-Z. Wang, D. Wexler, H.-K. Liu, *Carbon* 66 (2014) 637.
- [416] A.P. Cohn, L. Oakes, R. Carter, S. Chatterjee, A.S. Westover, K. Share, C.L. Pint, *Nanoscale* 6 (2014) 4669.
- [417] S. Chen, P. Chen, Y. Wang, *Nanoscale* 3 (2011) 4323.
- [418] R. Guo, L. Zhao, W. Yue, *Electrochim. Acta* 152 (2015) 338.
- [419] A.D. Roberts, X. Li, H. Zhang, *Chem. Soc. Rev.* 43 (2014) 4341.
- [420] U.N. Maiti, W.J. Lee, J.M. Lee, Y. Oh, J.Y. Kim, J.E. Kim, J. Shim, T.H. Han, S.O. Kim, *Adv. Mater.* 26 (2014) 40.
- [421] L. Qie, W.M. Chen, Z.H. Wang, Q.G. Shao, X. Li, L.X. Yuan, X.L. Hu, W.X. Zhang, Y. Huang, *Adv. Mater.* 24 (2012) 2047.
- [422] A. Dey, *J. Electrochem. Soc.* 118 (1971) 1547.
- [423] C.-M. Park, J.-H. Kim, H. Kim, H.-J. Sohn, *Chem. Soc. Rev.* 39 (2010) 3115.
- [424] M.R. Palacin, *Chem. Soc. Rev.* 38 (2009) 2565.
- [425] V. Aravindan, Y.S. Lee, S. Madhavi, *Adv. Energy Mater.* (2015) 1402225.
- [426] H. Wu, Y. Cui, *Nano Today* 7 (2012) 414.
- [427] M.T. McDowell, S. Woo Lee, C. Wang, Y. Cui, *Nano Energy* 1 (2012) 401.
- [428] C.-Y. Chou, H. Kim, G.S. Hwang, *J. Phys. Chem. C* 115 (2011) 20018.
- [429] M.R. Zafmif, H.T. Nguyen, E. Moya, Y.H. Lee, D. Pribat, *J. Mater. Chem. A* 1 (2013) 9566.
- [430] J.R. Szczech, S. Jin, *Energy Environ. Sci.* 4 (2011) 56.
- [431] Y. Wang, J. Dahn, *J. Electrochem. Soc.* 153 (2006) A2188.
- [432] X. Su, Q. Wu, J. Li, X. Xiao, A. Lott, W. Lu, B.W. Sheldon, J. Wu, *Adv. Energy Mater.* 4 (2014) 1300882.
- [433] K. Eom, T. Joshi, A. Bordes, I. Do, T.F. Fuller, *J. Power Sources* 249 (2014) 118.
- [434] D. Chen, R. Yi, S. Chen, T. Xu, M.L. Gordin, D. Wang, *Solid State Ion.* 254 (2014) 65.
- [435] H. Mi, Y. Li, P. Zhu, X. Chai, L. Sun, H. Zhuo, Q. Zhang, C. He, J. Liu, *J. Mater. Chem. A* 2 (2014) 11254.
- [436] N. Lin, J. Zhou, Y. Zhu, Y. Qian, *J. Mater. Chem. A* 2 (2014) 19604.
- [437] X. Zhao, M. Li, K.-H. Chang, Y.-M. Lin, *Nano Res.* 7 (2014) 1429.
- [438] H.-J. Kim, S.E. Lee, J. Lee, J.-Y. Jung, E.-S. Lee, J.-H. Choi, J.-H. Jung, M. Oh, S. Hyun, D.-G. Choi, *Phys. E—Low-Dimens. Syst. Nanostruct.* 61 (2014) 204.
- [439] Y. Yang, J.-G. Ren, X. Wang, Y.-S. Chui, Q.-H. Wu, X. Chen, W. Zhang, *Nanoscale* 5 (2013) 8689.
- [440] F.M. Hassan, A.R. Elsayed, V. Chabot, R. Batmaz, X. Xiao, Z. Chen, *ACS Appl. Mater. Interfaces* 6 (2014) 13757.
- [441] S. Jing, H. Jiang, Y. Hu, C. Li, *J. Mater. Chem. A* 2 (2014) 16360.
- [442] H.-C. Tao, X.-L. Yang, L.-L. Zhang, S.-B. Ni, *Mater. Chem. Phys.* 147 (2014) 528.
- [443] X. Chen, Y. Huang, J. Chen, X. Zhang, C. Li, H. Huang, *Ceram. Int.* 41 (2015) 8533.
- [444] S.-L. Chou, J.-Z. Wang, M. Chouair, H.-K. Liu, J.A. Stride, S.-X. Dou, *Electrochim. Commun.* 12 (2010) 303.
- [445] W. Sun, R. Hu, H. Liu, M. Zeng, L. Yang, H. Wang, M. Zhu, *J. Power Sources* 268 (2014) 610.
- [446] R. Hu, W. Sun, Y. Chen, M. Zeng, M. Zhu, *J. Mater. Chem. A* 2 (2014) 9118.
- [447] X. Gao, J. Li, Y. Xie, D. Guan, C. Yuan, *ACS Appl. Mater. Interfaces* 7 (2015) 7855.

- [448] Y. Du, G. Zhu, K. Wang, Y. Wang, C. Wang, Y. Xia, *Electrochem. Commun.* 36 (2013) 107.
- [449] D. He, F. Bai, L. Li, L. Shen, H.H. Kung, N. Bao, *Electrochim. Acta* 169 (2015) 409.
- [450] S. Zhu, C. Zhu, J. Ma, Q. Meng, Z. Guo, Z. Yu, T. Lu, Y. Li, D. Zhang, W.M. Lau, *RSC Adv.* 3 (2013) 6141.
- [451] S. Chen, P. Bao, X. Huang, B. Sun, G. Wang, *Nano Res.* 7 (2014) 85.
- [452] Y.Q. Zhang, X.H. Xia, X.L. Wang, Y.J. Mai, S.J. Shi, Y.Y. Tang, L. Li, J.P. Tu, *Electrochem. Commun.* 23 (2012) 17.
- [453] K. Evanoff, A. Magasinski, J.B. Yang, G. Yushin, *Adv. Energy Mater.* 1 (2011) 495.
- [454] F. Li, H. Yue, Z. Yang, X. Li, Y. Qin, D. He, *Mater. Lett.* 128 (2014) 132.
- [455] J.-G. Ren, Q.-H. Wu, G. Hong, W.-J. Zhang, H. Wu, K. Amine, J. Yang, S.-T. Lee, *Energy Technol.* 1 (2013) 77.
- [456] J.-G. Ren, C. Wang, Q.-H. Wu, X. Liu, Y. Yang, L. He, W. Zhang, *Nanoscale* 6 (2014) 3353.
- [457] X. Xin, X. Zhou, F. Wang, X. Yao, X. Xu, Y. Zhu, Z. Liu, *J. Mater. Chem.* 22 (2012) 7724.
- [458] C. Wang, Y.-S. Chui, R. Ma, T. Wong, J.-G. Ren, Q.-H. Wu, X. Chen, W. Zhang, *J. Mater. Chem. A* 1 (2013) 10092.
- [459] N. Li, S. Jin, Q. Liao, H. Cu, C.X. Wang, *Nano Energy* 5 (2014) 105.
- [460] M. Ko, S. Chae, S. Jeong, P. Oh, J. Cho, *ACS Nano* 8 (2014) 8591.
- [461] H. Xiang, K. Zhang, G. Ji, J.Y. Lee, C. Zou, X. Chen, J. Wu, *Carbon* 49 (2011) 1787.
- [462] H. Tang, Y.J. Zhang, Q.Q. Xiong, J.D. Cheng, Q. Zhang, X.L. Wang, C.D. Gu, J.P. Tu, *Electrochim. Acta* 156 (2015) 86.
- [463] J. Luo, X. Zhao, J. Wu, H.D. Jang, H.H. Kung, J. Huang, *J. Phys. Chem. Lett.* 3 (2012) 1824.
- [464] Y.-S. He, P. Gao, J. Chen, X. Yang, X.-Z. Liao, J. Yang, Z.-F. Ma, *RSC Adv.* 1 (2011) 958.
- [465] X. Zhou, A.-M. Cao, L.-J. Wan, Y.-G. Guo, *Nano Res.* 5 (2012) 845.
- [466] X. Zhao, C.M. Hayner, M.C. Kung, H.H. Kung, *Adv. Energy Mater.* 1 (2011) 1079.
- [467] J.-Z. Wang, C. Zhong, S.-L. Chou, H.-K. Liu, *Electrochem. Commun.* 12 (2010) 1467.
- [468] X. Zhou, Y.-X. Yin, L.-J. Wan, Y.-G. Guo, *Chem. Commun.* 48 (2012) 2198.
- [469] V. Chabot, K. Feng, H.W. Park, F.M. Hassan, A.R. Elsayed, A. Yu, X. Xiao, Z. Chen, *Electrochim. Acta* 130 (2014) 127.
- [470] L. Gan, H. Guo, Z. Wang, X. Li, W. Peng, J. Wang, S. Huang, M. Su, *Electrochim. Acta* 104 (2013) 117.
- [471] F.-H. Du, K.-X. Wang, W. Fu, P.-F. Gao, J.-F. Wang, J. Yang, J.-S. Chen, *J. Mater. Chem. A* 1 (2013) 13648.
- [472] X. Zhou, Y.-G. Guo, *J. Mater. Chem. A* 1 (2013) 9019.
- [473] S.Y. Kim, K.S. Yang, B.-H. Kim, *J. Power Sources* 273 (2015) 404.
- [474] D.P. Wong, R. Suriyaprabha, R. Yuvakumar, V. Rajendran, Y.-T. Chen, B.-J. Hwang, L.-C. Chen, K.-H. Chen, *J. Mater. Chem. A* 2 (2014) 13437.
- [475] D.P. Wong, H.-P. Tseng, Y.-T. Chen, B.-J. Hwang, L.-C. Chen, K.-H. Chen, *Carbon* 63 (2013) 397.
- [476] J.K. Lee, K.B. Smith, C.M. Hayner, H.H. Kung, *Chem. Commun.* 46 (2010) 2025.
- [477] F. Maroni, R. Raccichini, A. Birrozzi, G. Carbonari, R. Tossici, F. Croce, R. Marassi, F. Nobili, *J. Power Sources* 269 (2014) 873.
- [478] M. Zhou, T. Cai, F. Pu, H. Chen, Z. Wang, H. Zhang, S. Guan, *ACS Appl. Mater. Interfaces* 5 (2013) 3449.
- [479] Y. Zhu, W. Liu, X. Zhang, J. He, J. Chen, Y. Wang, T. Cao, *Langmuir* 29 (2013) 744.
- [480] G. Zhao, L. Zhang, Y. Meng, N. Zhang, K. Sun, *J. Power Sources* 240 (2013) 212.
- [481] Y. Wen, Y. Zhu, A. Langrock, A. Manivannan, S.H. Ehrman, C. Wang, *Small* 9 (2013) 2810.
- [482] Y.-S. Ye, X.-L. Xie, J. Rick, F.-C. Chang, B.-J. Hwang, *J. Power Sources* 247 (2014) 991.
- [483] G. Decher, *Science* 277 (1997) 1232.
- [484] F. Caruso, R.A. Caruso, H. Möhwald, *Science* 282 (1998) 1111.
- [485] J. Ji, H. Ji, L.L. Zhang, X. Zhao, X. Bai, X. Fan, F. Zhang, R.S. Ruoff, *Adv. Mater.* 25 (2013) 4673.
- [486] S. Xun, X. Song, L. Wang, M. Grass, Z. Liu, V. Battaglia, G. Liu, *J. Electrochem. Soc.* 158 (2011) A1260.
- [487] Y.S. Hu, R. Demir-Cakan, M.M. Titirici, J.O. Müller, R. Schlögl, M. Antonietti, J. Maier, *Angew. Chem. Int. Ed.* 47 (2008) 1645.
- [488] X. Zhou, Y.-X. Yin, L.-J. Wan, Y.-G. Guo, *Adv. Energy Mater.* 2 (2012) 1086.
- [489] Z.-F. Li, H. Zhang, Q. Liu, Y. Liu, L. Stanciu, J. Xie, *ACS Appl. Mater. Interfaces* 6 (2014) 5996.
- [490] B. Wang, X. Li, X. Zhang, B. Luo, M. Jin, M. Liang, S.A. Dayeh, S.T. Picraux, L. Zhi, *ACS Nano* 7 (2013) 1437.
- [491] G. Jeong, Y.-U. Kim, H. Kim, Y.-J. Kim, H.-J. Sohn, *Energy Environ. Sci.* 4 (2011) 1986.
- [492] Y. Zhao, X. Li, B. Yan, D. Li, S. Lawes, X. Sun, *J. Power Sources* 274 (2015) 869.
- [493] C. Wang, J.-Y. Yang, Y. Tang, H. Bi, F. Liao, J. Lin, Z. Shi, F. Huang, R.P.S. Han, *RSC Adv.* 3 (2013) 21588.
- [494] L. Ji, Z. Tan, T. Kuykendall, E.J. An, Y. Fu, V. Battaglia, Y. Zhang, *Energy Environ. Sci.* 4 (2011) 3611.
- [495] C. Wang, Y. Li, Y.-S. Chui, Q.-H. Wu, X. Chen, W. Zhang, *Nanoscale* 5 (2013) 10599.
- [496] J. Zhu, D. Wang, L. Cao, T. Liu, *J. Mater. Chem. A* 2 (2014) 12918.
- [497] Z. Chen, K. Xie, X. Hong, *Electrochim. Acta* 108 (2013) 674.
- [498] A.M. Chockla, M.G. Panthani, V.C. Holmberg, C.M. Hessel, D.K. Reid, T.D. Bogart, J.T. Harris, C.B. Mullins, B.A. Korgel, *J. Phys. Chem. C* 116 (2012) 11917.
- [499] F.-H. Du, Y.-S. Liu, J. Long, Q.-C. Zhu, K.-X. Wang, X. Wei, J.-S. Chen, *Chem. Commun.* 50 (2014) 9961.
- [500] W. Yue, S. Yang, Y. Liu, X. Yang, *Mater. Res. Bull.* 48 (2013) 1575.
- [501] S. Liang, X. Zhu, P. Lian, W. Yang, H. Wang, *J. Solid State Chem.* 184 (2011) 1400.
- [502] Y. Zou, Y. Wang, *ACS Nano* 5 (2011) 8108.
- [503] S. Chen, Y. Wang, H. Ahn, G. Wang, *J. Power Sources* 216 (2012) 22.
- [504] Z. Wen, S. Cui, H. Kim, S. Mao, K. Yu, G. Lu, H. Pu, O. Mao, J. Chen, *J. Mater. Chem.* 22 (2012) 3300.
- [505] G. Wang, B. Wang, X. Wang, J. Park, S. Dou, H. Ahn, K. Kim, *J. Mater. Chem.* 19 (2009) 8378.
- [506] W. Yue, S. Yang, Y. Ren, X. Yang, *Electrochim. Acta* 92 (2013) 412.
- [507] F.R. Beck, R. Epur, D. Hong, A. Manivannan, P.N. Kumta, *Electrochim. Acta* 127 (2014) 299.
- [508] P. Lian, J. Wang, D. Cai, G. Liu, Y. Wang, H. Wang, *J. Alloys Compd.* 604 (2014) 188.
- [509] X. Zhou, Y. Zou, J. Yang, *J. Power Sources* 253 (2014) 287.
- [510] B. Luo, B. Wang, X. Li, Y. Jia, M. Liang, L. Zhi, *Adv. Mater.* 24 (2012) 3538.
- [511] Y. Yu, L. Gu, C. Wang, A. Dhanabalan, P.A. van Aken, J. Maier, *Angew. Chem. Int. Ed.* 48 (2009) 6485.
- [512] D. Deng, J.Y. Lee, *Angew. Chem. Int. Ed.* 48 (2009) 1660.
- [513] D. Wang, X. Li, J. Yang, J. Wang, D. Geng, R. Li, M. Cai, T.-K. Sham, X. Sun, *Phys. Chem. Chem. Phys.* 15 (2013) 3535.
- [514] S. Chen, P. Chen, M. Wu, D. Pan, Y. Wang, *Electrochem. Commun.* 12 (2010) 1302.
- [515] B. Luo, B. Wang, M. Liang, J. Ning, X. Li, L. Zhi, *Adv. Mater.* 24 (2012) 1405.
- [516] N. Li, H. Song, H. Cui, G. Yang, C. Wang, *J. Mater. Chem. A* 2 (2014) 2526.
- [517] J. Qin, C. He, N. Zhao, Z. Wang, C. Shi, E.-Z. Liu, J. Li, *ACS Nano* 8 (2014) 1728.
- [518] N. Li, H. Song, H. Cui, C. Wang, *Nano Energy* 3 (2014) 102.
- [519] C. Fuller, J. Severiens, *Phys. Rev.* 96 (1954) 21.
- [520] J. Graetz, C. Ahn, R. Yazami, B. Fultz, *J. Electrochem. Soc.* 151 (2004) A698.
- [521] M.-H. Park, Y. Cho, K. Kim, J. Kim, M. Liu, J. Cho, *Angew. Chem. Int. Ed.* 50 (2011) 9647.
- [522] K.H. Seng, M.-H. Park, Z.P. Guo, H.K. Liu, J. Cho, *Angew. Chem. Int. Ed.* 51 (2012) 5657.
- [523] X. Zhong, J. Wang, W. Li, X. Liu, Z. Yang, L. Gu, Y. Yu, *RSC Adv.* 4 (2014) 58184.
- [524] J. Cheng, J. Du, *CrystEngComm* 14 (2012) 397.
- [525] C. Zhong, J.-Z. Wang, X.-W. Gao, D. Wexler, H.-K. Liu, *J. Mater. Chem. A* 1 (2013) 10798.
- [526] F.-W. Yuan, H.-Y. Tuan, *Chem. Mater.* 26 (2014) 2172.
- [527] S. Jin, N. Li, H. Cui, C. Wang, *ACS Appl. Mater. Interfaces* 6 (2014) 19397.
- [528] J.-G. Ren, Q.-H. Wu, H. Tang, G. Hong, W. Zhang, S.-T. Lee, *J. Mater. Chem. A* 1 (2013) 1821.
- [529] C.D. Wang, Y.S. Chui, Y. Li, X.F. Chen, W.J. Zhang, *Appl. Phys. Lett.* 103 (2013) 253903.
- [530] D. Li, K.H. Seng, D. Shi, Z. Chen, H.K. Liu, Z. Guo, *J. Mater. Chem. A* 1 (2013) 14115.
- [531] D.-J. Xue, S. Xin, Y. Yan, K.-C. Jiang, Y.-X. Yin, Y.-G. Guo, L.-J. Wan, *J. Am. Chem. Soc.* 134 (2012) 2512.
- [532] C. Wang, J. Ju, Y. Yang, Y. Tang, J. Lin, Z. Shi, R.P.S. Han, F. Huang, *J. Mater. Chem. A* 1 (2013) 8897.
- [533] H. Kim, Y. Son, C. Park, J. Cho, H.C. Choi, *Angew. Chem. Int. Ed.* 52 (2013) 5997.
- [534] Y. Xu, X. Zhu, X. Zhou, X. Liu, Y. Liu, Z. Dai, J. Bao, *J. Phys. Chem. C* 118 (2014) 28502.
- [535] J. Qin, X. Wang, M. Cao, C. Hu, *Chem. Eur. J.* 20 (2014) 9675.
- [536] S. Fang, L. Shen, H. Zheng, X. Zhang, *J. Mater. Chem. A* 3 (2015) 1498.
- [537] M. Wagemaker, F.M. Mulder, *Acc. Chem. Res.* 46 (2012) 1206.
- [538] M.V. Reddy, G.V. Subba Rao, B.V.R. Chowdari, *Chem. Rev.* 113 (2013) 5364.
- [539] J. Cabana, L. Monconduit, D. Larcher, M.R. Palacin, *Adv. Mater.* 22 (2010) E170.
- [540] K.X. Wang, X.H. Li, J.S. Chen, *Adv. Mater.* 27 (2015) 527.
- [541] J. Zai, X. Qian, *RSC Adv.* 5 (2015) 8814.
- [542] S.K. Behera, *Chem. Commun.* 47 (2011) 10371.
- [543] X. Zhu, Y. Zhu, S. Murali, M.D. Stollers, R.S. Ruoff, *ACS Nano* 5 (2011) 3333.
- [544] D. Lv, M.L. Gordin, R. Yi, T. Xu, J. Song, Y.-B. Jiang, D. Choi, D. Wang, *Adv. Funct. Mater.* 24 (2014) 1059.
- [545] Y. Sun, X. Hu, W. Luo, F. Xia, Y. Huang, *Adv. Funct. Mater.* 23 (2013) 2436.
- [546] H. Kim, D.H. Seo, S.W. Kim, J. Kim, K. Kang, *Carbon* 49 (2011) 326.
- [547] X.D. Huang, X.F. Zhou, L.A. Zhou, K. Qian, Y.H. Wang, Z.P. Liu, C.Z. Yu, *Chem-PhysChem* 12 (2011) 278.
- [548] Y. Sun, X. Hu, W. Luo, Y. Huang, *ACS Nano* 5 (2011) 7100.
- [549] X. Xin, X. Zhou, J. Wu, X. Yao, Z. Liu, *ACS Nano* 6 (2012) 11035.
- [550] S. Ding, J.S. Chen, D. Luan, F.Y.C. Boey, S. Madhavi, X.W. Lou, *Chem. Commun.* 47 (2011) 5780.
- [551] Y. Huang, D. Wu, S. Han, S. Li, L. Xiao, F. Zhang, X. Feng, *ChemSusChem* 6 (2013) 1510.
- [552] X. Li, X. Meng, J. Liu, D. Geng, Y. Zhang, M.N. Banis, Y. Li, J. Yang, R. Li, X. Sun, M. Cai, M.W. Verbrugge, *Adv. Funct. Mater.* 22 (2012) 1647.
- [553] K. Zhang, P. Han, L. Gu, L. Zhang, Z. Liu, Q. Kong, C. Zhang, S. Dong, Z. Zhang, J. Yao, H. Xu, G. Cui, L. Chen, *ACS Appl. Mater. Interfaces* 4 (2012) 658.
- [554] L. Zhuo, Y. Wu, W. Zhou, L. Wang, Y. Yu, X. Zhang, F. Zhao, *ACS Appl. Mater. Interfaces* 5 (2013) 7065.
- [555] Z. Sun, K. Xie, Z.A. Li, I. Sinev, P. Ebbinghaus, A. Erbe, M. Farle, W. Schuhmann, M. Muhler, E. Ventosa, *Chem. Eur. J.* 20 (2014) 2022.
- [556] Y. Chen, B. Song, X. Tang, L. Lu, J. Xue, *J. Mater. Chem.* 22 (2012) 17656.
- [557] Z. Chen, M. Zhou, Y. Cao, X. Ai, H. Yang, J. Liu, *Adv. Energy Mater.* 2 (2012) 95.
- [558] Y. Yang, X. Fan, G. Casillas, Z. Peng, G. Ruan, G. Wang, M.J. Yacamán, J.M. Tour, *ACS Nano* 8 (2014) 3939.
- [559] N. Li, G. Liu, C. Zhen, F. Li, L. Zhang, H.-M. Cheng, *Adv. Funct. Mater.* 21 (2011) 1717.
- [560] S. Yang, W. Yue, J. Zhu, Y. Ren, X. Yang, *Adv. Funct. Mater.* 23 (2013) 3570.
- [561] C. Peng, B. Chen, Y. Qin, S. Yang, C. Li, Y. Zuo, S. Liu, J. Yang, *ACS Nano* 6 (2012) 1074.
- [562] R. Mo, Z. Lei, K. Sun, D. Rooney, *Adv. Mater.* 26 (2014) 2084.

- [563] J. Qu, Y.-X. Yin, Y.-Q. Wang, Y. Yan, Y.-G. Guo, W.-G. Song, *ACS Appl. Mater. Interfaces* 5 (2013) 3932.
- [564] Y. Chen, C. Yan, O.G. Schmidt, *Adv. Energy Mater.* 3 (2013) 1269.
- [565] H. Wang, Y. Yang, Y. Liang, L.-F. Cui, H.S. Casalongue, Y. Li, G. Hong, Y. Cui, H. Dai, *Angew. Chem. Int. Ed.* 50 (2011) 7364.
- [566] L. He, R. Ma, N. Du, J. Ren, T. Wong, Y. Li, S.T. Lee, *J. Mater. Chem.* 22 (2012) 19061.
- [567] G. Zhou, D.-W. Wang, L.-C. Yin, N. Li, F. Li, H.-M. Cheng, *ACS Nano* 6 (2012) 3214.
- [568] S. Ding, D. Luan, F.Y.C. Boey, J.S. Chen, X.W. Lou, *Chem. Commun.* 47 (2011) 7155.
- [569] H. Liu, J. Huang, X. Li, J. Liu, Y. Zhang, K. Du, *Appl. Surf. Sci.* 258 (2012) 4917.
- [570] S. Bai, S. Chen, X. Shen, G. Zhu, G. Wang, *RSC Adv.* 2 (2012) 10977.
- [571] Y. Shi, L. Wen, F. Li, H.-M. Cheng, *J. Power Sources* 196 (2011) 8610.
- [572] H.-Y. Dong, Y.-B. He, B. Li, C. Zhang, M. Liu, F. Su, W. Lv, F. Kang, Q.-H. Yang, *Electrochim. Acta* 142 (2014) 247.
- [573] Y. Ding, G. Li, C. Xiao, X. Gao, *Electrochim. Acta* 102 (2013) 282.
- [574] Y. Tang, Z. Liu, X. Lu, B. Wang, F. Huang, *RSC Adv.* 4 (2014) 36372.
- [575] V. Etacheri, J.E. Yourey, B.M. Bartlett, *ACS Nano* 8 (2014) 1491.
- [576] B. Zhao, R. Liu, X. Cai, Z. Jiao, M. Wu, X. Ling, B. Lu, Y. Jiang, *J. Appl. Electrochem.* 44 (2014) 53.
- [577] D.Y. Chen, G. Ji, Y. Ma, J.Y. Lee, J.M. Lu, *ACS Appl. Mater. Interfaces* 3 (2011) 3078.
- [578] A. Hu, X. Chen, Y. Tang, Q. Tang, L. Yang, S. Zhang, *Electrochem. Commun.* 28 (2013) 139.
- [579] J. Zhao, B. Yang, Z. Zheng, J. Yang, Z. Yang, P. Zhang, W. Ren, X. Yan, *ACS Appl. Mater. Interfaces* 6 (2014) 9890.
- [580] J. Luo, J. Liu, Z. Zeng, C.F. Ng, L. Ma, H. Zhang, J. Lin, Z. Shen, H.J. Fan, *Nano Lett.* 13 (2013) 6136.
- [581] Z.S. Wu, W.C. Ren, L. Wen, L.B. Gao, J.P. Zhao, Z.P. Chen, G.M. Zhou, F. Li, H.M. Cheng, *ACS Nano* 4 (2010) 3187.
- [582] H. Sun, X. Sun, T. Hu, M. Yu, F. Lu, J. Lian, *J. Phys. Chem. C* 118 (2014) 2263.
- [583] L. Tao, J. Zai, K. Wang, H. Zhang, M. Xu, J. Shen, Y. Su, X. Qian, *J. Power Sources* 202 (2012) 230.
- [584] H. Sun, Y. Liu, Y. Yu, M. Ahmad, D. Nan, J. Zhu, *Electrochim. Acta* 118 (2014) 1.
- [585] N. Lavoie, P.R. Malenfant, F.M. Courtel, Y. Abu-Lebdeh, I.J. Davidson, *J. Power Sources* 213 (2012) 249.
- [586] C.X. Guo, M. Wang, T. Chen, X.W. Lou, C.M. Li, *Adv. Energy Mater.* 1 (2011) 736.
- [587] A. Yu, H.W. Park, A. Davies, D.C. Higgins, Z. Chen, X. Xiao, *J. Phys. Chem. Lett.* 2 (2011) 1855.
- [588] Q. Wang, J. Zhao, W. Shan, X. Xia, L. Xing, X. Xue, *J. Alloys Compd.* 590 (2014) 424.
- [589] Y. Liu, W. Wang, L. Gu, Y. Wang, Y. Ying, Y. Mao, L. Sun, X. Peng, *ACS Appl. Mater. Interfaces* 5 (2013) 9850.
- [590] X. Zhou, J. Shi, Y. Liu, Q. Su, J. Zhang, G. Du, *J. Alloys Compd.* 615 (2014) 390.
- [591] S.H. Choi, Y.N. Ko, J.-K. Lee, Y.C. Kang, *Sci. Rep.* 4 (2014) 5786.
- [592] M. Yu, A. Wang, Y. Wang, C. Li, G. Shi, *Nanoscale* 6 (2014) 11419.
- [593] J. Lin, Z. Peng, C. Xiang, G. Ruan, Z. Yan, D. Natelson, J.M. Tour, *ACS Nano* 7 (2013) 6001.
- [594] J. Zhu, G. Zhang, X. Yu, Q. Li, B. Lu, Z. Xu, *Nano Energy* 3 (2014) 80.
- [595] Q. Han, J. Zai, Y. Xiao, B. Li, M. Xu, X. Qian, *RSC Adv.* 3 (2013) 20573.
- [596] C. Xu, J. Sun, L. Gao, *J. Mater. Chem.* 22 (2012) 975.
- [597] F.-Y. Su, Y.-B. He, B. Li, X.-C. Chen, C.-H. You, W. Wei, W. Lv, Q.-H. Yang, F. Kang, *Nano Energy* 1 (2012) 429.
- [598] N. Zhu, W. Liu, M. Xue, Z. Xie, D. Zhao, M. Zhang, J. Chen, T. Cao, *Electrochim. Acta* 55 (2010) 5813.
- [599] Y. Cao, X. Lin, C. Zhang, C. Yang, Q. Zhang, W. Hu, M. Zheng, Q. Dong, *RSC Adv.* 4 (2014) 30150.
- [600] Y. Qiu, K. Yan, S. Yang, L. Jin, H. Deng, W. Li, *ACS Nano* 4 (2010) 6515.
- [601] K. Chang, W.X. Chen, *ACS Nano* 5 (2011) 4720.
- [602] W. Song, J. Xie, W. Hu, S. Liu, G. Cao, T. Zhu, X. Zhao, *J. Power Sources* 229 (2013) 6.
- [603] D. Wu, F. Zhang, H. Liang, X. Feng, *Chem. Soc. Rev.* 41 (2012) 6160.
- [604] H.-P. Cong, J.-F. Chen, S.-H. Yu, *Chem. Soc. Rev.* 43 (2014) 7295.
- [605] D. Wang, D. Choi, J. Li, Z. Yang, Z. Nie, R. Kou, D. Hu, C. Wang, L.V. Saraf, J. Zhang, I.A. Aksay, J. Liu, *ACS Nano* 3 (2009) 907.
- [606] S.J.R. Prabakar, Y.-H. Hwang, E.-G. Bae, S. Shim, D. Kim, M.S. Lah, K.-S. Sohn, M. Pyo, *Adv. Mater.* 25 (2013) 3307.
- [607] D. Wang, R. Kou, D. Choi, Z. Yang, Z. Nie, J. Li, L.V. Saraf, D. Hu, J. Zhang, G.L. Graff, J. Liu, M.A. Pope, I.A. Aksay, *ACS Nano* 4 (2010) 1587.
- [608] X.-I. Huang, R.-Z. Wang, D. Xu, Z.-I. Wang, H.-G. Wang, J.-J. Xu, Z. Wu, Q.-C. Liu, Y. Zhang, X.-B. Zhang, *Adv. Funct. Mater.* 23 (2013) 4345.
- [609] S. Yang, X. Feng, K. Muellen, *Adv. Mater.* 23 (2011) 3575.
- [610] S. Yang, X. Feng, L. Wang, K. Tang, J. Maier, K. Muellen, *Angew. Chem. Int. Ed.* 49 (2010) 4795.
- [611] X. Wang, X. Cao, L. Bourgeois, H. Guan, S. Chen, Y. Zhong, D.-M. Tang, H. Li, T. Zhai, L. Li, Y. Bando, D. Golberg, *Adv. Funct. Mater.* 22 (2012) 2682.
- [612] W. Yue, S. Jiang, W. Huang, Z. Gao, J. Li, Y. Ren, X. Zhao, X. Yang, *J. Mater. Chem. A* 1 (2013) 6928.
- [613] L. Zhao, M. Gao, W. Yue, Y. Jiang, Y. Wang, Y. Ren, F. Hu, *ACS Appl. Mater. Interfaces* 7 (2015) 9709.
- [614] S. Yang, C. Cao, P. Huang, L. Peng, Y. Sun, F. Wei, W. Song, *J. Mater. Chem. A* 3 (2015) 8701.
- [615] R. Chen, T. Zhao, W. Wu, F. Wu, L. Li, J. Qian, R. Xu, H. Wu, H.M. Al-Bishri, A.S. Al-Bogami, *Nano Lett.* 14 (2014) 5899.
- [616] J. Tang, J. Yang, L. Zhou, J. Xie, G. Chen, X. Zhou, *J. Mater. Chem. A* 2 (2014) 6292.
- [617] A. Abouimrane, O.C. Compton, K. Amine, S.T. Nguyen, *J. Phys. Chem. C* 114 (2010) 12800.
- [618] N. Li, G. Zhou, R. Fang, F. Li, H.-M. Cheng, *Nanoscale* 5 (2013) 7780.
- [619] G.M. Zhou, D.W. Wang, F. Li, L.L. Zhang, N. Li, Z.S. Wu, L. Wen, G.Q. Lu, H.M. Cheng, *Chem. Mater.* 22 (2010) 5306.
- [620] Y. Shi, J.-Z. Wang, S.-L. Chou, D. Wexler, H.-J. Li, K. Ozawa, H.-K. Liu, Y.-P. Wu, *Nano Lett.* 13 (2013) 4715.
- [621] Z. Zheng, Y. Cheng, X. Yan, R. Wang, P. Zhang, *J. Mater. Chem. A* 2 (2014) 149.
- [622] H. Huang, Y. Huang, M. Wang, X. Chen, Y. Zhao, K. Wang, H. Wu, *Electrochim. Acta* 147 (2014) 201.
- [623] Y. Zhao, Y. Huang, W. Zhang, Q. Wang, K. Wang, M. Zong, X. Sun, *RSC Adv.* 3 (2013) 23489.
- [624] D. Kong, W. Ren, Y. Luo, Y. Yang, C. Cheng, *J. Mater. Chem. A* 2 (2014) 20221.
- [625] J. Ma, T. Yuan, Y.-S. He, J. Wang, W. Zhang, D. Yang, X.-Z. Liao, Z.-F. Ma, *J. Mater. Chem. A* 2 (2014) 16925.
- [626] W. Zhou, F. Zhang, S. Liu, J. Wang, X. Du, D. Yin, L. Wang, *RSC Adv.* 4 (2014) 51362.
- [627] F. Zhang, R. Zhang, J. Feng, L. Ci, S. Xiong, J. Yang, Y. Qian, L. Li, *Nanoscale* 7 (2015) 232.
- [628] P. Wu, X. Xu, Q. Zhu, X. Zhu, Y. Tang, Y. Zhou, T. Lu, *J. Alloys Compd.* 626 (2015) 234.
- [629] L. Li, A.-R.O. Raji, J.M. Tour, *Adv. Mater.* 25 (2013) 6298.
- [630] S. Yang, X. Feng, S. Ivanovici, K. Muellen, *Angew. Chem. Int. Ed.* 49 (2010) 8408.
- [631] X. Yang, K. Fan, Y. Zhu, J. Shen, X. Jiang, P. Zhao, C. Li, *J. Mater. Chem.* 22 (2012) 17278.
- [632] J.-Z. Wang, C. Zhong, D. Wexler, N.H. Idris, Z.-X. Wang, L.-Q. Chen, H.-K. Liu, *Chem. Eur. J.* 17 (2011) 661.
- [633] Z. Xiu, X. Hao, Y. Wu, Q. Lu, S. Liu, *J. Power Sources* 287 (2015) 334.
- [634] L. Yang, X. Zhang, Y. Li, F. Hao, H. Chen, M. Yang, D. Fang, *Electrochim. Acta* 155 (2015) 272.
- [635] Y.-T. Xu, Y. Guo, C. Li, X.-Y. Zhou, M.C. Tucker, X.-Z. Fu, R. Sun, C.-P. Wong, *Nano Energy* 11 (2015) 38.
- [636] S.-M. Paek, E. Yoo, I. Honma, *Nano Lett.* 9 (2009) 72.
- [637] M. Zhang, D. Lei, Z. Du, X. Yin, L. Chen, Q. Li, Y. Wang, T. Wang, *J. Mater. Chem.* 21 (2011) 1673.
- [638] B. Li, H. Cao, J. Shao, M. Qu, J.H. Warner, *J. Mater. Chem.* 21 (2011) 5069.
- [639] B. Li, H. Cao, J. Shao, M. Qu, *Chem. Commun.* 47 (2011) 10374.
- [640] Z. Jian, M. Zheng, Y. Liang, X. Zhang, S. Gheyfani, Y. Lan, Y. Shi, Y. Yao, *Chem. Commun.* 51 (2015) 229.
- [641] X.Y. Wang, X.F. Zhou, K. Yao, J.G. Zhang, Z.P. Liu, *Carbon* 49 (2011) 133.
- [642] J. Yao, Y. Gong, S. Yang, P. Xiao, Y. Zhang, K. Keyshar, G. Ye, S. Ozden, R. Vajtai, P.M. Ajayan, *ACS Appl. Mater. Interfaces* 6 (2014) 20414.
- [643] L.S. Zhang, L.Y. Jiang, H.J. Yan, W.D. Wang, W. Wang, W.G. Song, Y.G. Guo, L.J. Wan, *J. Mater. Chem.* 20 (2010) 5462.
- [644] J. Guo, B. Jiang, X. Zhang, H. Liu, *J. Power Sources* 262 (2014) 15.
- [645] D. Cai, T. Yang, D. Wang, X. Duan, B. Liu, L. Wang, Y. Liu, Q. Li, T. Wang, *Electrochim. Acta* 159 (2015) 46.
- [646] H. Xu, S. Yuan, Z. Wang, Y. Zhao, J. Fang, L. Shi, *RSC Adv.* 4 (2014) 8472.
- [647] C. Chen, Q. Ru, S. Hu, B. An, X. Song, X. Hou, *Electrochim. Acta* 151 (2015) 203.
- [648] M. Christy, H. Jang, K.S. Nahm, *J. Power Sources* 288 (2015) 451.
- [649] J. Zhang, L. Chang, F. Wang, D. Xie, Q. Su, G. Du, *Mater. Res. Bull.* 68 (2015) 120.
- [650] H. Wang, J.T. Robinson, G. Diankov, H. Dai, *J. Am. Chem. Soc.* 132 (2010) 3270.
- [651] Z.-S. Wu, D.-W. Wang, W. Ren, J. Zhao, G. Zhou, F. Li, H.-M. Cheng, *Adv. Funct. Mater.* 20 (2010) 3595.
- [652] A.K. Rai, T.V. Thi, B.J. Paul, J. Kim, *Electrochim. Acta* 146 (2014) 577.
- [653] D. Cai, T. Yang, B. Liu, D. Wang, Y. Liu, L. Wang, Q. Li, T. Wang, *J. Mater. Chem. A* 2 (2014) 13990.
- [654] X. Li, W. Qi, D. Mei, M.L. Sushko, I. Aksay, J. Liu, *Adv. Mater.* 24 (2012) 5136.
- [655] H. Wang, L.-F. Cui, Y. Yang, H. Sanchez-Casalogue, J.T. Robinson, Y. Liang, Y. Cui, H. Dai, *J. Am. Chem. Soc.* 132 (2010) 13978.
- [656] W. Wei, S. Yang, H. Zhou, I. Lieberwirth, X. Feng, K. Muellen, *Adv. Mater.* 25 (2013) 2909.
- [657] M. Zhang, Y. Wang, M. Jia, *Electrochim. Acta* 129 (2014) 425.
- [658] Z.-Y. Sui, C. Wang, K. Shu, Q.-S. Yang, Y. Ge, G.G. Wallace, B.-H. Han, *J. Mater. Chem. A* 3 (2015) 10403.
- [659] G. Zeng, N. Shi, M. Hess, X. Chen, W. Cheng, T. Fan, M. Niederberger, *ACS Nano* 9 (2015) 4227.
- [660] Y.J. Mai, X.L. Wang, J.Y. Xiang, Y.Q. Qiao, D. Zhang, C.D. Gu, J.P. Tu, *Electrochim. Acta* 56 (2011) 2306.
- [661] S.Q. Chen, Y. Wang, *J. Mater. Chem.* 20 (2010) 9735.
- [662] N. Mahmood, C. Zhang, H. Yin, Y. Hou, *J. Mater. Chem. A* 2 (2014) 15.
- [663] C. Xu, B. Xu, Y. Gu, Z. Xiong, J. Sun, X.S. Zhao, *Energy Environ. Sci.* 6 (2013) 1388.
- [664] Y. Zhong, M. Yang, X. Zhou, Y. Luo, J. Wei, Z. Zhou, *Adv. Mater.* 27 (2015) 806.
- [665] L. Li, A. Kovalchuk, H. Fei, Z. Peng, Y. Li, N.D. Kim, C. Xiang, Y. Yang, G. Ruan, J.M. Tour, *Adv. Energy Mater.* 5 (2015) 1500171.
- [666] T. Yang, T. Qian, M. Wang, J. Liu, J. Zhou, Z. Sun, M. Chen, C. Yan, *J. Mater. Chem. A* 3 (2015) 6291.
- [667] L. Lin, Q. Pan, *J. Mater. Chem. A* 3 (2015) 1724.
- [668] Z. Zhang, F. Wang, Q. An, W. Li, P. Wu, *J. Mater. Chem. A* 3 (2015) 7036.
- [669] T. Shen, X. Zhou, H. Cao, C. Zheng, Z. Liu, *RSC Adv.* 5 (2015) 22449.
- [670] H. Wang, Y. Yan, G. Chen, *J. Mater. Chem. A* 3 (2015) 10275.
- [671] H. Huang, L. Zhang, Y. Xia, Y. Gan, X. Tao, C. Liang, W. Zhang, *New J. Chem.* 38 (2014) 4743.
- [672] X. Zhou, L.-J. Wan, Y.-G. Guo, *Adv. Mater.* 25 (2013) 2152.
- [673] S. Tao, W. Yue, M. Zhong, Z. Chen, Y. Ren, *ACS Appl. Mater. Interfaces* 6 (2014) 6332.
- [674] C. Zhang, X. Peng, Z. Guo, C. Cai, Z. Chen, D. Wexler, S. Li, H. Liu, *Carbon* 50 (2012) 1897.

- [675] M.S. Whittingham, *Chem. Rev.* 104 (2004) 4271.
- [676] G. Ceder, Y.M. Chiang, D.R. Sadoway, M.K. Aydinol, Y.I. Jang, B. Huang, *Nature* 392 (1998) 694.
- [677] J.W. Fergus, *J. Power Sources* 195 (2010) 939.
- [678] Y. Wang, G. Cao, *Adv. Mater.* 20 (2008) 2251.
- [679] L.-X. Yuan, Z.-H. Wang, W.-X. Zhang, X.-L. Hu, J.-T. Chen, Y.-H. Huang, J.B. Goodenough, *Energy Environ. Sci.* 4 (2011) 269.
- [680] B. Ammundsen, J. Paulsen, *Adv. Mater.* 13 (2001) 943.
- [681] B. Xu, D. Qian, Z. Wang, Y.S. Meng, *Mater. Sci. Eng. R* 73 (2012) 51.
- [682] Z.-L. Wang, D. Xu, H.-G. Wang, Z. Wu, X.-B. Zhang, *ACS Nano* 7 (2013) 2422.
- [683] T. Bhardwaj, A. Antic, B. Pavan, V. Barone, B.D. Fahlman, *J. Am. Chem. Soc.* 132 (2010) 12556.
- [684] F. Liu, S. Song, D. Xue, H. Zhang, *Adv. Mater.* 24 (2012) 1089.
- [685] S.W. Lee, B.M. Gallant, Y. Lee, N. Yoshida, D.Y. Kim, Y. Yamada, S. Noda, A. Yamada, Y. Shao-Horn, *Energy Environ. Sci.* 5 (2012) 5437.
- [686] H. Chen, M. Armand, G. Demailly, F. Dolhem, P. Poizot, J.-M. Tarascon, *ChemSusChem* 1 (2008) 348.
- [687] S.W. Lee, N. Yabuuchi, B.M. Gallant, S. Chen, B.-S. Kim, P.T. Hammond, Y. Shao-Horn, *Nat. Nanotechnol.* 5 (2010) 531.
- [688] S.H. Ha, Y.S. Jeong, Y.J. Lee, *ACS Appl. Mater. Interfaces* 5 (2013) 12295.
- [689] Y. Su, Y. Liu, P. Liu, D. Wu, X. Zhuang, F. Zhang, X. Feng, *Angew. Chem. Int. Ed.* 54 (2015) 1812.
- [690] G. Kucinskis, G. Bajars, J. Kleperis, *J. Power Sources* 240 (2013) 66.
- [691] H. Liu, P. Gao, J. Fang, G. Yang, *Chem. Commun.* 47 (2011) 9110.
- [692] C. Nethravathi, B. Viswanath, J. Michael, M. Rajamath, *Carbon* 50 (2012) 4839.
- [693] B. Pei, Z. Jiang, W. Zhang, Z. Yang, A. Manthiram, *J. Power Sources* 239 (2013) 475.
- [694] S. Praneetha, A.V. Murugan, *RSC Adv.* 3 (2013) 25403.
- [695] X. Zhao, C.M. Hayner, M.C. Kung, H.H. Kung, *Chem. Commun.* 48 (2012) 9909.
- [696] Y. Jiang, R. Liu, W. Xu, Z. Jiao, M. Wu, Y. Chu, L. Su, H. Cao, M. Hou, B. Zhao, *J. Mater. Res.* 28 (2013) 2584.
- [697] Y. Huang, H. Liu, Y.-C. Lu, Y. Hou, Q. Li, *J. Power Sources* 284 (2015) 236.
- [698] X. Zhu, J. Hu, W. Wu, W. Zeng, H. Dai, Y. Du, Z. Liu, L. Li, H. Ji, Y. Zhu, *J. Mater. Chem. A* 2 (2014) 7812.
- [699] X. Rui, D. Sim, K. Wong, J. Zhu, W. Liu, C. Xu, H. Tan, N. Xiao, H.H. Hng, T.M. Lim, Q. Yan, *J. Power Sources* 214 (2012) 171.
- [700] K.-C. Jiang, X.-L. Wu, Y.-X. Yin, J.-S. Lee, J. Kim, Y.-G. Guo, *ACS Appl. Mater. Interfaces* 4 (2012) 4858.
- [701] R. Ma, Z. Lu, C. Wang, H.-E. Wang, S. Yang, L. Xi, J.C.Y. Chung, *Nanoscale* 5 (2013) 6338.
- [702] K. Zhu, X. Yan, Y. Zhang, Y. Wang, A. Su, X. Bie, D. Zhang, F. Du, C. Wang, G. Chen, Y. Wei, *ChemPlusChem* 79 (2014) 447.
- [703] Y. Yin, Y. Hu, P. Wu, H. Zhang, C. Cai, *Chem. Commun.* 48 (2012) 2137.
- [704] S. Han, J. Wang, S. Li, D. Wu, X. Feng, *J. Mater. Chem. A* 2 (2014) 6174.
- [705] B. Li, D.W. Rooney, N. Zhang, K. Sun, *ACS Appl. Mater. Interfaces* 5 (2013) 5057.
- [706] H. Fei, Z. Peng, Y. Yang, L. Li, A.-R.O. Raji, E.L.G. Samuel, J.M. Tour, *Chem. Commun.* 50 (2014) 7117.
- [707] J. Hu, G. Lei, Z. Lu, K. Liu, S. Sang, H. Liu, *Chem. Commun.* 51 (2015) 9983.
- [708] R. Ma, Y. Dong, L. Xi, S. Yang, Z. Lu, C. Chung, *ACS Appl. Mater. Interfaces* 5 (2013) 892.
- [709] X.-J. Wang, F. Krumeich, R. Nesper, *Electrochim. Commun.* 34 (2013) 246.
- [710] W. Kim, W. Ryu, D. Han, S. Lim, J. Eom, H. Kwon, *ACS Appl. Mater. Interfaces* 6 (2014) 4731.
- [711] X. Guo, Q. Fan, L. Yu, J. Liang, W. Ji, L. Peng, X. Guo, W. Ding, Y. Chen, *J. Mater. Chem. A* 1 (2013) 11534.
- [712] S.H. Choi, Y.C. Kang, *Chem. Eur. J.* 20 (2014) 6294.
- [713] X. Zhu, Z. Yan, W. Wu, W. Zeng, Y. Du, Y. Zhong, H. Zhai, H. Ji, Y. Zhu, *Sci. Rep.* 4 (2014) 5768.
- [714] Y. Jiang, W. Xu, D. Chen, Z. Jiao, H. Zhang, Q. Ma, X. Cai, B. Zhao, Y. Chu, *Electrochim. Acta* 85 (2012) 377.
- [715] L. Zhang, S. Wang, D. Cai, P. Lian, X. Zhu, W. Yang, H. Wang, *Electrochim. Acta* 91 (2013) 108.
- [716] H. Liu, G. Yang, X. Zhang, P. Gao, L. Wang, J. Fang, J. Pinto, X. Jiang, *J. Mater. Chem.* 22 (2012) 11039.
- [717] K. Wang, Y. Wang, C. Wang, Y. Xia, *Electrochim. Acta* 146 (2014) 8.
- [718] L.-L. Zhang, S. Duan, X.-L. Yang, G. Peng, G. Liang, Y.-H. Huang, Y. Jiang, S.-B. Ni, M. Li, *ACS Appl. Mater. Interfaces* 5 (2013) 12304.
- [719] H. Zhu, X. Wu, L. Zan, Y. Zhang, *ACS Appl. Mater. Interfaces* 6 (2014) 11724.
- [720] J.-R. He, Y.-F. Chen, P.-J. Li, Z.-G. Wang, F. Qi, J.-B. Liu, *RSC Adv.* 4 (2014) 2568.
- [721] Y.H. Ding, H.M. Ren, Y.Y. Huang, F.H. Chang, X. He, J.Q. Fen, P. Zhang, *Nanotechnology* 24 (2013) 375401.
- [722] C.V. Rao, A.L.M. Reddy, Y. Ishikawa, P.M. Ajayan, *ACS Appl. Mater. Interfaces* 3 (2011) 2966.
- [723] X. Fang, M. Ge, J. Rong, C. Zhou, *J. Mater. Chem. A* 1 (2013) 4083.
- [724] X. Zhao, C.M. Hayner, H.H. Kung, *J. Mater. Chem.* 21 (2011) 17297.
- [725] S.-M. Bak, K.-W. Nam, C.-W. Lee, K.-H. Kim, H.-C. Jung, X.-Q. Yang, K.-B. Kim, *J. Mater. Chem.* 21 (2011) 17309.
- [726] K.V. Sreelakshmi, S. Sasi, A. Balakrishnan, N. Sivakumar, A.S. Nair, S.V. Nair, K.R.V. Subramanian, *Energy Technol.* 2 (2014) 257.
- [727] K.-Y. Jo, S.-Y. Han, J.M. Lee, I.Y. Kim, S. Nahm, J.-W. Choi, S.-J. Hwang, *Electrochim. Acta* 92 (2013) 188.
- [728] G. Du, K.H. Seng, Z. Guo, J. Liu, W. Li, D. Jia, C. Cook, Z. Liu, H. Liu, *RSC Adv.* 1 (2011) 690.
- [729] J. Cheng, B. Wang, H.L. Xin, G. Yang, H. Cai, F. Nie, H. Huang, *J. Mater. Chem. A* 1 (2013) 10814.
- [730] K. Zhu, H. Qiu, Y. Zhang, D. Zhang, G. Chen, Y. Wei, *ChemSusChem* 8 (2015) 1017.
- [731] Y.H. Ding, H.M. Ren, Y.Y. Huang, F.H. Chang, P. Zhang, *Mater. Res. Bull.* 48 (2013) 3713.
- [732] Y. Zhang, W. Wang, P. Li, Y. Fu, X. Ma, *J. Power Sources* 210 (2012) 47.
- [733] Y. Wu, Z. Wen, H. Feng, J. Li, *Chem. Eur. J.* 19 (2013) 5631.
- [734] H. Bi, F. Huang, Y. Tang, Z. Liu, T. Lin, J. Chen, W. Zhao, *Electrochim. Acta* 88 (2013) 414.
- [735] R. Mo, Z. Lei, D. Rooney, K. Sun, *Electrochim. Acta* 130 (2014) 594.
- [736] C. Su, X. Bu, L. Xu, J. Liu, C. Zhang, *Electrochim. Acta* 64 (2012) 190.
- [737] X. Zhou, F. Wang, Y. Zhu, Z. Liu, *J. Mater. Chem.* 21 (2011) 3353.
- [738] P. Gibot, M. Casas-Cabanas, L. Laffont, S. Levasseur, P. Carlsch, S. Hamelet, J.-M. Tarascon, C. Masquelier, *Nat. Mater.* 7 (2008) 741.
- [739] Y. Zhao, L. Peng, B. Liu, G. Yu, *Nano Lett.* 14 (2014) 2849.
- [740] Y. Wang, Y. Wang, E. Hosono, K. Wang, H. Zhou, *Angew. Chem. Int. Ed.* 47 (2008) 7461.
- [741] S.-Y. Chung, J.T. Bloking, Y.-M. Chiang, *Nat. Mater.* 1 (2002) 123.
- [742] L.-H. Hu, F.-Y. Wu, C.-T. Lin, A.N. Khlobystov, L.-J. Li, *Nat. Commun.* 4 (2013) 1687.
- [743] S.H. Ha, Y.J. Lee, *Chem. Eur. J.* 21 (2015) 2132.
- [744] B. Wang, B. Xu, T. Liu, P. Liu, C. Guo, S. Wang, Q. Wang, Z. Xiong, D. Wang, X.S. Zhao, *Nanoscale* 6 (2014) 986.
- [745] J. Livage, *Chem. Mater.* 3 (1991) 578.
- [746] E. Potiron, A. Le Gal La Salle, A. Verbaere, Y. Piffard, D. Guyomard, *Electrochim. Acta* 45 (1999) 197.
- [747] F. Lantelme, A. Mantoux, H. Groult, D. Lincot, *J. Electrochem. Soc.* 150 (2003) A1202.
- [748] H. Liu, W. Yang, *Energy Environ. Sci.* 4 (2011) 4000.
- [749] X. Rui, J. Zhu, D. Sim, C. Xu, Y. Zeng, H.H. Hng, T.M. Lim, Q. Yan, *Nanoscale* 3 (2011) 4752.
- [750] Q. Liu, Z.-F. Li, Y. Liu, H. Zhang, Y. Ren, C.-J. Sun, W. Lu, Y. Zhou, L. Stanciu, E.A. Stach, J. Xie, *Nat. Commun.* 6 (2015) 6127.
- [751] M. Winter, R.J. Brodd, *Chem. Rev.* 104 (2004) 4245.
- [752] J.R. Miller, P. Simon, *Science* 321 (2008) 651.
- [753] A. Burke, *Electrochim. Acta* 53 (2007) 1083.
- [754] M.S. Whittingham, *MRS Bull.* 33 (2008) 411.
- [755] H.-J. Choi, S.-M. Jung, J.-M. Seo, D.W. Chang, L. Dai, J.-B. Baek, *Nano Energy* 1 (2012) 534.
- [756] E. Frackowiak, F. Béguin, *Carbon* 39 (2001) 937.
- [757] A.G. Pandolfo, A.F. Hollenkamp, *J. Power Sources* 157 (2006) 11.
- [758] J.L. Xia, F. Chen, J.H. Li, N.J. Tao, *Nat. Nanotechnol.* 4 (2009) 505.
- [759] S.R.C. Vivekchand, C. Rout, K.S. Subrahmanyam, A. Govindaraj, C.N.R. Rao, *J. Chem. Sci.* 120 (2008) 9.
- [760] M.D. Stoller, S.J. Park, Y.W. Zhu, J.H. An, R.S. Ruoff, *Nano Lett.* 8 (2008) 3498.
- [761] Y. Zhu, S. Murali, M.D. Stoller, A. Velamakanni, R.D. Piner, R.S. Ruoff, *Carbon* 48 (2010) 2118.
- [762] Y. Wang, Z.Q. Shi, Y. Huang, Y.F. Ma, C.Y. Wang, M.M. Chen, Y.S. Chen, *J. Phys. Chem. C* 113 (2009) 13103.
- [763] H. Feng, R. Cheng, X. Zhao, X. Duan, J. Li, *Nat. Commun.* 4 (2013) 1539.
- [764] M.F. El-Kady, V. Strong, S. Dubin, R.B. Kaner, *Science* 335 (2012) 1326.
- [765] L.L. Zhang, X. Zhao, M.D. Stoller, Y. Zhu, H. Ji, S. Murali, Y. Wu, S. Perales, B. Clevenger, R.S. Ruoff, *Nano Lett.* 12 (2012) 1806.
- [766] X.W. Yang, J.W. Zhu, L. Qiu, D. Li, *Adv. Mater.* 23 (2011) 2833.
- [767] X. Yang, C. Cheng, Y. Wang, L. Qiu, D. Li, *Science* 341 (2013) 534.
- [768] S. Nardecchia, D. Carriazo, M.L. Ferrer, M.C. Gutierrez, F. del Monte, *Chem. Soc. Rev.* 42 (2013) 794.
- [769] D.R. Rolison, J.W. Long, J.C. Lytle, A.E. Fischer, C.P. Rhodes, T.M. McEvoy, M.E. Bourg, A.M. Lubers, *Chem. Soc. Rev.* 38 (2009) 226.
- [770] J.N. Tiwari, R.N. Tiwari, K.S. Kim, *Prog. Mater. Sci.* 57 (2012) 724.
- [771] C. Li, G. Shi, *Nanoscale* 4 (2012) 5549.
- [772] H. Bi, K. Yin, X. Xie, Y. Zhou, N. Wan, F. Xu, F. Banhart, L. Sun, R.S. Ruoff, *Adv. Mater.* 24 (2012) 5124.
- [773] L. Zhang, G. Shi, *J. Phys. Chem. C* 115 (2011) 17206.
- [774] Q. Wu, Y.Q. Sun, H. Bai, G.Q. Shi, *Phys. Chem. Chem. Phys.* 13 (2011) 11193.
- [775] F.-P. Du, J.-J. Wang, C.-Y. Tang, C.-P. Tsui, X.-P. Zhou, X.-L. Xie, Y.-G. Liao, *Nanotechnology* 23 (2012) 475704.
- [776] Y. Sun, Q. Wu, G. Shi, *Phys. Chem. Chem. Phys.* 13 (2011) 17249.
- [777] Q. Zhou, J. Gao, C. Li, J. Chen, G. Shi, *J. Mater. Chem. A* 1 (2013) 9196.
- [778] Y. Zhu, S. Murali, M.D. Stoller, K.J. Ganesh, W. Cai, P.J. Ferreira, A. Pirkle, R.M. Wallace, K.A. Cychoz, M. Thommes, D. Su, E.A. Stach, R.S. Ruoff, *Science* 332 (2011) 1537.
- [779] L. Zhang, F. Zhang, X. Yang, G. Long, Y. Wu, T. Zhang, K. Leng, Y. Huang, Y. Ma, A. Yu, Y. Chen, *Sci. Rep.* 3 (2013) 1408.
- [780] J. Chen, K. Sheng, P. Luo, C. Li, G. Shi, *Adv. Mater.* 24 (2012) 4569.
- [781] S. Wang, B. Pei, X. Zhao, R.A.W. Dryfe, *Nano Energy* 2 (2013) 530.
- [782] Y. Xu, Z. Lin, X. Huang, Y. Liu, Y. Huang, X. Duan, *ACS Nano* 7 (2013) 4042.
- [783] F. Zhang, Y. Lu, X. Yang, L. Zhang, T. Zhang, K. Leng, Y. Wu, Y. Huang, Y. Ma, Y. Chen, *Small* 10 (2014) 2285.
- [784] Z. Weng, Y. Su, D.W. Wang, F. Li, J.H. Du, H.M. Cheng, *Adv. Energy Mater.* 1 (2011) 917.
- [785] M.F. El-Kady, R.B. Kaner, *Nat. Commun.* 4 (2013) 1475.
- [786] W. Li, S. Gao, L. Wu, S. Qiu, Y. Guo, X. Geng, M. Chen, S. Liao, C. Zhu, Y. Gong, M. Long, J. Xu, X. Wei, M. Sun, L. Liu, *Sci. Rep.* 3 (2013) 2125.
- [787] X. Cao, Z. Zeng, W. Shi, P. Yip, Q. Yan, H. Zhang, *Small* 9 (2013) 1703.
- [788] J.-C. Yoon, J.-S. Lee, S.-I. Kim, K.-H. Kim, J.-H. Jang, *Sci. Rep.* 3 (2013) 1788.

- [789] X. Cao, Y. Shi, W. Shi, G. Lu, X. Huang, Q. Yan, Q. Zhang, H. Zhang, *Small* 7 (2011) 3163.
- [790] Z. Bo, W. Zhu, W. Ma, Z. Wen, X. Shuai, J. Chen, J. Yan, Z. Wang, K. Cen, X. Feng, *Adv. Mater.* 25 (2013) 5799.
- [791] J.R. Miller, R.A. Outlaw, B.C. Holloway, *Science* 329 (2010) 1637.
- [792] X. Wang, Y. Zhang, C. Zhi, X. Wang, D. Tang, Y. Xu, Q. Weng, X. Jiang, M. Mitome, D. Golberg, Y. Bando, *Nat. Commun.* 4 (2013) 2905.
- [793] L. Qiu, X. Yang, X. Gou, W. Yang, Z.F. Ma, G.G. Wallace, D. Li, *Chem. Eur. J.* 16 (2010) 10653.
- [794] V.C. Tung, L.-M. Chen, M.J. Allen, J.K. Wassei, K. Nelson, R.B. Kaner, Y. Yang, *Nano Lett.* 9 (2009) 1949.
- [795] S. Wang, R.A.W. Dryfe, *J. Mater. Chem. A* 1 (2013) 5279.
- [796] S.Y. Yang, K.H. Chang, H.W. Tien, Y.F. Lee, S.M. Li, Y.S. Wang, J.Y. Wang, C.C.M. Ma, C.C. Hu, *J. Mater. Chem.* 21 (2011) 2374.
- [797] M. Beidaghi, C. Wang, *Adv. Funct. Mater.* 22 (2012) 4501.
- [798] F. Du, D. Yu, L. Dai, S. Ganguli, V. Varshney, A. Roy, *Chem. Mater.* 23 (2011) 4810.
- [799] Z.J. Fan, J. Yan, L.J. Zhi, Q. Zhang, T. Wei, J. Feng, M.L. Zhang, W.Z. Qian, F. Wei, *Adv. Mater.* 22 (2010) 3723.
- [800] W. Wang, S. Guo, M. Penchev, I. Ruiz, K.N. Bozhilov, D. Yan, M. Ozkan, C.S. Ozkan, *Nano Energy* 2 (2013) 294.
- [801] Z. Lei, N. Christov, X.S. Zhao, *Energy Environ. Sci.* 4 (2011) 1866.
- [802] C.X. Guo, C.M. Li, *Energy Environ. Sci.* 4 (2011) 4504.
- [803] X.J. Lu, H. Dou, B. Gao, C.Z. Yuan, S.D. Yang, L. Hao, L.F. Shen, X.G. Zhang, *Electrochim. Acta* 56 (2011) 5115.
- [804] D. Yu, L. Dai, *J. Phys. Chem. Lett.* 1 (2010) 467.
- [805] I. Shakir, *Electrochim. Acta* 129 (2014) 396.
- [806] K.-S. Kim, S.-J. Park, *Electrochim. Acta* 56 (2011) 1629.
- [807] Z.-D. Huang, B. Zhang, S.-W. Oh, Q.-B. Zheng, X.-Y. Lin, N. Yousefi, J.-K. Kim, *J. Mater. Chem.* 22 (2012) 3591.
- [808] L.-Y. Lin, M.-H. Yeh, J.-T. Tsai, Y.-H. Huang, C.-L. Sun, K.-C. Ho, *J. Mater. Chem. A* 1 (2013) 11237.
- [809] R. Liu, L. Wan, S. Liu, L. Pan, D. Wu, D. Zhao, *Adv. Funct. Mater.* 25 (2015) 526.
- [810] P. Duy Tho, T.H. Lee, D.H. Luong, F. Yao, A. Ghosh, L. Viet Thong, T.H. Kim, B. Li, J. Chang, Y.H. Lee, *ACS Nano* 9 (2015) 2018.
- [811] X. Yun, J. Wang, L. Shen, H. Dou, X. Zhang, *RSC Adv.* 5 (2015) 22173.
- [812] N. Jung, S. Kwon, D. Lee, D.-M. Yoon, Y.M. Park, A. Benayad, J.-Y. Choi, J.S. Park, *Adv. Mater.* 25 (2013) 6854.
- [813] D. Yu, K. Goh, H. Wang, L. Wei, W. Jiang, Q. Zhang, L. Dai, Y. Chen, *Nat. Nanotechnol.* 9 (2014) 555.
- [814] Q. Cheng, J. Tang, J. Ma, H. Zhang, N. Shinya, L.C. Qin, *Phys. Chem. Chem. Phys.* 13 (2011) 17615.
- [815] Y. Ma, P. Li, J.W. Sedloff, X. Zhang, H. Zhang, J. Liu, *ACS Nano* 9 (2015) 1352.
- [816] M.-Q. Zhao, Q. Zhang, J.-Q. Huang, G.-L. Tian, T.-C. Chen, W.-Z. Qian, F. Wei, *Carbon* 54 (2013) 403.
- [817] Y. Chen, X. Zhang, H. Zhang, X. Sun, D. Zhang, Y. Ma, *RSC Adv.* 2 (2012) 7747.
- [818] C. Zheng, X. Zhou, H. Cao, G. Wang, Z. Liu, *J. Power Sources* 258 (2014) 290.
- [819] S. Yu, Y. Li, N. Pan, *RSC Adv.* 4 (2014) 48758.
- [820] Y. Cao, M. Zhu, P. Li, R. Zhang, X. Li, Q. Gong, K. Wang, M. Zhong, D. Wu, F. Lin, H. Zhu, *Phys. Chem. Chem. Phys.* 15 (2013) 19550.
- [821] K. Gao, Z. Shao, J. Li, X. Wang, X. Peng, W. Wang, F. Wang, *J. Mater. Chem. A* 1 (2013) 63.
- [822] J. Ma, Q. Guo, H.-L. Gao, X. Qin, *Fuller., Nanotub., Carbon Nanostruct.* 23 (2014) 477.
- [823] J. Yan, Q. Wang, C. Lin, T. Wei, Z. Fan, *Adv. Energy Mater.* 4 (2014) 1400500.
- [824] H.-F. Ju, W.-L. Song, L.-Z. Fan, *J. Mater. Chem. A* 2 (2014) 10895.
- [825] W.-L. Song, K. Song, L.-Z. Fan, *ACS Appl. Mater. Interfaces* 7 (2015) 4257.
- [826] G. Wang, X. Sun, F. Lu, H. Sun, M. Yu, W. Jiang, C. Liu, J. Lian, *Small* 8 (2012) 452.
- [827] Y. Gogotsi, P. Simon, *Science* 334 (2011) 917.
- [828] M.R. Lukatskaya, O. Mashtalir, C.E. Ren, Y. Dall'Agnese, P. Rozier, P.L. Taberna, M. Naguib, P. Simon, M.W. Barsoum, Y. Gogotsi, *Science* 341 (2013) 1502.
- [829] Y. Tao, X. Xie, W. Lv, D.-M. Tang, D. Kong, Z. Huang, H. Nishihara, T. Ishii, B. Li, D. Golberg, F. Kang, T. Kyotani, Q.-H. Yang, *Sci. Rep.* 3 (2013) 2975.
- [830] J. Yan, Q. Wang, T. Wei, L. Jiang, M. Zhang, X. Jing, Z. Fan, *ACS Nano* 8 (2014) 4720.
- [831] Y. Yoon, K. Lee, S. Kwon, S. Seo, H. Yoo, S. Kim, Y. Shin, Y. Park, D. Kim, J.-Y. Choi, H. Lee, *ACS Nano* 8 (2014) 4580.
- [832] L.L. Zhang, R. Zhou, X.S. Zhao, *J. Mater. Chem.* 20 (2010) 5983.
- [833] H. Li, J. Wang, Q. Chu, Z. Wang, F. Zhang, S. Wang, *J. Power Sources* 190 (2009) 578.
- [834] N.A. Kumar, J.-B. Baek, *Chem. Commun.* 50 (2014) 6298.
- [835] Y. Luo, D. Kong, Y. Jia, J. Luo, Y. Lu, D. Zhang, K. Qiu, C.M. Li, T. Yu, *RSC Adv.* 3 (2013) 5851.
- [836] Y. Liu, Y. Ma, S. Guang, H. Xu, X. Su, *J. Mater. Chem. A* 2 (2014) 813.
- [837] H.-P. Cong, X.-C. Ren, P. Wang, S.-H. Yu, *Energy Environ. Sci.* 6 (2013) 1185.
- [838] Q. Zhang, Y. Li, Y. Feng, W. Feng, *Electrochim. Acta* 90 (2013) 95.
- [839] K. Zhang, L.L. Zhang, X.S. Zhao, J. Wu, *Chem. Mater.* 22 (2010) 1392.
- [840] X.-M. Feng, R.-M. Li, Y.-W. Ma, R.-F. Chen, N.-E. Shi, Q.-L. Fan, W. Huang, *Adv. Funct. Mater.* 21 (2011) 2989.
- [841] D.-W. Wang, F. Li, J. Zhao, W. Ren, Z.-G. Chen, J. Tan, Z.-S. Wu, I. Gentle, G.Q. Lu, H.-M. Cheng, *ACS Nano* 3 (2009) 1745.
- [842] H. Wang, Q. Hao, X. Yang, L. Lu, X. Wang, *Nanoscale* 2 (2010) 2164.
- [843] Q. Wu, Y. Xu, Z. Yao, A. Liu, G. Shi, *ACS Nano* 4 (2010) 1963.
- [844] S. Zhou, H. Zhang, Q. Zhao, X. Wang, J. Li, F. Wang, *Carbon* 52 (2013) 440.
- [845] Z.-F. Li, H. Zhang, Q. Liu, L. Sun, L. Stanciu, J. Xie, *ACS Appl. Mater. Interfaces* 5 (2013) 2685.
- [846] J. Lu, W. Liu, H. Ling, J. Kong, G. Ding, D. Zhou, X. Lu, *RSC Adv.* 2 (2012) 10537.
- [847] Y. Tang, N. Wu, S. Luo, C. Liu, K. Wang, L. Chen, *Macromol. Rapid Commun.* 33 (2012) 1780.
- [848] M. Xue, F. Li, J. Zhu, H. Song, M. Zhang, T. Cao, *Adv. Funct. Mater.* 22 (2012) 1284.
- [849] T. Huang, B. Zheng, L. Kou, K. Gopalsamy, Z. Xu, C. Gao, Y. Meng, Z. Wei, *RSC Adv.* 3 (2013) 23957.
- [850] Z.-F. Li, H. Zhang, Q. Liu, Y. Liu, L. Stanciu, J. Xie, *Carbon* 71 (2014) 257.
- [851] N.A. Kumar, H.-J. Choi, Y.R. Shin, D.W. Chang, L. Dai, J.-B. Baek, *ACS Nano* 6 (2012) 1715.
- [852] L. Lai, H. Yang, L. Wang, B.K. Teh, J. Zhong, H. Chou, L. Chen, W. Chen, Z. Shen, R.S. Ruoff, J. Lin, *ACS Nano* 6 (2012) 5941.
- [853] M. Kim, C. Lee, J. Jang, *Adv. Funct. Mater.* 24 (2014) 2489.
- [854] S. Chatterjee, R.K. Layek, A.K. Nandi, *Carbon* 52 (2013) 509.
- [855] X. Yan, J. Chen, J. Yang, Q. Xue, P. Miele, *ACS Appl. Mater. Interfaces* 2 (2010) 2521.
- [856] J. Xu, K. Wang, S.-Z. Zu, B.-H. Han, Z. Wei, *ACS Nano* 4 (2010) 5019.
- [857] L. Wang, Y. Ye, X. Lu, Z. Wen, Z. Li, H. Hou, Y. Song, *Sci. Rep.* 3 (2013) 3568.
- [858] H.-H. Chang, C.-K. Chang, Y.-C. Tsai, C.-S. Liao, *Carbon* 50 (2012) 2331.
- [859] A. Osterholm, T. Lindfors, J. Kauppila, P. Damlin, C. Kvarnstrom, *Electrochim. Acta* 83 (2012) 463.
- [860] Y. Liu, Y. Zhang, G. Ma, Z. Wang, K. Liu, H. Liu, *Electrochim. Acta* 88 (2013) 519.
- [861] J. Li, H. Xie, Y. Li, J. Power Sources 241 (2013) 388.
- [862] L. Lai, L. Wang, H. Yang, N.G. Sahoo, Q.X. Tam, J. Liu, C.K. Poh, S.H. Lim, Z. Shen, J. Lin, *Nano Energy* 1 (2012) 723.
- [863] C. Zhu, J. Zhai, D. Wen, S. Dong, J. Mater. Chem. 22 (2012) 6300.
- [864] H. Zhou, G. Han, Y. Xiao, Y. Chang, H.-J. Zhai, *J. Power Sources* 263 (2014) 259.
- [865] J. Zhang, Y. Yu, L. Liu, Y. Wu, *Nanoscale* 5 (2013) 3052.
- [866] J. Zhang, X.S. Zhao, *J. Phys. Chem. C* 116 (2012) 5420.
- [867] J. Jiang, Y. Li, J. Liu, X. Huang, C. Yuan, X.W. Lou, *Adv. Mater.* 24 (2012) 5166.
- [868] V. Ozolins, F. Zhou, M. Asta, *Acc. Chem. Res.* 46 (2013) 1084.
- [869] L.Y. Chen, Y. Hou, J.L. Kang, A. Hirata, T. Fujita, M.W. Chen, *Adv. Energy Mater.* 3 (2013) 851.
- [870] W. Wang, S. Guo, I. Lee, K. Ahmed, J. Zhong, Z. Favors, F. Zaera, M. Ozkan, C.S. Ozkan, *Sci. Rep.* 4 (2014) 4452.
- [871] M. Toupin, T. Brousse, D. Bélanger, *Chem. Mater.* 16 (2004) 3184.
- [872] D. Bélanger, L. Brousse, J.W. Long, *Electrochem. Soc. Interface* 17 (2008) 49.
- [873] Y. He, W. Chen, X. Li, Z. Zhang, J. Fu, C. Zhao, E. Xie, *ACS Nano* 7 (2013) 174.
- [874] L. Deng, J. Wang, G. Zhu, L. Kang, Z. Hao, Z. Lei, Z. Yang, Z.-H. Liu, *J. Power Sources* 248 (2014) 407.
- [875] J. Zhang, J. Jiang, H. Li, X.S. Zhao, *Energy Environ. Sci.* 4 (2011) 4009.
- [876] B.G. Choi, Y.S. Huh, W.H. Hong, D. Erickson, H.S. Park, *Nanoscale* 5 (2013) 3976.
- [877] N. Sooin, S.S. Roy, S.K. Mitra, T. Thundat, J.A. McLaughlin, *J. Mater. Chem.* 22 (2012) 14944.
- [878] G. Yu, L. Hu, N. Liu, H. Wang, M. Vosgueritchian, Y. Yang, Y. Cui, Z. Bao, *Nano Lett.* 11 (2011) 4438.
- [879] S. Chen, J. Zhu, X. Wu, Q. Han, X. Wang, *ACS Nano* 4 (2010) 2822.
- [880] Z.-S. Wu, W. Ren, D.-W. Wang, F. Li, B. Liu, H.-M. Cheng, *ACS Nano* 4 (2010) 5835.
- [881] G. Zhu, Z. He, J. Chen, J. Zhao, X. Feng, Y. Ma, Q. Fan, L. Wang, W. Huang, *Nanoscale* 6 (2014) 1079.
- [882] S. Wu, W. Chen, L. Yan, *J. Mater. Chem. A* 2 (2014) 2765.
- [883] M. Liu, W.W. Tjiu, J. Pan, C. Zhang, W. Gao, T. Liu, *Nanoscale* 6 (2014) 4233.
- [884] G. Yu, L. Hu, M. Vosgueritchian, H. Wang, X. Xie, J.R. McDonough, X. Cui, Y. Cui, Z. Bao, *Nano Lett.* 11 (2011) 2905.
- [885] T. Lu, Y.P. Zhang, H.B. Li, L.K. Pan, Y.L. Li, Z. Sun, *Electrochim. Acta* 55 (2010) 4170.
- [886] X. Dong, Y. Cao, J. Wang, M.B. Chan-Park, L. Wang, W. Huang, P. Chen, *RSC Adv.* 2 (2012) 4364.
- [887] Y. Haldorai, W. Voit, J.-J. Shim, *Electrochim. Acta* 120 (2014) 65.
- [888] X. Xia, J. Tu, Y. Mai, R. Chen, X. Wang, C. Gu, X. Zhao, *Chem. Eur. J.* 17 (2011) 10898.
- [889] B. Zhao, J.S. Song, P. Liu, W.W. Xu, T. Fang, Z. Jiao, H.J. Zhang, Y. Jiang, *J. Mater. Chem.* 21 (2011) 18792.
- [890] C. Wu, S. Deng, H. Wang, Y. Sun, J. Liu, H. Yan, *ACS Appl. Mater. Interfaces* 6 (2014) 1106.
- [891] F.H. Li, J.F. Song, H.F. Yang, S.Y. Gan, Q.X. Zhang, D.X. Han, A. Ivaska, L. Niu, *Nanotechnology* 20 (2009) 455602.
- [892] Z. Li, T. Chang, G. Yun, J. Guo, B. Yang, *J. Alloys Compd.* 586 (2014) 353.
- [893] M. Chen, H. Wang, L. Li, Z. Zhang, C. Wang, Y. Liu, W. Wang, J. Gao, *ACS Appl. Mater. Interfaces* 6 (2014) 14327.
- [894] Y. Wang, C.X. Guo, J. Liu, T. Chen, H. Yang, C.M. Li, *Dalton Trans.* 40 (2011) 6388.
- [895] L. Li, K.H. Seng, Z. Chen, H. Liu, I.P. Nevirkovets, Z. Guo, *Electrochim. Acta* 87 (2013) 801.
- [896] B. Wang, J. Park, C. Wang, H. Ahn, G. Wang, *Electrochim. Acta* 55 (2010) 6812.
- [897] Y. Wu, S. Liu, H. Wang, X. Wang, X. Zhang, G. Jin, *Electrochim. Acta* 90 (2013) 210.
- [898] S. Yang, X. Song, P. Zhang, L. Gao, *J. Mater. Chem. A* 1 (2013) 14162.
- [899] C.-L. Liu, K.-H. Chang, C.-C. Hu, W.-C. Wen, *J. Power Sources* 217 (2012) 184.
- [900] Q. Jiangying, G. Feng, Z. Quan, W. Zhiyu, H. Han, L. Beibei, W. Wubo, W. Xuzhen, Q. Jieshan, *Nanoscale* 5 (2013) 2999.
- [901] J.W. Lee, A.S. Hall, J.-D. Kim, T.E. Mallouk, *Chem. Mater.* 24 (2012) 1158.
- [902] Q. Qu, S. Yang, X. Feng, *Adv. Mater.* 23 (2011) 5574.
- [903] T. Qi, J. Jiang, H. Chen, H. Wan, L. Miao, L. Zhang, *Electrochim. Acta* 114 (2013) 674.
- [904] W. Shi, J. Zhu, D.H. Sim, Y.Y. Tay, Z. Lu, X. Zhang, Y. Sharma, M. Srinivasan, H. Zhang, H.H. Hng, Q. Yan, *J. Mater. Chem.* 21 (2011) 3422.
- [905] M. Liu, J. Sun, *J. Mater. Chem. A* 2 (2014) 12068.

- [906] S. Park, S. Kim, *Electrochim. Acta* 89 (2013) 516.
- [907] J. Yan, T. Wei, W. Qiao, B. Shao, Q. Zhao, L. Zhang, Z. Fan, *Electrochim. Acta* 55 (2010) 6973.
- [908] C. Xiang, M. Li, M. Zhi, A. Manivannan, N. Wu, *J. Power Sources* 226 (2013) 65.
- [909] W. Zhou, J. Liu, T. Chen, K.S. Tan, X. Jia, Z. Luo, C. Cong, H. Yang, C.M. Li, T. Yu, *Phys. Chem. Chem. Phys.* 13 (2011) 14462.
- [910] S.D. Perera, A.D. Liyanage, N. Nijem, J.P. Ferraris, Y.J. Chabal, K.J. Balkus Jr., *J. Power Sources* 230 (2013) 130.
- [911] H. Zhang, A. Xie, C. Wang, H. Wang, Y. Shen, X. Tian, *ChemPhysChem* 15 (2014) 366.
- [912] C.Y. Foo, A. Sumboja, D.J.H. Tan, J. Wang, P.S. Lee, *Adv. Energy Mater.* 4 (2014) 1400236.
- [913] Y. Wu, G. Gao, G. Wu, *J. Mater. Chem. A* 3 (2015) 1828.
- [914] D. Nagaraju, Q. Wang, P. Beaujuge, H.N. Alshareef, *J. Mater. Chem. A* 2 (2014) 17146.
- [915] S. Chen, J. Zhu, X. Wang, *J. Phys. Chem. C* 114 (2010) 11829.
- [916] S. Gao, Y. Sun, F. Lei, L. Liang, J. Liu, W. Bi, B. Pan, Y. Xie, *Angew. Chem. Int. Ed.* 53 (2014) 12789.
- [917] U.M. Patil, M.S. Nam, J.S. Sohn, S.B. Kulkarni, R. Shin, S. Kang, S. Lee, J.H. Kim, S.C. Jun, *J. Mater. Chem. A* 2 (2014) 19075.
- [918] H. Wang, H.S. Casalongue, Y. Liang, H. Dai, *J. Am. Chem. Soc.* 132 (2010) 7472.
- [919] J. Yan, Z. Fan, W. Sun, G. Ning, T. Wei, Q. Zhang, R. Zhang, L. Zhi, F. Wei, *Adv. Funct. Mater.* 22 (2012) 2632.
- [920] S. Bag, C.R. Raj, *J. Mater. Chem. A* 2 (2014) 17848.
- [921] B. Dong, H. Zhou, J. Liang, L. Zhang, G. Gao, S. Ding, *Nanotechnology* 25 (2014) 435403.
- [922] C.-Y. Chen, C.-Y. Fan, M.-T. Lee, J.-K. Chang, *J. Mater. Chem.* 22 (2012) 7697.
- [923] S. Yang, X. Song, P. Zhang, L. Gao, *ACS Appl. Mater. Interfaces* 5 (2013) 3317.
- [924] X. Zhao, L. Zhang, S. Murali, M.D. Stoller, Q. Zhang, Y. Zhu, R.S. Ruoff, *ACS Nano* 6 (2012) 5404.
- [925] H. Chen, S. Zhou, M. Chen, L. Wu, *J. Mater. Chem.* 22 (2012) 25207.
- [926] J. Chang, M. Jin, F. Yao, T.H. Kim, L. Viet Thong, H. Yue, F. Gunes, B. Li, A. Ghosh, S. Xie, Y.H. Lee, *Adv. Funct. Mater.* 23 (2013) 5074.
- [927] Z. Fan, J. Yan, T. Wei, L. Zhi, G. Ning, T. Li, F. Wei, *Adv. Funct. Mater.* 21 (2011) 2366.
- [928] J. Yan, Z.J. Fan, T. Wei, W.Z. Qian, M.L. Zhang, F. Wei, *Carbon* 48 (2010) 3825.
- [929] Y. Li, N. Zhao, C. Shi, E. Liu, C. He, *J. Phys. Chem. C* 116 (2012) 25226.
- [930] J. Ge, H.-B. Yao, W. Hu, X.-F. Yu, Y.-X. Yan, L.-B. Mao, H.-H. Li, S.-S. Li, S.-H. Yu, *Nano Energy* 2 (2013) 505.
- [931] C.-C. Wang, H.-C. Chen, S.-Y. Lu, *Chem. Eur. J.* 20 (2014) 517.
- [932] K. Karthikeyan, D. Kalpana, S. Amareesh, Y.S. Lee, *RSC Adv.* 2 (2012) 12322.
- [933] M. Li, G. Sun, P. Yin, C. Ruan, K. Ai, *ACS Appl. Mater. Interfaces* 5 (2013) 11462.
- [934] S. Chen, J. Duan, Y. Tang, S.Z. Qiao, *Chem. Eur. J.* 19 (2013) 7118.
- [935] G. Han, Y. Liu, L. Zhang, E. Kan, S. Zhang, J. Tang, W. Tang, *Sci. Rep.* 4 (2014) 4824.
- [936] W.R. Grove, *Philos. Mag.* 14 (1839) 127.
- [937] L. Carrette, K.A. Friedrich, U. Stimming, *ChemPhysChem* 1 (2000) 162.
- [938] B.C.H. Steele, A. Heinzel, *Nature* 414 (2001) 345.
- [939] K. Dutta, P. Kumar, S. Das, P.P. Kundu, *Polym. Rev.* 54 (2014) 1.
- [940] X. Zhao, M. Yin, L. Ma, L. Liang, C. Liu, J. Liao, T. Lu, W. Xing, *Energy Environ. Sci.* 4 (2011) 2736.
- [941] R. Bashyam, P. Zelenay, *Nature* 443 (2006) 63.
- [942] M. Lefèvre, E. Proietti, F. Jaouen, J.-P. Dodelet, *Science* 324 (2009) 71.
- [943] S. Guo, E. Wang, *Nano Today* 6 (2011) 240.
- [944] V.R. Stamenkovic, B. Fowler, B.S. Mun, G. Wang, P.N. Ross, C.A. Lucas, N.M. Marković, *Science* 315 (2007) 493.
- [945] P. Song, Y. Zhang, J. Pan, L. Zhuang, W. Xu, *Chem. Commun.* 51 (2015) 1972.
- [946] F. Su, Z. Tian, C.K. Poh, Z. Wang, S.H. Lim, Z. Liu, J. Lin, *Chem. Mater.* 22 (2009) 832.
- [947] K. Gong, F. Du, Z. Xia, M. Durstock, L. Dai, *Science* 323 (2009) 760.
- [948] A.L. Dicks, *J. Power Sources* 156 (2006) 128.
- [949] K. Elumeeva, J. Ren, M. Antonietti, T.P. Feller, *ChemElectroChem* 2 (2015) 584.
- [950] Y.-J. Wang, D.P. Wilkinson, J. Zhang, *Chem. Rev.* 111 (2011) 7625.
- [951] N. Kakati, J. Maiti, S.H. Lee, S.H. Jee, B. Viswanathan, Y.S. Yoon, *Chem. Rev.* 114 (2014) 12397.
- [952] N.G. Sahoo, Y. Pan, L. Li, S.H. Chan, *Adv. Mater.* 24 (2012) 4203.
- [953] T.M. Gür, *Chem. Rev.* 113 (2013) 6179.
- [954] W. Wang, C. Su, Y. Wu, R. Ran, Z. Shao, *Chem. Rev.* 113 (2013) 8104.
- [955] Y.-K. Yang, C.-E. He, W.-J. He, L.-J. Yu, R.-G. Peng, X.-L. Xie, X.-B. Wang, Y.-W. Mai, *J. Nanoparticle Res.* 13 (2011) 5571.
- [956] B. Seger, P.V. Kamat, *J. Phys. Chem. C* 113 (2009) 7990.
- [957] C. Huang, C. Li, G. Shi, *Energy Environ. Sci.* 5 (2012) 8848.
- [958] C. Su, K.P. Loh, *Acc. Chem. Res.* 46 (2013) 2275.
- [959] Y. Li, L. Tang, J. Li, *Electrochem. Commun.* 11 (2009) 846.
- [960] J.D. Qiu, G.C. Wang, R.P. Liang, X.H. Xia, H.W. Yu, *J. Phys. Chem. C* 115 (2011) 15639.
- [961] D. Higgins, M.A. Hoque, M.H. Seo, R. Wang, F. Hassan, J.-Y. Choi, M. Pritzker, A. Yu, J. Zhang, Z. Chen, *Adv. Funct. Mater.* 24 (2014) 4325.
- [962] H. Qiu, X. Dong, B. Sana, T. Peng, D. Paramelle, P. Chen, S. Lim, *ACS Appl. Mater. Interfaces* 5 (2013) 782.
- [963] M.A. Hoque, F.M. Hassan, D. Higgins, J.-Y. Choi, M. Pritzker, S. Knights, S. Ye, Z. Chen, *Adv. Mater.* 27 (2015) 1229.
- [964] C.X. Guo, L.Y. Zhang, J. Miao, J. Zhang, C.M. Li, *Adv. Energy Mater.* 3 (2013) 167.
- [965] L. Ren, K.S. Hui, K.N. Hui, *J. Mater. Chem. A* 1 (2013) 5689.
- [966] H. Gao, Y. Wang, F. Xiao, C.B. Ching, H. Duan, *J. Phys. Chem. C* 116 (2012) 7719.
- [967] X.-R. Li, X.-L. Li, M.-C. Xu, J.-J. Xu, H.-Y. Chen, *J. Mater. Chem. A* 2 (2014) 1697.
- [968] M. Govindhan, A. Chen, *J. Power Sources* 274 (2015) 928.
- [969] S.H. Lee, N. Kakati, S.H. Jee, J. Maiti, Y.-S. Yoon, *Mater. Lett.* 65 (2011) 3281.
- [970] C.V. Rao, C.R. Cabrera, Y. Ishikawa, *J. Phys. Chem. C* 115 (2011) 21963.
- [971] G. Yang, Y. Li, R.K. Rana, J.-J. Zhu, *J. Mater. Chem. A* 1 (2013) 1754.
- [972] H. Zhang, X. Xu, P. Gu, C. Li, P. Wu, C. Cai, *Electrochim. Acta* 56 (2011) 7064.
- [973] H.-P. Cong, X.-C. Ren, S.-H. Yu, *ChemCatChem* 4 (2012) 1555.
- [974] C.-C. Kung, P.-Y. Lin, Y. Xue, R. Akolkar, L. Dai, X. Yu, C.-C. Liu, *J. Power Sources* 256 (2014) 329.
- [975] M. Zhang, Z. Yan, Q. Sun, J. Xie, J. Jing, *New J. Chem.* 36 (2012) 2533.
- [976] R. Zhang, W. Chen, *J. Mater. Chem. A* 1 (2013) 11457.
- [977] M. Liu, Y. Dong, Y. Wu, H. Feng, J. Li, *Chem. Eur. J.* 19 (2013) 14781.
- [978] C.V. Rao, A.L.M. Reddy, Y. Ishikawa, P.M. Ajayan, *Carbon* 49 (2011) 931.
- [979] C. Hu, H. Cheng, Y. Zhao, Y. Hu, Y. Liu, L. Dai, L. Qu, *Adv. Mater.* 24 (2012) 5493.
- [980] J. Duan, S. Chen, S. Dai, S.Z. Qiao, *Adv. Funct. Mater.* 24 (2014) 2072.
- [981] Y. Liang, Y. Li, H. Wang, J. Zhou, J. Wang, T. Regier, H. Dai, *Nat. Mater.* 10 (2011) 780.
- [982] Z.-S. Wu, S. Yang, Y. Sun, K. Parvez, X. Feng, K. Müllen, *J. Am. Chem. Soc.* 134 (2012) 9082.
- [983] Y. Liang, H. Wang, J. Zhou, Y. Li, J. Wang, T. Regier, H. Dai, *J. Am. Chem. Soc.* 134 (2012) 3517.
- [984] W. Song, Z. Chen, C. Yang, Z. Yang, J. Tai, Y. Nan, H. Lu, *J. Mater. Chem. A* 3 (2015) 1049.
- [985] Z. Xia, S. Wang, L. Jiang, H. Sun, F. Qi, J. Jin, G. Sun, *J. Mater. Chem. A* 3 (2015) 1641.
- [986] Y. Wu, Q. Shi, Y. Li, Z. Lai, H. Yu, H. Wang, F. Peng, *J. Mater. Chem. A* 3 (2015) 1142.
- [987] Y. Xin, J.-G. Liu, Y. Zhou, W. Liu, J. Gao, Y. Xie, Y. Yin, Z. Zou, *J. Power Sources* 196 (2011) 1012.
- [988] P. Kundu, C. Nethravathi, P.A. Deshpande, M. Rajamathi, G. Madras, N. Ravishanker, *Chem. Mater.* 23 (2011) 2772.
- [989] Y.G. Zhou, J.J. Chen, F.B. Wang, Z.H. Sheng, X.H. Xia, *Chem. Commun.* 46 (2010) 5951.
- [990] E. Yoo, T. Okada, T. Akita, M. Kohyama, I. Honma, J. Nakamura, *J. Power Sources* 196 (2011) 110.
- [991] Y. Shao, S. Zhang, C. Wang, Z. Nie, J. Liu, Y. Wang, Y. Lin, *J. Power Sources* 195 (2010) 4600.
- [992] T. Maiyalagan, X. Dong, P. Chen, X. Wang, *J. Mater. Chem.* 22 (2012) 5286.
- [993] E. Yoo, T. Okada, T. Akita, M. Kohyama, J. Nakamura, I. Honma, *Nano Lett.* 9 (2009) 2255.
- [994] W. Qian, R. Hao, J. Zhou, M. Eastman, B.A. Manhat, Q. Sun, A.M. Goforth, J. Jiao, *Carbon* 52 (2013) 595.
- [995] M. Wakisaka, S. Mitsui, Y. Hirose, K. Kawashima, H. Uchida, M. Watanabe, *J. Phys. Chem. B* 110 (2006) 23489.
- [996] H. Wang, C. Xu, F. Cheng, M. Zhang, S. Wang, S.P. Jiang, *Electrochem. Commun.* 10 (2008) 1575.
- [997] S. Guo, S. Dong, E. Wang, *ACS Nano* 4 (2009) 547.
- [998] Q. Yue, K. Zhang, X. Chen, L. Wang, J. Zhao, J. Liu, J. Jia, *Chem. Commun.* 46 (2010) 3369.
- [999] M. Stojmenović, M. Momčilović, N. Gavrilov, I.A. Pašti, S. Mentus, B. Jokić, B. Babić, *Electrochim. Acta* 153 (2015) 130.
- [1000] M.H. Seo, S.M. Choi, H.J. Kim, W.B. Kim, *Electrochem. Commun.* 13 (2011) 182.
- [1001] C.-T. Hsieh, Y.-Y. Liu, A.K. Roy, *Electrochim. Acta* 64 (2012) 205.
- [1002] L. Truong-Phuoc, C. Pham-Huu, V. Da Costa, I. Janowska, *Chem. Commun.* 50 (2014) 14433.
- [1003] H. Ghanbarlou, S. Rowshanzamir, B. Kazeminasab, M.J. Parnian, *J. Power Sources* 273 (2015) 981.
- [1004] H. Yin, C. Zhang, F. Liu, Y. Hou, *Adv. Funct. Mater.* 24 (2014) 2930.
- [1005] H. Zhao, T. Zhao, *J. Mater. Chem. A* 1 (2013) 183.
- [1006] S.S. Kim, Y.R. Kim, T.D. Chung, B.H. Sohn, *Adv. Funct. Mater.* 24 (2014) 2764.
- [1007] K. Han, P. Miao, H. Tong, T. Liu, W. Cheng, X. Zhu, Y. Tang, *Appl. Phys. Lett.* 104 (2014) 053101.
- [1008] K. Kakaei, M. Dorraji, *Electrochim. Acta* 143 (2014) 207.
- [1009] S. Jin, M. Chen, H. Dong, B. He, H. Lu, L. Su, W. Dai, Q. Zhang, X. Zhang, *J. Power Sources* 274 (2015) 1173.
- [1010] D.J. Davis, A.R.O. Raji, T.N. Lambert, J.A. Vigil, L. Li, K. Nan, J.M. Tour, *Electroanalysis* 26 (2014) 164.
- [1011] Q. Liu, J. Zhang, *Langmuir* 29 (2013) 3821.
- [1012] Z. Bo, D. Hu, J. Kong, J. Yan, K. Cen, *J. Power Sources* 273 (2015) 530.
- [1013] J.-N. Zheng, S.-S. Li, F.-Y. Chen, N. Bao, A.-J. Wang, J.-R. Chen, J.-J. Feng, *J. Power Sources* 266 (2014) 259.
- [1014] L. Dong, R.R.S. Gari, Z. Li, M.M. Craig, S. Hou, *Carbon* 48 (2010) 781.
- [1015] C. Venkateswara Rao, C.R. Cabrera, Y. Ishikawa, *J. Phys. Chem. C* 115 (2011) 21963.
- [1016] Y. Hu, H. Zhang, P. Wu, H. Zhang, B. Zhou, C. Cai, *Phys. Chem. Chem. Phys.* 13 (2011) 4083.
- [1017] S. Zhang, Y. Shao, H.-g. Liao, J. Liu, I.A. Aksay, G. Yin, Y. Lin, *Chem. Mater.* 23 (2011) 1079.
- [1018] F. Han, X. Wang, J. Lian, Y. Wang, *Carbon* 50 (2012) 5498.
- [1019] S. Guo, S. Sun, *J. Am. Chem. Soc.* 134 (2012) 2492.
- [1020] Y. Hu, P. Wu, Y. Yin, H. Zhang, C. Cai, *Appl. Catal. B* 111 (2012) 208.
- [1021] K. Zhang, Q. Yue, G. Chen, Y. Zhai, L. Wang, H. Wang, J. Zhao, J. Liu, J. Jia, H. Li, *J. Phys. Chem. C* 115 (2010) 379.
- [1022] Y. Hu, P. Wu, H. Zhang, C. Cai, *Electrochim. Acta* 85 (2012) 314.
- [1023] P. Divya, S. Ramaprabhu, *J. Mater. Chem. A* 2 (2014) 4912.
- [1024] L. Gan, S. Rudi, C. Cui, P. Strasser, *ChemCatChem* 5 (2013) 2691.

- [1025] J.-J. Lv, S.-S. Li, A.-J. Wang, L.-P. Mei, J.-R. Chen, J.-J. Feng, *Electrochim. Acta* 136 (2014) 521.
- [1026] G.H. Jeong, D. Choi, M. Kang, J. Shin, J.-G. Kang, S.-W. Kim, *RSC Adv.* 3 (2013) 8864.
- [1027] M. Liu, Y. Lu, W. Chen, *Adv. Funct. Mater.* 23 (2013) 1289.
- [1028] N. Cao, J. Su, W. Luo, G. Cheng, *Catal. Commun.* 43 (2014) 47.
- [1029] Y. Zhang, Y.-E. Gu, S. Lin, J. Wei, Z. Wang, C. Wang, Y. Du, W. Ye, *Electrochim. Acta* 56 (2011) 8746.
- [1030] Z. Lu, H. Wang, D. Kong, K. Yan, P.-C. Hsu, G. Zheng, H. Yao, Z. Liang, X. Sun, Y. Cui, *Nat. Commun.* 5 (2014) 4345.
- [1031] Y. Zhao, S. Chen, B. Sun, D. Su, X. Huang, H. Liu, Y. Yan, K. Sun, G. Wang, *Sci. Rep.* 5 (2015) 7629.
- [1032] Q. He, Q. Li, S. Khene, X. Ren, F.E. López-Suárez, D. Lozano-Castelló, A.N. Bueno-López, G. Wu, *J. Phys. Chem. C* 117 (2013) 8697.
- [1033] Y. Chen, K.P. Prasad, X. Wang, H. Pang, R. Yan, A. Than, M.B. Chan-Park, P. Chen, *Phys. Chem. Chem. Phys.* 15 (2013) 9170.
- [1034] Q. He, Q. Li, S. Khene, X. Ren, F.E. Lopez-Suarez, D. Lozano-Castello, A. Bueno-Lopez, G. Wu, *J. Phys. Chem. C* 117 (2013) 8697.
- [1035] A. Ramírez, P. Hillebrand, D. Stellmach, M.M. May, P. Bogdanoff, S. Fiechter, *J. Phys. Chem. C* 118 (2014) 14073.
- [1036] Q. Tang, L. Jiang, J. Liu, S. Wang, G. Sun, *ACS Catal.* 4 (2014) 457.
- [1037] S. Khilari, S. Pandit, M.M. Ghangrekar, D. Das, D. Pradhan, *RSC Adv.* 3 (2013) 7902.
- [1038] Q. Wen, S. Wang, J. Yan, L. Cong, Z. Pan, Y. Ren, Z. Fan, *J. Power Sources* 216 (2012) 187.
- [1039] Y. Ma, H. Wang, J. Key, V. Linkov, S. Ji, X. Mao, Q. Wang, R. Wang, *Int. J. Hydrogen Energy* 39 (2014) 14777.
- [1040] X.-Y. Yan, X.-L. Tong, Y.-F. Zhang, X.-D. Han, Y.-Y. Wang, G.-Q. Jin, Y. Qin, X.-Y. Guo, *Chem. Commun.* 48 (2012) 1892.
- [1041] M. Sun, H. Liu, Y. Liu, J. Qu, J. Li, *Nanoscale* 7 (2015) 1250.
- [1042] L.-S. Zhang, X.-Q. Liang, W.-G. Song, Z.-Y. Wu, *Phys. Chem. Chem. Phys.* 12 (2010) 12055.
- [1043] R.I. Jafri, N. Rajalakshmi, S. Ramaprabhu, *J. Mater. Chem.* 20 (2010) 7114.
- [1044] Y. Xin, J.-G. Liu, X. Jie, W. Liu, F. Liu, Y. Yin, J. Gu, Z. Zou, *Electrochim. Acta* 60 (2012) 354.
- [1045] D. Higgins, F.M. Hassan, M.H. Seo, J.-Y. Choi, M.A. Hoque, D.U. Lee, Z. Chen, *J. Mater. Chem. A* 3 (2015) 6340.
- [1046] M.A. Hoque, F.M. Hassan, D. Higgins, J.Y. Choi, M. Pritzker, S. Knights, S. Ye, Z. Chen, *Adv. Mater.* 27 (2015) 1229.
- [1047] S.Y. Wang, X. Wang, S.P. Jiang, *Phys. Chem. Chem. Phys.* 13 (2011) 6883.
- [1048] S. Li, Y. Hu, Q. Xu, J. Sun, B. Hou, Y. Zhang, *J. Power Sources* 213 (2012) 265.
- [1049] M.S. Wietecha, J. Zhu, G. Gao, N. Wang, H. Feng, M.L. Goring, M.L. Kasner, S. Hou, *J. Power Sources* 198 (2012) 30.
- [1050] Y. Wang, K.S. Chen, J. Mishler, S.C. Cho, X.C. Adroher, *Appl. Energy* 88 (2011) 981.
- [1051] F. Jaouen, E. Proietti, M. Lefèvre, R. Chenitz, J.-P. Dodelet, G. Wu, H.T. Chung, C.M. Johnston, P. Zelenay, *Energy Environ. Sci.* 4 (2011) 114.
- [1052] A. Chandan, M. Hattenberger, A. El-Kharouf, S. Du, A. Dhir, V. Self, B.G. Pollet, A. Ingram, W. Bujalski, *J. Power Sources* 231 (2013) 264.
- [1053] T. Yuan, L. Pu, Q. Huang, H. Zhang, X. Li, H. Yang, *Electrochim. Acta* 117 (2014) 393.
- [1054] D.C. Lee, H.N. Yang, S.H. Park, W.J. Kim, *J. Membr. Sci.* 452 (2014) 20.
- [1055] Y.-C. Cao, C. Xu, X. Wu, X. Wang, L. Xing, K. Scott, *J. Power Sources* 196 (2011) 8377.
- [1056] S. Khilari, S. Pandit, M.M. Ghangrekar, D. Pradhan, D. Das, *Ind. Eng. Chem. Res.* 52 (2013) 11597.
- [1057] C. Xue, J. Zou, Z. Sun, F. Wang, K. Han, H. Zhu, *Int. J. Hydrogen Energy* 39 (2014) 7931.
- [1058] H. Zarrin, D. Higgins, Y. Jun, Z. Chen, M. Fowler, *J. Phys. Chem. C* 115 (2011) 20774.
- [1059] C.W. Lin, Y.S. Lu, *J. Power Sources* 237 (2013) 187.
- [1060] Z. Jiang, X. Zhao, Y. Fu, A. Manthiram, *J. Mater. Chem.* 22 (2012) 24862.
- [1061] Y.-S. Ye, M.-Y. Cheng, X.-L. Xie, J. Rick, Y.-J. Huang, F.-C. Chang, B.-J. Hwang, *J. Power Sources* 239 (2013) 424.
- [1062] K. Scott, *Chem. Commun.* 48 (2012) 5584.
- [1063] B.G. Choi, J. Hong, Y.C. Park, D.H. Jung, W.H. Hong, P.T. Hammond, H. Park, *ACS Nano* 5 (2011) 5167.
- [1064] H.-C. Chien, L.-D. Tsai, C.-P. Huang, C.-y. Kang, J.-N. Lin, F.-C. Chang, *Int. J. Hydrogen Energy* 38 (2013) 13792.
- [1065] I. Nicotera, C. Simari, L. Coppola, P. Zygori, D. Gournis, S. Brutti, F.D. Minuto, A.S. Arico, D. Sebastian, V. Baglio, *J. Phys. Chem. C* 118 (2014) 24357.
- [1066] M. He, J. Jung, F. Qiu, Z. Lin, *J. Mater. Chem.* 22 (2012) 24254.
- [1067] X. Li, D. Xie, H. Park, T.H. Zeng, K. Wang, J. Wei, M. Zhong, D. Wu, J. Kong, H. Zhu, *Adv. Energy Mater.* 3 (2013) 1029.
- [1068] H. Bi, F. Huang, J. Liang, X. Xie, M. Jiang, *Adv. Mater.* 23 (2011) 3202.
- [1069] J. Wu, H.A. Becerril, Z. Bao, Z. Liu, Y. Chen, P. Peumans, *Appl. Phys. Lett.* 92 (2008) 263302.
- [1070] D. Zhang, W.C.H. Choy, C.C.D. Wang, X. Li, L. Fan, K. Wang, H. Zhu, *Appl. Phys. Lett.* 99 (2011) 223302.
- [1071] G. Eda, Y.Y. Lin, S. Miller, C.W. Chen, W.F. Su, M. Chhowalla, *Appl. Phys. Lett.* 92 (2008) 233305.
- [1072] D. Liu, Y. Li, S. Zhao, A. Cao, C. Zhang, Z. Liu, Z. Bian, Z. Liu, C. Huang, *RSC Adv.* 3 (2013) 13720.
- [1073] Z. Liu, Q. Liu, Y. Huang, Y. Ma, S. Yin, X. Zhang, W. Sun, Y. Chen, *Adv. Mater.* 20 (2008) 3924.
- [1074] Q. Liu, Z. Liu, X. Zhang, N. Zhang, L. Yang, S. Yin, Y. Chen, *Appl. Phys. Lett.* 92 (2008) 223303.
- [1075] M.M. Stylianakis, G.D. Spyropoulos, E. Stratakis, E. Kymakis, *Carbon* 50 (2012) 5554.
- [1076] Y. Gao, H.-L. Yip, K.-S. Chen, K.M. O'Malley, O. Acton, Y. Sun, G. Ting, H. Chen, A.K.Y. Jen, *Adv. Mater.* 23 (2011) 1903.
- [1077] K.D.G.I. Jayawardena, R. Rhodes, K.K. Gandhi, M.R.R. Prabhath, G.D.M.R. Dabera, M.J. Beliat, L.J. Rozanski, S.J. Henley, S.R.P. Silva, *J. Mater. Chem. A* 1 (2013) 9922.
- [1078] X. Liu, H. Kim, L.J. Guo, *Org. Electron.* 14 (2013) 591.
- [1079] A. Chuchmala, M. Palewicz, A. Sikora, A. Iwan, *Synth. Met.* 169 (2013) 33.
- [1080] J. Kim, V.C. Tung, J.X. Huang, *Adv. Energy Mater.* 1 (2011) 1052.
- [1081] X. Li, H. Zhu, K. Wang, A. Cao, J. Wei, C. Li, Y. Jia, Z. Li, X. Li, D. Wu, *Adv. Mater.* 22 (2010) 2743.
- [1082] C. Xie, J. Jie, B. Nie, T. Yan, Q. Li, P. Lv, F. Li, M. Wang, C. Wu, L. Wang, L. Luo, *Appl. Phys. Lett.* 100 (2012) 193103.
- [1083] X. Li, H. Zhu, K. Wang, A. Cao, J. Wei, C. Li, Y. Jia, Z. Li, X. Li, D. Wu, *Adv. Mater.* 22 (2010) 2743.
- [1084] V. Yong, J.M. Tour, *Small* 6 (2010) 313.
- [1085] G. Li, R. Zhu, Y. Yang, *Nat. Photonics* 6 (2012) 153.
- [1086] S. Günes, H. Neugebauer, N.S. Sariciftci, *Chem. Rev.* 107 (2007) 1324.
- [1087] Z. He, C. Zhong, S. Su, M. Xu, H. Wu, Y. Cao, *Nat. Photonics* 6 (2012) 591.
- [1088] C.J. Brabec, S. Gowrisanker, J.J.M. Halls, D. Laird, S. Jia, S.P. Williams, *Adv. Mater.* 22 (2010) 3839.
- [1089] H. Zhou, Q. Chen, G. Li, S. Luo, T.-B. Song, H.-S. Duan, Z. Hong, J. You, Y. Liu, Y. Yang, *Science* 345 (2014) 542.
- [1090] M.A. Green, K. Emery, Y. Hishikawa, W. Warta, E.D. Dunlop, *Prog. Photovolt.* 21 (2013) 1.
- [1091] A. Iwan, A. Chuchmala, *Prog. Polym. Sci.* 37 (2012) 1805.
- [1092] X. Guo, M. Baumgarten, K. Müllen, *Prog. Polym. Sci.* 38 (2013) 1832.
- [1093] W. Wan, G. Long, L. Huang, Y. Chen, *Adv. Mater.* 23 (2011) 5342.
- [1094] Y. Sun, W. Zhang, H. Chi, Y. Liu, C.L. Hou, D. Fang, *Renew. Sustain. Energy Rev.* 43 (2015) 973.
- [1095] L. Valentini, M. Cardinali, S.B. Bon, D. Bagnis, R. Verdejo, M.A. Lopez-Manchado, J.M. Kenny, *J. Mater. Chem.* 20 (2010) 995.
- [1096] N.M. Gabor, *Acc. Chem. Res.* 46 (2013) 1348.
- [1097] F. Chen, N.J. Tao, *Acc. Chem. Res.* 42 (2009) 429.
- [1098] Q. Liu, Z. Liu, X. Zhong, L. Yang, N. Zhang, G. Pan, S. Yin, Y. Chen, J. Wei, *Adv. Funct. Mater.* 19 (2009) 894.
- [1099] M.M. Stylianakis, E. Stratakis, E. Koudoumas, E. Kymakis, S.H. Anastasiadis, *ACS Appl. Mater. Interfaces* 4 (2012) 4864.
- [1100] J.Y. Kim, K. Lee, N.E. Coates, D. Moses, T.-Q. Nguyen, M. Dante, A.J. Heeger, *Science* 317 (2007) 222.
- [1101] V. Gupta, N. Chaudhary, R. Srivastava, G.D. Sharma, R. Bhardwaj, S. Chand, *J. Am. Chem. Soc.* 133 (2011) 9960.
- [1102] Y. Li, Y. Hu, Y. Zhao, G. Shi, L. Deng, Y. Hou, L. Qu, *Adv. Mater.* 23 (2011) 776.
- [1103] J. Liu, G.-H. Kim, Y. Xue, J.Y. Kim, J.-B. Baek, M. Durstock, L. Dai, *Adv. Mater.* 26 (2014) 786.
- [1104] M. Jørgensen, K. Norrman, F.C. Krebs, *Sol. Energy Mater. Sol. Cells* 92 (2008) 686.
- [1105] D. Yang, L. Zhou, L. Chen, B. Zhao, J. Zhang, C. Li, *Chem. Commun.* 48 (2012) 8078.
- [1106] Y.-J. Jeon, J.-M. Yun, D.-Y. Kim, S.-I. Na, S.-S. Kim, *Sol. Energy Mater. Sol. Cells* 105 (2012) 96.
- [1107] S.-S. Li, K.-H. Tu, C.-C. Lin, C.-W. Chen, M. Chhowalla, *ACS Nano* 4 (2010) 3169.
- [1108] J.-M. Yun, J.-S. Yeo, J. Kim, H.-G. Jeong, D.-Y. Kim, Y.-J. Noh, S.-S. Kim, B.-C. Ku, S.-I. Na, *Adv. Mater.* 23 (2011) 4923.
- [1109] M. Li, W. Ni, B. Kan, X. Wan, L. Zhang, Q. Zhang, G. Long, Y. Zuo, Y. Chen, *Phys. Chem. Chem. Phys.* 15 (2013) 18973.
- [1110] D.H. Wang, J.K. Kim, J.H. Seo, I. Park, B.H. Hong, J.H. Park, A.J. Heeger, *Angew. Chem. Int. Ed.* 52 (2013) 2874.
- [1111] S. Qu, M. Li, L. Xie, X. Huang, J. Yang, N. Wang, S. Yang, *ACS Nano* 7 (2013) 4070.
- [1112] J. Liu, Y. Xue, Y. Gao, D. Yu, M. Durstock, L. Dai, *Adv. Mater.* 24 (2012) 2228.
- [1113] S.S. Li, K.H. Tu, C.C. Lin, C.W. Chen, M. Chhowalla, *ACS Nano* 4 (2010) 3169.
- [1114] C.N. Eisler, R.A. Ze'ev, M.T. Sheldon, X. Zhang, H.A. Atwater, *Energy Environ. Sci.* 7 (2014) 3600.
- [1115] S. Roland, S. Neubert, S. Albrecht, B. Stannowski, M. Seger, A. Facchetti, R. Schlattmann, B. Rech, D. Neher, *Adv. Mater.* 27 (2015) 1262.
- [1116] X. Che, X. Xiao, J.D. Zimmerman, D. Fan, S.R. Forrest, *Adv. Energy Mater.* 4 (2014) 1400568.
- [1117] C.-C. Chen, W.-H. Chang, K. Yoshimura, K. Ohya, J. You, J. Gao, Z. Hong, Y. Yang, *Adv. Mater.* 26 (2014) 5670.
- [1118] V.S. Gevaerts, A. Furlan, M.M. Wienk, M. Turbiez, R.A. Janssen, *Adv. Mater.* 24 (2012) 2130.
- [1119] J. You, L. Dou, K. Yoshimura, T. Kato, K. Ohya, T. Moriarty, K. Emery, C.-C. Chen, J. Gao, G. Li, Y. Yang, *Nat. Commun.* 4 (2013) 1446.
- [1120] S.W. Tong, Y. Wang, Y. Zheng, M.-F. Ng, K.P. Loh, *Adv. Funct. Mater.* 21 (2011) 4430.
- [1121] V.C. Tung, J. Kim, L.J. Cote, J. Huang, *J. Am. Chem. Soc.* 133 (2011) 9262.
- [1122] V.C. Tung, J. Kim, J. Huang, *Adv. Energy Mater.* 2 (2012) 299.
- [1123] K.L. Chopra, S. Major, D.K. Pandya, *Thin Solid Films* 102 (1983) 1.
- [1124] B.G. Lewis, D.C. Paine, *MRS Bull.* 25 (2000) 22.
- [1125] R.G. Gordon, *MRS Bull.* 25 (2000) 52.
- [1126] D.S. Hecht, L. Hu, G. Irvin, *Adv. Mater.* 23 (2011) 1482.
- [1127] S. Pang, Y. Hernandez, X. Feng, K. Müllen, *Adv. Mater.* 23 (2011) 2779.
- [1128] J.K. Wassei, R.B. Kaner, *Mater. Today* 13 (2010) 52.

- [1129] X. Wang, L. Zhi, N. Tsao, Ž. Tomović, J. Li, K. Müllen, *Angew. Chem. Int. Ed.* 47 (2008) 2990.
- [1130] X. Li, Y. Zhu, W. Cai, M. Borysian, B. Han, D. Chen, R.D. Piner, L. Colombo, R.S. Ruoff, *Nano Lett.* 9 (2009) 4359.
- [1131] C. Gómez-Navarro, J.C. Meyer, R.S. Sundaram, A. Chuvilin, S. Kurasch, M. Burghard, K. Kern, U. Kaiser, *Nano Lett.* 10 (2010) 1144.
- [1132] L. Hu, D.S. Hecht, G. Grüner, *Nano Lett.* 4 (2004) 2513.
- [1133] X. Han, Y. Chen, H. Zhu, C. Preston, J. Wan, Z. Fang, L. Hu, *Nanotechnology* 24 (2013) 205304.
- [1134] B. Dan, G.C. Irvin, M. Pasquali, *ACS Nano* 3 (2009) 835.
- [1135] S. De, P.J. King, P.E. Lyons, U. Khan, J.N. Coleman, *ACS Nano* 4 (2010) 7064.
- [1136] J.D. Caldwell, T.J. Anderson, J.C. Culbertson, G.G. Jernigan, K.D. Hobart, F.J. Kub, M.J. Tadjer, J.L. Tedesco, J.K. Hite, M.A. Mastro, *ACS Nano* 4 (2010) 1108.
- [1137] G.J. Fechine, I. Martin-Fernandez, G. Yiapanis, R. Bentini, E.S. Kulkarni, R.V.B. de Oliveira, X. Hu, I. Yarovsky, A.H.C. Neto, B. Özyilmaz, *Carbon* 83 (2015) 224.
- [1138] D. Lee, H. Lee, Y. Ahn, Y. Lee, *Carbon* 81 (2015) 439.
- [1139] E.H. Lock, M. Baraket, M. Laskoski, S.P. Mulvaney, W.K. Lee, P.E. Sheehan, D.R. Hines, J.T. Robinson, J. Tosado, M.S. Fuhrer, *Nano Lett.* 12 (2011) 102.
- [1140] S. Gilje, S. Han, M. Wang, K.L. Wang, R.B. Kaner, *Nano Lett.* 7 (2007) 3394.
- [1141] S. De, J.N. Coleman, *ACS Nano* 4 (2010) 2713.
- [1142] H.E. Unalan, G. Fanchini, A. Kanwal, A. Du Pasquier, M. Chhowalla, *Nano Lett.* 6 (2006) 677.
- [1143] S. De, J.N. Coleman, *MRS Bull.* 36 (2011) 774.
- [1144] Z. Wu, Y. Han, R. Huang, X. Chen, Y. Guo, Y. He, W. Li, Y. Cai, N. Wang, *Nanoscale* 6 (2014) 13196.
- [1145] F. Schedin, A.K. Geim, S.V. Morozov, E.W. Hill, P. Blake, M.I. Katsnelson, K.S. Novoselov, *Nat. Mater.* 6 (2007) 652.
- [1146] J. Shim, C.H. Lui, T.Y. Ko, Y.-J. Yu, P. Kim, T.F. Heinz, S. Ryu, *Nano Lett.* 12 (2012) 648.
- [1147] H.E. Romero, N. Shen, P. Joshi, H.R. Gutierrez, S.A. Tadigadapa, J.O. Sofo, P.C. Klund, *ACS Nano* 2 (2008) 2037.
- [1148] V.C. Tung, M.J. Allen, Y. Yang, R.B. Kaner, *Nat. Nanotechnol.* 4 (2009) 25.
- [1149] S. Wang, P.K. Ang, Z. Wang, A.L.L. Tang, J.T. Thong, K.P. Loh, *Nano Lett.* 10 (2009) 92.
- [1150] Q. Zhang, J. Jie, S. Diao, Z. Shao, Q. Zhang, L. Wang, W. Deng, W. Hu, H. Xia, X. Yuan, *ACS Nano* 9 (2015) 1561.
- [1151] F. Bausi, A. Schlierf, E. Treossi, M.G. Schwab, V. Palermo, F. Cacialli, *Org. Electron.* 18 (2015) 53.
- [1152] Z. Shan, Q. Li, Z. Zhao, Z. Wang, Y. Wu, W. Cai, *Carbon* 84 (2015) 9.
- [1153] C.-L. Hsu, C.-T. Lin, J.-H. Huang, C.-W. Chu, K.-H. Wei, L.-J. Li, *ACS Nano* 6 (2012) 5031.
- [1154] Y. Wang, S.W. Tong, X.F. Xu, B. Oezylmaz, K.P. Loh, *Adv. Mater.* 23 (2011) 1514.
- [1155] Y. Wang, X. Chen, Y. Zhong, F. Zhu, K.P. Loh, *Appl. Phys. Lett.* 95 (2009) 063302.
- [1156] H. Park, P.R. Brown, V. Bulovic, J. Kong, *Nano Lett.* 12 (2012) 133.
- [1157] Y.-Y. Choi, S.J. Kang, H.-K. Kim, W.M. Choi, S.-I. Na, *Sol. Energy Mater. Sol. Cells* 96 (2012) 281.
- [1158] L. Gomez De Arco, Y. Zhang, C.W. Schlenker, K. Ryu, M.E. Thompson, C. Zhou, *ACS Nano* 4 (2010) 2865.
- [1159] D. Zhang, F. Xie, P. Lin, W.C.H. Choy, *ACS Nano* 7 (2013) 1740.
- [1160] Y. Wu, X. Zhang, J. Jie, C. Xie, X. Zhang, B. Sun, Y. Wang, P. Gao, *J. Phys. Chem. C* 117 (2013) 11968.
- [1161] Y.-Y. Lee, K.-H. Tu, C.-C. Yu, S.-S. Li, J.-Y. Hwang, C.-C. Lin, K.-H. Chen, L.-C. Chen, H.-L. Chen, C.-W. Chen, *ACS Nano* 5 (2011) 6564.
- [1162] M. Choe, B.H. Lee, G. Jo, J. Park, W. Park, S. Lee, W.-K. Hong, M.-J. Seong, Y.H. Kahng, K. Lee, T. Lee, *Org. Electron.* 11 (2010) 1864.
- [1163] Z. Wang, C.P. Puls, N.E. Staley, Y. Zhang, A. Todd, J. Xu, C.A. Howsare, M.J. Hollander, J.A. Robinson, Y. Liu, *Phys. E—Low-Dimens. Syst. Nanostruct.* 44 (2011) 521.
- [1164] Y. Xu, G. Long, L. Huang, Y. Huang, X. Wan, Y. Ma, Y. Chen, *Carbon* 48 (2010) 3308.
- [1165] Z. Yin, S. Wu, X. Zhou, X. Huang, Q. Zhang, F. Boey, H. Zhang, *Small* 6 (2010) 307.
- [1166] Z. Yin, S. Sun, T. Salim, S. Wu, X. Huang, Q. He, Y.M. Lam, H. Zhang, *ACS Nano* 4 (2010) 5263.
- [1167] Q. Zhang, X. Wan, F. Xing, L. Huang, G. Long, N. Yi, W. Ni, Z. Liu, J. Tian, Y. Chen, *Nano Res.* 6 (2013) 478.
- [1168] G. Kalita, M. Matsushima, H. Uchida, K. Wakita, M. Umeno, *J. Mater. Chem.* 20 (2010) 9713.
- [1169] B. O'regan, M. Grätzel, *Nature* 353 (1991) 737.
- [1170] M. Grätzel, *Nature* 414 (2001) 338.
- [1171] J. Burschka, N. Pellet, S.-J. Moon, R. Humphry-Baker, P. Gao, M.K. Nazeeruddin, M. Grätzel, *Nature* 499 (2013) 316.
- [1172] B.E. Hardin, H.J. Snaith, M.D. McGehee, *Nat. Photonics* 6 (2012) 162.
- [1173] A. Hagfeldt, G. Boschloo, L. Sun, L. Kloo, H. Pettersson, *Chem. Rev.* 110 (2010) 6595.
- [1174] J.D. Roy-Mayhew, I.A. Aksay, *Chem. Rev.* 114 (2014) 6323.
- [1175] H. Wang, Y.H. Hu, *Energy Environ. Sci.* 5 (2012) 8182.
- [1176] H. Choi, H. Kim, S. Hwang, Y. Han, M. Jeon, *J. Mater. Chem.* 21 (2011) 7548.
- [1177] H.-S. Jang, J.-M. Yun, D.-Y. Kim, D.-W. Park, S.-I. Na, S.-S. Kim, *Electrochim. Acta* 81 (2012) 301.
- [1178] D.W. Zhang, X.D. Li, H.B. Li, S. Chen, Z. Sun, X.J. Yin, S.M. Huang, *Carbon* 49 (2011) 5382.
- [1179] J.D. Roy-Mayhew, D.J. Bozym, C. Punckt, I.A. Aksay, *ACS Nano* 4 (2010) 6203.
- [1180] M.J. Ju, I.-Y. Jeon, J.C. Kim, K. Lim, H.-J. Choi, S.-M. Jung, I.T. Choi, Y.K. Eom, Y.J. Kwon, J. Ko, J.-J. Lee, H.K. Kim, J.-B. Baek, *Adv. Mater.* 26 (2014) 3055.
- [1181] M.-H. Yeh, L.-Y. Lin, L.-Y. Chang, Y.-A. Leu, W.-Y. Cheng, J.-J. Lin, K.-C. Ho, *ChemPhysChem* 15 (2014) 1175.
- [1182] H.-W. Liu, S.-P. Liang, T.-J. Wu, H. Chang, P.-K. Kao, C.-C. Hsu, J.-Z. Chen, P.-T. Chou, I.C. Cheng, *ACS Appl. Mater. Interfaces* 6 (2014) 15105.
- [1183] J.E. Trancik, S.C. Barton, J. Hone, *Nano Lett.* 8 (2008) 982.
- [1184] S.-Y. Jang, Y.-G. Kim, D.Y. Kim, H.-G. Kim, S.M. Jo, *ACS Appl. Mater. Interfaces* 4 (2012) 3500.
- [1185] H.-K. Seo, M. Song, S. Ameen, M.S. Akhtar, H.S. Shin, *Chem. Eng. J.* 222 (2013) 464.
- [1186] W.-Y. Cheng, C.-C. Wang, S.-Y. Lu, *Carbon* 54 (2013) 291.
- [1187] M. Song, S. Ameen, M.S. Akhtar, H.-K. Seo, H.-S. Shin, *Mater. Res. Bull.* 48 (2013) 4538.
- [1188] W. Wei, K. Sun, Y.H. Hu, *J. Mater. Chem. A* 2 (2014) 16842.
- [1189] K. Yu, Z. Wen, H. Pu, G. Lu, Z. Bo, H. Kim, Y. Qian, E. Andrew, S. Mao, J. Chen, *J. Mater. Chem. A* 1 (2013) 188.
- [1190] H. Zheng, C.Y. Neo, X. Mei, J. Qiu, J. Ouyang, *J. Mater. Chem.* 22 (2012) 14465.
- [1191] X. Pan, K. Zhu, G. Ren, N. Islam, J. Warzywoda, Z. Fan, *J. Mater. Chem. A* 2 (2014) 12746.
- [1192] H. Wang, K. Sun, F. Tao, D.J. Stacchiola, Y.H. Hu, *Angew. Chem. Int. Ed.* 52 (2013) 9210.
- [1193] J. Ma, C. Li, F. Yu, J. Chen, *J. Power Sources* 273 (2015) 1048.
- [1194] H.-J. Ahn, I.-H. Kim, J.-C. Yoon, S.-I. Kim, J.-H. Jang, *Chem. Commun.* 50 (2014) 2412.
- [1195] F. Gong, H. Wang, Z.-S. Wang, *Phys. Chem. Chem. Phys.* 13 (2011) 17676.
- [1196] D. Van-Duong, H. Nguyen Thi Quynh, L.L. Larina, J.-K. Lee, H.-S. Choi, *Nanoscale* 5 (2013) 12237.
- [1197] M.-Y. Yen, C.-C. Teng, M.-C. Hsiao, P.-I. Liu, W.-P. Chuang, C.-C.M. Ma, C.-K. Hsieh, M.-C. Tsai, C.-H. Tsai, *J. Mater. Chem.* 21 (2011) 12880.
- [1198] V. Tjoa, J. Chua, S.S. Pramana, J. Wei, S.G. Mhaisalkar, N. Mathews, *ACS Appl. Mater. Interfaces* 4 (2012) 3447.
- [1199] G. Yue, J. Wu, Y. Xiao, M. Huang, J. Lin, L. Fan, Z. Lan, *Electrochim. Acta* 92 (2013) 64.
- [1200] R. Bajpai, S. Roy, P. Kumar, P. Bajpai, N. Kulshrestha, J. Rafiee, N. Koratkar, D.S. Misra, *ACS Appl. Mater. Interfaces* 3 (2011) 3884.
- [1201] Y.-G. Kim, Z.A. Akbar, D.Y. Kim, S.M. Jo, S.-Y. Jang, *ACS Appl. Mater. Interfaces* 5 (2013) 2053.
- [1202] M. Al-Mamun, J.-H. Lim, Y.-E. Sung, S.-R. Kim, *Chem. Lett.* 42 (2013) 31.
- [1203] V.-D. Dao, L.L. Larina, K.-D. Jung, J.-K. Lee, H.-S. Choi, *Nanoscale* 6 (2014) 477.
- [1204] R. Bajpai, S. Roy, N. Koratkar, D.S. Misra, *Carbon* 56 (2013) 56.
- [1205] Q. Chang, Z. Ma, J. Wang, Y. Yan, W. Shi, Q. Chen, Y. Huang, Q. Yu, L. Huang, *Electrochim. Acta* 151 (2015) 459.
- [1206] G. Wang, J. Zhang, S. Kuang, S. Liu, S. Zhuo, *J. Power Sources* 269 (2014) 473.
- [1207] X. Miao, K. Pan, G. Wang, Y. Liao, L. Wang, W. Zhou, B. Jiang, Q. Pan, G. Tian, *Chem. Eur. J.* 20 (2014) 474.
- [1208] X. Duan, Z. Gao, J. Chang, D. Wu, P. Ma, J. He, F. Xu, S. Gao, K. Jiang, *Electrochim. Acta* 114 (2013) 173.
- [1209] G. Yue, J.-Y. Lin, S.-Y. Tai, Y. Xiao, J. Wu, *Electrochim. Acta* 85 (2012) 162.
- [1210] H. Bi, W. Zhao, S. Sun, H. Cui, T. Lin, F. Huang, X. Xie, M. Jiang, *Carbon* 61 (2013) 116.
- [1211] G. Li, X. Chen, G. Gao, *Nanoscale* 6 (2014) 3283.
- [1212] S.-Q. Guo, T.-Z. Jing, X. Zhang, X.-B. Yang, Z.-H. Yuan, F.-Z. Hu, *Nanoscale* 6 (2014) 14433.
- [1213] Y.Y. Dou, G.R. Li, J. Song, X.P. Gao, *Phys. Chem. Chem. Phys.* 14 (2012) 1339.
- [1214] Q. Zhang, Y. Liu, Y. Duan, N. Fu, Q. Liu, Y. Fang, Q. Sun, Y. Lin, *RSC Adv.* 4 (2014) 15091.
- [1215] J. Velten, A.J. Mozer, D. Li, D. Officer, G. Wallace, R. Baughman, A. Zakhidov, *Nanotechnology* 23 (2012) 085201.
- [1216] J. Ma, L. Zhou, C. Li, J. Yang, T. Meng, H. Zhou, M. Yang, F. Yu, J. Chen, *J. Power Sources* 247 (2014) 999.
- [1217] L.-H. Chang, C.-K. Hsieh, M.-C. Hsiao, J.-C. Chiang, P.-I. Liu, K.-K. Ho, C.-C.M. Ma, M.-Y. Yen, M.-C. Tsai, C.-H. Tsai, *J. Power Sources* 222 (2013) 518.
- [1218] M.-H. Yeh, L.-Y. Lin, C.-L. Sun, Y.-A. Leu, J.-T. Tsai, C.-Y. Yeh, R. Vittal, K.-C. Ho, *J. Phys. Chem. C* 118 (2014) 16626.
- [1219] G. Zhu, L. Pan, T. Lu, T. Xu, Z. Sun, *J. Mater. Chem.* 21 (2011) 14869.
- [1220] X. Miao, K. Pan, G. Wang, Y. Liao, G. Tian, G. Wang, *Electrochim. Acta* 96 (2013) 155.
- [1221] W. Sun, T. Peng, Y. Liu, N. Huang, S. Guo, X. Zhao, *Carbon* 77 (2014) 18.
- [1222] M.-S. Wu, Y.-J. Zheng, *Phys. Chem. Chem. Phys.* 15 (2013) 1782.
- [1223] F. Gong, X. Xu, G. Zhou, Z.-S. Wang, *Phys. Chem. Chem. Phys.* 15 (2013) 546.
- [1224] S.P. Lim, A. Pandikumar, Y.S. Lim, N.M. Huang, H.N. Lim, *Sci. Rep.* 4 (2014) 5305.
- [1225] C.-Y. Liu, K.-C. Huang, P.-H. Chung, C.-C. Wang, C.-Y. Chen, R. Vittal, C.-G. Wu, W.-Y. Chiu, K.-C. Ho, *J. Power Sources* 217 (2012) 152.
- [1226] B. He, Q. Tang, M. Wang, C. Ma, S. Yuan, *J. Power Sources* 256 (2014) 8.
- [1227] W. Sun, T. Peng, Y. Liu, S. Xu, J. Yuan, S. Guo, X.-Z. Zhao, *J. Mater. Chem. A* 1 (2013) 2762.
- [1228] H. Cai, Q. Tang, B. He, M. Wang, S. Yuan, H. Chen, *Electrochim. Acta* 121 (2014) 136.
- [1229] G. Wang, W. Xing, S. Zhuo, *Electrochim. Acta* 66 (2012) 151.
- [1230] M. Wang, Q. Tang, P. Xu, B. He, L. Lin, H. Chen, *Electrochim. Acta* 137 (2014) 175.
- [1231] B. He, Q. Tang, M. Wang, H. Chen, S. Yuan, *ACS Appl. Mater. Interfaces* 6 (2014) 8230.
- [1232] K.S. Lee, Y. Lee, J.Y. Lee, J.-H. Ahn, J.H. Park, *ChemSusChem* 5 (2012) 379.
- [1233] A. Nikolakopoulou, D. Tasis, L. Sygellou, V. Dracopoulos, C. Galiotis, P. Lianos, *Electrochim. Acta* 111 (2013) 698.
- [1234] M.-H. Yeh, C.-L. Sun, J.-S. Su, L.-Y. Lin, C.-P. Lee, C.-Y. Chen, C.-G. Wu, R. Vittal, K.-C. Ho, *Carbon* 50 (2012) 4192.
- [1235] M. Wang, Q. Tang, H. Chen, B. He, *Electrochim. Acta* 125 (2014) 510.

- [1236] X. Li, L. Liu, G. Liu, Y. Rong, Y. Yang, H. Wang, Z. Ku, M. Xu, C. Zhong, H. Han, *Adv. Funct. Mater.* 23 (2013) 3344.
- [1237] Y. Peng, J. Zhong, K. Wang, B. Xue, Y.-B. Cheng, *Nano Energy* 2 (2013) 235.
- [1238] X. Xu, D. Huang, K. Cao, M. Wang, S.M. Zakeeruddin, M. Grätzel, *Sci. Rep.* 3 (2013) 1489.
- [1239] W. Liu, Y. Fang, P. Xu, Y. Lin, X. Yin, G. Tang, M. He, *ACS Appl. Mater. Interfaces* 6 (2014) 16249.
- [1240] L. Chen, C.X. Guo, Q. Zhang, Y. Lei, J. Xie, S. Ee, G. Guai, Q. Song, C.M. Li, *ACS Appl. Mater. Interfaces* 5 (2013) 2047.
- [1241] H. Zheng, C.Y. Neo, J. Ouyang, *ACS Appl. Mater. Interfaces* 5 (2013) 6657.
- [1242] J. Ma, C. Li, F. Yu, J. Chen, *ChemSusChem* 7 (2014) 3304.
- [1243] M. Dürr, A. Bamedi, A. Yasuda, G. Nelles, *Appl. Phys. Lett.* 84 (2004) 3397.
- [1244] K.-S. Ahn, S.J. Yoo, M.-S. Kang, J.-W. Lee, Y.-E. Sung, *J. Power Sources* 168 (2007) 533.
- [1245] W. Hong, Y. Xu, G. Lu, C. Li, G. Shi, *Electrochem. Commun.* 10 (2008) 1555.
- [1246] P.-T. Shih, R.-X. Dong, S.-Y. Shen, R. Vittal, J.-J. Lin, K.-C. Ho, *J. Mater. Chem. A* 2 (2014) 8742.
- [1247] M. Al-Mamun, J.-Y. Kim, Y.-E. Sung, J.-J. Lee, S.-R. Kim, *Chem. Phys. Lett.* 561 (2013) 115.
- [1248] R. Cruz, J.P. Araujo, L. Andrade, A. Mendes, *J. Mater. Chem. A* 2 (2014) 2028.
- [1249] L. Kavan, J.H. Yum, M. Grätzel, *ACS Nano* 5 (2011) 165.
- [1250] D. Van-Duong, N. Lam Van, E.-T. Kim, J.-K. Lee, H.-S. Choi, *ChemSusChem* 6 (2013) 1316.
- [1251] A. Kaniyoor, S. Ramaprabhu, *Nano Energy* 1 (2012) 757.
- [1252] J.-Y. Lin, C.-Y. Chan, S.-W. Chou, *Chem. Commun.* 49 (2013) 1440.
- [1253] L. Kavan, J.-H. Yum, M. Grätzel, *ACS Appl. Mater. Interfaces* 4 (2012) 6999.
- [1254] L. Kavan, J.-H. Yum, M.K. Nazeeruddin, M. Grätzel, *ACS Nano* 5 (2011) 9171.
- [1255] L. Kavan, J.-H. Yum, M. Grätzel, *Nano Lett.* 11 (2011) 5501.
- [1256] B. Tang, G. Hu, *J. Power Sources* 220 (2012) 95.
- [1257] J. Song, Z. Yin, Z. Yang, P. Amaladass, S. Wu, J. Ye, Y. Zhao, W.-Q. Deng, H. Zhang, X.-W. Liu, *Chem. Eur. J.* 17 (2011) 10832.
- [1258] Z. He, P. Hung, J. Liu, N. Thuc-Quyen, T.T.Y. Tan, *Adv. Mater.* 25 (2013) 6900.
- [1259] Y. Kusumawati, M.A. Martoprawiro, T. Pauporte, *J. Phys. Chem. C* 118 (2014) 9974.
- [1260] M. Zhu, X. Li, W. Liu, Y. Cui, *J. Power Sources* 262 (2014) 349.
- [1261] N. Yang, J. Zhai, D. Wang, Y. Chen, L. Jiang, *ACS Nano* 4 (2010) 887.
- [1262] G. Cheng, M.S. Akhtar, O.B. Yang, F.J. Stadler, *ACS Appl. Mater. Interfaces* 5 (2013) 6635.
- [1263] X. Luan, L. Chen, J. Zhang, G. Qu, J.C. Flake, Y. Wang, *Electrochim. Acta* 111 (2013) 216.
- [1264] Z. He, G. Guai, J. Liu, C. Guo, J.S.C. Loo, C.M. Li, T.T.Y. Tan, *Nanoscale* 3 (2011) 4613.
- [1265] M. Zhu, X. Li, W. Liu, Y. Cui, *J. Power Sources* 262 (2014) 349.
- [1266] S.R. Kim, M.K. Parvez, M. Chhowalla, *Chem. Phys. Lett.* 483 (2009) 124.
- [1267] S. Chatterjee, A.K. Patra, A. Bhaumik, A.K. Nandi, *Chem. Commun.* 49 (2013) 4646.
- [1268] S. Sun, L. Gao, Y. Liu, *Appl. Phys. Lett.* 96 (2010) 083113.
- [1269] J. Chang, J. Yang, P. Ma, D. Wu, L. Tian, Z. Gao, K. Jiang, L. Yang, *J. Colloid Interface Sci.* 394 (2013) 231.
- [1270] Y.-B. Tang, C.-S. Lee, J. Xu, Z.-T. Liu, Z.-H. Chen, Z. He, Y.-L. Cao, G. Yuan, H. Song, L. Chen, *ACS Nano* 4 (2010) 3482.
- [1271] J. Fan, S. Liu, J. Yu, *J. Mater. Chem.* 22 (2012) 17027.
- [1272] A. Du, Y.H. Ng, N.J. Bell, Z. Zhu, R. Amal, S.C. Smith, *J. Phys. Chem. Lett.* 2 (2011) 894.
- [1273] S. Sun, L. Gao, Y. Liu, *Appl. Phys. Lett.* 96 (2010) 083113.
- [1274] J. Zhao, J. Wu, M. Zheng, J. Huo, Y. Tu, *Electrochim. Acta* 156 (2015) 261.
- [1275] M.-Y. Yen, M.-C. Hsiao, S.-H. Liao, P.-I. Liu, H.-M. Tsai, C.-C.M. Ma, N.-W. Pu, M.-D. Ger, *Carbon* 49 (2011) 3597.
- [1276] L. Chen, Y. Zhou, W. Tu, Z. Li, C. Bao, H. Dai, T. Yu, J. Liu, Z. Zou, *Nanoscale* 5 (2013) 3481.
- [1277] Y. Liu, Y. Cheng, W. Shu, Z. Peng, K. Chen, J. Zhou, W. Chen, G.S. Zakharova, *Nanoscale* 6 (2014) 6755.
- [1278] J. Wu, Z. Lan, J. Lin, M. Huang, Y. Huang, L. Fan, G. Luo, *Chem. Rev.* 115 (2015) 2136.
- [1279] A. Yella, H.-W. Lee, H.N. Tsao, C. Yi, A.K. Chandiran, M.K. Nazeeruddin, E.W.-G. Diau, C.-Y. Yeh, S.M. Zakeeruddin, M. Grätzel, *Science* 334 (2011) 629.
- [1280] S. Mathew, A. Yella, P. Gao, R. Humphry-Baker, F.E. Curchod-Basile, N. Ashari-Astani, I. Tavernelli, U. Rothlisberger, K. Nazeeruddin, M. Grätzel, *Nat. Chem.* 6 (2014) 242.
- [1281] S.-Q. Bi, F.-L. Meng, Y.-Z. Zheng, X. Han, X. Tao, J.-F. Chen, *J. Power Sources* 272 (2014) 485.
- [1282] J. Gun, S.A. Kulkarni, W. Xiu, S.K. Batabyal, S. Sladkevich, P.V. Prikhodchenko, V. Gutkin, O. Lev, *Electrochem. Commun.* 19 (2012) 108.
- [1283] J.A. Velten, J. Carretero-González, E. Castillo-Martínez, J. Bykova, A. Cook, R. Baughman, A. Zakhidov, *J. Phys. Chem. C* 115 (2011) 25125.
- [1284] B. Lin, H. Shang, F. Chu, Y. Ren, N. Yuan, B. Jia, S. Zhang, X. Yu, Y. Wei, J. Ding, *Electrochim. Acta* 134 (2014) 209.
- [1285] M.-H. Jung, M.G. Kang, M.-J. Chu, *J. Mater. Chem.* 22 (2012) 16477.
- [1286] L.J. Brennan, S.T. Barwich, A. Satti, A. Faure, Y.K. Gun'ko, *J. Mater. Chem. A* 1 (2013) 8379.
- [1287] I. Ahmad, U. Khan, Y.K. Gun'ko, *J. Mater. Chem.* 21 (2011) 16990.
- [1288] O. Byrne, I. Ahmad, P.K. Suroliya, Y.K. Gun'ko, K.R. Thampi, *Sol. Energy* 110 (2014) 239.
- [1289] C.Y. Neo, J. Ouyang, *Carbon* 54 (2013) 48.
- [1290] C.Y. Neo, N.K. Gopalan, J. Ouyang, *J. Mater. Chem. A* 2 (2014) 9226.
- [1291] M.S. Akhtar, S. Kwon, F.J. Stadler, O.B. Yang, *Nanoscale* 5 (2013) 5403.
- [1292] S. Yuan, Q. Tang, B. Hu, C. Ma, J. Duan, B. He, *J. Mater. Chem. A* 2 (2014) 2814.
- [1293] S. Yuan, Q. Tang, B. He, Y. Zhao, *J. Power Sources* 260 (2014) 225.
- [1294] M.A. Green, A. Ho-Baillie, H.J. Snaith, *Nat. Photonics* 8 (2014) 506.
- [1295] A. Kojima, K. Teshima, Y. Shirai, T. Miyasaka, *J. Am. Chem. Soc.* 131 (2009) 6050.
- [1296] M.M. Lee, J. Teuscher, T. Miyasaka, T.N. Murakami, H.J. Snaith, *Science* 338 (2012) 643.
- [1297] N.J. Jeon, J.H. Noh, Y.C. Kim, W.S. Yang, S. Ryu, S.I. Seok, *Nat. Mater.* 13 (2014) 897.
- [1298] V. Rofati, S. Colella, G. Lerario, L. De Marco, A. Rizzo, A. Listorti, G. Gigli, *Energy Environ. Sci.* 7 (2014) 1889.
- [1299] J.M. Ball, M.M. Lee, A. Hey, H.J. Snaith, *Energy Environ. Sci.* 6 (2013) 1739.
- [1300] T. Leijtens, G.E. Eperon, S. Pathak, A. Abate, M.M. Lee, H.J. Snaith, *Nat. Commun.* 4 (2013) 2885.
- [1301] M. Liu, M.B. Johnston, H.J. Snaith, *Nature* 501 (2013) 395.
- [1302] D. Liu, T.L. Kelly, *Nat. Photonics* 8 (2014) 133.
- [1303] Q. Chen, H. Zhou, Z. Hong, S. Luo, H.-S. Duan, H.-H. Wang, Y. Liu, G. Li, Y. Yang, *J. Am. Chem. Soc.* 136 (2014) 622.
- [1304] S. Luo, W.A. Daoud, *J. Mater. Chem. A* 3 (2015) 8992.
- [1305] H.S. Jung, N.G. Park, *Small* 11 (2015) 10.
- [1306] S. Kazim, M.K. Nazeeruddin, M. Grätzel, S. Ahmad, *Angew. Chem.—Int. Ed.* 53 (2014) 2812.
- [1307] A. Mei, X. Li, L. Liu, Z. Ku, T. Liu, Y. Rong, M. Xu, M. Hu, J. Chen, Y. Yang, M. Grätzel, H. Han, *Science* 345 (2014) 295.
- [1308] G. Xing, N. Mathews, S. Sun, S.S. Lim, Y.M. Lam, M. Grätzel, S. Mhaisalkar, T.C. Sum, *Science* 342 (2013) 344.
- [1309] S.D. Stranks, G.E. Eperon, G. Grancini, C. Menelaou, M.J.P. Alcocer, T. Leijtens, L.M. Herz, A. Petrozza, H.J. Snaith, *Science* 342 (2013) 341.
- [1310] P.E. Shaw, A. Ruseckas, I.D.W. Samuel, *Adv. Mater.* 20 (2008) 3516.
- [1311] D. Zhitomirsky, O. Voznyy, S. Hoogland, E.H. Sargent, *ACS Nano* 7 (2013) 5282.
- [1312] G. Hodes, *Science* 342 (2013) 317.
- [1313] M. Grätzel, *Nat. Mater.* 13 (2014) 838.
- [1314] P. Qin, S. Tanaka, S. Ito, N. Tetreault, K. Manabe, H. Nishino, M.K. Nazeeruddin, M. Grätzel, *Nat. Commun.* 5 (2014) 3834.
- [1315] Z. Zhu, J. Ma, Z. Wang, C. Mu, Z. Fan, L. Du, Y. Bai, L. Fan, H. Yan, D.L. Phillips, S. Yang, *J. Am. Chem. Soc.* 136 (2014) 3760.
- [1316] J. Liu, Y. Xue, L. Dai, *J. Phys. Chem. Lett.* 3 (2012) 1928.
- [1317] Z. Wu, S. Bai, J. Xiang, Z. Yuan, Y. Yang, W. Cui, X. Gao, Z. Liu, Y. Jin, B. Sun, *Nanoscale* 6 (2014) 10505.
- [1318] P. Docampo, J.M. Ball, M. Darwich, G.E. Eperon, H.J. Snaith, *Nat. Commun.* 4 (2013) 2761.
- [1319] W. Li, H. Dong, X. Guo, N. Li, J. Li, G. Niu, L. Wang, *J. Mater. Chem. A* 2 (2014) 20105.
- [1320] H. Li, K. Fu, A. Hagfeldt, M. Grätzel, S.G. Mhaisalkar, A.C. Grimsdale, *Angew. Chem. Int. Ed.* 53 (2014) 4085.
- [1321] H.-S. Kim, I. Mora-Sero, V. Gonzalez-Pedro, F. Fabregat-Santiago, E.J. Juarez-Perez, N.-G. Park, J. Bisquert, *Nat. Commun.* 4 (2013) 2242.
- [1322] E. Edri, S. Kirmayer, S. Mukhopadhyay, K. Gartsman, G. Hodes, D. Cahen, *Nat. Commun.* 5 (2014) 3461.
- [1323] B.S. Ong, C. Li, Y. Li, Y. Wu, R. Loutfy, *J. Am. Chem. Soc.* 129 (2007) 2750.
- [1324] J.T.-W. Wang, J.M. Ball, E.M. Barea, A. Abate, J.A. Alexander-Webber, J. Huang, M. Saliba, I. Mora-Sero, J. Bisquert, H.J. Snaith, R.J. Nicholas, *Nano Lett.* 14 (2014) 724.
- [1325] X. Wang, K. Jiang, G. Shen, *Mater. Today* 18 (2015) 265.
- [1326] L. Nyholm, G. Nyström, A. Mitranyan, M. Strømme, *Adv. Mater.* 23 (2011) 3751.
- [1327] L. Li, Z. Wu, S. Yuan, X.-B. Zhang, *Energy Environ. Sci.* 7 (2014) 2101.
- [1328] X. Wang, X. Lu, B. Liu, D. Chen, Y. Tong, G. Shen, *Adv. Mater.* 26 (2014) 4763.
- [1329] Z. Niu, L. Zhang, L. Liu, B. Zhu, H. Dong, X. Chen, *Adv. Mater.* 25 (2013) 4035.
- [1330] K. Shu, C. Wang, S. Li, C. Zhao, Y. Yang, H. Liu, G. Wallace, *J. Mater. Chem. A* 3 (2015) 4428.
- [1331] M. Lee, B.H. Wee, J.D. Hong, *Adv. Energy Mater.* 5 (2014) 1401890.
- [1332] K. Rana, S.D. Kim, J.-H. Ahn, *Nanoscale* 7 (2015) 7065.
- [1333] N. Li, Z. Chen, W. Ren, F. Li, H.-M. Cheng, *Proc. Natl. Acad. Sci. USA* 109 (2012) 17360.
- [1334] H. Tang, J.-P. Tu, X.-Y. Liu, Y.-J. Zhang, S. Huang, W.-Z. Li, X.-I. Wang, C.-D. Gu, *J. Mater. Chem. A* 2 (2014) 5834.
- [1335] W. Qiu, J. Jiao, J. Xia, H. Zhong, L. Chen, *Chem. Eur. J.* 21 (2015) 4359.
- [1336] G. Zhou, L. Li, D.W. Wang, X.Y. Shan, S. Pei, F. Li, H.M. Cheng, *Adv. Mater.* 27 (2015) 641.
- [1337] G. Zhou, Y. Zhao, A. Manthiram, *Adv. Energy Mater.* 5 (2015) 1402263.
- [1338] G. Zhou, L. Li, C. Ma, S. Wang, Y. Shi, N. Koratkar, W. Ren, F. Li, H.-M. Cheng, *Nano Energy* 11 (2015) 356.
- [1339] H. Wang, G. Wang, Y. Ling, F. Qian, Y. Song, X. Lu, S. Chen, Y. Tong, Y. Li, *Nanoscale* 5 (2013) 10283.
- [1340] Z. Liu, J. Li, F. Yan, *Adv. Mater.* 25 (2013) 4296.
- [1341] C.J. An, S.J. Kim, H.O. Choi, D.W. Kim, S.W. Jang, M.L. Jin, J.-M. Park, J.K. Choi, H.-T. Jung, *J. Mater. Chem. A* 2 (2014) 20474.
- [1342] E. Kymakis, K. Savva, M.M. Stylianakis, C. Fotakis, E. Stratakis, *Adv. Funct. Mater.* 23 (2013) 2742.
- [1343] D. Konios, C. Petridis, G. Kakavelakis, M. Sygletou, K. Savva, E. Stratakis, E. Kymakis, *Adv. Funct. Mater.* 25 (2015) 2213.
- [1344] J. Zhi, H. Cui, A. Chen, Y. Xie, F. Huang, *J. Power Sources* 281 (2015) 404.
- [1345] K.S. Lee, Y. Lee, J.Y. Lee, J.H. Ahn, J.H. Park, *ChemSusChem* 5 (2012) 379.
- [1346] X. Wang, G. Shi, *Energy Environ. Sci.* 8 (2015) 790.